Oxidative Activation of Iron- and Ruthenium-Alkynyl Complexes: Toward Square-Shaped Molecules with Four Redox-Active Metal Centres

A Thesis Submitted Towards the Degree of Doctor of Philosophy

By

Alexandre Burgun

October 2011

CONTENTS

Abstract

The synthesis of square molecules containing four redox-active metal centres and two positive charges which would be interesting as potential candidates for molecular Quantum-dot Cellular Automata (QCA) models constitutes the aim of this thesis. In this new paradigm, the binary information is encoded in the charge configuration of the QCA cell, and in the case of a molecular QCA, in the charge configuration of a single molecule.

In order to synthesise such molecules with metal centres of general formula M(PP)Cp' [M = Fe, Ru; PP = dppe, $(PPh_3)_2$; Cp' = Cp, Cp*], new synthetic methods have been developed. By chemically oxidising mono- or bi-metallic alkynyl complexes, radical coupling can occur, mainly depending on the nature of the metal (Fe or Ru) and the length of the carbon chain (C_2, C_4 or C_6), to give dimers with original geometry. Therefore, this thesis describes the oxidation studies of iron- and ruthenium-alkynyl complexes containing short (C_2) to long carbon chains (C_6), and the characterisations of the oxidised products.

The reactivity of the mononuclear 17-electron species $[Ru(C{\equiv}CR)(PPh_3)_2Cp]^{\bullet+}$ (**16**, R = Ph; **19**, R = Tol) and $[Fe(C{\equiv}CC{\equiv}CR)(dppe)Cp^*]^{\bullet+}$ (**2a**, R = Ph; **2b** R = Tol) was investigated, dimerisation occurring in both cases. Intermolecular radical coupling of $\mathbf{16}^{\bullet+}$ afforded a linear dimer by coupling at the C_β and C_{para} positions, whereas dimerisation of $\mathbf{2}^{\bullet+}$ gives a single dicationic complex [**27**][PF_6]$_2$ containing a squared C_4 ring centre and two Fe(dppe)Cp* units.

The reactivity of the bimetallic 35-electron species [{Cp'(dppe)M}(C≡CC≡CC≡C){M(dppe)Cp'}]$^{\bullet+}$ (M = Fe, Ru; Cp' = Cp, Cp*) was also investigated. The mixed-valence systems containing the M(dppe)Cp* (M = Fe, Ru) fragments were revealed to be stable and isolable: the first crystal structures of mixed-valence complexes with a carbon chain longer than C_4 were resolved for [{Cp*(dppe)Fe}$_2$(μ-C≡CC≡CC≡C)]PF_6 [**30**]PF_6 and [{Cp*(dppe)Fe}(C≡CC≡CC≡C){Ru(dppe)Cp*}]PF_6 [**34**]PF_6. Electronic delocalisation in these stable mixed-valence complexes, between the two metal centres and through the C_6 bridge, was revealed to be strong which was unexpected for the unsymmetrical system [**34**]PF_6. In contrast, the mixed-valence systems containing the Ru(dppe)Cp fragment were

not stable at room temperature and dimerised to afford dicationic square-shaped tetrametallic complexes with a C_4 ring centre. Two unsymmetrical dimers were characterised: one containing four Ru(dppe)Cp centres [**43**][PF_6]$_2$ and the other containing two Ru(dppe)Cp and two Fe(dppe)Cp* fragments [**44**][PF_6]$_2$. Compound [**43**][PF_6]$_2$ has been fully characterised and the positive charge revealed to be fully delocalised over the whole molecule. Even if unsymmetrical, these molecules are interesting for being potential molecular QCA models.

It has been shown that TCNQ acts as an oxidising agent for iron- and ruthenium-alkynyl complexes. The organometallic 17-e species generated further react by coupling between the cationic and anionic radical $[TCNQ]^{\bullet -}$ to give specifically TCNQ adducts. These new complexes which contain two electrophores possess unique properties. The σ-linked electron donor organometallic centre and the organic electron withdrawing group via an alkyndiyl bridge allow intramolecular charge transfer. The X-ray crystal structure analyses, electrochemistry and UV-Vis spectroscopy have been investigated and reveal the interesting properties of these molecules.

Thesis declaration

I certify that this work contains no material which has been accepted for the award of any other degree or diploma in any university or other tertiary institution and, to the best of my knowledge and belief, contains no material previously published or written by another person, except where due reference has been made in the text. In addition, I certify that no part of this work will, in the future, be used in a submission for any other degree or diploma in any university or other tertiary institution without the prior approval of the University of Adelaide and where applicable, any partner institution responsible for the joint-award of this degree.

I give consent to this copy of my thesis, when deposited in the University Library, being made available for loan and photocopying, subject to the provisions of the Copyright Act 1968.

I also give permission for the digital version of my thesis to be made available on the web, via the University's digital research repository, the Library catalogue and also through web search engines, unless permission has been granted by the University to restrict access for a period of time.

Alexandre Burgun

Acknowledgements

This PhD research work was carried out in cotutelle between the Bruce group at the University of Adelaide (Australia) and the "Organometallics and Molecular Materials (OM2)" team (UMR-6226) at the Université de Rennes 1 (France).

Firstly, I would like to acknowledge both of my supervisors: Professor Michael Bruce and Dr. Claude Lapinte for giving me the wonderful opportunity to carry out my PhD between the University of Adelaide and the Université de Rennes 1 in their respective groups. I am grateful that they have provided me with a very interesting and enjoyable project, and for their help, availability and good advice throughout these three years.

I would also like to acknowledge the Rennes committee members for assessing my work: Professor Rinaldo Poli from the LCC-CNRS in Toulouse, Dr. Mark Whiteley from The University of Manchester, Dr. Jean-François Halet from the Université de Rennes 1, Associate Professor Jonathan Morris from The University of New South Wales and Dr. Christopher Sumby from The University of Adelaide.

I am grateful to Dr. Thierry Roisnel (Université de Rennes 1) and Dr. Brian Skelton (The University of Western Australia) for the X-ray structures, and also Dr. Christopher Sumby who resolved some of my crystal structures at the University of Adelaide. I also thank Professor Brian Nicholson (The University of Waikato, New Zealand) for running most of my mass spectra and for inviting me to spend ten days in his lab to learn how to use the mass spectrometer.

I would also like to acknowledge all the people I have collaborated with: Dr. Olivier Cador for the magnetism measurements; Dr. Sourisak Sinbadhit for the NMR experiments and discussions; Professor Paul Low and Dr. Phil Schauer (Durham University, UK) for spectroelectrochemical measurements; Dr. Jean-François Halet, Dr. Karine Costuas and Frédéric Gendron for the theoretical calculations and many fruitful discussions.

In France, I thank all of the group members I have worked with: Dr. Jean-René Hamon, Dr. Frédéric Paul, Dr. Gilles Argouarch and Paul Hamon for their help and good advice

during these three years. Thank you to Frédéric Justaud who introduced me to EPR spectroscopy and for all his good synthesis advice. I want to thank Guillaume Grelaud as well for his contributions to some parts of this work during his Master 1 internship in the Bruce group. To all the students I shared the lab with and for their good company: Florianne, Nicolas, Romain, Ayam and Katy who helped me a lot with my English. A special thanks to Gwen Colombel for his good company and more especially for being such a good loser to all the games and sports we played. I thank Cécile Peron as well for her help with the administrative tasks.

I must also thank the Université Européenne de Bretagne which gave me a grant for travelling between France and Australia. I acknowledge Mrs. Réminiac from the International Office (SAI) of the Université de Rennes 1 who facilitated the cotutelle agreement.

In Australia, I must acknowledge Dr. Natasha Zaitseva, who gave me precious help with crystallisations; it has been very enjoyable to work with her in the lab. Thank you to my good friend Dr. Christian Parker with who I had a lot of chemical discussions but also a lot of fun outside the lab. I also wish to thank the many members of Lab 9 for their good company, among them, Wit, Damien and my compatriot Antonio from Marseille. I thank my good french friend Maxime from the opposite building (CSIRO) for all the lunch and coffee breaks and more especially for his good friendship. I must thank the general staff of the Department of Chemistry and Physics for their availability and great assistance: Phil for NMR, John (store), Gino, Graham, Peter and Peter. A big thank you as well to Mary and Jeanette who have considerably helped me with the cotutelle administrative tasks.

I can’t forget all my friends in France and in Australia outside of chemistry who have made these three years very enjoyable and unforgettable, especially the fencing clubs in Rennes (CSGR) and in Adelaide (Adelaide Swords Club) for all the wonderful moments.

I also wish to thank all my family for their support throughout my PhD. Finally, I thank my partner Kate for all her support, attention, motivation and patience over distances and these PhD years.

Abbreviations

°	degrees
°C	degrees celsius
δ	chemical shift
A	amperes
Å	angstrom
Anal.	analysis
Ant	anthracene
Ar	aryl
Av.	average
br	broad
^{n}Bu	*n*-butyl
ca	approximately
Calcd	Calculated
cent	centroid
cm^{-1}	wavenumbers
Cp	cyclopentadienyl
Cp*	pentamethylcyclo-pentadienyl
CV	Cyclic Voltammetry
d	doublet
dbu	1,8-diazabicyclo[5.4.0] undec-7-ene
DFT	Density Functional Theory
dppe	1,2-bis(diphenylphoshine)-ethane
E	potential
ΔE	potential difference
e	electron
EPR	Electron Paramagnetic Resonance
eq.	equivalent
ES-MS	Electrospray Mass Spectrum
eV	electron volts
ε	molar extinction coefficient
Fc	ferrocene
Δg	anisotropy
h	hour(s)
HOMO	Highest Occupied Molecular Orbital
Hz	hertz
I	current
i_a	anodic peak current
i_c	cathodic peak current
IR	infrared
irr	irreversible
IVCT	Intervalence Charge Transfer
J	coupling constant
K	kelvin
K_c	comproportionation constant
L	litre
LMCT	Ligand-to-Metal Charge Transfer
LUMO	Lowest Unoccupied Molecular Orbital
λ	wavelength
m	medium or multiplet
M	metal or molarity or molecular ion

Me	Methyl
MeOH	Methanol
mg	milligrams
min	minutes
mL	millilitres
MLCT	Metal-to-Ligand Charge Transfer
mmol	millimoles
MO	Molecular Orbital
m/z	mass per unit charge
Near-IR	Near-Infrared
nm	nanometres
NMR	Nuclear Magnetic Resonance
ORTEP	Oak Ridge Thermal Ellipsoid Plot
OTTLE	Optically Transparent Thin-Layer Electrochemical
Ph	phenyl
PPh_3	triphenylphosphine
ppm	parts per million
^{i}Pr	isopropyl
R	general organic group
R_f	retention factor
s	strong or singlet or seconds
SAM	self-assembled monolayer
SCE	Saturated Calomel Electrode
SOMO	Singly Occupied Molecular Orbital
STM	Scanning Tunnelling Microscope
t	triplet
TCNE	tetracyanoethylene
TCNQ	7,7,8,8-tetracyanoquinodimethane
THF	tetrahydrofuran
t.l.c.	thin layer chromatography
TMS	trimethylsilyl
tol	*para*-tolyl
UV-Vis	Ultraviolet-Visible
V	volts
vs	versus
V_{ab}	electronic coupling parameter
w	weak

Chapter One

General Introduction

Today, electronic and computer devices are based on silicon technology. Until now, the "top-down" approach consisting in miniaturising the size of silicon-based chips was responding to the demands of increasing the capacities of computational devices. It was predicted by Gordon Moore in 1965 that the number of transistors per integrated circuit would double every 18-24 months[1] (Figure 1.1). Moore's Law, which is followed by the semi-conductor industry, is however about to end, as transistors cannot be scaled down indefinitely[2]. Indeed, we are approaching an intrinsic limit for micro-fabrication in the solid state[3], as electronic properties of bulk materials will be governed by quantum effects as the scale approaches molecular sizes. For example, at the three-atom-thick level, oxide layers used in the silicon chips become poorly insulating, resulting in charge leakage[4]. To bypass these physical limitations of downscaling, scientists have developed the alternative "bottom-up" approach in which single molecules are used as electronic components. This field has attracted much attention over these past few decades.

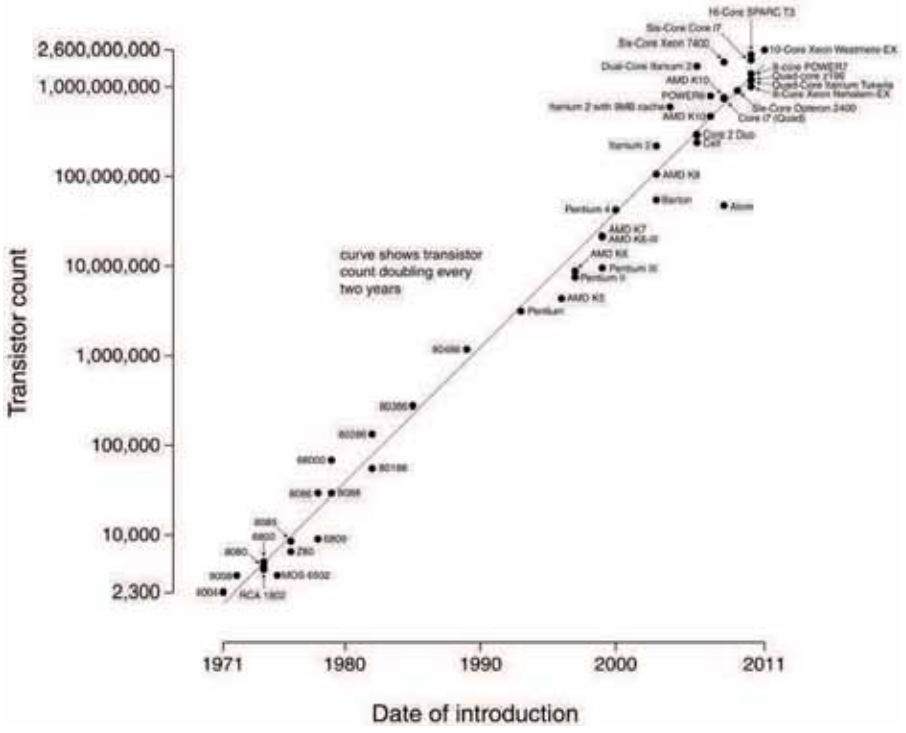

Figure 1.1. *Microprocessor transistor counts 1971-2011 and Moore's Law.*

1.1 Molecular electronics

In 1974, Aviram and Ratner[5] were the first to express the idea that a single molecule could act as an electronic component. The authors proposed that the molecule represented in Figure 1.2, which contains electron-donor and electron-acceptor sites insulated from each other by a saturated bridge, might act as a molecular rectifier when placed between two electrodes. Since that time, molecular electronics has attracted much interest and significant advances have been achieved towards the realisation of molecular circuits over the last decades. Many examples of molecular components have been reported such as molecular wires[4b, 6], switches[7], memories[6c, 8] and rectifiers[9]. Additionally, one of the advantages of molecular-scale electronics is that molecules can be synthesised on a large scale, which would considerably reduce the cost of the electronic circuits.

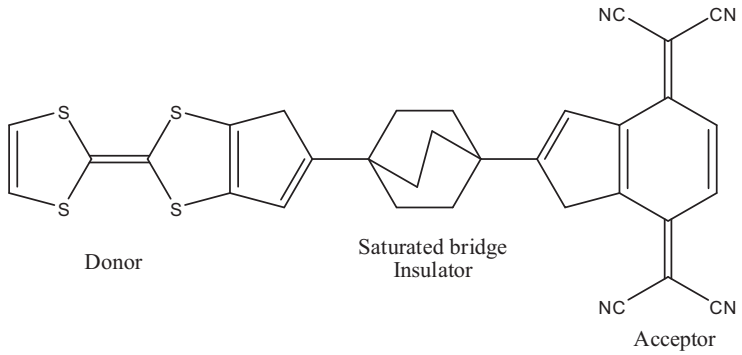

Figure 1.2. *Aviram and Ratner molecular rectifier.*

The wire is the most basic electronic component, its unique function being to facilitate the passage of current between two points[3]. Therefore, molecules which could act as molecular wires have been widely studied over the last years, with the only requirement being that they have to be able to conduct electrons or holes in order to carry a current through the circuit. Linear molecules with conjugated π systems, alternating carbon-carbon single and double (or triple) bonds are thus excellent candidates for molecular wires due to their ability to conduct electrons through their π systems. Many examples of single molecules in which carbon-carbon double or triple bonds alternate with aromatic groups such as phenyl or thienyl are described in the literature[4a] as being efficient molecular wires. Besides, these organic building blocks allow the construction of very long single molecules with a precise length[10] by polymerisation reactions. In this regard, remarkably long oligothiophene[11], oligo(phenylene-ethynylene)[4a, 6c, 12] and oligo(thiophene- ethynylene)[13] derivatives with the aromatic units bearing various functional groups, in order to modify the molecular properties, have been reported (Figure 1.3).

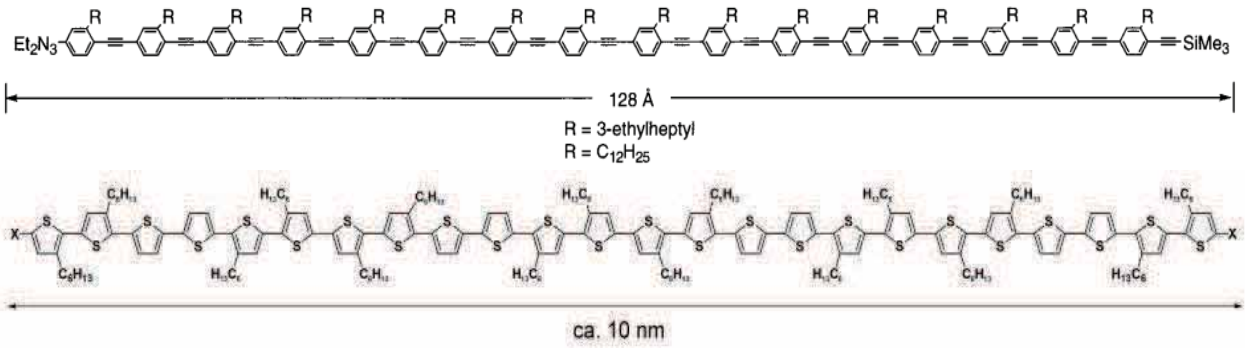

Figure 1.3. *Examples of single molecular wire: oligo(phenylene-ethynylene) (top) and oligothiophene (bottom).*

However, the simplest molecular wire is a linear carbon chain made of C(*sp*) atoms: R-$(C\equiv C)_n$-R where R are end-groups which improve the stability of the polyyne chain. Although extended polyynes are very challenging to synthesise because of their instability, a few general synthesis methods are available and have recently been reviewed[14]. Therefore, many single molecules containing long polyyne chains end-capped by organic[15] or organometallic[16] fragments have been reported as potential molecular wires.

Many technological challenges are however required for the solid-state to molecular electronics transition, some of the most important being the measurement, interpretation and application of the electronic characteristics of the molecular devices[17]. For the molecular wire example, the major challenge consists in finding methods to enable the measurement of its conductivity. This can be achieved by two different approaches: the measurement of a bulk sample and the direct measurement using single molecules which has been extensively developed over the last few years.

1.2 Bulk measurements of molecular wires

One approach to approximate the degree of conductivity of a molecular wire is to end-cap the wire between two redox-active metal centres. Transfer of electrons across the molecular wire can thus be studied, the metal centres acting as donor and acceptor sites. The advantage of this method is that there is no need to attach the molecule to a macroscopic system; the electron is generated "in-situ"[4b]. By oxidising one of the metal centres, mixed-valence systems which exhibit inter-valence charge-transfer (IVCT) transitions between the two end-capping metal units can be generated. These mixed-valence systems show unique properties and have been extensively studied as a way of testing potential components of molecular-scale electronic devices.

1.2.1 Mixed-valence theory

Molecular wires end-capped by two redox-active transition metal centres which are in different oxidation states have attracted much attention because they are the simplest model systems for studying electron transfer and delocalisation. This kind of mixed-valence complex incorporates two metal centres, one in oxidation state (n) and the other in oxidation state (n + 1), linking by a bridging ligand (L) (Figure 1.4). In these complexes,

exchange of the unpaired electron or hole between the two end groups occurs through the molecular bridge and a barrier to this interconversion exists.

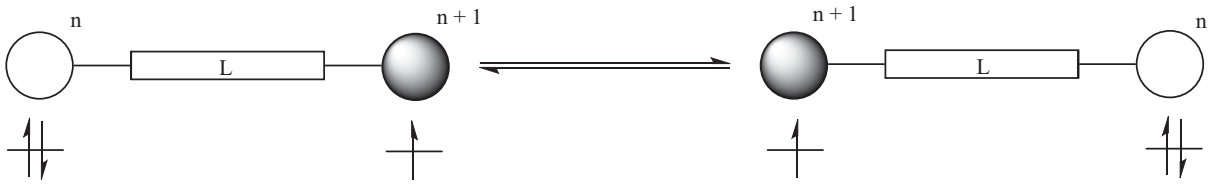

Figure 1.4. *Schematic representation of electron transfer in a mixed-valence complex.*

Creutz and Taube[18] were the first to report a mixed-valence system: it contains two pentaamine-ruthenium centres linked by a pyrazine ligand (Scheme 1.1). The overall charge of this biruthenium complex is 5+ with one metal site formally being in the +II oxidation state and the second in the +III oxidation state.

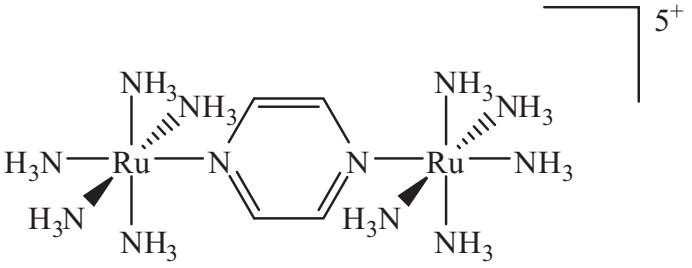

Scheme 1.1. *The Creutz-Taube ion.*

In 1967, a classification of mixed-valence species based on the degree of delocalisation of the unpaired electron was proposed by Robin and Day[19]. They ranked mixed-valence systems in three classes:

- Class I: there is no (or negligible) electronic interaction between the two redox sites. The charge is completely localised on one of the redox centres and each centre can be distinguished, as they exhibit unique properties.

- Class III: there is extremely strong electronic interaction between the two redox sites. The charge is completely delocalised over the entire length of the molecule and the two redox centres can not be distinguished. Formally, they each have the average valence state [(2n + 1)/2].

- Class II: systems in between class I and III belong to class II. The charge is neither completely localised nor delocalised and at least one spectroscopic method should allow the two redox centres to be distinguished.

Recently, an additional class borderline between classes II and III has been proposed[20]. In class II-III systems, the charge is "almost delocalised"; the Creutz-Taube ion belongs to this class.

Two key factors have to be considered to determine in which class a mixed-valence compound belongs: the electronic coupling (H_{ab}) between the two redox centres, and the reorganisation energy (λ) associated with the electron transfer between them[21]. In class I systems, $H_{ab} = 0$ and vertical electronic transitions from one potential well to the other are not observed [Figure 1.5 (a)]. In class II systems, H_{ab} is moderate and vertical electronic transitions from the minimum of one potential well to a vibrationally excited state of the second potential energy surface are possible. The energetic position of the intervalence absorption band maximum, E_{op}, corresponds to the reorganisation energy λ [Figure 1.5 (b)]. In class III systems, there is a single minimum at X = 0.5 (reaction coordinate), H_{ab} is strong and E_{op} measures its magnitude [Figure 1.5 (c)].

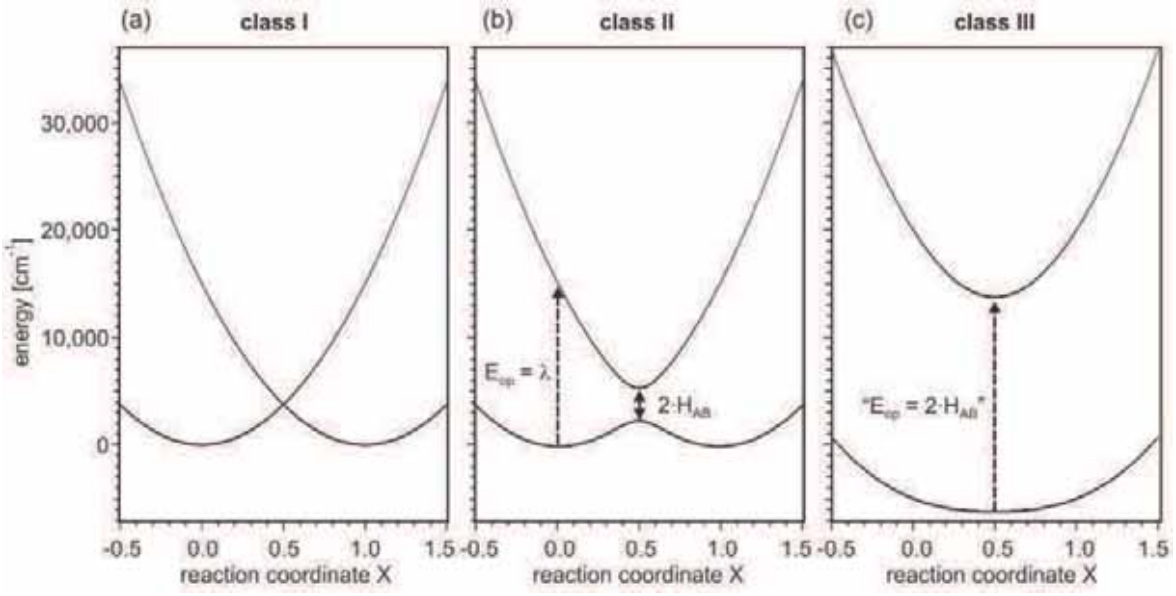

Figure 1.5. *Potential energy surfaces for electron transfer in mixed-valence systems with (a) negligible, (b) weak, and (c) strong electronic coupling.*

Extensive studies of organometallic mixed-valence complexes containing different combinations of bridges and metal centres have been described[22]. The redox centres do not necessarily have to be metal-centred; purely organic mixed-valence systems are also known and have recently been reviewed[23].

1.2.2 Evaluation of the electronic interaction between two redox sites in mixed-valence systems

The two analytical techniques which are mainly used to assess the degree of electronic interaction between the two redox-active sites of a mixed-valence complex are cyclic voltammetry (CV) and Near-IR spectroscopy. Cyclic voltammetry is the easiest way to look at electronic interactions for symmetric mixed-valence systems and, in the case of a sufficiently strong interaction, two one-electron events are found. The potential difference (ΔE) between two redox waves is a measure of the thermodynamic stability of the corresponding mixed-valence states relative to the other states of the comproportionation/disproportionation equilibrium shown in Figure 1.6[6b]. The comproportionation constant, K_c, is related to the free energy of comproportionation (ΔG_c) by Equation 1.1.

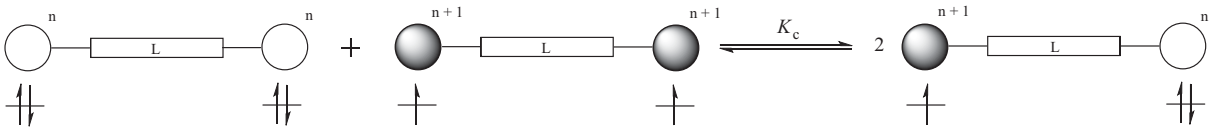

Figure 1.6. *Comproportionation/disproportionation equilibrium.*

$$\Delta G_c = \Delta E = E_2 - E_1 = -\,(RT/F)\log K_c \qquad \textbf{Equation 1.1}$$

Four distinct energetic factors make the main contribution to the magnitude of the free energy of comproportionation ΔG_c (and thus K_c), and recently two additional terms have been added. These factors are given in Equation 1.2 [24].

$$\Delta G_c = \Delta G_s + \Delta G_e + \Delta G_i + \Delta G_r + \Delta G_{ST} + \Delta G_{ip} \qquad \textbf{Equation 1.2}$$

where ΔG_s is the entropic factor which represents the statistical distribution of the comproportionation equilibrium, ΔG_e is the electrostatic force factor which represents the

repulsion of two similarly charged and linked redox centres, ΔG_i is the inductive factor due to the stabilisation of the mixed-valence by electron polarisation, and ΔG_r accounts for the free energy of resonance exchange and is connected to the metal-metal coupling[25]. The two additional terms, ΔG_{ST} and ΔG_{ip}, consider the magnetic exchange which takes place between the unpaired electron of the doubly-oxidised complex (ΔG_{ST}), and the role of ion-pairing (ΔG_{ip}) and the electrolyte.

For class III mixed-valence systems, the delocalisation factor ΔG_r is usually dominant, whereas in class II systems, this term is small. However, the fifth term ΔG_{ST} cannot be neglected and its sign depends on the nature of the magnetic exchange. If the spin coupling in the dioxidised species is antiferromagnetic, it yields a singlet ground state which contributes to stabilising this species, so that the comproportionation equilibrium (Figure 1.6) will be displaced to the left-hand side. In contrast, if the coupling is ferromagnetic, it affords a triplet ground state which will have an effect in the opposite direction. A good example illustrating this competition between ΔG_r and ΔG_{ST} has been reported by Lapinte[25]: in the class III homonuclear iron and ruthenium mixed-valence complexes $[\{Cp^*(dppe)Fe\}_2(\mu\text{-}C{\equiv}CC{\equiv}C)]PF_6$ and $[\{Cp^*(dppe)Ru\}_2(\mu\text{-}C{\equiv}CC{\equiv}C)]PF_6$, the delocalisation factor ΔG_r is larger (by a factor of 2) in the ruthenium analogue, which indicates that there is better electronic communication between the two metal centres in the ruthenium than in the iron mixed-valence complex. However, the ΔG_{ST} factor is considerably larger (by a factor of 10) in the iron complex indicating that the triplet state is more stable, whereas in the ruthenium complex, the singlet state dominates. This leads to displacement of the comproportionation equilibrium to the right-hand side for iron and on the opposite side for ruthenium mixed-valence systems, resulting in a larger K_c (and ΔE) for the iron complex, whereas the electronic communication between the metal centres is greater in the ruthenium analogue. Therefore, the use of K_c and ΔE to interpret the degree of electronic communication between metal centres must be approached very judiciously[25].

When the mixed-valence species are stable enough to be isolated and studied, Near-IR spectroscopy is the most accurate method for evaluation of the degree of electron delocalisation in mixed-valence compounds. Indeed, if there is an electronic interaction between the two metal centres, the mixed-valence species exhibits an intervalence charge transfer (IVCT) band in the Near-IR region (which is not observed for class I systems), which is an experimental measure of the electronic coupling parameter, V_{ab}, of the mixed-

valence complex. The value of V_{ab} depends on the overlap between the electronic wave functions of the donor and the acceptor groups in the transition state[26] and, as a consequence, calculation of V_{ab} depends on the Robin-Day classification of the mixed-valence compound[19]. For class II mixed-valence systems, where electron delocalisation between the metal centres is moderate, equations based on the Hush theory[21, 27] (see Chapter 5) can be used to calculate V_{ab}. Additionally, the solvent dependence of the IVCT band (Equation 1.3) can establish whether the mixed-valence compound belongs to class II[6b].

$$\nu_{max}(\text{solvent}) = 1/\hbar[\lambda_i + (e^2/2r)\,(1/\varepsilon_{op} - 1/\varepsilon)] \qquad \textbf{Equation 1.3}$$

In Equation 1.3, ν_{max} (cm^{-1}) is the IVCT band maximum, e (eV) is the electron charge, $\hbar$ is Planck's constant, λ_i is the inner-sphere reorganisation energy, ε is the solvent dielectric constant and ε_{op} is the squared solvent refractive index.

For class III mixed-valence systems where the electron delocalisation is strong, V_{ab} cannot be calculated from the equation based on the Hush model. Indeed, in the ideal class III complex, the unpaired electron is delocalised in one molecular orbital which extends over the whole molecule, and the V_{ab} model, based on the use of only two wave functions centred on the donor and the acceptor sites for describing the transfer, is not valid. However, V_{ab} can be approximated by the equation: $V_{ab} = \nu_{max}/2$ [28] (see Chapter 5). Typically, class III mixed-valence complexes exhibit more intense and narrower IVCT bands than the class II species; besides, their IVCT bands are not solvent dependent.

So far, both of these methods, CV and Near-IR, have been used to measure the degree of electronic interaction in many mixed-valence complexes of classes II and III, with different combinations of metal centres[22] (nature of the metals) and bridges (degree of π conjugation[29] and length[30]), which allows a determination of the effectiveness of the bridging ligand to mediate electron transfer. With their unique electronic properties, mixed-valence complexes are potentially essential components for the construction and study of new molecular devices.

1.3 Direct measurements on molecular wires

Addressing individual molecules has been one of the biggest challenges in molecular electronics this last decade. Indeed, to measure the conductance of a single molecule, some rules have to be respected: one must (1) provide a signature to identify that the measured conductance is a property of not only the sample molecules, but also of a single sample molecule, (2) ensure that the molecule is properly attached to the two probe electrodes, and (c) perform the measurement in a well-defined environment[31]. Several methods have been investigated and have been shown to be efficient; they can be ranked in three categories: scanning probe methods, fixed electrodes, and mechanically controlled molecular junctions[31].

Development of scanning tunnelling microscopy (STM) has become very important in the field of molecular electronics. Indeed, it allows one to image individual molecules adsorbed on a conductive substrate, to perform tunnelling spectroscopy measurements on the molecule by placing the scanning tunnelling microscope tip on it, and to manipulate atoms and molecules on surfaces. One of the most widespread techniques to measure the conductance of a single molecular wire consists in using self-assembled monolayers (SAMs) on a gold surface[32]. Insulating molecules such as alkanethiols are adsorbed onto a gold surface forming well-assembled monolayers, then the molecular wire which also contains a thiol[33] (or isocyanide[34]) surface-linking group is inserted at the grain boundaries of the alkanethiol matrix (Figure 1.7). The molecular wires, which are topographically above the gold surface, can be individually imaged and their conductance measured, the molecular wires being more highly conducting than the surrounding alkanethiols. Many other methods based on this example, using STM, have been developed over the years in order to be more efficient for the conductance measurements[35]. For example, molecular wires can be inserted at controlled rather than random locations[36]; or a single dithiolate molecule can be end-capped by the gold surface and a gold nanoparticle. By placing the STM tip onto the nanoparticle, the Coulomb blockade effect[37] is observed and by fitting the measurements with this model, the conductance of the single molecule can be extracted.

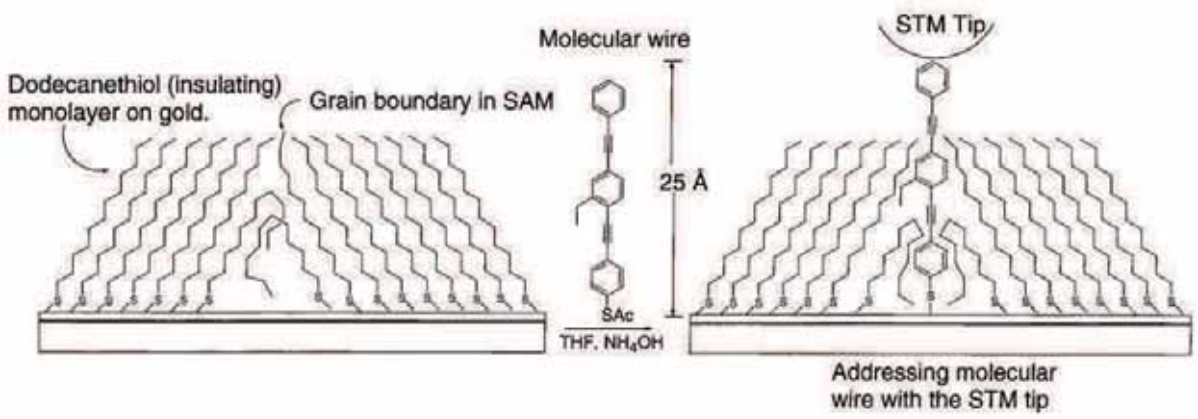

Figure 1.7. *Protocol for inserting molecular wires into dodecanethiolate (SAM)s at grain boundaries. Relative conductance recording is done with a STM tip*[4a].

The fixed-electrode method consists in fabricating a pair of facing electrodes on a solid substrate, and then bridging the electrodes with the target single molecule which is end-capped by two anchoring groups that can attach to the electrodes (Figure 1.8). The fabrication of such small gaps on the nanometre scale is not easy and makes this technique very complicated to carry out; although, several examples of single-molecule conductance measurements using this method have been reported[38]. Additionally, when using this method, it is not possible to be sure if the molecules are indeed covalently bound to the two electrodes, and the positions of both the molecules and electrodes are not precisely known, making the determination of atomic-scale structural information difficult.

NOTE:
This figure is included on page 11 of the print copy of the thesis held in the University of Adelaide Library.

Figure 1.8. *A single molecule bridged between two electrodes with a molecular scale separation*[31].

In order to form a small gap between the two electrodes, the mechanically controlled break-junction is one of the most efficient and widely used methods. It consists in breaking a thin metal wire supported on a solid substrate between two facing electrodes. The bending of the substrate, which then breaks the wire, can be controlled with a mechanical actuator (Figure 1.9 left)[31]. In 1997 Reed et al.[39] were the first to measure electron

transport in molecules using the mechanically controlled break-junction. They exposed the two preformed electrodes to a benzenedithiol solution, and after removing the solvent, a finite current was measured between the electrodes and was attributed to electron transport through the molecules (Figure 1.9 right). Since then, many experiments on molecular devices using this method have been described in the literature[40]. Several derivative methods of the mechanically controlled break-junction were developed over the last decade[41]; for example, the STM-break junction method consists in quickly creating thousands of molecular junctions by repeatedly moving a STM tip electrode, into and out of contact with the substrate electrode in the presence of the molecules to be measured[42].

Figure 1.9. *Schematics of a microfabricated mechanically controllable break-junction (left)[31], and a schematic of benzenedithiol molecules between proximal gold electrodes (right)[39].*

So far, a wide variety of organic compounds has been tested on surfaces using the different techniques described above; however, only a few organometallic complexes have been assembled on surfaces and tested as molecular devices despite their promising potential in molecular electronics. Some organometallic complexes have been attached to gold surfaces assembled into SAMs[34, 43], in contact with gold nanoparticules[44] and in nanogap molecular junctions[45]. These studies have revealed that conductance in organometallic complexes is far better than in analogous organic molecules of similar length[43a]. Silicon surfaces have also been shown to be very efficient at covalently attaching organometallic complexes and in generating their redox states. Qi et al.[46] and Gauthier et al.[47] grafted organometallic complexes onto silicon surfaces by formation of strong Si-N

and Si-C bonds, respectively (Figure 1.10), and studied the redox properties of the surface-bound molecules.

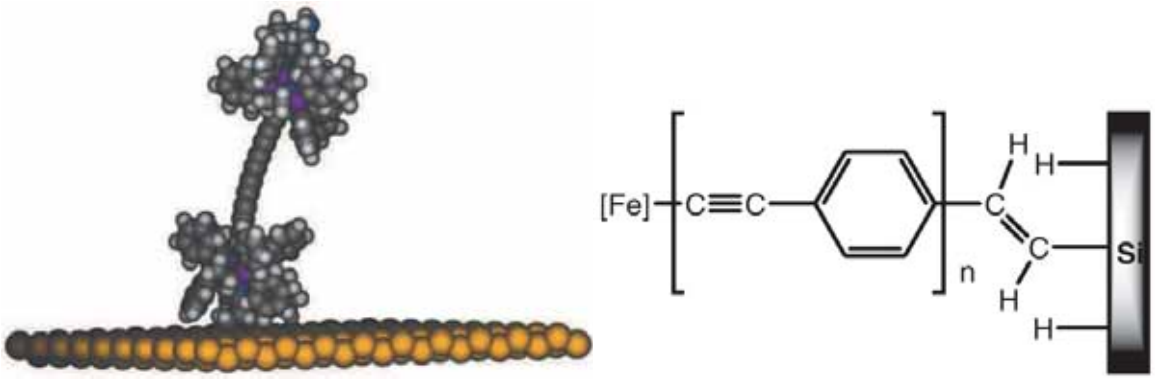

Figure 1.10. *Space-filling model of docking of a diruthenium complex on a Si(111) surface by Si-N bond formation (left)[46b], organoiron species on a hydrogen-terminated silicon surface by Si-C bond formation (right)[47].*

Attaching mixed-valence complexes on silicon surfaces has recently attracted much attention[46a] as a method of investigating the potential of mixed-valence systems as devices for a new paradigm: the Quantum-dot Cellular Automata (QCA) paradigm.

1.4 Quantum-dot Cellular Automata (QCA)

1.4.1 Theory

In 1993, Lent et al.[48] introduced a novel approach to molecular electronics: the Quantum-dot Cellular Automata (QCA) paradigm, in which the binary representation of information is encoded in the charge configuration within a QCA cell. This contrasts with the usual storage as on/off states of a current switch in transistor-based devices. The QCA cell consists of four dots and contains two mobile electrons, which naturally occupy antipodal sites (Figure 1.11). For this purpose, a dot can be defined as a region in which the charge is localised, and each cell in isolation has two degenerate ground states ("1" or "0"). The Coulombic interaction between cells is exploited and induces the same states in neighbouring cells, but no current flows between adjoining cells. A full four-dot QCA cell can also be viewed as a pair of half-cells (with two dots each) in which the sign of the dipole alternates[49].

Figure 1.11. *Schematic of QCA cells. A "1" or "0" bit is encoded in the arrangement of charge*[49].

Using this new approach, QCA wires could be constructed by juxtaposing cells in a linear array [Figure 1.12 (a)], and so can transmit binary information from one end of the line to the other. Similarly, a QCA majority logic gate can be constructed with three input lines converging at a device cell [Figure 1.12 (b)], the state of the last one being determined by the states of the majority of the inputs[49].

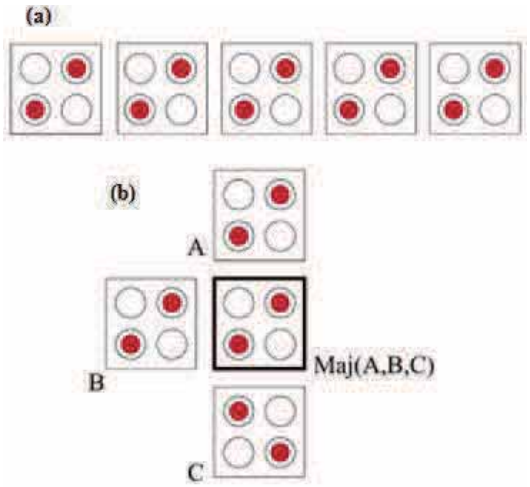

Figure 1.12. *(a) Representation of a QCA wire. (b) Representation of a QCA majority logic gate with three inputs (A, B, C) and one output (device cell)*[49].

QCA circuits have already been constructed using small metallic islands as the dots, which are connected to other islands by small tunnel-junction barriers[50]. These experiments have shown that the rearrangement of single charges in one cell effectively changes the state of the neighbouring cell and computational tasks can be performed. Operation of a QCA three-input majority logic[50b], QCA wires[51] and more complex circuits such as adders[52] within the QCA paradigm have all been demonstrated. Unfortunately, because of their large size, these circuits only work at cryogenic temperatures (below 100 mK)[48b].

Molecular QCA

The low temperature constraints of the QCA circuits described above can be avoided if the QCA cell is a single molecule. Indeed, theory predicts that shrinking the QCA cell to molecular scales will increase the relevant energies and enable room temperature operation[48b]. A molecular QCA cell requires a molecule in which charge is localised but can tunnel between sites. In QCA molecules, redox-active sites can play the role of the dots and bridging ligands the role of the tunnelling paths; individual cells are coupled to, and switched by, the fields of adjacent cells. The simplest molecular QCA cell could be viewed as a combination of two identical molecules of a symmetric mixed-valence complex in which the binary states are represented by the locations of a mobile electron at one or other metal centres. Class II mixed-valence systems are most likely to be the most suitable candidates for molecular QCA devices: the mobile electron can be localised at one redox site. However, a molecular QCA cell with four redox centres would be a more versatile building block for the construction of logic units than one with only two redox centres. Several molecules containing four metal centres with a square geometry have already been identified as potential molecular QCAs[53] (see Chapter 6). QCA operation in a single molecule has not yet been experimentally demonstrated, but demonstration of a QCA majority logic gate operating at the single molecule level has been shown theoretically[49]. In order to demonstrate molecular QCA operations experimentally, substantial challenges such as attaching the molecules to a surface with a predetermined geometry, applying inputs, clocking signals and reading the states of the output cells, need to be overcome[48b]. Recently, a few advances toward operating molecular QCAs have been made.

1.4.2 Toward a molecular QCA

Because of the growing interest in mixed-valence homometallic systems as molecular QCA devices, Braun-Sand et al.[54] studied theoretically three ruthenium mixed-valence complexes as representatives of the three Robin-Day classes[19]. Intra-cell communication in the three complexes was explored by studying their geometric and electronic structures. These theoretical studies are useful tools for the design of mixed-valence compounds for use in molecular QCA. Analysis of the orbital energies provided insights into the degree of delocalisation as a function of the Robin-Day classification. They also studied polarisation

of the three ruthenium mixed-valence complexes (class I, II and III) when a biasing charge (lithium ion) is added to the system[55].

Other experimental steps toward molecular QCA devices have also been overcome: mixed-valence ruthenium complexes have been covalently attached to silicon surfaces [Figure 1.10 (left)] and controlled switching of the oriented mixed-valence species by an applied electric field has been demonstrated[46a]. Using this technique, Qi et al.[46b] also investigated the effects of unsymmetric and symmetric mixed-valence complexes, of short- and long-chain alkyne linkers between metal centres, and of counterion size on the switching potential. For example, it has been demonstrated that the switching potential of a mixed-valence complex increases when the size of the counterion decreases.

Significant advances have been achieved in the deposition of molecular QCA candidates on surfaces over the last five years. Molecules of the large biruthenium complex *trans*-[Cl(dppe)$_2$Ru(C≡C)$_6$Ru(dppe)$_2$Cl] (**Ru$_2$**) have been successfully adsorbed on Au(111) surfaces using pulse deposition[56] (in this case, there is no covalent bonding with the gold surface), although solvent remained on the surface[57]. Using an ultra-high-vacuum STM, the molecular structures and imaging properties of the deposited molecules were investigated, and isolated molecules were clearly observed in the high-resolution STM images (Figure 1.13). Additionally, using the STM tip, translation and rotation motions of individual molecules were demonstrated.

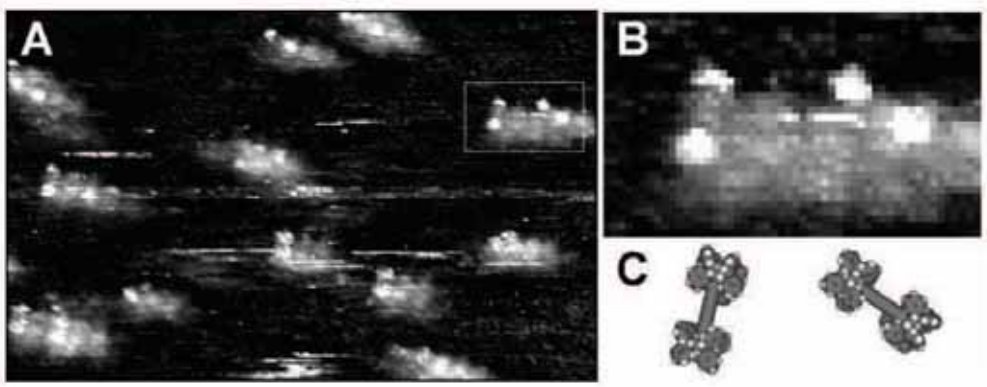

Figure 1.13. *(A) STM image of **Ru$_2$** molecules on Au(111). Each single molecule is imaged as a feature consisting of two closely paired bright dots. (B) Expanded view of two **Ru$_2$** molecules. (C) Space-filling model of two **Ru$_2$** molecules, drawn to the same scale as the image shown in panel B*[56].

Finally, in 2010, using the method described above, Lu et al.[58] clearly observed isolated molecules of the mixed-valence species [1,3-{Cp*(dppe)Fe(C≡C-)}$_2$C$_6$H$_4$]$^{\bullet+}$ in high-resolution STM images (Figure 1.14). This molecule, which has previously been synthesised and well-studied by the Lapinte group[59], is a typical class II mixed-valence system. Charge localisation reflecting the bistable configuration of the class II mixed-valence Fe(II)-Fe(III)/Fe(III)-Fe(II) system was observed by comparing the STM images of the neutral and mono-oxidised species: for the neutral species, the molecules have a symmetrical "dumbbell" structure (the two sides of the molecules are identical); whereas the molecules of the mixed-valence species have an asymmetric double-dot structure (Figure 1.14).

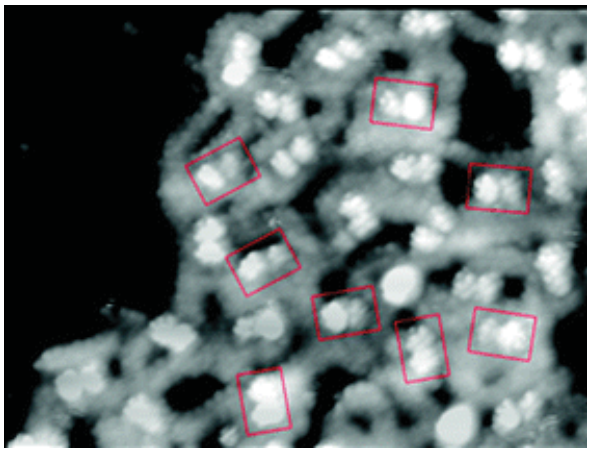

Figure 1.14. *STM image of [{Cp*(dppe)Fe(C≡C-)}$_2$(1,3-C$_6$H$_4$)]$^{\bullet+}$ molecules on Au(111). The framed areas are assigned to images of mixed-valence complexes. The bright-dim double-dot structures demonstrate the uneven charge distribution. The mobile charge is localised on one site or the other*[58].

Imaging mixed-valence complexes and recognising the oxidation state of each metal moiety using STM is a major step toward the design of molecular QCA devices. Indeed, mixed-valence complexes can be viewed as binary information encoders and the STM enables the logic value of the molecular electronic devices to be "read" (output signal). The next challenge is to manipulate neighbouring molecules in order to fabricate devices and demonstrate their logic function[58].

1.5 Work described in this Thesis

Over the last few decades, much attention has been focussed upon the electronic properties of metal complexes containing unsaturated carbon chains and their possible applications as devices for molecular electronics. One example is the one-dimensional poly-yne chains end-capped by metallic fragments of general formula $[M](C{\equiv}C)_n[M]$ which have proved to be effective models of molecular-scale wires[60]. In order to investigate further and understand the electronic behaviour of such complexes, studies of their redox properties need to be carried out. However, metallic complexes containing an unpaired electron and a long carbon chain are known to be extremely sensitive and in most cases unstable. Some exceptions are the stable bimetallic cationic complexes containing an odd electron of general formula $[M](C{\equiv}C)_n[M]^{+\bullet}$ (n = 1, 2 and [M] = Fe(dppe)Cp*, Ru(dppe)Cp*, $Re(NO)(PPh_3)Cp^*$)[61] and $[M](C{\equiv}CR)^{+\bullet}$ ([M] = Fe(dppe)Cp*, Mo(dppe)(η-C_7H_7), W(dppe)(η-C_7H_7))[62] which have been extensively studied, but when the length of the carbon bridge is increased further, the stability of the organometallic radicals is dramatically decreased.

The objective of the work described in this Thesis is to synthesise square molecules containing four redox-active metal centres and two positive charges with the aim of studying them as potential candidates for molecular Quantum-dot Cellular Automata (QCA) devices. To accomplish this goal, the synthesis, electronic properties and oxidation studies of novel mono- and bi-metallic organo-iron and -ruthenium complexes containing C_2, C_4 or C_6 chains are described. Some organometallic radical cations have been characterised and their stability and reactivity have been investigated. In some cases, further chemical reactions occurred by intermolecular radical coupling to give new di- or tetra-nuclear dimers with unique square geometries, which are interesting for potential molecular QCA applications.

After the general introduction to the subject, the second Chapter describes the synthesis of new diynyl complexes M(C≡CC≡CR)(dppe)Cp* (M = Fe, Ru). The electrochemical behaviour of these new compounds and other related complexes will be described. Guided by these electrochemical data, radical monocations were prepared by chemical oxidation and characterised "in-situ" by EPR spectroscopy.

In the third Chapter, the behaviour of the oxidised species $[M(CCR)(dppe)Cp^*]^{+\bullet}$ (M = Fe, Ru) will be described. In the ruthenium case and when R = phenyl, intermolecular coupling occurred between the C_β and the C_{para} of the phenyl group to give a new bimetallic dimer. When the phenyl group is replaced by a tolyl group, where the *para* position is blocked by methyl, coupling of C_β with one C_{Cp} of the cyclopentadienyl ligand occurred. These results are rationalised by DFT calculations from the Halet group in Rennes.

Behaviour of the 17-electron species $[M(C{\equiv}CC{\equiv}CR)(dppe)Cp^*]^{+\bullet}$ (M = Fe, Ru) containing a C_4 chain will be discussed in the fourth Chapter. Dimerisation also occurs to give new bimetallic complexes containing a cyclobutene centre. Characterisation of the dimers will be described and their properties investigated.

In Chapter Five, the synthesis, characterisation and electronic properties of the novel bimetallic complexes $[\{Cp'(dppe)M\}(C{\equiv}CC{\equiv}CC{\equiv}C)\{M(dppe)Cp'\}]^{n+}$ (n = 0, 1, 2; M = Fe, Ru; Cp' = Cp, Cp*) will be investigated. The first X-ray structures of stable mixed-valence complexes containing a C_6 chain have been determined while other unstable mixed-valence complexes were characterised by EPR spectroscopy. Electronic interactions between the two metal fragments through the hexatriyndiyl bridge have been studied using cyclic voltammetry, EPR, IR and Near-IR spectroscopy. The magnetic properties of the new dication $[\{Cp^*(dppe)Fe\}_2(C{\equiv}CC{\equiv}CC{\equiv}C)][PF_6]_2$ will be also be reported in this Chapter.

In Chapter Six, radical coupling and dimerisation of the unstable cationic species $[\{Cp'(dppe)M\}(C{\equiv}CC{\equiv}CC{\equiv}C)\{M(dppe)Cp'\}]^{\bullet+}$ (M = Fe, Ru; Cp' = Cp, Cp*) will be described. Novel dicationic dimers containing four redox-active metal centres with unique geometries have been characterised and their physical properties studied. These new complexes can be considered as molecular QCA models.

Finally, in the seventh Chapter, reactions between the oxidising agent TCNQ and metal acetylides containing carbon chains of different lengths linking iron or ruthenium centres will be described. Several different products were fully characterised, their structures depending on the metal (Fe or Ru) and the length of the carbon chain. For the products in which TCNQ has added to the carbon chain, the resulting tetracyano ligand acts as a strong

electron-withdrawing group and dramatically changes the electronic properties of the organometallic complexes.

References

1. Moore, G. E., *Electronics* **1965,** *38*.
2. Lundstrom, M., *Science* **2003,** *299*, 210-211.
3. Low, P. J., *Dalton Trans.* **2005**, 2821-2824.
4. (a) Tour, J. M., *Acc. Chem. Res.* **2000,** *33*, 791-804; (b) Robertson, N.; McGowan, C. A., *Chem. Soc. Rev.* **2003,** *32*, 96-103.
5. Aviram, A.; Ratner, M. A., *Chem. Phys. Lett.* **1974,** *29*, 277-283.
6. (a) Ward, M. D., *Chem. Ind.* **1996**, p568(6); (b) Paul, F.; Lapinte, C., *Coord. Chem. Rev.* **1998,** *178-180*, 431-509; (c) Tour, J. M.; Rawlett, A. M.; Kozaki, M.; Yao, Y.; Jagessar, R. C.; Dirk, S. M.; Price, D. W.; Reed, M. A.; Zhou, C.-W.; Chen, J.; Wang, W.; Campbell, I., *Chem. Eur. J.* **2001,** *7*, 5118-5134.
7. (a) Ward, M. D., *Chem. Ind.* **1997**, p640(6); (b) Donhauser, Z. J.; Mantooth, B. A.; Kelly, K. F.; Bumm, L. A.; Monnell, J. D.; Stapleton, J. J.; Price, D. W.; Rawlett, A. M.; Allara, D. L.; Tour, J. M.; Weiss, P. S., *Science* **2001,** *292*, 2303-2307; (c) Green, K. A.; Cifuentes, M. P.; Corkery, T. C.; Samoc, M.; Humphrey, M. G., *Angew. Chem. Int. Ed.* **2009,** *48*, 7867-7870.
8. (a) Chen, J.; Reed, M. A.; Rawlett, A. M.; Tour, J. M., *Science* **1999,** *286*, 1550-1552; (b) de Ruiter, G.; Tartakovsky, E.; Oded, N.; van der Boom, M. E., *Angew. Chem. Int. Ed.* **2010,** *49*, 169–172; (c) de Ruiter, G.; Motiei, L.; Choudhury, J.; Oded, N.; van der Boom, M. E., *Angew. Chem. Int. Ed.* **2010,** *49*, 4780–4783.
9. Metzger, R. M., *Chem. Rev.* **2003,** *103*, 3803-3834.
10. Tour, J. M., *Chem. Rev.* **1996,** *96*, 537-554.
11. (a) Izumi, T.; Kobashi, S.; Takimiya, K.; Aso, Y.; Otsubo, T., *J. Am. Chem. Soc.* **2003,** *125*, 5286-5287; (b) Endou, M.; Ie, Y.; Kaneda, T.; Aso, Y., *J. Org. Chem.* **2007,** *72*, 2659-2661; (c) Ie, Y.; Endou, M.; Lee, S. K.; Yamada, R.; Tada, H.; Aso, Y., *Angew. Chem. Int. Ed.* **2011**, DOI.10.1002/anie.201104700.
12. (a) Wang, C.; Batsanov, A. S.; Bryce, M. R., *J. Org. Chem.* **2005,** *71*, 108-116; (b) Jones, L.; Schumm, J. S.; Tour, J. M., *J. Org. Chem.* **1997,** *62*, 1388-1410.
13. Pearson, D. L.; Tour, J. M., *J. Org. Chem.* **1997,** *62*, 1376-1387.
14. (a) Diederich, F., *Nature* **1994,** *369*, 199-207; (b) Chalifoux, W. A.; Tykwinski, R. R., *C. R. Chimie* **2009,** *12*, 341-358; (c) Kim, S., *Angew. Chem. Int. Ed.* **2009,** *48*, 7740-7743.
15. (a) Luu, T.; Elliott, E.; Slepkov, A. D.; Eisler, S.; McDonald, R.; Hegmann, F. A.; Tykwinski, R. R., *Org. Lett.* **2005,** *7*, 51-54; (b) Sugiyama, J.; Tomita, I., *Eur. J. Org. Chem.* **2007**, 4651–4653; (c) Chalifoux, W. A.; McDonald, R.; Ferguson, M. J.; Tykwinski, R. R., *Angew. Chem. Int. Ed.* **2009,** *48*, 7915-7919.
16. (a) Antonova, A. B.; Bruce, M. I.; Ellis, B. G.; Gaudio, M.; Humphrey, P. A.; Jevric, M.; Melino, G.; Nicholson, B. K.; Perkins, G. J.; Skelton, B. W.; Stapleton, B.; White, A. H.; Zaitseva, N. N., *Chem. Commun.* **2004**, 960–961; (b) Szafert, S.; Gladysz, J. A., *Chem. Rev.* **2006,** *106*, PR1-PR33; (c) Zheng, Q.;

Bohling, J. C.; Peters, T. B.; Frisch, A. C.; Hampel, F.; Gladysz, J. A., *Chem. Eur. J.* **2006,** *12*, 6486–6505.
17. Higgins, S. J.; Nichols, R. J.; Martin, S.; Cea, P.; van der Zant, H. S. J.; Richter, M. M.; Low, P. J., *Organometallics* **2011,** *30*, 7-12.
18. (a) Creutz, C.; Taube, H., *J. Am. Chem. Soc.* **1973,** *95*, 1086-1094; (b) Creutz, C.; Taube, H., *J. Am. Chem. Soc.* **1969,** *91*, 3988-3989.
19. Robin, M. B.; Day, P., *Adv. Inorg. Chem. Radiochem.* **1967,** *10*, 247.
20. (a) Demadis, K. D.; Hartshorn, C. M.; Meyer, T. J., *Chem. Rev.* **2001,** *101*, 2655-2686; (b) Brunschwig, B. S.; Creutz, C.; Sutin, N., *Chem. Soc. Rev.* **2002,** *31*, 168-184.
21. Hush, N. S., *Prog. Inorg. Chem.* **1967,** *8*, 391.
22. Aguirre-Etcheverry, P.; O'Hare, D., *Chem. Rev.* **2010,** *110*, 4839-4864.
23. Hankache, J.; Wenger, O. S., *Chem. Rev.* **2011,** *111*, 5138-5178.
24. (a) Sutton, J. E.; Sutton, P. M.; Taube, H., *Inorg. Chem.* **1979,** *18*, 1017-1021; (b) Evans, C. E. B.; Naklicki, M. L.; Rezvani, A. R.; White, C. A.; Kondratiev, V. V.; Crutchley, R. J., *J. Am. Chem. Soc.* **1998,** *120*, 13096-13103; (c) Barrière, F.; Geiger, W. E., *J. Am. Chem. Soc.* **2006,** *128*, 3980-3989.
25. Lapinte, C., *J. Organomet. Chem.* **2008,** *693*, 793-801.
26. Ward, M. D., *Chem. Soc. Rev.* **1995,** *24*, 121-134.
27. Hush, N. S., *Coord. Chem. Rev.* **1985,** *64*, 135-157.
28. Creutz, C., *Prog. Inorg. Chem.* **1983,** *30*, 1.
29. Roué, S.; Lapinte, C.; Bataille, T., *Organometallics* **2004,** *23*, 2558-2567.
30. (a) Ribou, A.-C.; Launay, J.-P.; Sachtleben, M. L.; Li, H.; Spangler, C. W., *Inorg. Chem.* **1996,** *35*, 3735-3740; (b) Launay, J.-P., *Chem. Soc. Rev.* **2001,** *30*, 386-397.
31. Chen, F.; Hihath, J.; Huang, Z.; Li, X.; Tao, N. J., *Annu. Rev. Phys. Chem.* **2007,** *58*, 535-564.
32. Bumm, L. A.; Arnold, J. J.; Cygan, M. T.; Dunbar, T. D.; Burgin, T. P.; Ii, L. J.; Allara, D. L.; Tour, J. M.; Weiss, P. S., *Science* **1996,** *271*, 1705-1707.
33. Cygan, M. T.; Dunbar, T. D.; Arnold, J. J.; Bumm, L. A.; Shedlock, N. F.; Burgin, T. P.; Jones, L.; Allara, D. L.; Tour, J. M.; Weiss, P. S., *J. Am. Chem. Soc.* **1998,** *120*, 2721-2732.
34. Kim, B.; Beebe, J. M.; Olivier, C.; Rigaut, S.; Touchard, D.; Kushmerick, J. G.; Zhu, X. Y.; Frisbie, C. D., *J. Phys. Chem. C* **2007,** *111*, 7521-7526.
35. Langlais, V. J.; Schlittler, R. R.; Tang, H.; Gourdon, A.; Joachim, C.; Gimzewski, J. K., *Phys. Rev. Lett.* **1999,** *83*, 2809.
36. Chen, J.; Reed, M. A.; Asplund, C. L.; Cassell, A. M.; Myrick, M. L.; Rawlett, A. M.; Tour, J. M.; Van Patten, P. G., *Appl. Phys. Lett.* **1999,** *75*, 624-626.
37. (a) Andres, R. P.; Bein, T.; Dorogi, M.; Feng, S.; Jason, I. H.; Kubiak, C. P.; Mahoney, W.; Osifchin, R. G.; Reifenberger, R., *Science* **1996,** *272*, 1323-1325; (b) Blum, A. S.; Kushmerick, J. G.; Long, D. P.; Patterson, C. H.; Yang, J. C.; Henderson, J. C.; Yao, Y.; Tour, J. M.; Shashidhar, R.; Ratna, B. R., *Nat. Mater.* **2005,** *4*, 167-172; (c) Kim, B.; Beebe, J. M.; Jun, Y.; Zhu, X. Y.; Frisbie, C. D., *J. Am. Chem. Soc.* **2006,** *128*, 4970-4971.

38. (a) Li, C. Z.; Bogozi, A.; Huang, W.; Tao, N. J., *Nanotechnology* **1999,** *10*, 221; (b) Kubatkin, S.; Danilov, A.; Hjort, M.; Cornil, J.; Bredas, J.-L.; Stuhr-Hansen, N.; Hedegard, P.; Bjornholm, T., *Nature* **2003,** *425*, 698-701; (c) Kervennic, Y.-V.; Thijssen, J. M.; Vanmaekelbergh, D.; Dabirian, R.; Jenneskens, L. W.; van Walree, C. A.; van der Zant, H. S. J., *Angew. Chem. Int. Ed.* **2006,** *45*, 2540-2542.
39. Reed, M. A.; Zhou, C.; Muller, C. J.; Burgin, T. P.; Tour, J. M., *Science* **1997,** *278*, 252-254.
40. (a) Kergueris, C.; Bourgoin, J. P.; Palacin, S.; Esteve, D.; Urbina, C.; Magoga, M.; Joachim, C., *Phys. Rev. B* **1999,** *59*, 12505; (b) Reichert, J.; Ochs, R.; Beckmann, D.; Weber, H. B.; Mayor, M.; Löhneysen, H. v., *Phys. Rev. Lett.* **2002,** *88*, 176804; (c) Mayor, M.; von Hänisch, C.; Weber, H. B.; Reichert, J.; Beckmann, D., *Angew. Chem. Int. Ed.* **2002,** *41*, 1183-1186.
41. (a) Xu, B.; Xiao, X.; Tao, N. J., *J. Am. Chem. Soc.* **2003,** *125*, 16164-16165; (b) Yasuda, S.; Yoshida, S.; Sasaki, J.; Okutsu, Y.; Nakamura, T.; Taninaka, A.; Takeuchi, O.; Shigekawa, H., *J. Am. Chem. Soc.* **2006,** *128*, 7746-7747.
42. Xu, B.; Tao, N. J., *Science* **2003,** *301*, 1221-1223.
43. (a) Blum, A. S.; Ren, T.; Parish, D. A.; Trammell, S. A.; Moore, M. H.; Kushmerick, J. G.; Xu, G.-L.; Deschamps, J. R.; Pollack, S. K.; Shashidhar, R., *J. Am. Chem. Soc.* **2005,** *127*, 10010-10011; (b) Liu, K.; Wang, X.; Wang, F., *ACS Nano* **2008,** *2*, 2315-2323.
44. Seo, K.; Konchenko, A. V.; Lee, J.; Bang, G. S.; Lee, H., *J. Am. Chem. Soc.* **2008,** *130*, 2553-2559.
45. Mahapatro, A. K.; Ying, J.; Ren, T.; Janes, D. B., *Nano Lett.* **2008,** *8*, 2131-2136.
46. (a) Qi, H.; Sharma, S.; Li, Z.; Snider, G. L.; Orlov, A. O.; Lent, C. S.; Fehlner, T. P., *J. Am. Chem. Soc.* **2003,** *125*, 15250-15259; (b) Qi, H.; Gupta, A.; Noll, B. C.; Snider, G. L.; Lu, Y.; Lent, C.; Fehlner, T. P., *J. Am. Chem. Soc.* **2005,** *127*, 15218-15227.
47. Gauthier, N.; Argouarch, G.; Paul, F.; Humphrey, M. G.; Toupet, L.; Ababou-Girard, S.; Sabbah, H.; Hapiot, P.; Fabre, B., *Adv. Mater.* **2008,** *20*, 1952-1956.
48. (a) Lent, C. S.; Tougaw, P. D.; Porod, W.; Bernstein, G. H., *Nanotechnology* **1993,** *4*, 49-57; (b) Lent, C. S., *Science* **2000,** *288*, 1597-1599.
49. Lent, C. S.; Isaksen, B.; Lieberman, M., *J. Am. Chem. Soc.* **2003,** *125*, 1056-1063.
50. (a) Orlov, A. O.; Amlani, I.; Bernstein, G. H.; Lent, C. S.; Snider, G. L., *Science* **1997,** *277*, 928-930; (b) Amlani, I.; Orlov, A. O.; Toth, G.; Bernstein, G. H.; Lent, C. S.; Snider, G. L., *Science* **1999,** *284*, 289-291.
51. Orlov, A. O.; Amlani, I.; Toth, G.; Lent, C. S.; Bernstein, G. H.; Snider, G. L., *Appl. Phys. Lett.* **1999,** *74*, 2875-2877.
52. Lent, C. S.; Tougaw, P. D., *Proc. IEEE* **1997,** *85*, 541.
53. Jiao, J.; Long, G. J.; Rebbouh, L.; Grandjean, F.; Beatty, A. M.; Fehlner, T. P., *J. Am. Chem. Soc.* **2005,** *127*, 17819-17831.
54. Braun-Sand, S. B.; Wiest, O., *J. Phys. Chem. A* **2003,** *107*, 285-291.
55. Braun-Sand, S. B.; Wiest, O., *J. Phys. Chem. C* **2003,** *107*, 9624-9628.
56. Wei, Z.; Guo, S.; Kandel, S. A., *J. Phys. Chem. B* **2006,** *110*, 21846-21849.
57. Guo, S.; Kandel, S. A., *J. Chem. Phys.* **2008,** *128*, 014702.

58. Lu, Y.; Quardokus, R.; Lent, C. S.; Justaud, F.; Lapinte, C.; Kandel, S. A., *J. Am. Chem. Soc.* **2010,** *132*, 13519-13524.
59. Weyland, T.; Costuas, K.; Toupet, L.; Halet, J.-F.; Lapinte, C., *Organometallics* **2000,** *19*, 4228-4239.
60. (a) Coat, F.; Lapinte, C., *Organometallics* **1996,** *15*, 477-479; (b) Bartik, T.; Bartik, B.; Brady, M.; Dembinski, R.; Gladysz, J. A., *Angewandte Chemie International Edition in English* **1996,** *35*, 414-417.
61. (a) Narvor, N. L.; Lapinte, C., *J. Chem. Soc., Chem. Commun.* **1993**, 357-359; (b) Seyler, J. W.; Weng, W.; Zhou, Y.; Gladysz, J. A., *Organometallics* **1993,** *12*, 3802-3804; (c) Le Narvor, N.; Toupet, L.; Lapinte, C., *J. Am. Chem. Soc.* **1995,** *117*, 7129-7138; (d) Bruce, M. I.; Ellis, B. G.; Low, P. J.; Skelton, B. W.; White, A. H., *Organometallics* **2003,** *22*, 3184-3198; (e) Paul, F.; Meyer, W. E.; Toupet, L.; Jiao, H.; Gladysz, J. A.; Lapinte, C., *J. Am. Chem. Soc.* **2000,** *122*, 9405-9414; (f) Bruce, M. I.; Costuas, K.; Davin, T.; Ellis, B. G.; Halet, J.-F.; Lapinte, C.; Low, P. J.; Smith, M. E.; Skelton, B. W.; Toupet, L.; White, A. H., *Organometallics* **2005,** *24*, 3864-3881; (g) Bruce, M. I.; Low, P. J.; Costuas, K.; Halet, J.-F.; Best, S. P.; Heath, G. A., *J. Am. Chem. Soc.* **2000,** *122*, 1949-1962.
62. (a) Denis, R.; Toupet, L.; Paul, F.; Lapinte, C., *Organometallics* **2000,** *19*, 4240-4251; (b) Brown, N. J.; Collison, D.; Edge, R.; Fitzgerald, E. C.; Helliwell, M.; Howard, J. A. K.; Lancashire, H. N.; Low, P. J.; McDouall, J. J. W.; Raftery, J.; Smith, C. A.; Yufit, D. S.; Whiteley, M. W., *Organometallics* **2010,** *29*, 1261-1276; (c) Lancashire, H. N.; Brown, N. J.; Carthy, L.; Collison, D.; Fitzgerald, E. C.; Edge, R.; Helliwell, M.; Holden, M.; Low, P. J.; McDouall, J. J. W.; Whiteley, M. W., *Dalton Trans.* **2011,** *40*, 1267-1278.

Chapter Two

Syntheses, Characterisation and EPR Studies of $M\{(C\equiv C)_nR\}(dppe)Cp^*$ [n = 1, 2, 3; M = Fe, Ru; R = TMS, C_6H_5, $Au(PPh_3)$]

2.1 Introduction

Diynyl complexes are very useful intermediates for the construction of organometallic complexes containing long poly-ynyl carbon chains[1], thus, their syntheses are well-described. Diynyl complexes of the general formula $[M](C\equiv CC\equiv CR)_n$ (n = 1,2) incorporate a C_4 chain end-capped by a metallic fragment on one side, and an organic group on the other side, which may vary from a simple hydrogen atom to a trimethylsilyl protecting group or an aromatic group such as phenyl or ferrocene[2]. Especially, diynyl complexes having hydrogen, trimethylsilyl or $Au(PPh_3)$ end-groups are considered to be very useful synthetic intermediates for the construction of long poly-ynediyl structures which are synthesised via Hay coupling conditions[3] or Sonogashira conditions[4]. Well-known synthetic routes for the preparation of alkynyl-metal complexes of general formula $[M](C\equiv CR)$[5] via a vinylidene intermediate cannot be extended to the preparation of butadiynyl complexes. Indeed, formation of the highly reactive butatrienylidene species

$[M](=C=C=C=CHR)^+$ is favoured rather than the stable vinylidene intermediates[6]. Butatrienylidene intermediates are very sensitive toward nucleophiles such as phosphines, amines, H_2O[7] and solvents like MeOH[8], to afford substituted products. Several synthetic routes have been explored in the literature for the preparation of diynyl complexes: the most widely used are listed below:

i. Reactions of diynyl anions with metal halides or triflates.

ii. Reactions of 1,3-diynes with metal halides in the presence of Cu(I) catalysts.

iii. Reactions between metal halide complexes and trimethyltin-diynes.

iv. Oxidative addition of 1,3-diynes to electron-rich metal centres.

v. Reactions of 1,3-diynes with metal halides via the butatrienylidene intermediates.

2.1.1 Synthetic strategy (i)

Reactions of the organolithium diynyl $LiC{\equiv}CC{\equiv}CSiMe_3$ with metal halides or triflates to give the corresponding diynyl complexes and the associated lithium salt are widely described (Scheme 2.1). The trimethylsilyl-protected diynyl ligand has been chosen in most of the examples because of its stability and easy preparation from the stable 1,4-bis(trimethylsilyl)buta-1,3-diyne and CH_3Li-LiBr. This route has been used for the preparation of mono or bisubstituted organometallic complexes with metal fragments such as $Ru(PPh_3)_2Cp$[9], $Fe(CO)_2Cp$[10], TiL_2[11] or Mo(*N*-*N*)(η-C_7H_7)[12].

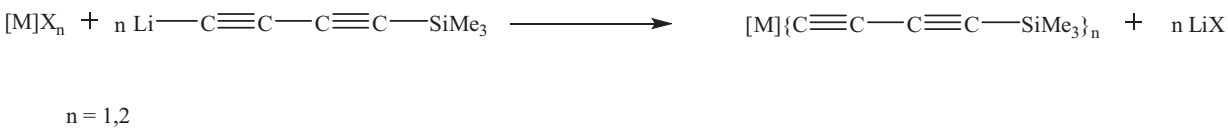

Scheme 2.1

Butadiynyl complexes with a trimethylsilyl end-group are interesting synthetic targets, as they can be deprotected by addition of the desilylation agent N^nBu_4F[10] to afford

[M](C≡CC≡CH) which can then be easily functionalised using the rich chemistry of the C≡CH moiety.

More recently, "one-pot" syntheses have been described. Trimethylsilyl-protected organic poly-ynes react with KF and metal halides in the presence of a few drops of DBU in MeOH (Scheme 2.2) to give poly-ynyl complexes with a wide variety of end groups R[13] in relatively good yields. As the products generally precipitate out of the solution, no further purification is needed.

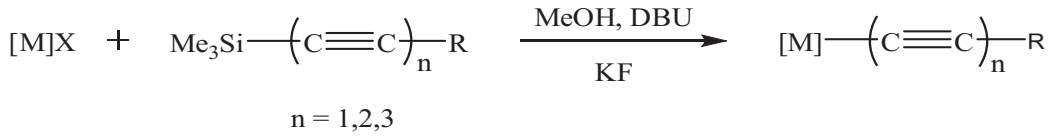

Scheme 2.2

2.1.2 Synthetic strategy (ii)

Sonogashira et al.[14] first described the synthesis of bis(diynyl)platinum complexes via the coupling of platinum halide precursors with buta-1,3-diyne in the presence of diethylamine and a copper(I) catalyst. It is considered that the first step of this reaction is the formation of the intermediate alkynyl-copper which by alkynyl-halide exchange with the metal halide gives the target diynyl complex and regenerates the copper(I) catalyst. This method has been successfully extended to several transition metal halides (Scheme 2.3) such as $WCl(CO)_3Cp$, $MoCl(CO)_3Cp$ and $FeCl(CO)_2Cp$[15].

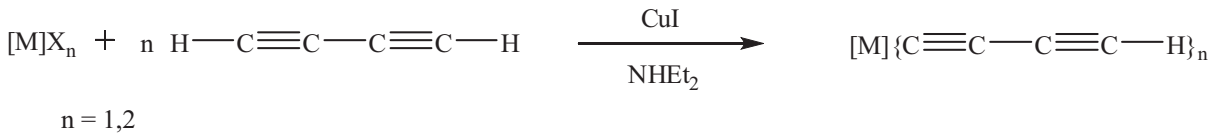

Scheme 2.3

2.1.3 Synthetic strategy (iii)

Trimethyltin-diynes are synthesised by reacting the organolithium diynyl LiC≡CC≡CR with trimethyltin chloride, 1,4-bis(trimethylstannyl)buta-1,3-diyne also being accessible by this route. Reactions between the trialkyltin-diynyl derivatives $Me_3SnC{\equiv}CC{\equiv}CR$ and $FeI(CO)_2Cp$ in the presence of palladium catalyst afford the desired diynyl-iron complexes (Scheme 2.4)[16]. When the halide atom is replaced by a hydroxy group, reaction can be

achieved without the necessity for palladium catalysts, formation of $Sn(OH)R_3$ being the driving force of the reaction[17].

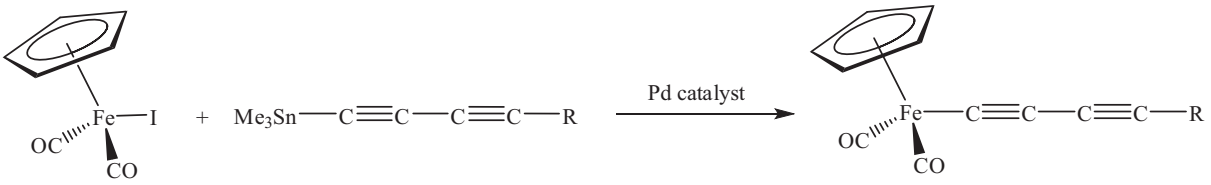

Scheme 2.4

2.1.4 Synthetic strategy (iv)

The preparation of diynyl-rhodium complexes containing $RhCl(P^iPr_3)_2$ fragments has been described by Werner et al.[18]. Reaction between the highly reactive and electron-rich organometallic precursor $\{RhCl(P^iPr_3)_2\}_n$ and an organic mono-substituted butadiyne HC≡CC≡CR afforded the oxidative addition product as a diynyl(hydrido)rhodium(III) complex (Scheme 2.5). It is assumed that the first intermediate formed during this reaction is the π-bonded diyne complex which has been characterised by ^{31}P NMR spectroscopy, to transform afterwards to the diynyl-hydrido complex by oxidative addition.

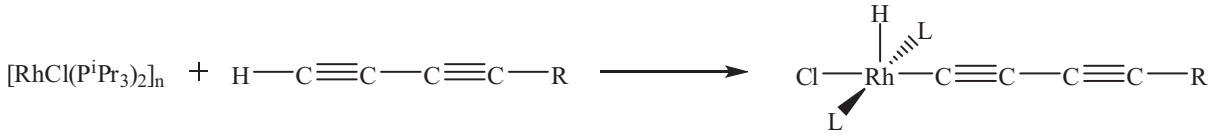

Scheme 2.5

2.1.5 Synthetic strategy (v)

Diynyl complexes can be synthesised via a butatrienylidene intermediate which is deprotonated instantaneously to prevent further reactions or decomposition. Examples of stable butatrienylidenes are extremely rare and only one complex of this type has been characterised by X-ray studies to date[19]. Organoiron complex **7** has been synthesised via this method: FeCl(dppe)Cp* **1** reacts with trimethylsilylbutadiyne $HC{\equiv}CC{\equiv}CSiMe_3$ in the presence of $NaBPh_4$ which, with a non-coordinating anion, promotes the ionisation of the metal-halide bond. Triethylamine is used both as solvent and base for the "in-situ" deprotonation of the butatrienylidene intermediate (Scheme 2.6)[20]. Several ruthenium

complexes have been synthesised using this synthetic route[2a, 8a] always with an amine (or a mixture of solvent and amine) as the solvent.

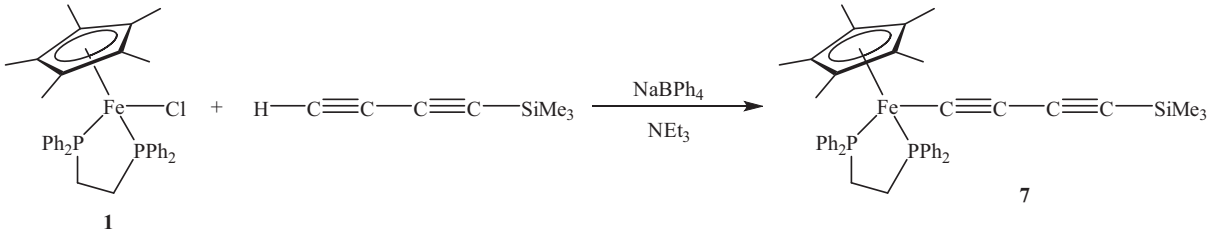

Scheme 2.6

2.1.6 Oxidation of diynyl complexes

Complexes containing a butadiynyl unit end-capped by two metal fragments have been extensively studied[3a, 21] and have attracted attention because of their unique electronic behaviour. Their redox properties have been investigated and for most of the examples stable radical monocations $[MC{\equiv}CC{\equiv}CM']^{\bullet+}$ have been isolated[22] and fully characterised.

However, there are only a few examples of oxidation studies on diynyl complexes containing just one metal centre and an organic end group[23]. This is probably due to the high instability of the radical monocation $[MC{\equiv}CC{\equiv}CR]^{\bullet+}$ in which the odd electron is delocalised over the butadiynyl unit[24] and possibly also onto the R group (Scheme 2.7), depending on the nature of the metal. Besides, the absence of the second metal fragment at the end of the carbon chain decreases the stability of the 17-electron complex because of the large unpaired spin density residing on the carbon chain, which is not sterically protected.

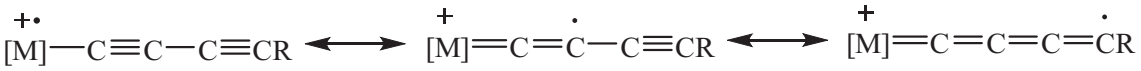

Scheme 2.7

To date, there is only one example of a stable diynyl monometallic radical cation which has been isolated and characterised by X-ray studies. Recently, Whiteley et al.[25] chemically oxidised the molybdenum complex $Mo(C{\equiv}CC{\equiv}CSiMe_3)(bipy)(\eta\text{-}C_7H_7)$ with $[FeCp_2]PF_6$ to afford the first stable radical cationic diynyl complex $[Mo(C{\equiv}CC{\equiv}CSiMe_3)(bipy)(\eta\text{-}C_7H_7)]PF_6$ as an orange-red solid (Scheme 2.8). The η-

cycloheptatrienyl-molybdenum fragment is known to be extremely effective in promoting the stability of 17-electron organometallic complexes[26].

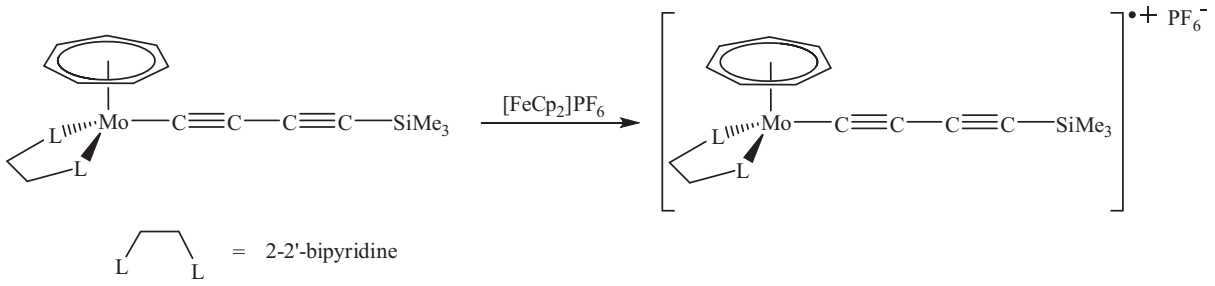

Scheme 2.8

The stability of the diynyl radical cations can be measured by cyclic voltammetry, where the reversibility of the oxidation wave indicates the stability of the 17-electron species at the electrode and whether it is a viable synthetic target.

2.2 Aims

Although monometallic diynyl complexes represent interesting synthetic intermediates for the construction of models of molecular wires containing long poly-yne chains, their electronic properties have not been extensively studied. In comparison with the well-known and studied M(C≡CR)(dppe)Cp* (M = Fe, Ru) complexes containing a C_2 chain, electronic properties of the diynyl complexes M(C≡CC≡CR)(dppe)Cp* (M = Fe, Ru) containing a longer carbon chain (C_4) are investigated using electrochemistry and EPR spectroscopy in this Chapter. The effects of the carbon chain length, end group R and the nature of the metal on the electronic behaviour of this type of complexes will be discussed.

This Chapter details the synthesis of new iron and ruthenium diynyl complexes M(C≡CC≡CR)(dppe)Cp* with different R end groups. The synthesis of Fe(C≡CC≡CC≡CSiMe$_3$)(dppe)Cp* (**9**) containing a longer carbon chain is also reported. Then, electrochemical and EPR studies of the new diynyl complexes and other related compounds are investigated.

2.3 Results and discussion

2.3.1 Synthesis of M(C≡CC≡CR)(dppe)Cp [M = Fe, Ru; R = Ph, Tol, Au(PPh$_3$)]*

Syntheses of unsymmetrical $SiMe_3$-protected organic 1,3-diynes were the first objectives to achieve the preparation of organometallic diynyl complexes. They are well described in the literature and there are many routes to them[28]. The Cadiot-Chodkiewicz coupling of halogenated alkynes with terminal alkynes based on copper(I) catalysis in the presence of a base (amine) is widely described[29]. However, an easier synthetic strategy based on the Sonogashira coupling (Scheme 2.9) has been used here and gave the protected diynes $RC{\equiv}CC{\equiv}CSiMe_3$ (R = Ph, Tol) in 70% yield[30]. Terminal organic diynes $RC{\equiv}CC{\equiv}CH$ have been synthesised by simple deprotection of $RC{\equiv}CC{\equiv}CSiMe_3$ (R = Ph, Tol) using K_2CO_3 in a 1:1 THF/MeOH mixture. Organic deprotected diynes are well known to be highly unstable[31], indeed they easily polymerise[32]. However, they can be stored in solution in a freezer for several weeks without noticeable decomposition[33].

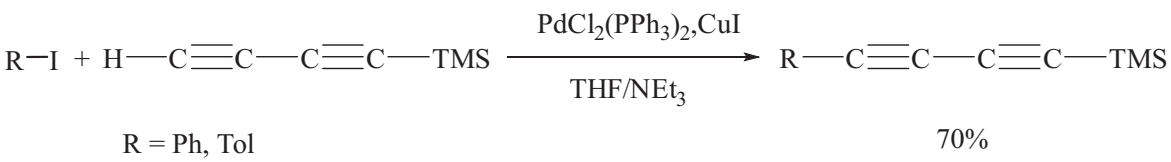

Scheme 2.9

Syntheses of the two new diynyl complexes Fe(C≡CC≡CR)(dppe)Cp* [R = Ph (**2a**), Tol (**2b**)] were successfully achieved [Synthetic strategy (*v*)] by the reaction of the organoiron precursor FeCl(dppe)Cp* (**1**) with one equivalent of the diyne RC≡CC≡CH (R = Ph, Tol) in the presence of $NaBPh_4$ in triethylamine (Scheme 2.10). After one night at room temperature, the solution had changed from black to bright orange. Before removing the solvents under reduced pressure, an excess of ^{t}BuOK was added to prevent the facile protonation and then decomposition of the product. The orange residue was extracted with toluene and after removing the solvent, a second extraction with diethyl ether was carried out. Compounds **2a** and **2b** were obtained as orange powders in 85% and 80% yield respectively. If a strong base as ^{t}BuOK is not added at the end of the reaction, the residue become green after removal of the solvents (presumably the highly instable butatrienylidene species is formed) and decomposition of the product was observed.

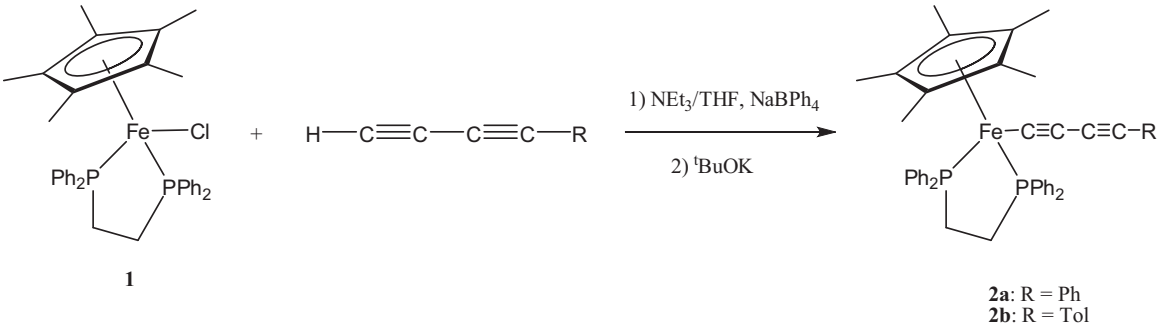

1

2a: R = Ph
2b: R = Tol

Scheme 2.10

The ruthenium analogue Ru(C≡CC≡CPh)(dppe)Cp* (**4**) has been synthesised via a different route [Synthetic strategy (*i*)]. In this case, a suspension of organoruthenium precursor RuCl(dppe)Cp* (**3**), KF and the protected organic diyne PhC≡CC≡CSiMe$_3$ in MeOH containing 1% H_2O and two drops of DBU was heated at the reflux point for one hour (Scheme 2.11). The resulting green precipitate was collected and purified on a basic alumina column, eluting with a dichloromethane/triethylamine mixture. Compound **4** was obtained as a bright yellow powder in 87% yield. The use of a small amount of H_2O in this reaction helps toward better precipitation of the product **4** and the yield is significantly improved. A base such as DBU is also very important because it avoids the formation and then decomposition of the butatrienylidene species. As for its iron analogues **2a** and **2b**, compound **4** is very sensitive toward protonation; indeed, solutions of **4** become green very quickly and another purification step is needed.

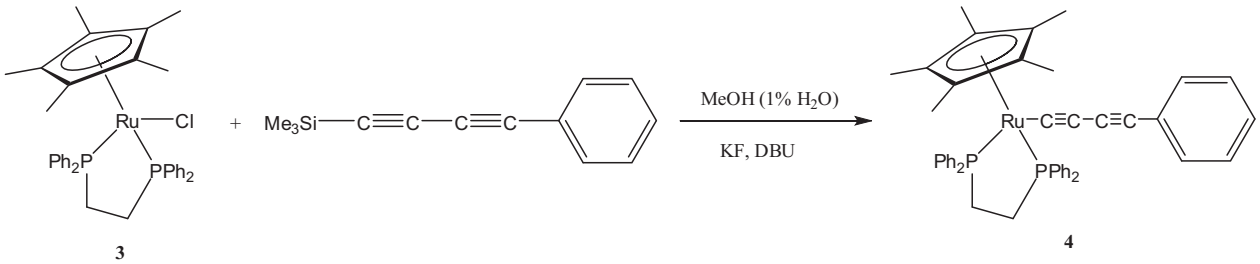

3 **4**

Scheme 2.11

Finally, the last diynyl-complex of this study, namely Fe{C≡CC≡CAu(PPh$_3$)}(dppe)Cp* (**8**), has been synthesised via a similar route to its ruthenium analogue Ru{C≡CC≡CAu(PPh$_3$)}(dppe)Cp* (**6**). The synthesis of **6** has previously been reported by Bruce et al.[2a], who reacted the trimethylsilyl-protected organoruthenium diynyl **5** with one equivalent of AuCl(PPh$_3$) in a sodium methoxide

solution (Scheme 2.12). Pure compound **6** precipitates out of the solution as a bright yellow solid in 98% yield.

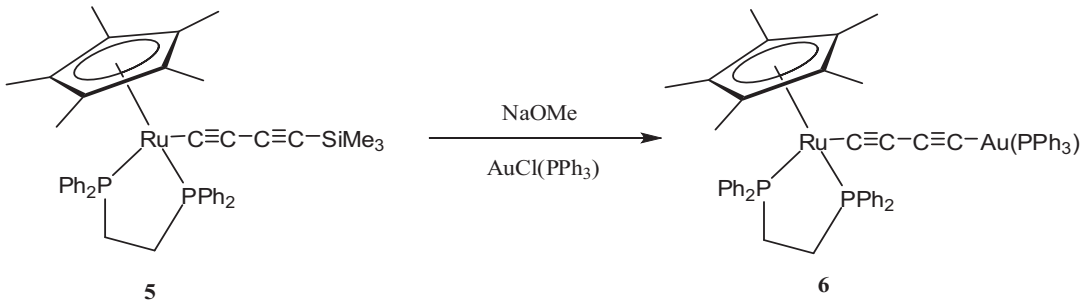

5 **6**

Scheme 2.12

In the iron case, sodium methoxide was added to a THF solution of the trimethylsilyl-protected Fe(C≡CC≡CSiMe$_3$)(dppe)Cp* (**7**) and after stirring for 20 minutes, one equivalent of AuCl(PPh$_3$) was added (Scheme 2.13). After stirring for four hours, the precipitate was collected and washed with cold methanol to give **8** as an orange solid in 74% yield. In contrast to the ruthenium chemistry, a 1:1 mixture of THF/methanol is used to promote the solubility of the complex **7**; no reaction was observed when only methanol was used as a solvent.

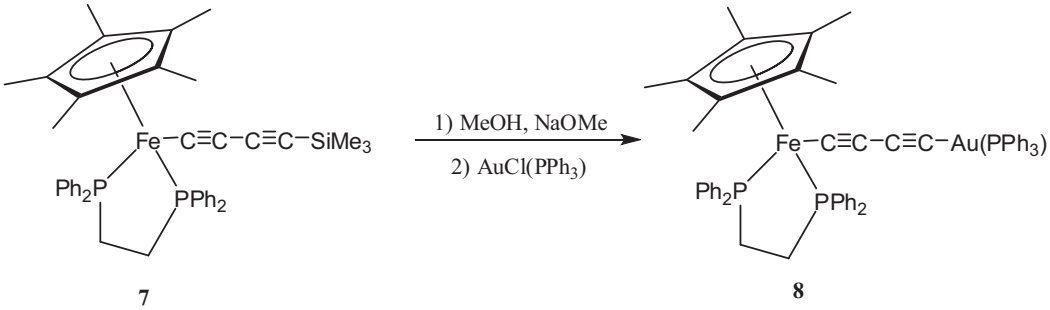

7 **8**

Scheme 2.13

2.3.2 Characterisation of M(C≡CC≡CR)(dppe)Cp [M = Fe, Ru; R = Ph, Tol, Au(PPh$_3$)]*

New diynyl complexes **2a**, **2b**, **4** and **8** have been fully characterised by the usual spectroscopic methods and single-crystal X-ray structural determinations for all compounds. Spectroscopic features are all as expected for the aryldiynyl complexes **2a** and **2b**. The IR spectrum of **2a** showed three ν(C≡C) bands at 2150, 2007 and 1987 cm^{-1}, one of the vibration modes being assigned to a Fermi coupling of the low energy C≡C

vibration. However, the IR spectrum of **2b** contains only two ν(C≡C) bands at 2149 and 1999 cm^{-1}. NMR spectra displayed all expected resonances for the Fe(dppe)Cp* fragment. In the ^{1}H NMR spectra the Cp* group gave singlets at δ 1.45 and 1.47, and CH_2 of the dppe multiplets at δ 1.77, 2.58 and 1.78, 2.60 for **2a** and **2b**, respectively. In the ^{31}P NMR spectra, singlets were observed at δ 100.2 (**2a**) and 100.3 (**2b**) for the two equivalent phosphorus atoms of the dppe ligand. In the ^{13}C NMR spectra, C_α of the C_4 chain were observed as triplets because of coupling with the phosphorus atoms at δ 144.74 ($^{2}J_{CP}$ = 38 Hz) and 142.98 ($^{2}J_{CP}$ = 38 Hz) for **2a** and **2b** respectively. The Me group in compound **2b** was observed at δ 1.97 in ^{1}H NMR and δ 19.86 in ^{13}C NMR. In the high resolution ES-mass spectra, $[M]^+$ ions were found at *m/z* 714.2275 (calculated: 714.2268) for **2a** and 728.2427 (calculated: 728.2424) for **2b**.

The analogous diynyl-ruthenium complex **4** containing a phenyl end-group has also been characterised, with ν(C≡C) bands in the IR spectrum at 2153 and 2016 cm^{-1}. In the ^{1}H NMR spectrum the Cp* resonance was observed at δ 1.59 while multiplets at δ 1.84 and 2.60 were assigned to the CH_2 units of the dppe. The ^{31}P NMR spectrum showed the usual resonance of the fragment Ru(dppe)Cp* at δ 80.3. Unfortunately, in the ^{13}C NMR spectrum, C_α is under the aromatic carbons. The high resolution ES-mass spectrum displayed $[M + H]^+$ at *m/z* 761.2065 (calculated: 761.2040).

For the diynyl iron complex **8** with the $Au(PPh_3)$ fragment, the ν(C≡C) bands were observed in the IR spectrum at 2069 and 1969 cm^{-1}. In the ^{1}H NMR spectrum, a singlet at δ 1.53 was assigned to the Cp*. In the ^{13}C NMR spectrum, the C_α resonance was observed at δ 123.26 ($^{2}J_{CP}$ = 40 Hz) which is significantly lower than for the other iron diynyl complexes **2a** and **2b** (Δδ ≈ 20 ppm). This difference is probably due to the electronic effect of the $Au(PPh_3)$ fragment on the carbon chain. However, the other three carbon atoms of the chain were observed as three singlets at δ 88.84, 94.18 and 104.06. ^{31}P NMR spectroscopy has proven to be very useful to characterise the gold complex **8**, indeed, the phosphorus resonance of the PPh_3 ligand was observed as a singlet at δ 42.0 whereas the singlet of the dppe ligand was observed at δ 100.0, the ratio between the two peaks being 1:2 respectively. Finally, $[M]^+$ was found in the ES-mass spectrum at *m/z* 1096.2525 (calculated: 1096.2453).

Selected spectroscopic data of the new diynyl complexes described in this part are collected in Table 2.1.

Table 2.1. Selected spectroscopic data for **2a**, **2b**, **4** and **8**.

Compound	IR $\nu_{C\equiv C}$ (cm^{-1})	NMR (δ)		
		^{1}H	^{13}C	^{31}P
2a	2150, 2007, 1987[a]	1.45 (s, 15H, Cp*), 1.77, 2.58 (2m, 4H, PCH_2)	8.89 (s, $C_5\mathit{Me}_5$), 87.26 (s, C_5Me_5), 144.74 (t, $^{2}J_{CP}$ = 38 Hz, C_α)	100.2 (s)
2b	2149, 1999[a]	1.47 (s, 15H, Cp*), 1.78, 2.60 (2m, 4H, PCH_2), 1.97 (s, 3H, Me)	8.91 (s, $C_5\mathit{Me}_5$), 19.86 (s, Me), 87.20 (s, C_5Me_5), 142.98 (t, $^{2}J_{CP}$ = 38 Hz, C_α)	100.3 (s)
4	2153, 2016[b]	1.59 (s, 15H, Cp*), 1.84, 2.60 (2m, 4H, PCH_2)	9.88 (s, $C_5\mathit{Me}_5$), 93.10 (s, C_5Me_5)	80.3 (s)
8	2069, 1969[b]	1.53 (s, 15H, Cp*), 1.83, 2.73 (2m, 4H, PCH_2)	10.45 (s, $C_5\mathit{Me}_5$), 88.25 (s, C_5Me_5), 123.26 (t, $^{2}J_{CP}$ = 40 Hz, C_α)	100.0 (s, dppe), 42.0 (s, PPh_3)

[a]KBr. [b]CH_2Cl_2.

Molecular structures

Crystallographic studies have been carried out on the four organometallic diynyl complexes described above. Single crystals of compounds **2a** and **2b** have been obtained by slow diffusion of pentane into a concentrated toluene solution of the complex. Figure 2.1 shows ORTEP plots of single molecules of **2a** and **2b** while selected structural data are collected in Table 2.2.

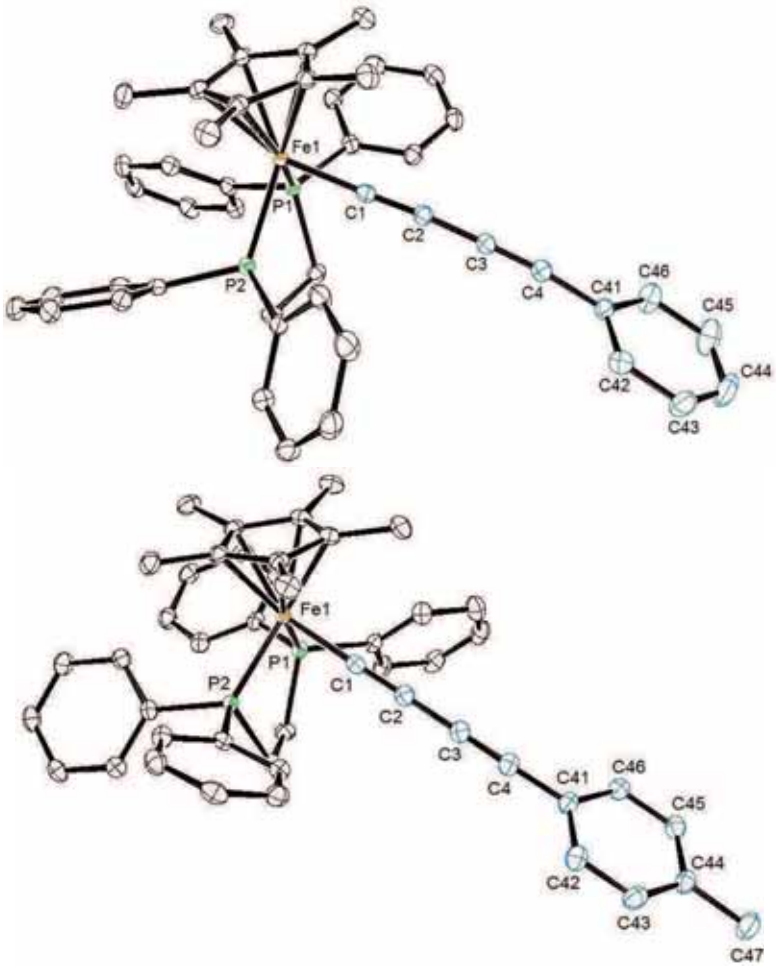

Figure 2.1. *ORTEP views of Fe(C≡CC≡CPh)(dppe)Cp* **2a** (top) and Fe(C≡CC≡CC$_6$H$_4$Me-4)(dppe)Cp* **2b** (bottom).*

Table 2.2. Selected structural parameters for **2a**, **2b** and **4**.

	2a	**2b**	**4**
Bond Distances (Å)			
M-P(1)	2.1808(4)	2.1789(5)	2.260(2)
M-P(2)	2.1955(4)	2.1906(5)	2.277(2)
M-Cp*$_{cent}$	1.746	1.746	1.896
M-C(1)	1.8733(13)	1.8779(17)	1.995(6)
C(1)-C(2)	1.2302(19)	1.230(2)	1.201(9)
C(2)-C(3)	1.3718(19)	1.379(2)	1.371(9)
C(3)-C(4)	1.211(2)	1.210(2)	1.220(9)
C(4)-C(41)	1.4336(19)	1.437(2)	1.41(1)
C(41)-C(42)	1.400(2)	1.404(3)	1.41(1)
C(41)-C(46)	1.398(2)	1.401(2)	1.38(1)
C(42)-C(43)	1.387(2)	1.387(3)	1.34(1)
C(43)-C(44)	1.384(3)	1.395(3)	1.39(1)
C(44)-C(45)	1.388(3)	1.394(3)	1.37(1)
C(45)-C(46)	1.390(2)	1.388(2)	1.40(1)
C(44)-C(47)		1.514(3)	
Bond Angles (°)			
P(1)-M-P(2)	84.995(14)	85.191(18)	82.33(7)
C(1)-M-P(1)	84.82(4)	84.88(5)	83.3(2)
C(1)-M-P(2)	85.75(4)	85.09(5)	84.9(2)
M-C(1)-C(2)	177.33(12)	178.37(14)	176.6(6)
C(1)-C(2)-C(3)	176.45(14)	177.78(18)	175.2(8)
C(2)-C(3)-C(4)	178.59(15)	179.45(18)	178.5(8)
C(3)-C(4)-C(41)	174.47(15)	177.3(2)	173.6(8)

Compounds **2a** and **2b** are very similar structurally but crystallised in different space groups. Crystals of **2a** are monoclinic $P2_1/a$ with the unit cell parameters: a = 10.3375(4), b = 35.2980(11), c = 10.6050(3) Å and β = 107.5780(10)°; whereas crystals of **2b** are triclinic *P*-1 with unit cell parameters: a = 10.4685(3), b = 10.6498(3), c = 18.4355(5) Å, α = 93.2620(10), β = 105.8030(10) and γ = 106.3860(10)°. In each case, the unit cell contains one molecule of the diynyl complex. The two iron centres adopt a pseudo-octahedral geometry which is typical for these complexes, the average Fe-P and Fe-C(1) bond lengths are 2.18 and 1.88 Å respectively, normal for this type of organoiron compound. The C_4 chains are quasi-linear with angles being between 174.5(2) and 179.5(2)°; the carbon-carbon distances in the chain are alternately short C(1)-C(2), long

C(2)-C(3) and short C(3)-C(4) confirming the diynyl nature of the chain, the furthest triple bond from the metal being the shorter.

The analogous ruthenium complex **4** crystallised from a dichloromethane/hexane solution with a single molecule in the unit cell. The ORTEP plot of **4** is illustrated in Figure 2.2 and selected structural parameters are also collected in Table 2.2. **4** crystallised as monoclinic $P2_1/c$ with unit cell parameters: a = 10.6569(7), b = 35.760(3), c = 10.2624(8) Å and β = 107.406(8)°.

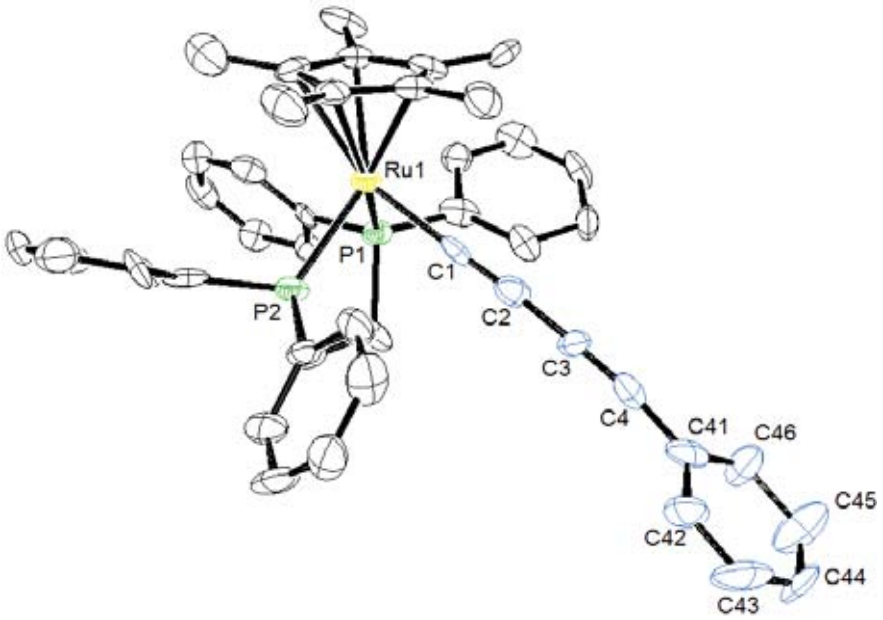

Figure 2.2. *ORTEP view of Ru(C≡CC≡CPh)(dppe)Cp* **4**.*

Similarly to the iron complexes **2a** and **2b**, the ruthenium atom has a pseudo-octahedral geometry; however, Ru-P(1,2) [2.260(2) and 2.277(2) Å] and Ru-C(1) [1.995(6) Å] distances are clearly different. This is due to the different atomic radii between the two metal atoms: Fe = 1.26 and Ru = 1.34 Å. The C_4 carbon chain is also very close to linear with angles being in the range of 173.6(8)-178.5(8)°.

Suitable crystals of **8** for X-ray crystallographic determination were obtained by slow evaporation of a dichloromethane solution. The structure determination confirmed the presence of the gold fragment. The unit cell contained one molecule of **8** and three molecules of dichloromethane, the compound is triclinic *P*-1 space group and the unit cell dimensions are: a = 12.6624(5), b = 14.5461(6), c = 16.4850(7) Å, α = 93.418(4), β=

102.305(4) and γ = 99.647(4)°. An ORTEP plot of a molecule is shown in Figure 2.3 and important structural data are given in Table 2.3. Substitution of the aryl group in compounds **2a** and **2b** by the gold fragment in **8** has not significantly affected the structural parameters. As expected, the metal centre has a pseudo-octahedral geometry and bond lengths in the Fe(dppe)Cp* fragment are characteristic for a Fe(II) complex. The organometallic Fe-C_4-Au-P chain is also quasi-linear with angles between 172.8(4) and 179.0(5)°.

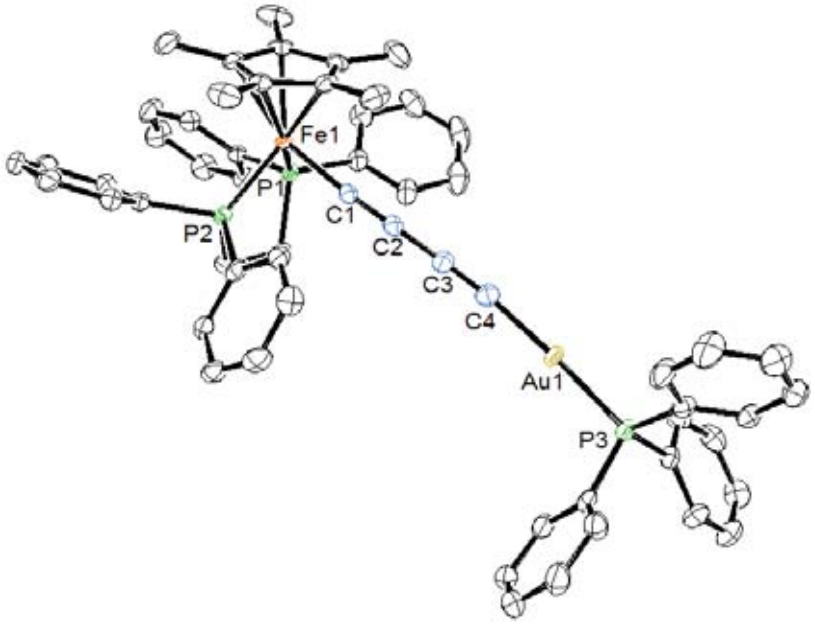

Figure 2.3. *ORTEP view of Fe{C≡CC≡CAu(PPh$_3$)}(dppe)Cp* **8**.*

Table 2.3. Selected structural parameters for **8**

Bond Distances (Å)		**Bond Angles (°)**	
Fe-P(1)	2.1807(13)	P(1)-Fe-P(2)	86.08(5)
Fe-P(2)	2.1799(12)	C(1)-Fe-P(1)	83.99(14)
Fe-Cp*$_{cent}$	1.741	C(1)-Fe-P(2)	87.54(13)
Fe-C(1)	1.875(4)	Fe-C(1)-C(2)	174.9(4)
C(1)-C(2)	1.237(6)	C(1)-C(2)-C(3)	178.0(5)
C(2)-C(3)	1.371(6)	C(2)-C(3)-C(4)	179.0(5)
C(3)-C(4)	1.217(6)	C(3)-C(4)-Au(1)	172.8(4)
C(4)-Au(1)	1.986(5)	C(4)-Au(1)-P(3)	174.25(14)
Au(1)-P(3)	2.2707(11)		

2.3.3 Synthesis and characterisation of Fe(C≡CC≡CC≡CSiMe$_3$)(dppe)Cp (9)*

Mononuclear iron complexes containing the Fe(dppe)Cp* fragment and a chain longer than four carbons have never been synthesised before. However, syntheses of their ruthenium analogues such as Ru(C≡CC≡CC≡CSiMe$_3$)(dppe)Cp* (**10**) are well known and described[34] by the Bruce group. The same synthetic strategy, via a gold coupling reaction, as the synthesis of hexatriynyl-ruthenium complex **10** has been used to prepare its iron analogue Fe(C≡CC≡CC≡CSiMe$_3$)(dppe)Cp* (**9**). The diynyl-gold complex **8** was treated with an excess of iodo(trimethylsilyl)ethyne in a THF/triethylamine (1:1) mixture in the presence of the catalysts Pd(PPh$_3$)$_4$ and CuI (Scheme 2.14). After one night at room temperature, the solvent was removed under reduced pressure and a triethylamine extract of the residue was purified on a basic alumina column, eluting with a mixture of triethylamine/hexane. Compound **9** was obtained as an orange powder in 55% yield.

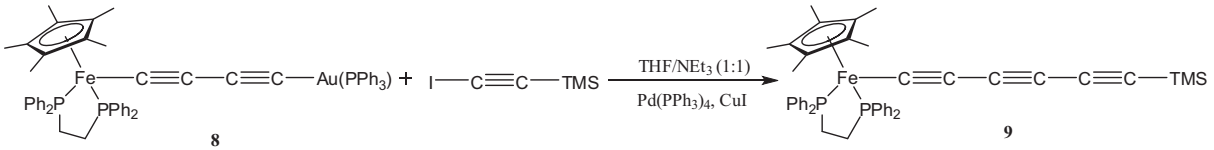

Scheme 2.14

Only two ν(C≡C) bands were observed in the IR spectrum of **9** at 2092 and 1952 cm^{-1}. The TMS resonance was observed at δ 0.13 (^{1}H NMR) and at δ 0.35 (^{13}C NMR) while the Fe(dppe)Cp* fragment showed all the expected resonances in ^{1}H NMR, ^{13}C NMR and ^{31}P NMR spectra, with a singlet at δ 97.9 corresponding to the two equivalent phosphorus atoms of the dppe ligand. In the ^{13}C NMR spectrum, the six quaternary carbons of the chain were found at δ 151.07 as a triplet ($^2J_{PC}$ = 38 Hz) for C$_\alpha$ and at δ 47.06, 69.29, 77.18, 94.34, 100.95 for the other five carbons. The high resolution ES-mass spectrum contained [M]$^+$ at *m/z* 734.2388 (calculated: 734.2350).

Crystals of **9** were grown by slow diffusion of hexane into a triethylamine solution of the hexatriynyl complex. Complex **9** crystallised with two molecules in the unit cell. ORTEP plots of the unit cell and one molecule are displayed in Figure 2.4 while distances and angles are given in Table 2.4. Arrangement between the two unique molecules is unusual and might result from π-π interaction through the Cp* rings. In the Fe(dppe)Cp*series, π-π stacking has previously been observed between anthracene

moieties connected to Fe(dppe)Cp* fragments through a C_2 chain, and between TCNE and Cp* when the anthracenyl-iron complex was oxidised with TCNE[35]. However, in the case of complex **9**, the distance between the two Cp* centroids, $d[Cp^*(1)_{cent} - Cp^*(2)_{cent}]$ = 4.388 Å, is probably too long to be assigned to π-π stacking interaction. Nevertheless, short contacts are observed between protons of methyl groups of the Cp* ligand on one molecule and the carbon atoms of the Cp* attached to the other molecule of the same crystal unit. These short contacts range between 2.688 and 2.826 Å, which are shorter than the sum of the Van der Waals radii of hydrogen and carbon atoms [$r_w(H) + r_w(C)$ = 2.9 Å]. This intermolecular arrangement between Cp* rings is unprecedented for this organoiron series.

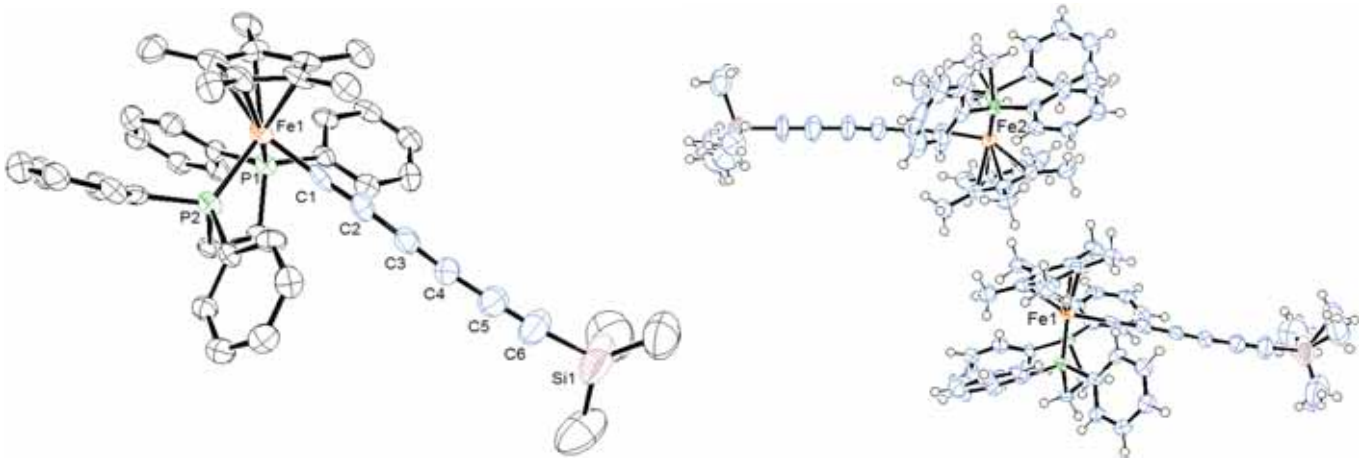

Figure 2.4. *ORTEP view of Fe(C≡CC≡CC≡CSiMe₃)(dppe)Cp*9 (left) and view of the unit cell (right).*

Table 2.4. Selected structural parameters for **9** (Italicised values refer to the second molecule).

Bond Distances (Å)		Bond Angles (°)	
Fe-P(1)	2.1847(15), *2.1831(17)*	P(1)-Fe-P(2)	85.73(6), *85.35(6)*
Fe-P(2)	2.1938(15), *2.1999(16)*	C(1)-Fe-P(1)	83.07(16), *84.17(18)*
$Fe-Cp^*_{cent}$	1.733, *1.740*	C(1)-Fe-P(2)	87.28(16), *89.41(17)*
Fe-C(1)	1.850(6), *1.849(6)*	Fe-C(1)-C(2)	177.9(5), *173.7(5)*
C(1)-C(2)	1.230(7), *1.238(8)*	C(1)-C(2)-C(3)	173.5(6), *175.3(7)*
C(2)-C(3)	1.354(8), *1.376(9)*	C(2)-C(3)-C(4)	177.6(6), *177.4(7)*
C(3)-C(4)	1.227(8), *1.200(8)*	C(3)-C(4)-C(5)	175.7(7), *173.2(8)*
C(4)-C(5)	1.358(9), *1.396(9)*	C(4)-C(5)-C(6)	177.9(8), *178.8(8)*
C(5)-C(6)	1.212(9), *1.216(9)*	C(5)-C(6)-Si	172.0(7), *172.6(8)*
C(6)-Si	1.826(8), *1.815(7)*		

Crystals are monoclinic $P2_1/n$ with unit cell parameters: a = 47.893(3), b = 17.882(2), c = 20.3130(10) Å and β = 102.660(10)°. Compound **9** shows structural parameters similar to those of the organoiron complexes **2a**, **2b** and **8** described above, although there is a small difference in the Fe-C(1) bond length which is slightly shorter for the TMS-protected complex (1.85 vs 1.87 Å). This difference can be attributed to the σ-donor behaviour of the TMS fragment which results in a shortening of the Fe-C(1) bond. The bridge between the six carbons and the silicon atom is close to linear with angles in the range of 172.0(7)-177.9(8)°, although it is noticeable that the angle C(5)-C(6)-Si [172.0(7), *172.6(8)°*] is slightly smaller than the others, which induces a small bending at the end of the chain as shown in Figure 2.4.

2.3.4 Electrochemistry

The electrochemical behaviour of the new complexes **2a**, **2b**, **4**, **8** and **9** has been investigated and further compared with related complexes containing shorter and longer carbon chains with different end-groups. The aim of this work was first, to investigate the electrochemical oxidation potentials of the new compounds and afterwards, if appropriate, to oxidise them chemically for EPR studies. All cyclic voltammograms (CVs) were recorded in CH_2Cl_2 at room temperature with 0.1 M $[Bu^n_4N]PF_6$ as the supporting electrolyte and with a 100 $mV.s^{-1}$ scan rate. $[FeCp_2]/[FeCp_2]^+$ = +0.46 V (vs SCE) or $[FeCp^*_2]/[FeCp^*_2]^+$ = -0.02 V (vs SCE) couples were used as internal references.

CVs of the aryldiynyl complexes **2a** and **2b** are given in Figure 2.5. For each compound, one 1-e oxidation wave is observed at E^0(**2a**) = -0.02 and E^0(**2b**) = -0.04 V, respectively, which is fully reversible (i_a/i_c = 1). The oxidation potential of **2b** is slightly lower because of the electronic effect of the toluene fragment which is more electron-donating than phenyl. This clearly indicates that the electronic effect of the phenyl ring is sensed by the metal centre.

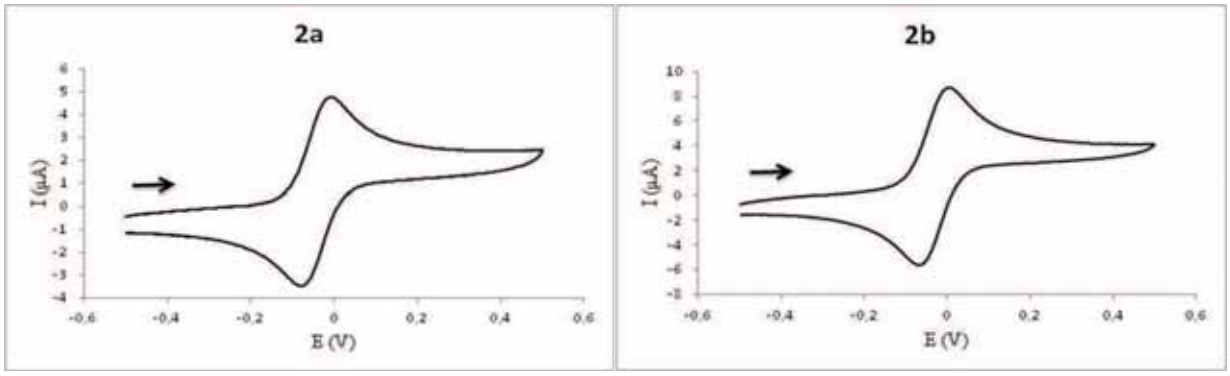

Figure 2.5. *Cyclic voltammograms (V vs SCE) of **2a** (left) and **2b** (right).*

When the aryl group is substituted by the gold fragment $Au(PPh_3)$, the oxidation potential of the iron complex $Fe\{C{\equiv}CC{\equiv}CAu(PPh_3)\}(dppe)Cp^*$ is significantly lower at E^0(**8**) = -0.16 V. This phenomenon has already been observed for the ruthenium analogue (see Table 2.5) and has been attributed to the $Au(PPh_3)$ group enhancing the σ-donor ability of the diynyl ligand[2a], resulting in a decrease in the oxidation potential. In the CV of **8** other waves were observed and have been attributed to decomposition products due to the electrochemical instability of the couple **8**/[**8**]$^+$; indeed, the E^0(**8**) process is only partially reversible: i_a/i_c = 0.61. Increasing the scan rate did not result in a fully reversible process.

The electrochemical behaviour of the diynyl-ruthenium complex **4** (Figure 2.6) is dramatically different from its iron analogue. The formal oxidation potential increases significantly to E^0(**4**) = 0.44 V [ΔE^0(**4**-**2a**) = 0.46 V]. This effect can be explained by ruthenium being more difficult to oxidise than iron. The E^0(**4**) process is also irreversible and suggests that the oxidised species is highly unstable even at the electrode surface.

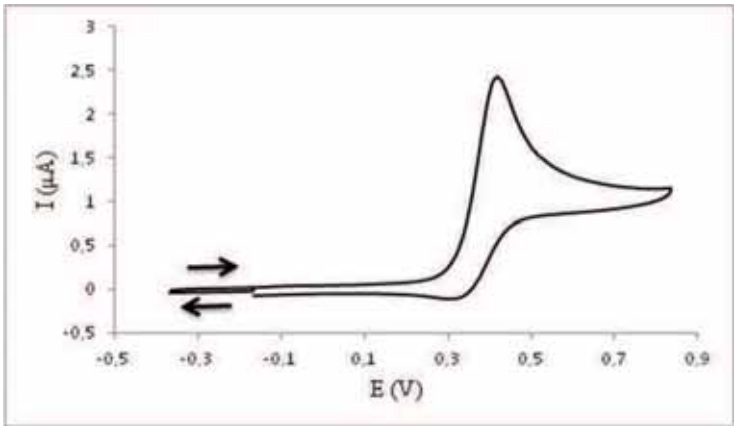

Figure 2.6. *Cyclic voltammogram of **4** (V vs SCE).*

The electrochemical behaviour of **9** has also been investigated. The CV (Figure 2.7) shows one fully reversible oxidation wave (i_a/i_c = 1) at E^0(**9**) = 0.08 V. The oxidation potential of the hexatriynyl complex is higher than those of the related iron diynyl complexes (see Table 2.5); the oxidation potentials increase with the length of the carbon chain[3c].

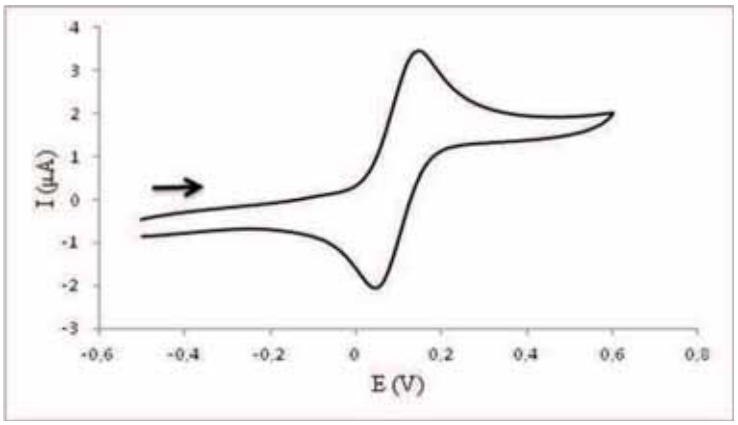

Figure 2.7. *Cyclic voltammogram of **9**.*

Table 2.5 summarises the electrochemical oxidation potentials and the IR ν(C≡C) bands of the new compounds described in this Chapter and some related organoiron and ruthenium complexes. As found previously, oxidation potentials of ruthenium complexes are higher than those of the iron analogues by ca 0.4 V. The reversibility of the processes is considerably affected by the nature of the metal, almost all processes for the iron complexes being fully reversible (apart compound **8**) whereas those of the ruthenium analogues are not. Irreversibility of the ruthenium processes is due to the formation of highly unstable 17-e species on the electrode surface, which then rapidly decompose. Indeed, it has already been observed that the 17-e iron species are more stable than the ruthenium ones[27b]. The length of the carbon chain is also a significant factor which strongly affects the oxidation potentials: $E^0(C_2) < E^0(C_4) < E^0(C_6)$, while the gold fragment "$Au(PPh_3)$" facilitates oxidation of the complexes.

Table 2.5. Electrochemical and IR data for M{(C≡C)$_n$R}(dppe)Cp* [n = 1, 2, 3; M = Fe, Ru; R = TMS, C_6H_5, Au(PPh_3)].

Compound	E^0 (V)	i_a/i_c	$\nu_{C\equiv C}$ (cm^{-1})	Ref
Fe(C≡CC_6H_5)(dppe)Cp* **11**	-0.15	1	2053[c]	36
Fe(C≡CC≡CC_6H_5)(dppe)Cp* **2a**	-0.02	1	2150, 2007, 1987[b]	This work
Fe(C≡C$SiMe_3$)(dppe)Cp* **12**[a]	-0.15	1	1968[b]	This work
Fe(C≡CC≡C$SiMe_3$)(dppe)Cp* **7**	0.00	1	2165, 2090, 1980[b]	37
Fe(C≡CC≡CC≡C$SiMe_3$)(dppe)Cp* **9**	+0.08	1	2092, 1952[c]	This work
Fe{C≡CC≡CAu(PPh_3)}(dppe)Cp* **8**	-0.16	0.61	2069, 1969[c]	This work
Ru(C≡CC_6H_5)(dppe)Cp* **13**	+0.23	> 0.90	2071[c]	27b
Ru(C≡CC≡CC_6H_5)(dppe)Cp* **4**	+0.44	Irr	2153, 2016[c]	This work
Ru(C≡C$SiMe_3$)(dppe)Cp* **14**[a]	+0.26	1	1996[c]	This work
Ru(C≡CC≡C$SiMe_3$)(dppe)Cp* **5**	+0.43	Irr	2171, 2095, 1990[c]	2a
Ru(C≡CC≡CC≡C$SiMe_3$)(dppe)Cp* **10**	+0.41	Irr	2110, 1971[c]	34
Ru{C≡CC≡CAu(PPh_3)}(dppe)Cp* **6**	+0.15	Irr	2119, 2072, 1981[c]	2a
Ru{C≡CC≡CC≡CAu(PPh_3)}(dppe)Cp* **15**			2121, 2088, 1965[c]	34

[a]Complexes prepared using the cited methods[38]. [b]KBr. [c]CH_2Cl_2.

2.3.5 Glass EPR spectroscopy

Electronic paramagnetic resonance (EPR) spectroscopy is a very useful technique for the characterisation of molecules with unpaired electrons. Indeed, 17-e iron and ruthenium complexes $[M(C{\equiv}CR)(dppe)Cp^*]^{\bullet+}$ have been characterised by EPR analyses[27], each metal complex having a unique signature containing three g-tensors. Signal anisotropy correlates with the delocalisation of the odd electron in the organometallic complex; when the unpaired electron is more localised on the metal atom the anisotropy is large, while when the unpaired electron is more delocalised over the whole molecule, the anisotropy is small. EPR spectra can be recorded at liquid nitrogen temperature and below, in the solid state or in solution which in the case of non-stable monoradical cation is a very efficient analysis technique. Indeed, for an unstable radical monocation such as an oxidised diynyl complex, solutions can be frozen in liquid nitrogen immediately after chemical oxidation to trap the EPR-active 17-e species, hopefully preventing further reactions or decomposition.

A series of compounds of general formula $Cp^*(dppe)M(C{\equiv}C)_nR$ (M = Fe and Ru, n = 1, 2, and 3, R = Ph, $SiMe_3$, and $AuPPh_3$) were treated with less than one equivalent of $[FeCp_2]PF_6$ in a CH_2Cl_2 at -80°C, providing green solutions that were transferred into an EPR tube before being cooled to 77 K. The X-band EPR spectra of the hexafluorophosphate salts of the monocations were run at 66 K and displayed three well-resolved features corresponding to the components of the *g* tensors as depicted in Figure 2.8 for $[Cp^*(dppe)Fe(C{\equiv}C)_2Ph]PF_6$ ([**2a**]PF_6) and $[Cp^*(dppe)RuC{\equiv}CSiMe_3]PF_6$ ([**14**]PF_6), chosen as representative examples for this series of 17-e complexes. The general pattern of the spectra with three *g*-tensor components is characteristic of low-spin d^5 Fe(III) and Ru(III) in a pseudo-octahedral environment. The *g* values extracted from the spectra are collected in Table 2.6.

Solutions of these radical cations are all stable at low temperature when they are kept as glass. As the temperature was allowed to increase, rapid decomposition of the organometallic materials takes place except for the Fe(III) radical cations $[Cp^*(dppe)FeC{\equiv}CPh]PF_6$ ([**11**]PF_6) and $[Cp^*(dppe)FeC{\equiv}CSiMe_3]PF_6$ ([**12**]PF_6) which are stable at 20 °C. Replacing iron by ruthenium or increasing the number of carbons in the alkynyl ligand decreases the kinetic stability of the radical cations. In the case of R = Ph, n = 2, the disappearance of the radical is associated with a decrease of the intensity of the

EPR signal suggesting that a clean chemical process has occurred. In the other cases, the appearance of several new signals in the spectra suggests that the radical decomposes to give several by-products, some of them being paramagnetic.

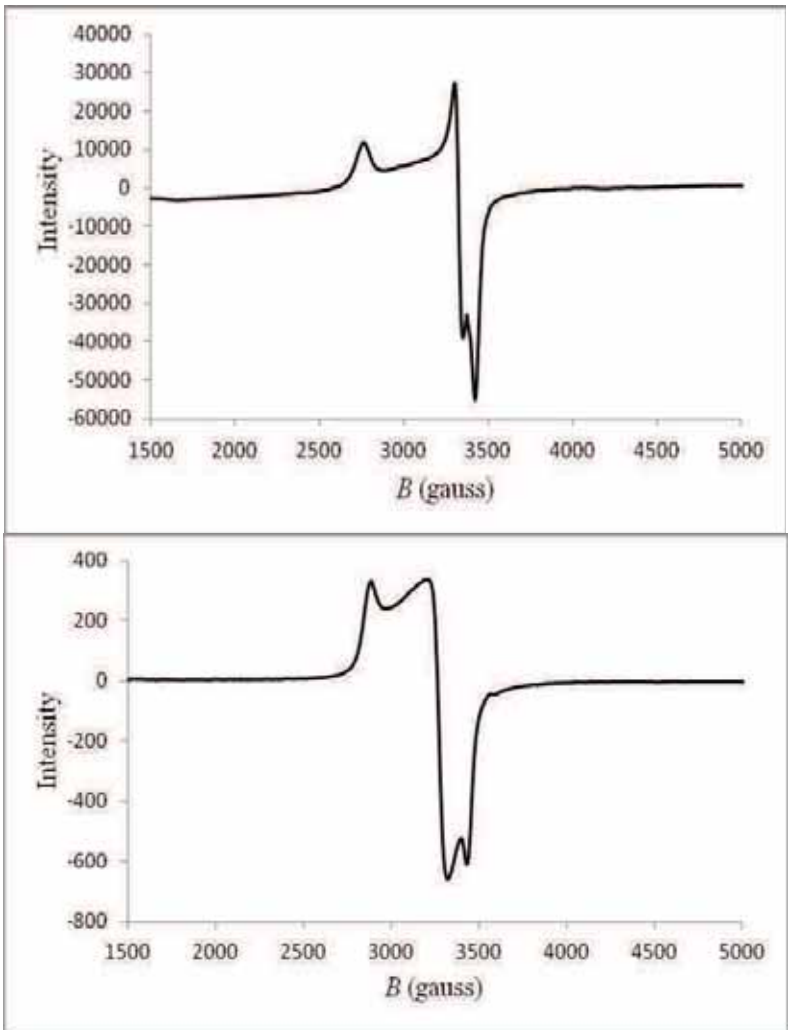

Figure 2.8. *EPR spectra of [**2a**]PF_6 (top) and [**14**]PF_6 (bottom).*

Table 2.6. Experimental EPR data[a] for $[Cp^*(dppe)M(C{\equiv}C)_nR]PF_6$ complexes

Cpnd	M	R	n	g_1	g_2	g_3	Δg	g_{iso}	ref
11[c]	Fe	C_6H_5	1	2.464	2.033	1.975	0.489	2.157	5c
2a[c]	Fe	C_6H_5	2	2.335	1.937	1.881	0.454	2.051	This work
12[b,c]	Fe	$SiMe_3$	1	2.488	2.030	1.975	0.513	2.164	This work
7[b,d]	Fe	$SiMe_3$	2	2.476	2.032	1.971	0.505	2.160	This work
9[d]	Fe	$SiMe_3$	3	2.475	2.030	1.971	0.504	2.159	This work
8[d,e]	Fe	$AuPPh_3$	2	2.401	2.084	1.994	0.407	2.160	This work
13[c]	Ru	C_6H_5	1	2.227	2.057	1.988	0.239	2.091	27b
4[d]	Ru	C_6H_5	2	2.418	2.086 (35)	1.998 (55)	0.420	2.167	This work
14[b,d]	Ru	$SiMe_3$	1	2.345	2.069	1.974	0.371	2.129	This work
5[b,d,e]	Ru	$SiMe_3$	2	2.273	2.048	1.988	0.285	2.103	This work
10[b,d]	Ru	$SiMe_3$	3	2.299	2.040 (41)	1.975 (40)	0.324	2.105	This work
6[b,d]	Ru	$Au(PPh_3)$	2	2.275	2.051	1.986	0.289	2.104	This work
15[b,d,e]	Ru	$Au(PPh_3)$	3	2.100	2.034 (40)	2.004 (25)	0.096	2.046	This work

[a]At 66 K in CH_2Cl_2 glass; $[FeCp_2]PF_6$ is used as oxidising reagent unless otherwise specified. [b]Complexes prepared using the cited methods[2a, 34, 37-38]. [c]The M(III) radical cation is thermally stable at 20 °C for at least a few minutes in the EPR tube. [d]The M(III) radical cation is not thermally stable above -20 °C. [e]The EPR spectrum contains significant amounts of impurities.

For the iron complexes of this series, the anisotropy tensors (Δg) are large, ranging from 0.513 to 0.407; they are not very sensitive to the number of carbons on the alkynyl ligand and the nature of R. In contrast, for the ruthenium analogues, the Δg parameters range from 0.420 to 0.096, showing that the nature of the SOMO strongly depends on the number of carbons in the alkynyl fragment and the nature of the terminal substituents. Comparing the Fe and Ru analogues overall (same chain length, same substituent), the Δg parameters are smaller in the ruthenium series. These observations are in line with previous experimental and theoretical results which concluded that the spin density is mainly localised on the

metal centre in the iron series and largely distributed between the metal and the unsaturated ligand in the case of the ruthenium complexes[27b].

More in-depth analysis of the Δg values in the case of the ruthenium series shows that this parameter decreases when the number of carbon increases for R = $SiMe_3$, Ph and $AuPPh_3$, but this effect is far from linear. In addition, for a given value of n, the Δg values are generally smaller for R = $SiMe_3$ and $AuPh_3$ which present a spherical symmetry, than for the phenyl as a terminal substituent (Note: this feature is not true for n = 2, M = Fe)

Calculations of the *g* tensors are in progress and the preliminary results obtained by Gendron support the fact the anisotropy of the *g*-tensor is larger overall in the Fe series. This is illustrated by the atomic spin density distribution which is more localised on the metal atom in that case (range: 0.77-0.90 e for Fe, 0.44-0.54 e for Ru). In the case of R = Ph, the calculations reveal an additional factor, namely a strong relationship between the orientation of the phenyl substituent toward the metallic fragment in both series. When the phenyl is rotated from a plane perpendicular to the cyclopentadienyl to one quasi-parallel to it, the spin densities on the carbon atoms of the phenyl substituent significantly decrease (for symmetry reasons) leading to an important increase in Δg (up to 1.88 in the iron series, for example). Nevertheless, only a limited amount of these structures are stable enough to be populated at room temperature (small rotation < 20°). The substituent effect is currently under investigation.

2.4 Conclusion

New organo-iron and -ruthenium complexes M{$(C\equiv C)_nR$}(dppe)Cp* containing C_4 and C_6 chains with different R end-groups have been synthesised, characterised and their structures determined. From the electrochemical investigations, some clear conclusions can be drawn: as expected, iron complexes are easier to oxidise than their ruthenium analogues. Oxidation potentials are also very sensitive to the chain length: the shorter the carbon chain, the easier it is to oxidise the organometallic complex. Finally, with more electron-rich R end-groups, such as $Au(PPh_3)$, the oxidation is easier.

Additionally, conclusions from the EPR investigations can be drawn. As expected, the anisotropy parameters in the iron complexes are larger overall than those in the ruthenium

ones. However, the effect of the carbon chain length seems to be negligible, as observed in the $[Cp^*(dppe)Fe(C{\equiv}C)_nSiMe_3]PF_6$ (n = 1, 2, 3) series where the g values are almost identical. In this series, the Δg values are constant suggesting that the metal / carbons ratio in the HOMO of the 17-e species is almost constant with the carbon chain length. The effects of the R end groups only slightly change the EPR data, but the effects are opposite in the iron and ruthenium series. An exception was observed for complexes containing the $Au(PPh_3)$ end-group, which slightly decreases the anisotropy parameters in both the iron and ruthenium series. The $Au(PPh_3)$ seems to play an unique role, it is a strong electron donor group which has been shown by electrochemistry, but surprisingly it decreases the stability of the 17-e species. The Δg values in EPR are small suggesting a strong contribution of the carbon ligand in the HOMO which could be at the origin of the kinetic unstability of the gold derivatives. Theoretical calculations are currently under way to further understand and take advantage of these results.

Experimental

General Considerations. All reactions were carried out under dry high-purity nitrogen or argon using standard Schlenk techniques unless otherwise stated. Common solvents were dried, distilled under nitrogen or argon, and degassed before use. Separations were carried out by preparative thin-layer chromatography (TLC) on glass plates (20 × 20 cm) coated with silica (Merck 60 GF254, 0.5 mm thick). Chromatography columns used silica (Scharlau 60, 0.04-0.06 mm, 230-400 mesh) or basic alumina (Fluka, Brockmann activity II, basic, pH10 ± 0.5).

Instruments. IR spectra were obtained on a Bruker IFS28 FT-IR spectrometer (4000-400 cm^{-1}). Spectra in CH_2Cl_2 were obtained using a 0.5 mm path length solution cell with NaCl windows. Nujol mull spectra were obtained from samples mounted between NaCl disks. NMR spectra were recorded on Varian Gemini 2000 (^1H at 199.98 MHz, ^{13}C at 50.29 MHz), Varian Gemini 3000 (^1H at 300.15 MHz, ^{13}C at 75.47 MHz, ^{31}P at 121.105 MHz), Varian Inova 600 (^{13}C at 150.87 MHz) or multinuclear Bruker 300 or 200 MHz instruments (AM300WB and 200DPX). Samples were dissolved in $CDCl_3$, $(CD_3)_2CO$ or C_6D_6 (Sigma-Aldrich), contained in 5 mm sample tubes. Chemical shifts are given in ppm relative to internal tetramethylsilane using the residual solvent resonances as internal references for ^1H and ^{13}C NMR spectra and external H_3PO_4 for ^{31}P NMR spectra. UV-Vis and Near-IR spectra were recorded with a Varian Cary 5000 spectrometer. EPR spectra were recorded with a Bruker EMX-8/2.7 (X-band) spectrometer. Electrospray mass spectra (ES-MS) were obtained from samples dissolved in MeOH or CH_2Cl_2 . ES-MS analyses were carried out at the "Centre Regional de Mesures Physiques de l'Ouest" (CRMPO, Rennes, France) on a high-resolution MS/MS ZabSpec TOF Micromass spectrometer (8 kV) or on a Varian Platform II spectrometer via a 10 mL injection loop. Ions listed are the most intense peaks in the isotopic envelope. Nitrogen was used as the drying and nebulising gas. Electrochemical samples were dissolved in CH_2Cl_2 containing 0.1 M $[NBu_4]PF_6$ as the supporting electrolyte. Cyclic voltammograms were recorded using a Pt working electrode, Pt counter electrode with a saturated calomel electrode as the reference electrode (Rennes), or using a Pt working electrode, Ag wire counter electrode with Ag wire as the reference electrode (Adelaide). Potentials are given in V vs SCE, with ferrocene or $FeCp^*_2$ as internal calibrants $\{[FeCp_2]/[FeCp_2]^+ = +0.46$ V (vs SCE) or

$[FeCp^*_2]/[FeCp^*_2]^+$ = -0.02 V (vs SCE)}. Elemental analyses were performed at the "Service central d'analyses" (USR CNRS 59 at Lyon-Vernaison), at the "Centre Regional de Mesures Physiques de l'Ouest" (CRMPO, University of Rennes1), and at the "Campbell Microanalytical Laboratory" (University of Otago, Dunedin, New Zealand).

Reagents. $NaBPh_4$, ^tBuOK, KF, DBU, Na and CuI (Aldrich) were commercial products and were used as received. $Me_3Si(C{\equiv}C)_2R$ (R = Ph, C_6H_4Me-4)[30], $H(C{\equiv}C)_2R$ (R = Ph, C_6H_4Me-4)[33], $IC{\equiv}CSiMe_3$[34], FeCl(dppe)Cp*[39], RuCl(dppe)Cp*[21c], $AuCl(PPh_3)$[40], $Pd(PPh_3)_4$[41], Fe(C≡CC≡CSiMe$_3$)(dppe)Cp* (**7**)[20], $Ru(C{\equiv}C)_n$(dppe)Cp* [**14**[38b]: n = 1, R = $SiMe_3$; **5**[2a]: n = 2, R = $SiMe_3$; **10**[34]: n = 3, R = $SiMe_3$; **6**[2a]: n = 2, R = $Au(PPh_3)$; **15**[34]: n = 3, R = $Au(PPh_3)$] were prepared by the cited literature methods.

Synthesis of Fe(C≡CC≡CPh)(dppe)Cp* (2a)

To a suspension of FeCl(dppe)Cp* (100 mg, 0.16 mmol) and $NaBPh_4$ (66 mg, 0.19 mmol) in triethylamine (15 ml), a solution of HC≡CC≡CPh (24 mg, 0.19 mmol) in THF (1 ml) was added. The mixture turned slowly from dark green to orange. After one night at room temperature, ^tBuOK (excess) was added to the solution before removal of the solvent under reduced pressure. The solid residue was then extracted with toluene (3 × 10 ml) and the solvent was removed under reduced pressure. The residue was extracted a second time with diethyl ether (3 × 10 ml) and after removal of the solvent under reduced pressure, the resulting orange powder was dried under vacuum to afford Fe(C≡CC≡CPh)(dppe)Cp* (**2a**; 97 mg, 85%). Anal. Calcd for $C_{46}H_{44}FeP_2$: C, 77.31; H, 6.21. Found: C, 76.59; H, 6.18. IR (KBr): ν(C≡C) 2150, 2007, 1987 cm^{-1}. ^1H NMR (C_6D_6, 300 MHz): δ 1.45 (s, 15H, Cp*), 1.77, 2.58 (2 × m, 4H, PCH_2), 6.87-8.02 (m, 25H, Ph). ^{13}C NMR (C_6D_6, 75 MHz, ppm): δ 8.89 (s, $C_5\mathit{Me}_5$), 28.79-29.91 (m, dppe), 59.70 (s, C≡CC≡*C*Ph), 80.98 (s, C≡C*C*≡CPh), 87.26 (s, *C*$_5$Me$_5$), 100.06 (s, C≡*C*C≡CPh), 124.42-137.88 (m, Ph), 144.74 (t, $^2J_{CP}$ = 38 Hz, *C*≡CC≡CPh). ^{31}P NMR (C_6D_6, 121 MHz): δ 100.2 (s). ES-MS (*m/z*): calcd for $C_{46}H_{44}FeP_2$ 714.2268, found 714.2275 $[M]^+$.

Synthesis of Fe{C≡CC≡C(C_6H_4Me-4)}(dppe)Cp* (2b)

Similarly, from FeCl(dppe)Cp* (100 mg, 0.16 mmol), $NaBPh_4$ (66 mg, 0.19 mmol) and HC≡CC≡C(C_6H_4Me-4) (27 mg, 0.19 mmol) was obtained Fe{C≡CC≡C(C_6H_4Me-

4)}(dppe)Cp* (**2b**; 93 mg, 80%) as an orange powder. Anal. Calcd for $C_{47}H_{46}FeP_2$: C, 77.47; H, 6.36. Found: C, 77.11; H, 6.36. IR (KBr): ν(C≡C) 2149, 1999 cm^{-1}. ^1H NMR (C_6D_6, 300 MHz): δ 1.47 (s, 15H, Cp*), 1.78 (m, 2H, PCH_2), 1.97 (s, 3H, Me), 2.60 (m, 2H, PCH_2), 6.76 (d, $^3J_{HH}$ = 8.0 Hz, 2H, CH), 6.99-7.29 (m, 16H, Ph), 7.46 (d, $^3J_{HH}$ = 8.0 Hz, 2H, CH), 8.01 (t, $^3J_{HH}$ = 8.7 Hz, 4H, Ph). ^{13}C NMR (C_6D_6, 75 MHz, ppm): δ 8.91 (s, $C_5\mathit{Me}_5$), 19.86 (s, Me), 28.79-29.21 (m, dppe), 59.79 [s, C≡CC≡*C*(C_6H_4Me-4)], 80.20 [s, C≡C*C*≡C(C_6H_4Me-4)], 87.20 (s, C_5Me_5), 100.11 [s, C≡*C*C≡C(C_6H_4Me-4)], 122.77-137.88 (m, Ph), 142.98 [t, $^2J_{CP}$ = 38 Hz, *C*≡CC≡C(C_6H_4Me-4)], 154.70 (s, Ph). ^{31}P NMR (C_6D_6, 121 MHz): δ 100.3 (s). ES-MS (*m/z*): calcd for $C_{47}H_{46}FeP_2$ 728.2424, found 728.2427 $[M]^+$.

Synthesis of Ru(C≡CC≡CPh)(dppe)Cp* (4)

A methanolic (7 ml, containing 1% of distilled H_2O) suspension of RuCl(dppe)Cp* (100 mg, 0.15 mmol), $Me_3SiC{\equiv}CC{\equiv}CPh$ (33 mg, 0.16 mmol), KF (10 mg, 0.16 mmol) and DBU (2 drops) was heated to the reflux point. After 1 h, the mixture was allowed to cool and the yellow-green precipitate filtered off and washed with cold MeOH. The resulting powder was then dissolved in DCM (containing 5% of NEt_3) and passed through a basic alumina column eluting with the same solvent. The yellow band was collected and the solvent removed to give Ru(C≡CC≡CPh)(dppe)Cp* (**4**; 99 mg, 87%) as a bright yellow powder. Anal. Calcd for $C_{46}H_{44}P_2Ru$: C, 72.71; H, 5.84. Found: C, 72.59; H, 6.00. IR (CH_2Cl_2): ν(C≡C) 2153, 2016 cm^{-1}. ^1H NMR (C_6D_6, 600 MHz): δ 1.59 (s, 15H, Cp*), 1.84, 2.60 (2 × m, 4H, PCH_2), 6.87-7.89 (m, 25H, Ph). ^{13}C NMR (C_6D_6, 150 MHz, ppm): δ 9.88 (s, $C_5\mathit{Me}_5$), 29.23-29.54 (m, dppe), 62.98, 82.34, 92.19 (s, C≡C), 93.10 (s, C_5Me_5), 125.47-138.55 (m, Ph and C_α). ^{31}P NMR (C_6D_6, 121 MHz): δ 80.3 (s). ES-MS (*m/z*): calcd for $C_{46}H_{45}P_2Ru$ 761.2040, found 761.2065 $[M + H]^+$.

Synthesis of Fe{C≡CC≡CAu(PPh_3)}(dppe)Cp* (8)

To a suspension of Fe(C≡CC≡C$SiMe_3$)(dppe)Cp* (**7**) (400 mg, 0.56 mmol) in THF (10 ml), a solution of methanol (10 ml) containing sodium (65 mg, 2.81 mmol) was added. After stirring for 20 min at room temperature, AuCl(PPh_3) (278 mg, 0.56 mmol) was added to the reaction mixture and the solution turned dark red. After 4 h, the orange precipitate was filtered off and washed with cold MeOH (3 × 10 ml) to afford

Fe{C≡CC≡CAu(PPh_3)}(dppe)Cp* as an orange powder (**8**; 452 mg, 74%). Anal. Calcd for $C_{58}H_{54}AuFeP_3$: C, 63.52; H, 4.96. Found: C, 63.10; H, 5.23. IR (CH_2Cl_2): ν(C≡C) 2069, 1969 cm^{-1}. ^1H NMR (C_6D_6, 300 MHz): δ 1.53 (s, 15H, Cp*), 1.83, 2.73 (2 × m, 4H, PCH_2), 6.88-8.19 (m, 35H, Ph). ^{13}C NMR (C_6D_6, 150 MHz, ppm): δ 10.45 (s, $C_5\mathit{Me}_5$), 30.22-31.39 (m, dppe), 88.25 (s, C_5Me_5), 88.84 (s), 94.18 (s), 104.06 (s), 123.26 [t, $^2J_{CP}$ = 40 Hz, C≡CC≡CAu(PPh_3)], 126.30-140.40 (m, Ph). ^{31}P NMR (C_6D_6, 121 MHz): δ 100.0 (s, dppe), 42.0 (s, PPh_3). ES-MS (*m/z*): calcd for $C_{58}H_{54}AuFeP_3$ 1096.2453, found 1096.2525 $[M]^+$.

Synthesis of Fe(C≡CC≡CC≡CSiMe_3)(dppe)Cp* (9):

To a stirring solution of Fe{C≡CC≡CAu(PPh_3)}(dppe)Cp* (**8**) (250 mg, 0.23 mmol) in a 1:1 mixture of THF / triethylamine (24 ml) was added IC≡CSiMe_3 (128 mg, 0.57 mmol) followed immediately by $Pd(PPh_3)_4$ (26 mg, 0.023 mmol) and CuI (8 mg, 0.041 mmol). The solution was stirred in the dark at room temperature overnight before solvent was removed under reduced pressure. The residue was extract with triethylamine and directly loaded on a basic alumina column which was eluted with triethylamine / hexane (1:1) and the orange band was collected to afford Fe(C≡CC≡CC≡CSiMe_3)(dppe)Cp* (**9**; 93 mg, 55%) as an orange powder. Anal. Calcd for $C_{45}H_{48}FeP_2Si$: C, 73.56; H, 6.58. Found: C, 73.80; H, 7.47. IR (CH_2Cl_2): ν(C≡C) 2092, 1952 cm^{-1}. ^1H NMR (C_6D_6, 300 MHz): δ 0.13 (s, 9H, SiMe_3), 1.37 (s, 15H, Cp*), 1.69, 2.42 (2 × m, 4H, PCH_2), 6.98-7.85 (m, 20H, Ph). ^{13}C NMR (C_6D_6, 150 MHz, ppm): δ 0.35 (s, SiMe_3), 10.12 (s, $C_5\mathit{Me}_5$), 30.23-31.08 (m, dppe), 47.06, 69.29, 77.18, 94.34, 100.95 (s, C≡C), 89.31 (s, C_5Me_5), 127.53-138.60 (m, Ph), 151.07 (t, $^2J_{PC}$ = 38 Hz, C_α). ^{31}P NMR (C_6D_6, 121 MHz): δ 97.9 (s). ES-MS (*m/z*): calcd for $C_{45}H_{48}FeP_2Si$ 734.2350, found 734.2388 $[M]^+$.

References

1. Bruce, M. I.; Ke, M.; Low, P. J., *Chem. Commun.* **1996**, 2405-2406.
2. (a) Bruce, M. I.; Ellis, B. G.; Gaudio, M.; Lapinte, C.; Melino, G.; Paul, F.; Skelton, B. W.; Smith, M. E.; Toupet, L.; White, A. H., *Dalton Trans.* **2004**, 1601-1609; (b) Bruce, M. I.; de Montigny, F.; Jevric, M.; Lapinte, C.; Skelton, B. W.; Smith, M. E.; White, A. H., *J. Organomet. Chem.* **2004,** *689*, 2860–2871.
3. (a) Dembinski, R.; Bartik, T.; Bartik, B.; Jaeger, M.; Gladysz, J. A., *J. Am. Chem. Soc.* **2000,** *122*, 810-822; (b) Mohr, W.; Stahl, J.; Hampel, F.; Gladysz, J. A., *Inorg. Chem.* **2001,** *40*, 3263-3264; (c) Zheng, Q.; Bohling, J. C.; Peters, T. B.; Frisch, A. C.; Hampel, F.; Gladysz, J. A., *Chem. Eur. J.* **2006,** *12*, 6486–6505.
4. Antonova, A. B.; Bruce, M. I.; Ellis, B. G.; Gaudio, M.; Humphrey, P. A.; Jevric, M.; Melino, G.; Nicholson, B. K.; Perkins, G. J.; Skelton, B. W.; Stapleton, B.; White, A. H.; Zaitseva, N. N., *Chem. Commun.* **2004**, 960–961.
5. (a) Bitcon, C.; Whiteley, M. W., *J. Organomet. Chem.* **1987,** *336*, 385-392; (b) Bruce, M. I.; Wallis, R. C., *Aust. J. Chem.* **1979,** *32*, 1471-1485; (c) Connelly, N. G.; Gamasa, M. P.; Gimeno, J.; Lapinte, C.; Lastra, E.; Maher, J. P.; Le Narvor, N.; Riegerd, A. L.; Riegerd, P. H., *J. Chem. Soc. Dalton Trans.* **1993**, 2575-2578.
6. Bruce, M. I., *Coord. Chem. Rev.* **2004,** *248*, 1603-1625.
7. Bruce, M. I.; Hinterding, P.; Low, P. J.; Skelton, B. W.; White, A. H., *J. Chem. Soc., Dalton Trans.* **1998**, 467-474.
8. (a) Haquette, P.; Touchard, D.; Toupet, L.; Dixneuf, P., *J. Organomet. Chem.* **1998,** *565*, 63-73; (b) Bruce, M. I.; Ellis, B. G.; Skelton, B. W.; White, A. H., *J. Organomet. Chem.* **2005,** *690*, 1772-1783.
9. Bruce, M. I.; Hinterding, P.; Tiekink, E. R. T.; Skelton, B. W.; White, A. H., *J. Organomet. Chem.* **1993,** *450*, 209-218.
10. Wong, A.; Kang, P. C. W.; Tagge, C. D.; Leon, D. R., *Organometallics* **1990,** *9*, 1992-1994.
11. Lang, H.; Weber, C., *Organometallics* **1995,** *14*, 4415-4417.
12. Lancashire, H. N.; Ahmed, R.; Hague, T. L.; Helliwell, M.; Hopgood, G. A.; Sharp, L.; Whiteley, M. W., *J. Organomet. Chem.* **2006,** *691*, 3617-3626.
13. (a) Bruce, M. I.; Hall, B. C.; Kelly, B. D.; Low, P. J.; Skelton, B. W.; White, A. H., *J. Chem. Soc., Dalton Trans.* **1999**, 3719–3728; (b) Bruce, M. I.; Humphrey, P. A.; Jevric, M.; Skelton, B. W.; White, A. H., *J. Organomet. Chem.* **2007,** *692*, 2564–2574.
14. (a) Sonogashira, K.; Yatake, T.; Tohda, Y.; Takahashi, S.; Hagihara, N., *J. Chem. Soc., Chem. Commun.* **1977**, 291-292; (b) Sonogashira, K.; Kataoka, S.; Takahashi, S.; Hagihara, N., *J. Organomet. Chem.* **1978,** *160*, 319-327.
15. Bruce, M. I.; Ke, M.; Low, P. J.; Skelton, B. W.; White, A. H., *Organometallics* **1998,** *17*, 3539-3549.
16. Crescenzi, R.; Sterzo, C. L., *Organometallics* **1992,** *11*, 4301-4305.
17. Gevert, O.; Wolf, J.; Werner, H., *Organometallics* **1996,** *15*, 2806-2809.

18. (a) Rappert, T.; Nuernberg, O.; Werner, H., *Organometallics* **1993,** *12*, 1359-1364; (b) Werner, H.; Gevert, O.; Steinert, P.; Wolf, J., *Organometallics* **1995,** *14*, 1786-1791.
19. Semenov, S. N.; Blacque, O.; Fox, T.; Venkatesan, K.; Berke, H., *Angew. Chem. Int. Ed.* **2009,** *48*, 5203 –5206.
20. Coat, F.; Thominot, P.; Lapinte, C., *J. Organomet. Chem.* **2001,** *629*, 39–43.
21. (a) Seyler, J. W.; Weng, W.; Zhou, Y.; Gladysz, J. A., *Organometallics* **1993,** *12*, 3802-3804; (b) Le Narvor, N.; Toupet, L.; Lapinte, C., *J. Am. Chem. Soc.* **1995,** *117*, 7129-7138; (c) Bruce, M. I.; Ellis, B. G.; Low, P. J.; Skelton, B. W.; White, A. H., *Organometallics* **2003,** *22*, 3184-3198; (d) Bruce, M. I.; Costuas, K.; Davin, T.; Ellis, B. G.; Halet, J.-F.; Lapinte, C.; Low, P. J.; Smith, M. E.; Skelton, B. W.; Toupet, L.; White, A. H., *Organometallics* **2005,** *24*, 3864-3881; (e) Yam, V. W.-W.; Lau, V. C.-Y.; Cheung, K.-K., *Organometallics* **1996,** *15*, 1740-1744; (f) Bruce, M. I.; Low, P. J.; Costuas, K.; Halet, J.-F.; Best, S. P.; Heath, G. A., *J. Am. Chem. Soc.* **2000,** *122*, 1949-1962.
22. (a) Kheradmandan, S.; Heinze, K.; Schmalle, H. W.; Berke, H., *Angew. Chem., Int. Ed. Engl.* **1999,** *38*, 2270-2273; (b) Semenov, S. N.; Blacque, O.; Fox, T.; Venkatesan, K.; Berke, H., *J. Am. Chem. Soc.* **2010,** *132*, 3115-3127; (c) Brady, M.; Weng, W.; Zhou, Y.; Seyler, J. W.; Amoroso, A. J.; Arif, A. M.; Böhme, M.; Frenking, G.; Gladysz, J. A., *J. Am. Chem. Soc.* **1997,** *119*, 775-788.
23. Weng, W.; Bartik, T.; Brady, M.; Bartik, B.; Ramsden, J. A.; Arif, A. M.; Gladysz, J. A., *J. Am. Chem. Soc.* **1995,** *117*, 11922-11931.
24. Koentjoro, O. F.; Rousseau, R.; Low, P. J., *Organometallics* **2001,** *20*, 4502-4509.
25. Brown, N. J.; Collison, D.; Edge, R.; Fitzgerald, E. C.; Low, P. J.; Helliwell, M.; Ta, Y. T.; Whiteley, M. W., *Chem. Commun.* **2010,** *46*, 2253-2255.
26. Aston, G. M.; Badriya, S.; Farley, R. D.; Grime, R. W.; Ledger, S. J.; Mabbs, F. E.; McInnes, E. J. L.; Morris, H. W.; Ricalton, A.; Rowlands, C. C.; Wagner, K.; Whiteley, M. W., *J. Chem. Soc., Dalton Trans.* **1999**, 4379-4388.
27. (a) Paul, F.; Toupet, L.; Thépot, J.-Y.; Costuas, K.; Halet, J.-F.; Lapinte, C., *Organometallics* **2005,** *24*, 5464-5478; (b) Paul, F.; Ellis, B. G.; Bruce, M. I.; Toupet, L.; Roisnel, T.; Costuas, K.; Halet, J.-F.; Lapinte, C., *Organometallics* **2006,** *25*, 649-665.
28. (a) Kende, A. S.; Smith, C. A., *J. Org. Chem.* **1988,** *53*, 2655-2657; (b) Karatholuvhu, M. S.; Fuchs, P. L., *J. Am. Chem. Soc.* **2004,** *126*, 14314-14315; (c) Luu, T.; Morisaki, Y.; Cunningham, N.; Tykwinski, R. R., *J. Org. Chem.* **2007,** *72*, 9622-9629.
29. (a) Eastmond, R.; Walton, D. R. M., *Tetrahedron* **1972,** *28*, 4591-4599; (b) Miller, J. A.; Zweifel, G., *Synthesis* **1983**, 128-130; (c) Alami, M.; Ferri, F., *Tetrahedron Lett.* **1996,** *37*, 2763-2766.
30. Fiandanese, V.; Bottalico, D.; Marchese, G.; Punzi, A., *Tetrahedron Lett.* **2003,** *44*, 9087–9090.
31. Morisaki, Y.; Luu, T.; Tykwinski, R. R., *Org. Lett.* **2006,** *8*, 689-692.

32. (a) Haley, M. M.; Bell, M. L.; English, J. J.; Johnson, C. A.; Weakley, T. J. R., *J. Am. Chem. Soc.* **1997,** *119*, 2956-2957; (b) Heuft, M. A.; Collins, S. K.; Yap, G. P. A.; Fallis, A. G., *Org. Lett.* **2001,** *3*, 2883-2886.
33. West, K.; Wang, C.; Batsanov, A. S.; Bryce, M. R., *J. Org. Chem.* **2006,** *71*, 8541-8544.
34. Bruce, M. I.; Cole, M. L.; Parker, C. R.; Skelton, B. W.; White, A. H., *Organometallics* **2008,** *27*, 3352–3367.
35. de Montigny, F.; Argouarch, G.; Roisnel, T.; Toupet, L.; Lapinte, C.; Lam, S. C.-F.; Tao, C.-H.; Yam, V. W.-W., *Organometallics* **2008,** *27*, 1912–1923.
36. Denis, R.; Toupet, L.; Paul, F.; Lapinte, C., *Organometallics* **2000,** *19*, 4240-4251.
37. Coat, F.; Guillevic, M.-A.; Toupet, L.; Paul, F.; Lapinte, C., *Organometallics* **1997,** *16*, 5988-5998.
38. (a) Hamon, P., *personal communication*; (b) Brown, N. J.; Fox, M. A.; Smith, M. E.; Yufit, D. S.; Howard, J. A. K.; Low, P. J., *J. Organomet. Chem.* **2009,** *694*, 4042-4048.
39. Roger, C.; Hamon, P.; Toupet, L.; Rabaa, H.; Saillard, J. Y.; Hamon, J. R.; Lapinte, C., *Organometallics* **1991,** *10*, 1045-1054.
40. Bruce, M. I.; Nicholson, B. K.; bin Shawkataly, O., *Inorg. Synth.* **1989,** *26*, 324.
41. Coulson, D. R., *Inorg. Synth.* **1990,** *28*, 107.

Chapter Three

Oxidative Dimerisation of Arylalkynyl-Ruthenium Complexes

3.1 Introduction

Extensive studies of arylalkynyl-metal complexes Fe(C≡CAr)(dppe)Cp[1], M(C≡CAr)(dppe)Cp* [M = Fe[2], Ru[3]; Ar = C_6H_4X-4, X = CF_3, Br, Me, ^{t}Bu (M = Fe), NO_2, CN, F, H, OMe, NH_2 (M = Fe, Ru)], *trans*-Cl(dppe)$_2$Ru[C≡C(C_6H_4X-4) (X = NO_2, CHO, C(O)Me, F, H, OMe, NMe_2][4] and M(C≡CR)(dppe)(η-C_7H_7) (M = Mo; R = ^{t}Bu, CO_2Me, Fc, C_6H_4X-4, X = CO_2Me, CHO, H, Me, OMe, NH_2; M = W, R = Ph, C_6H_4-Me-4)[5] have been reported recently, resulting from their potential as redox-active components of electronic[6], magnetic[7] and optical devices[8].

3.1.1 Properties of the 17-electron species [{M}(CCR)]$^+$ [{M} = Fe(dppe)Cp, Mo(dppe)(η-C_7H_7) and W(dppe)(η-C_7H_7)]*

Ready 1-e oxidation of many neutral arylalkynyl-metal complexes occurs to give 17-e mono-cations. Both neutral and charged species have been investigated by experimental (IR, NMR, UV-vis), structural and theoretical (DFT) means[2-5]. In particular, the neutral metal-ligand fragment, containing M(II), is electron-rich and behaves as an electron-

releasing group to the carbon-rich ligand. In the mono-cations [formally containing M(III)], the unpaired electron is largely metal-centred in the Fe, Mo and W complexes, but more delocalised on the arylalkynyl ligand in the Ru cations. Paramagnetic ^{1}H NMR measurements have allowed the charge distribution in the aryl group to be determined, while ionisation potential data correlate with electronic substituent parameters and are related to the effect of the *para* substituent on their electronic properties.

Representative examples of substituted alkynyl-metal complexes have been oxidised to 17-e species, either chemically or electrochemically. Various spectroscopic measurements and DFT studies showed that the HOMO is metal-centred, but a significant difference in electronic structures of the Mo and Ru series appears to reside in the nodal properties of the HOMO due to the C_7H_7 ring attached to Mo or W vs. the Cp* ring tethered to Ru. DFT calculations on models mimicking the 17-e radical cations $[M(CCPh)(PPh_3)_2Cp]^+$ (M = Fe, Ru) suggest a distribution of the unpaired electron between the metal centre, C_β and the *para* C of the Ph group, with the Ru complex showing a considerably higher coefficient of spin density on the arylalkynyl group[2,3].

In the course of these studies, attempts have been made to isolate the oxidised compounds. Chemical oxidation of $Fe(C{\equiv}CC_6H_4X\text{-}4)(dppe)Cp^*$ with $[FeCp_2]PF_6$ has given $[Fe(CCC_6H_4X\text{-}4)(dppe)Cp^*]PF_6$ (X = NO_2, CN, CF_3, F, Br, H, Me, ^{t}Bu, OMe, NH_2, NMe_2) and structural determinations of several of these salts were completed (Scheme 3.1)[2e]. As expected from the theoretical calculations, there is a general expansion of the Fe coordination sphere upon oxidation, but little change occurs within the arylalkynyl fragment. The only exceptions are found for X = NH_2, where the bond between the *para* carbon and NH_2 substituent is shorter by 0.036 Å, and for X = CN where the CN bond is shorter by 0.022 Å, changes resulting from π-bonding involving the substituents. Similar chemical oxidation studies have been achieved on the $M(C{\equiv}CR)(dppe)(\eta\text{-}C_7H_7)$ (M = Mo; R = ^{t}Bu, $C_6H_4X\text{-}4$, X = H, Me; M = W, R = Ph, $C_6H_4\text{-}Me\text{-}4$), few molybdenum salts being isolated and characterised by X-ray determinations[5b,9], whereas no structural determinations of the 17-e tungsten species were achieved, due to their slow decomposition into the carbonyl complex $[W(CO)(dppe)(\eta\text{-}C_7H_7)]^+$ [5c].

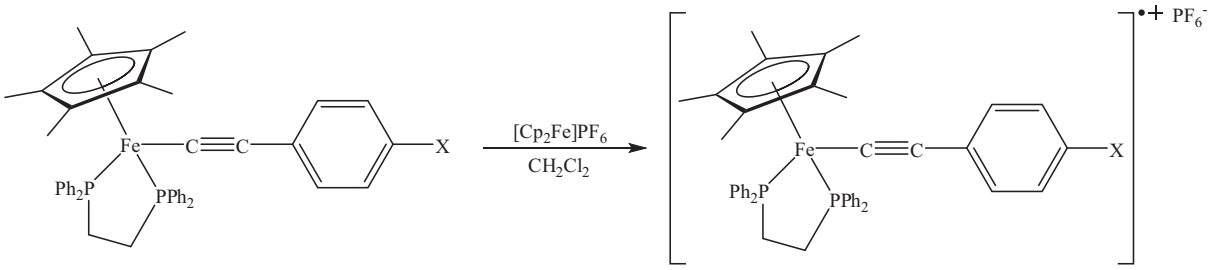

X = NO_2, CN, CF_3, Br, F, H, Me, ^{t}Bu, OMe, NH_2, NMe_2

Scheme 3.1

In the ruthenium series, a major difference in reactivity is found. Electrochemical oxidation showed that apparently reversible or quasi-reversible 1-e processes occur in the range 0.05-0.40 V (vs SCE), the potentials correlating with the electronic properties of the substituents[3]. Chemical oxidation of the neutral Ru(C≡CC_6H_4X-4)(dppe)Cp* (X = NO_2, CN, F, H, OMe, NH_2) with Ag[OTf] in dichloromethane resulted in rapid bleaching of the colour of the solutions before they turned darker, often blue. However, it was not possible to isolate any of the oxidised compounds, although in one case the vinylidene [Ru{=C=CH($C_6H_4NO_2$-4)}(dppe)Cp*]PF_6 could be characterised. IR spectroscopy suggested that alkynyl-Ru(III) complexes were the first-formed products, but this was then followed by the formation of mixtures of products. EPR studies of products formed by oxidation with [$FeCp_2$]PF_6 in CH_2Cl_2/1,2-dichloroethane glasses at 80 K indicated that a single radical is formed, but the signal disappeared upon warming to room temperature. In CH_2Cl_2, weak transient absorptions around 1300 nm were observed.

3.1.2 Dimerisation of 17-electron metal-alkynyl species

A few examples of unstable 17-electron alkynyl-metal complexes which dimerise are available in the literature. The most well-known example is the dimerisation of [M(CCH)(dppe)Cp*]PF_6 (M = Fe, Ru) to afford the stable bis(vinylidene) complexes [{Cp*(dppe)M}$_2$(μ-C=CHCH=C)][PF_6]$_2$, which by simple deprotonation (with dbu or KOBu^t) gave the extensively studied {Cp*(dppe)M}$_2$(μ-C≡CC≡C) complexes containing two metal centres linked by a butadiynyl bridge (Scheme 3.2)[10]. In the iron case, the 17-e species generated by chemical oxidation of the neutral parent complexes were stable enough at low temperature to be characterised by EPR spectroscopy. After stirring for

several hours at low temperature, coupling of two radical cations occurred at C_β to give the dimeric bis(vinylidene) products.

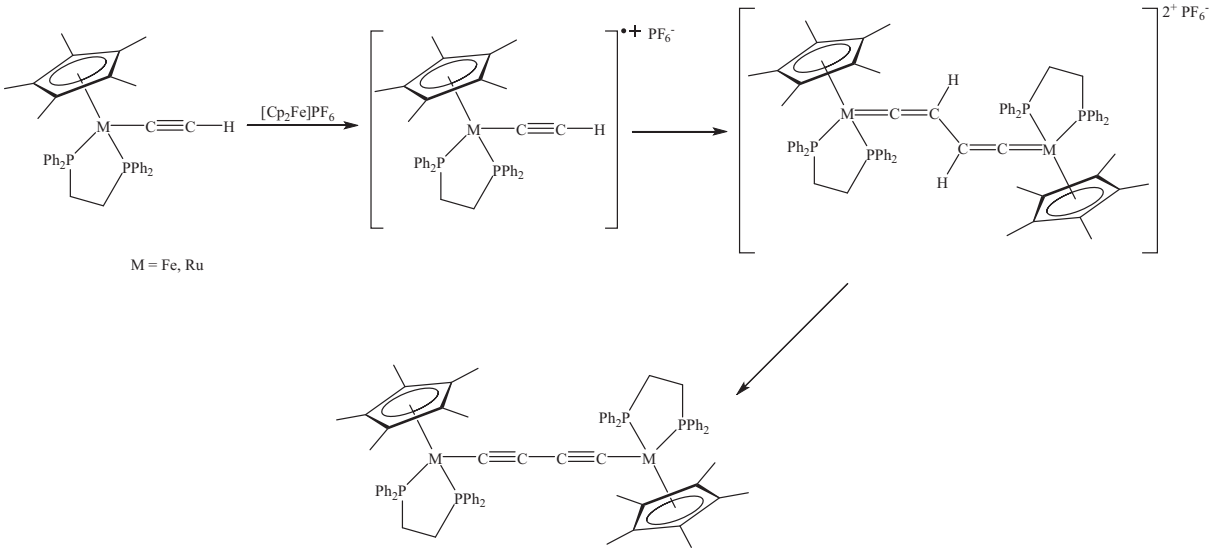

Scheme 3.2

The other example of alkynyl-metal radical cation dimerisation was published in 1989 by Whiteley et al.[11]. Chemical oxidation of the neutral molybdenum complex Mo(C≡CPh)(dppe)(η-C_7H_7) afforded the stable radical cation [Mo(CCPh)(dppe)(η-C_7H_7)]$^+$, whose X-ray structure determination has been completed. However, when the radical cation was left in a stirred THF solution during 24 hours, a colour change of the solution indicated further reaction had occurred to give the diamagnetic product [{(η-C_7H_7)(dppe)Mo}$_2$(μ-C=CPhCPh=C)][PF_6]$_2$ (Scheme 3.3). As before, this dimer was formed by coupling of two 17-e molecules at C_β.

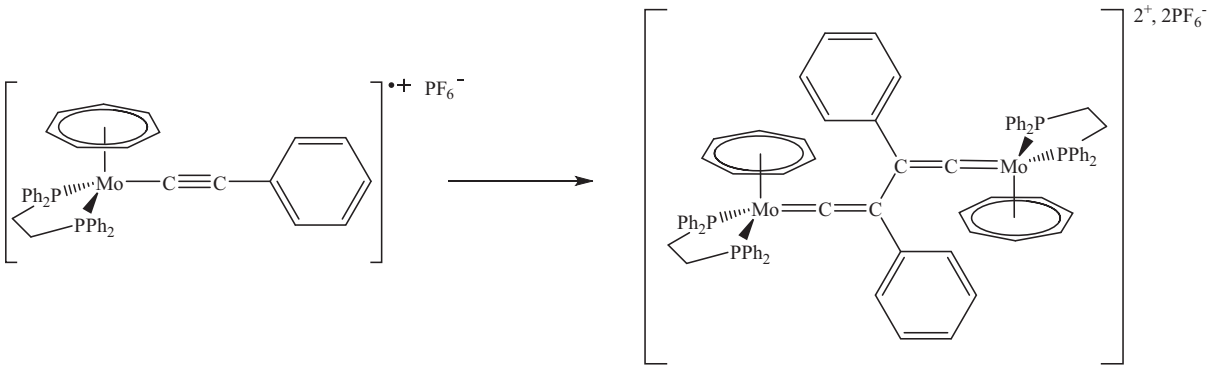

Scheme 3.3

3.2 Aims

The aim of the work described in this Chapter was to determine the structures of the products issuing from the chemical oxidation of arylalkynyl-ruthenium complexes. Therefore, some unstable 17-e arylalkynyl-ruthenium species were generated to give, by further reaction, novel bimetallic products which were fully characterised. These experimental results were rationalised by DFT calculations achieved by Gendron from the Halet group in Rennes. Guillaume Grelaud from Rennes contributed to some parts of this work, which has been recently published[12].

3.3 Results and discussion

3.3.1 Oxidation of Ru(C≡CPh)(PPh$_3$)$_2$Cp (16)

In contrast to the above results where the 17-e species were stable and isolable, we have now found that treatment of Ru(C≡CPh)(PPh$_3$)$_2$Cp (**16**; Scheme 3.4) with one equivalent of [FeCp$_2$]PF$_6$ in CH_2Cl_2 solution at room temperature results in a rapid colour change from orange to dark red. The ^{31}P NMR spectrum suggested that a mixture of several products had formed initially, but precipitation with diethyl ether afforded a single compound, which could be recrystallised from $CHCl_3$. Purification of the original reaction mixture by preparative t.l.c. (silica gel, acetone-ethyl acetate, 3/7) afforded a second product, also obtained as dark red crystals from $CHCl_3$. These two compounds were characterized as the mono- and bis-vinylidene complexes **17** and **18** by single crystal XRD structure determinations carried out on the isomorphous AsF_6^- salts formed by anion exchange. The original salts are readily interconvertible by treatment with HBF_4 or HPF_6, or NaOMe, respectively, and have the acid-conjugate base relationship similar to that found for precursor Ru(C≡CPh)(PPh$_3$)$_2$Cp and the vinylidene [Ru(=C=CHPh)(PPh$_3$)$_2$Cp]$^+$ [13].

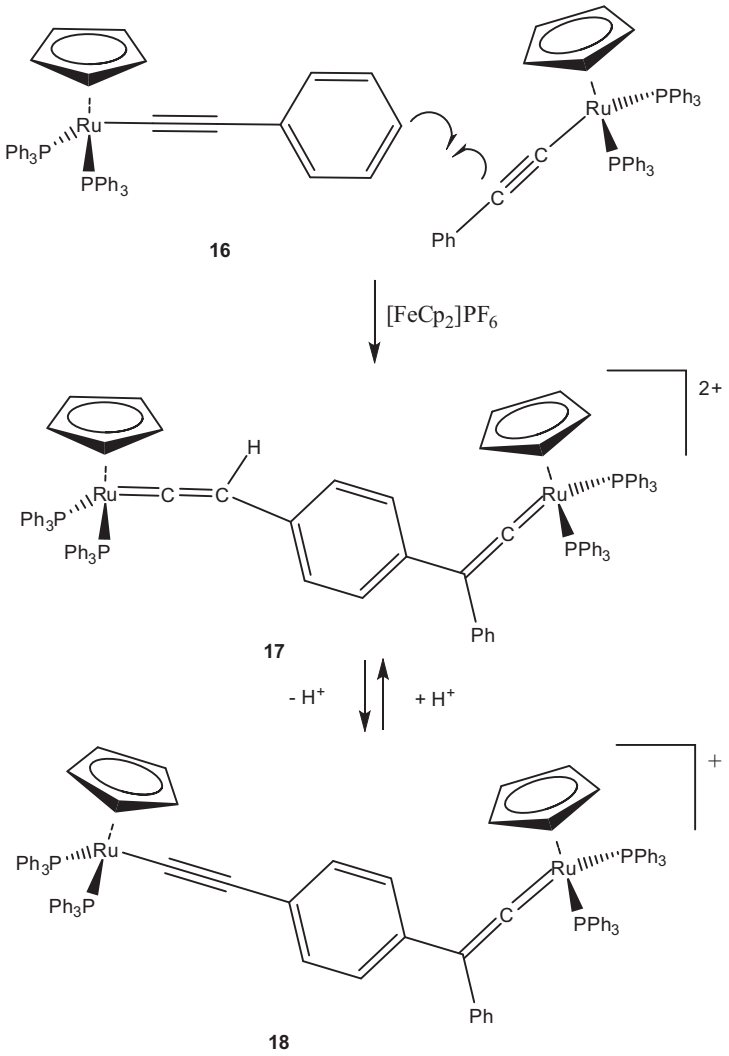

Scheme 3.4

Figure 3.1 depicts the cationic fragments of these salts, which each contain two $Ru(PPh_3)_2Cp$ fragments end-capping $=C=CH(C_6H_4)CPh=C=$ (**17**) [Figure 3.1 (top)] or $-C\equiv C(C_6H_4)CPh=C=$ (**18**) [Figure 3.1 (bottom)] linkers. Table 3.1 gives selected bond parameters for **17** and **18**.

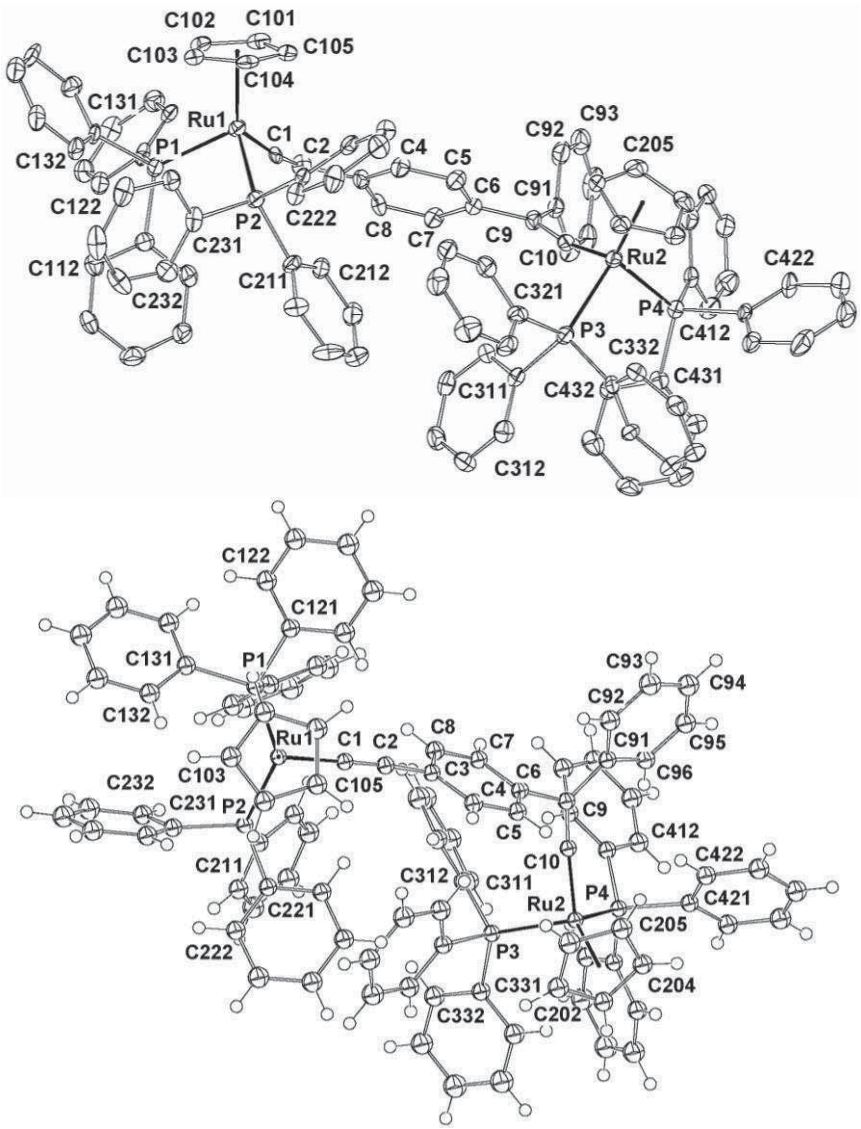

Figure 3.1. *ORTEP views of $[Cp(PPh_3)_2Ru\{=C=CHC_6H_4CPh=C=\}Ru(PPh_3)_2Cp][AsF_6]_2$ **17** (top) and $[Cp(PPh_3)_2Ru\{C\equiv C(C_6H_4)CPh=C=\}Ru(PPh_3)_2Cp]AsF_6$ **18** (bottom).*

Table 3.1. Selected bond parameters for **17**, **18** and **22** (all as AsF_6^- salts).

	17	**18**	**22**[a]
		Bond distances (Å)	
Ru(1)-P(1, 2)	2.339, 2.379(2)	2.2855, 2.2935(9)	2.3433, 2.3469(9)
Ru(2)-P(3, 4)	2.361, 2.351(2	2.3475, 2.3488(8)	2.3608, 2.3313(9)
Ru(1)-C(cp)	2.227-2.305(6)	2.227-2.273(3)	2.258-2.297(4)
(av.)	2.263	2.244	2.270
Ru(2)-C(cp)	2.227-2.277(6)	2.246-2.302(3)	2.238-2.284(3)
(av.)	2.260	2.265	2.260

Ru(1)-C(1)	1.822(7)	2.007(3)	1.844(3)
C(1)-C(2)	1.313(9)	1.212(5)	1.329(5)
C(2)-C(3)	1.483(8)	1.442(4)	
C(6)-C(9)	1.502(8)	1.504(4)	
C(9)-C(10)	1.336(8)	1.309(5)	
C(9)-C(91)	1.496(8)	1.489(5)	
C(10)-Ru(2)	1.837(6)	1.870(3)	
	Bond angles (º)		
P(1)-Ru(1)-P(2)	96.31(6)	101.54(3)	102.49(3)
P(1, 2)-Ru(1)-C(1)	90.2, 99.8(2)	88.01, 88.99(9)	95.20, 88.87(9)
P(3)-Ru(2)-P(4)	97.27(6)	95.87(3)	104.90(3)
P(3, 4)-Ru(2)-C(10)	97.7, 94.3(2)	96.96, 93.89(9)	88.16, 88.61(10) [CO]
Ru(1)-C(1)-C(2)	169.5(5)	177.6(3)	173.0(3)
C(1)-C(2)-C(3)	128.2(6)	175.1(4)	
C(6)-C(9)-C(10)	122.7(6)	114.7(3)	
C(6)-C(9)-C(91)	117.0(5)	117.9(3)	
C(9)-C(10)-Ru(2)	168.3(5)	166.4(3)	

[a]For **22**: Ru(2)-CO(1) = 1.871(3), C(2)-C(41) = 1.503(4), C(2)-C(201) = 1.477(4) Å; C(1)-C(2)-C(41) = 115.4(3), C(1)-C(2)-C(201) = 123.4(3)º.

As can be seen in Figure 3.1 (top), the bis-vinylidene cation in **17** consists of a central 1,4-C_6H_4 group bearing XC=C=[Ru(PPh_3)$_2$Cp] (X = H, Ph) substituents. The ruthenium atoms are pseudo-octahedrally coordinated by the PPh_3 [Ru(1)-P(1, 2) 2.339, 2.379(2), Ru(2)-P(3, 4) 2.361, 2.351(2) Å], Cp [Ru(1, 2)-C(Cp) av. 2.263, 2.260 Å] and vinylidene ligands [Ru(1)-C(1) 1.821(7), Ru(2)-C(10) 1.837(6)Å]. The shortening of the latter bonds from the normal Ru-C(sp) distance of ca 2.00 Å [cf. 2.007(3) Å for Ru(2)-C(10) in **18**, 2.016(3) Å in **16**[14]] is consistent with the presence of Ru=C double bonds expected for the vinylidene formulation, and supported by the strong down-field shifts of the Ru=C resonances to δ_C 352.1, 355.0 (both broad triplets). Within the organic ligand, the C(1)-C(2) and C(9)-C(10) separations are 1.314(9) and 1.336(8) Å, consistent with C=C double bonds. Angles at C(1) and C(10) are 169.5(5) and 168.3(5)º, supporting their assignment as C(sp) atoms. Atoms C(2) and C(9) are both C(sp^2) atoms, with angles C(1)-C(2)-C(3) and C(6)-C(9)-C(10) of 128.2(6) and 122.7(6)º, respectively.

Deprotonation of **17** to give **18** results in small changes to the geometry about C(1), consistent with the change in Ru(1)-C(1)-C(2) from vinylidene in **17** to alkynyl in **18**. Thus, Ru(1)-C(1) is 2.007(3) and C(1)-C(2) is 1.212(5) Å, both consistent with the Ru-C≡C formulation. Angles at C(1) and C(2) are 177.6(3) and 175.1(4)º. In contrast, the Ru(2)=C(10)=C(9) moiety differs little from that in **17**: Ru(2)-C(10) 1.870(3), C(9)-C(10) 1.309(5) Å and angles at C(10) and C(9) of 166.4(3) and 114.7(3)º, respectively. In the ^{13}C NMR spectrum, the metal-bonded carbons are found as triplet resonances at δ_C 354.3 and 121.4, assigned to C(1) and C(10), respectively. These values are also consistent with the Ru=C=C (vinylidene) and Ru-C≡C (alkynyl) formulations. The difference in the Ru-P distances are also noteworthy, with Ru(1)-P(1, 2) 2.2855(9), 2.2935(8) Å and Ru(2)-P(3, 4) 2.3475(8), 2.3488(8) Å, the shorter bonds to Ru(1) resulting from more efficient back-bonding from Ru to P and supporting the positive charge being resident upon Ru(2).

Spectroscopic properties of these complexes are consistent with their solid-state structures. The IR spectra contain ν(CC) bands at 1709s, 1625m cm^{-1} (**17**) and 2061m, 1705w, 1614w (**18**), consistent with the presence of two vinylidene C=C groups in the former, and one C≡C triple bond and a vinylidene C=C group in the latter. The two $Ru(PPh_3)_2Cp$ groups are different in each case, giving two Cp resonances at δ_H 5.09, 5.23, δ_C 95.08 (the two Cp resonances are accidentally equivalent) (**17**) or δ_H 4.33, 5.08, δ_C 85.43, 94.86 (**18**), the down-field shift of the latter confirming the presence of the neutral alkynyl-ruthenium moiety. Carbons of the linker group are found at δ_C 118.95, 126.79, 352.08, 355.03 (**17**) and at δ_C 114.72, 121.42, 123.08, 354.32 (**18**), while the ^{31}P NMR spectra each contain two signals at δ_P 42.5, 43.7 (**17**), and 42.5, 51.4 (**18**). In each case, the large down-field chemical shifts are consistent with the presence of two vinylidene groups in **17** and one vinylidene and one alkynyl group in **18**. The ES-MS of both complexes contain M^+ at *m/z* 1582; the lack of the expected M^{2+} in **17** may be the result of facile mono-deprotonation occurring in the source.

3.3.2 Oxidation of Ru(C≡CC$_6$H$_4$Me-4)(PPh$_3$)$_2$Cp (19)

Careful oxidation of Ru{C≡C(C_6H_4Me-4)}(dppe)Cp (**19**) with one equivalent of $[FeCp_2]PF_6$ afforded a dark red compound which is likely the bis(vinylidene) [Ru{=C=C(C_6H_4Me-4)-η-C_5H_4[$Ru(PPh_3)_2${=C=CH(C_6H_4Me-4)]}($PPh_3)_2$Cp]}]$(PF_6)_2$ (**20**, Scheme 3.5). This material was not isolated, being rapidly deprotonated to the

alkynyl(vinylidene) complex [Ru{=C=C(C_6H_4Me-4)-η-C_5H_4[Ru(PPh_3)$_2$(C≡CC_6H_4Me-4)]}(PPh_3)$_2$Cp]PF_6 (**21**), analogous to **18** but containing a substituted Cp group. The structure is assigned on the basis of its IR [ν(C≡C) 2070, ν(C=C) 1613 cm^{-1}], ^{1}H NMR [δ_H 2.35, 2.38 (2 x Me), 3.56, 4.51 (C_5H_4), 5.38 (Cp)], ^{13}C NMR [δ_C 20.94, 21.06 (2 x Me), 79.49, 83.73, 114.32 (C_5H_4), 94.86 (Cp), 69.34 (Ru=C=*C*), 121.30 (Ru-*C*≡C), 353.00 (Ru=*C*=)] and ^{31}P NMR spectra [δ_P 40.8, 49.6 (2 x Ru(PPh_3)$_2$)], and from the X-ray-determined structure of its further decomposition product described below.

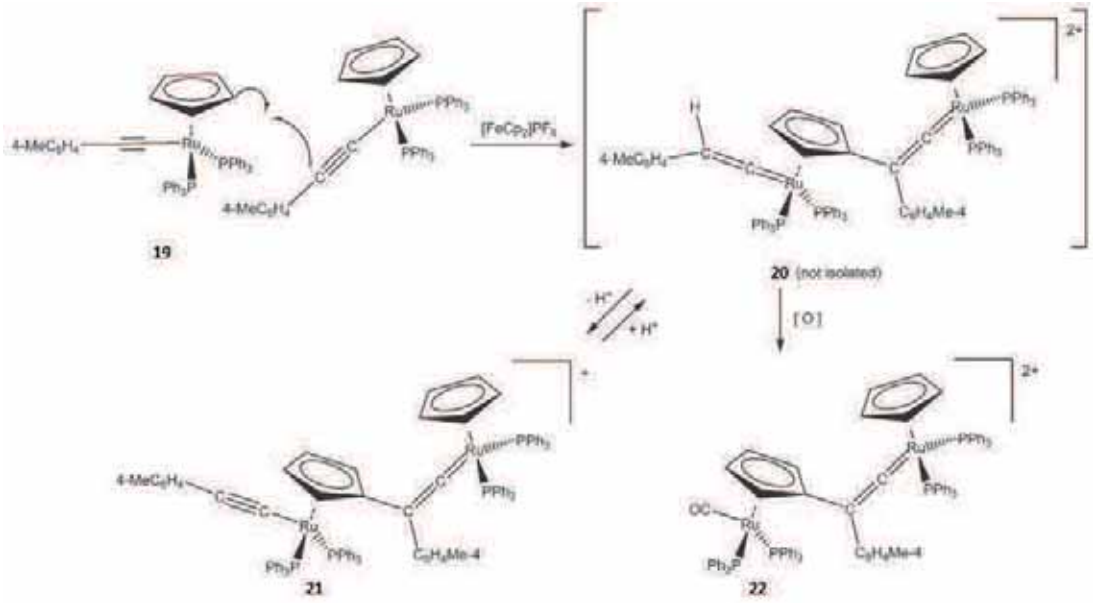

Scheme 3.5

Attempts to determine the structure of **21** by XRD methods were frustrated during attempted recrystallisation by its ready conversion to the carbonyl cation [Ru{=C=C(C_6H_4Me-4)-η-C_5H_4[Ru(CO)(PPh_3)$_2$]}(PPh_3)$_2$Cp][AsF_6]$_2$ (**22**, Scheme 3.5), as revealed by a strong ν(CO) band at 1980 cm^{-1} in the IR spectrum and an XRD structure determination of crystals which were readily obtained from the attempted purification of **21**.

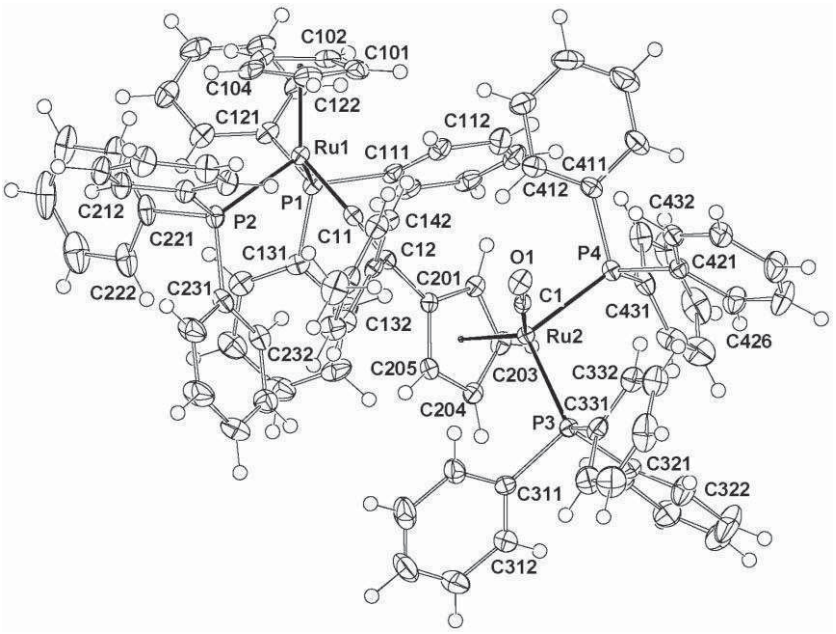

Figure 3.2. *ORTEP view of [Ru{=C=C(C_6H_4Me)-η-C_5H_4[Ru(CO)(PPh_3)$_2$]}(PPh_3)$_2$Cp][AsF_6]$_2$* ***22****.*

In the cation of **22** (Figure 3.2) the Ru(1)-C(1)-C(2) moiety (Ru(1)-C(1) 1.844(3), C(1)-C(2) 1.329(5) Å) closely resembles the Ru-vinylidene fragments present in **17** and **18**. Coordination about Ru(1) is completed by the Cp group and two PPh_3 ligands (Ru(1)-P(1,2) 2.3433, 2.3469(9) Å). Atom Ru(2) carries one CO (Ru(2)-CO 1.871(3) Å) and two PPh_3 ligands (Ru(2)-P(3,4) 2.3608(10), 2.3313(9) Å), the larger Ru-P separations resulting from competitive π-back-bonding into the CO ligand. In this case, however, the Cp group is substituted by the 4-tolylvinylidene group attached to Ru(1) (C(12)-C(201) 1.477(4) Å); atom C(12) also carries the 4-tolyl group (C(12)-C(41) = 1.503(4) Å). It is known that vinylidene-ruthenium complexes are extremely susceptible to oxidation or reaction with traces of water, with formation of the CO and corresponding aldehyde or acid[15], and it is likely that a similar process is occurring here. The substituted Cp group would be a much stronger electron donor than the unsubstituted Cp, increasing the electron density on the Ru-vinylidene fragment and hence its susceptibility towards oxidation.

3.3.3 Supporting DFT calculations

DFT calculations were performed on the precursor Ru(C≡CPh)(PPh_3)$_2$Cp (**16**) in two oxidation states (0/+1) in order to understand how oxidation affects the electronic properties of this arylalkynyl-ruthenium compound. The geometries of compound **16** and

its corresponding radical cation $[\mathbf{16}]^+$ were first geometrically optimized. Pertinent computed metric data are reported in Table 3.2 and compared to the available X-ray data measured for the neutral complex[14a]. Computed data match reasonably well with the experimental values, with the largest bond length deviations found for the Ru-C(Cp) distances. Upon oxidation, a substantial contraction of the Ru-C_α bond length (0.062 Å) and a lengthening (0.015 Å) of the C_α-C_β triple bond are computed. To a lesser extent, some shortening of the C_β-C(Ph) bonds (up to 0.013 Å) and on average some lengthening of the Ru-C(Cp) bond (0.015 Å) are noted.

Table 3.2. Selected computed bond parameters for **16** and $\mathbf{[16]}^+$.

	16[a]	$\mathbf{[16]}^+$
	Bond distances (Å)	
Ru-C(Cp)	2.339-2.373	2.339-2.375
	(av. 2.349) [2.227-2.256(3)]	(av. 2.364)
Ru-P_1	2.352 [2.303(1)]	2.404
Ru-P_2	2.349 [2.285(1)]	2.394
Ru-C_α	2.026 [2.016(3)]	1.964
C_α-C_β	1.238 [1.215(4)]	1.253
C_β-C(Ph)	1.424 [1.456(4)]	1.411
	Bond angles (°)	
P_1-Ru-P_2	104.75 [100.5(3)]	102.59
Ru-C_α-C_β	173.14 [178.0(2)]	176.00
C_α-C_β-C(Ph)	178.07 [171.9(3)]	173.65

[a]Experimental data[14a] are given in brackets for comparison.

These bond length changes can be interpreted by looking at the nodal properties of the highest occupied molecular orbitals HOMO and HOMO-1 of the neutral compound, shown in Figure 3.3. They are π-type in character, antibonding between the Ru atom and C_α and bonding between C_α and C_β. These HOMOs are analogous to those generally computed for arylalkynyl-metal complexes and result from an antibonding interaction between the "t_{2g}" orbitals of the metal atom with the π-type orbitals of the alkynyl ligand[2-4]. As generally observed for arylalkynyl-Ru compounds[3], their spatial distribution is rather delocalised on the Ru(C≡C)Ph backbone in **16** (see Figure 3.3). It is noteworthy that the participation of the phenyl ring in the HOMO (17 %) is quite important.

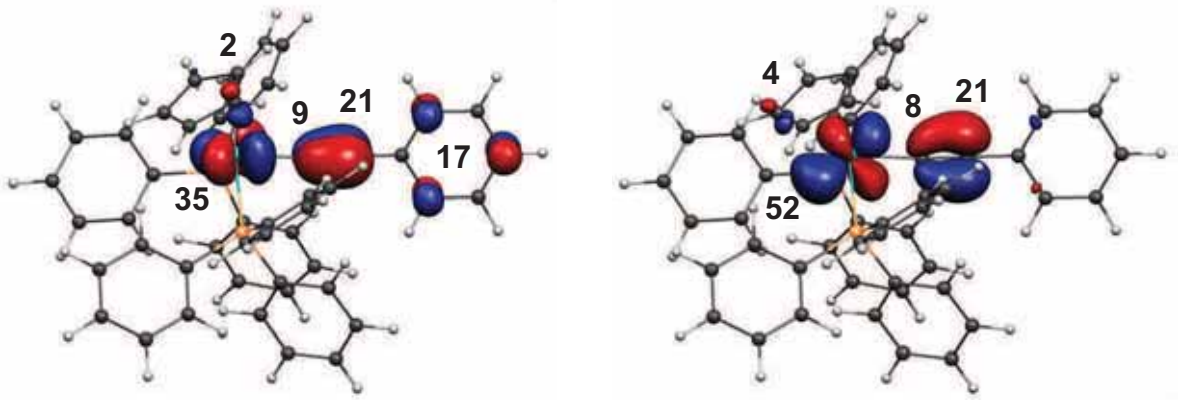

Figure 3.3. *Plots of the HOMO (left) and HOMO-1 (right) of* ***16*** *(isocontour value: ±0.05 [e/bohr^3]$^{1/2}$). The Ru, C_α, C_β and Ph percentage character is given.*

The calculated spin distribution for $[\mathbf{16}]^+$ is given in Figure 3.4. Its distribution is straightforward from a glance at the nodal properties of the HOMO which is partially depopulated with important contributions from the Ru, C_β and the C_{ortho}, C_{para} atoms of the phenyl ring. Interestingly, a small amount of spin density is also found on some carbon atoms of the Cp ring (from 0.03 up to 0.07). The spin density of the related arylalkynyl-iron complex $[Fe(C{\equiv}CPh)(dppe)Cp^*]^+$ was also computed for comparison. In contrast to $[\mathbf{16}]^+$, the largest part of the spin density resides on the iron atom (0.86e vs 0.39e) with a substantial contribution on C_β (0.23e vs 0.27e) but a very small contribution on the carbon atoms of the phenyl ring with respect to that in $[\mathbf{16}]^+$ (0.04e vs 0.09e and 0.05e vs 0.13e in for the C_{ortho}, C_{para} atoms of the phenyl ring, respectively).

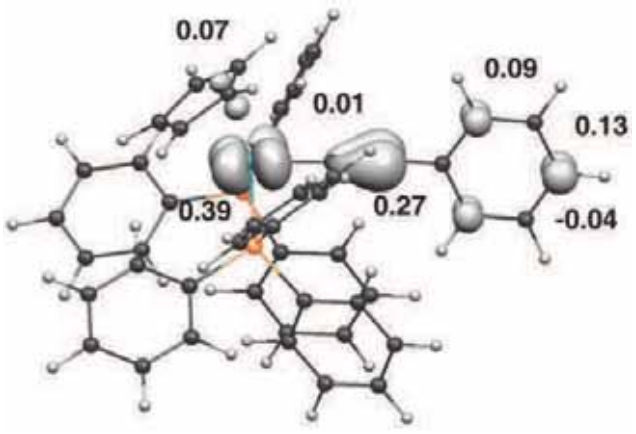

Figure 3.4. *Spatial distribution of computed spin density of* ***[16]***$^+$ *(isocontour value: ±0.005 [e/bohr^3]). Atomic spin densities (electrons) are given.*

3.3.4 Discussion

The various studies mentioned above are all in agreement with the differing electronic structures of the arylalkynyl-iron and -ruthenium based compounds, inasmuch as oxidation of the iron systems affords monocationic species (radicals) in which the charge is metal-centred. This allows the ready isolation of salts of the monocations, and such processes have also been observed with the complexes $\{Fe(dppe)Cp^*\}_2\{\mu\text{-}C{\equiv}CXC{\equiv}C\}$ (X = C_6H_4, $C_{10}H_6$-1,5, $C_{14}H_8$-1,8) in their reactions with tcnq, which afforded the radical anion salts $[\{Fe(dppe)Cp^*\}_2\{\mu\text{-}CCXCC\}]^{\bullet+}[tcnq]^{\bullet-}$[16].

Studies of the complexes $\{M(dppe)Cp^*\}(\mu\text{-}C{\equiv}CC{\equiv}C)\{M'(dppe)Cp^*\}$ (M = M' = Fe, Ru; M = Fe, M' = Ru) were also illuminating. Oxidation (both chemically and electrochemically) afforded cationic species, spectroscopic measurements of which showed that the charge was centred largely on the metal (M = M' = Fe) or the bridging ligand (M = M' = Ru), but was distributed unequally in the oxidized mixed complex[17]. These findings were supported by DFT calculations. Similarly and as mentioned above for $[Fe(C{\equiv}CPh)(dppe)Cp^*]^+$, charge rests on the iron centre in the range of oxidised arylalkynyl complexes. In contrast, calculations on the ruthenium compounds such as **16** suggest that the HOMO is more delocalised along the arylalkynyl ligand.

Electrochemical oxidation of the ruthenium compounds affords unstable oxidised species, i.e., the oxidation processes are often irreversible, in contrast to the situation found with the iron analogues.

When the fate of the oxidised species was probed, initial experiments using silver(I) as oxidant were unsuccessful[3]. However, when ferricinium salts are used, ready formation of the oxidised products occurs and these proved to be stable enough to isolate. X-ray structure determinations of the products showed that coupling had occurred at the sites bearing the largest charge, namely the *para* position of the Ph group and C_β (see Figure 3.4). The products were the bis(vinylidene) and alkynyl(vinylidene) complexes **17** and **18** (Scheme 3.4).

Blocking the *para* position did not result in coupling at the Ru-CC- centre, probably for steric reasons. Attempts to couple the tolyl complex alone afforded the derivative **20**

(Scheme 3.5), in which one of the Cp rings has been substituted, this site being prone to electrophilic substitution under the appropriate conditions. Indeed, some spin density is found on some carbon atoms of the Cp ring in [**16**]$^+$ (from 0.03 up to 0.07). While it was not possible to isolate the initial coupling product **20** for NMR or XRD studies, because extremely rapid oxidation of the more electron-rich vinylidene to a CO group occurred (the resulting complex **22** retained the substituted Cp group), nevertheless the NMR parameters of **22** and the deprotonated vinylidene **21** supported the postulated initial coupling and subsequent deprotonation to give products with structures entirely analogous to those found for **17** and **18** (Scheme 3.5).

3.4 Conclusion

In conclusion, we have demonstrated the thus far unreported oxidative coupling of arylalkynyl-ruthenium complexes to form dinuclear vinylidenes, an unprecedented route for alkyne coupling via the ruthenium intermediate. Further, these results demonstrate that, in contrast to arylalkynyl-iron complexes, facile linking of two arylalkynyl ligands may occur via coupling of the unpaired electrons on two cations. We note that previous examples of coupling at C_β have been found with $[M(CCH)(dppe)Cp^*]^+$ (M = Fe, Ru)[10] and with $[Mo(CCPh)(dppe)(\eta\text{-}C_7H_7)]^+$[11]. In the present examples, where the new C-C bond is formed between the electron-rich atoms C_β and C_{para} of the Ph group, coupling appears to be directed by a combination of the high spin densities at C_β and C_{para} and steric factors which preclude coupling between both C_β atoms. If the C_{para} position is blocked, e.g., as in the *p*-tolylethynyl complex, then attack by C_β proceeds at the Cp ring.

Experimental

General experimental conditions are detailed in Chapter 2, Experimental section.

Reagents. The compounds Ru(C≡CPh)(PPh_3)$_2$Cp (**16**)[18], Ru{C≡C(C_6H_4Me-4)}(dppe)Cp (**19**)[19] and [$FeCp_2$]PF_6[20] were prepared by standard literature methods.

Synthesis of [Cp(PPh_3)$_2$Ru{=C=CHC_6H_4CPh=C=}Ru(PPh_3)$_2$Cp][PF_6]$_2$ (17)

Dichloromethane (25 ml) was added to a mixture of Ru(C≡CPh)(PPh_3)$_2$Cp (792 mg, 1.0 mmol) and [$FeCp_2$]PF_6 (314 mg, 0.95 mmol), resulting in an instantaneous darkening of the solution. After 1 h, the solution was concentrated under vacuum and addition of hexane (50 ml) precipitated a dark red solid. The solid was filtered off, washed with hexane (3 × 10 ml) and Et_2O (3 × 10 ml), and redissolved in dichloromethane (25 ml). Addition of Et_2O (50ml) gave [Cp(PPh_3)$_2$Ru{=C=CHC_6H_4CPh=C=}Ru(PPh_3)$_2$Cp][PF_6]$_2$ (**17**; 597mg, 35%) as a dark red precipitate. X-ray quality crystals of the isomorphous AsF_6 salt were grown from $CHCl_3$. Anal. Calcd for $C_{98}H_{80}F_{12}P_6Ru_2$: C, 62.82; H, 4.30; *M*(cation), 1582. Found: C, 62.07; H, 4.22. IR (Nujol/cm^{-1}): ν(C=C) 1709s, 1625m, ν(PF) 839m. ^{1}H NMR ($CDCl_3$): δ 5.09, 5.23 [2x s (br), 2x5H, 2 x Cp], 5.33 [s (br), 1H, =C*H*-), 6.89-7.31 [m (br), 70H, Ph + C_6H_4]. ^{13}C NMR ($CDCl_3$): δ 95.08 (s, Cp), 118.95 (s, =*C*H-), 126.79 [s, =*C*Ph(C_6H_4)], 127.63-133.42 (m, Ph + C_6H_4), 352.08 [s (br), Ru=*C*=CPh(C_6H_4)], 355.03 [s (br), Ru=*C*=CH-(C_6H_4)]. ^{31}P NMR ($CDCl_3$): δ 42.5 (s), 43.7 (s), -147.6 (septet, $^1J_{PF}$ = 710 Hz, PF_6). ES-MS (*m/z*): 1582 [M]$^+$, 1320 [M - PPh_3]$^+$, 1059 [M - 2PPh_3]$^+$, 797 [M - 3PPh_3]$^+$, 690 [Ru(PPh_3)$_2$Cp]$^+$, 429 [Ru(PPh_3)Cp]$^+$.

Synthesis of [Cp(PPh_3)$_2$Ru{C≡CC_6H_4CPh=C=}Ru(PPh_3)$_2$Cp]PF_6 (18)

(a) Ru(C≡CPh)(PPh_3)$_2$Cp (79 mg, 0.1 mmol) and [$FeCp_2$]PF_6 (31 mg, 0.095 mmol) were dissolved in dichloromethane (15 ml) to give a dark solution. After 1 h, the solution was concentrated under vacuum and addition of hexane (50 ml) allowed precipitation of a dark red solid. The precipitate was filtered off and washed with hexane (3 × 10 ml) and Et_2O (3 × 10 ml). The residue was purified by preparative TLC (2/3 acetone/hexane), the brown band (R_f = 0.15) being collected to afford a pale brown solid which was purified by a second preparative TLC (3/7 acetone/ethyl acetate). The dark brown band (R_f = 0.76)

contained $[Cp(PPh_3)_2Ru\{C{\equiv}CC_6H_4CPh{=}C{=}\}Ru(PPh_3)_2Cp]PF_6$ (**18**; 48 mg, 56%) isolated as a dark red solid.

(b) $Ru(C{\equiv}CPh)(PPh_3)_2Cp$ (79 mg, 0.1 mmol) and $[FeCp_2]PF_6$ (31 mg, 0.095 mmol) were dissolved in dichloromethane (15 ml) as above. After 1 h, the solution was concentrated under vacuum and addition of hexane (50 ml) allowed precipitation of a dark red solid. The precipitate was filtered off and washed with hexane (3 × 10 ml) and Et_2O (3 × 10 ml). The solid was dissolved in MeOH (10 ml), 1ml of NaOMe solution (1M) in MeOH was added, and the solution was heated at the reflux point overnight to give an orange-brown precipitate. This was filtered off and washed with MeOH (3 × 5 ml) to give $[Cp(PPh_3)_2Ru\{C{\equiv}CC_6H_4CPh{=}C{=}\}Ru(PPh_3)_2Cp]PF_6$ (**18**; 55 mg, 64%). The colour changed to dark red after dissolution in $CDCl_3$ and evaporation of the solvent. X-ray quality crystals of the isomorphous AsF_6 salt were grown from acetone/hexane. Anal. Calcd for $C_{98}H_{79}F_6P_5Ru_2$: C, 68.13; H, 4.61; *M*(cation), 1583. Found: C, 67.94; H, 4.71. IR (Nujol/cm^{-1}): ν(C≡C) 2061, ν(C=C) 1705w, 1614w, ν(PF) 839m. ^{1}H NMR ($CDCl_3$): δ 4.33 [s, 5H, *Cp*Ru(C≡C)], 5.08 (s, 5H, *Cp*Ru=C=C), 6.52-7.49 (m, 70H, Ph). ^{13}C NMR ($CDCl_3$): δ 85.43 [s, *Cp*Ru(C≡C)], 94.86 (s, *Cp*Ru=C=C), 114.72 [s, =*C*Ph(C_6H_4)], 121.42 (t, $^3J_{CP}$ = 25 Hz, Ru-*C*≡C), 123.08 [s, ≡*C*(C_6H_4)], 127.21-139.07 (m, Ph), 354.32 (t, $^3J_{CP}$ = 15 Hz, Ru=*C*=C). ^{31}P NMR ($CDCl_3$): δ 42.5 (s), 51.4 (s), -147.6 (sept, PF_6). ES-MS (*m/z*): 1582 $[M]^+$, 1320 $[M - PPh_3]^+$, 1059 $[M - 2PPh_3]^+$, 797 $[M - 3PPh_3]^+$, 690 $[Ru(PPh_3)_2Cp]^+$, 429 $[RuPPh_3Cp]^+$.

Synthesis of $[Ru\{=C=C(C_6H_4Me\text{-}4)\text{-}\eta\text{-}C_5H_4[Ru(CO)(PPh_3)_2]\}(PPh_3)_2Cp][PF_6]_2$ (22)

$Ru\{C{\equiv}C(C_6H_4Me\text{-}4)\}(PPh_3)_2Cp$ (100 mg, 0.12 mmol) and $[FeCp_2]PF_6$ (41 mg, 0.12 mmol) were dissolved in 10 ml of THF at -78°C. After 1 h, the solution was slowly warmed to room temperature over 5 h. Then hexane (50 ml) was added to the mixture and the resulting precipitate was filtered off and washed with hexane (2 × 15 ml). The solid was purified by preparative TLC (1/1 acetone/hexane), and the orange band (R_f = 0.45) was collected to give $[Ru\{=C=C(C_6H_4Me\text{-}4)\text{-}\eta\text{-}C_5H_4[Ru(CO)(PPh_3)_2]\}(PPh_3)_2Cp][PF_6]_2$ (**22**; 29 mg, 27%). Crystals suitable for X-ray study were obtained from dichloromethane/benzene and by changing the anion from PF_6 to AsF_6. Anal. Calcd for $C_{92}H_{76}F_{12}OP_6Ru_2$: C, 60.93; H, 4.22; *M*(cation), 1524. Found: C, 60.16; H, 4.28. IR (Nujol/cm^{-1}): ν(CO) 1980, ν(C=C) 1607, 1596, ν(PF) 833 cm^{-1}. ^{1}H NMR (d_6-acetone): δ 2.47 (s, 3H, Me), 4.25 (s, 2H, Cp), 4.92 (s, 2H, Cp), 5.50 (s, 5H, Cp), 6.82-7.61 (m, 64H,

Ph). ^{13}C NMR (d_6-acetone): δ 20.49 (s, Me), 83.97 (s, CH, Cp), 94.98 (s, CH, Cp), 96.12 (s, Cp), 110.64 (s, C, Cp), 123.73 (s, Ru=C=*C*), 126.76-140.47 (m, Ph), 202.87 (t, $^3J_{CP}$ = 18 Hz, Ru-CO), 343.09 (t, $^3J_{CP}$ = 16 Hz, Ru=*C*=). ^{31}P NMR (d_6-acetone): δ 39.6 (s, Ru=C), 44.2 (s, Ru-CO), -143.1 (septet, $^1J_{PF}$ = 705 Hz, PF_6). ES-MS (*m/z*): calcd for $C_{92}H_{76}OP_4Ru_2$ 762.17, found 762.163 $[M]^{2+}$.

Synthesis of [Ru{=C=C(C$_6$H$_4$Me-4)-η-C$_5$H$_4$[Ru(PPh$_3$)$_2$(C≡CC$_6$H$_4$Me-4)]}(PPh$_3$)$_2$Cp] PF$_6$ (21)

(a) Ru{C≡C(C$_6$H$_4$Me-4)}(PPh$_3$)$_2$Cp (60 mg, 0.07 mmol) and [FeCp$_2$]PF$_6$ (25 mg, 0.07 mmol) were dissolved in THF (8 ml) at -78°C. After 1 h, the solution was slowly warmed to room temperature over 5 h. Then, NEt$_3$ (3 ml) was added to the solution, and after 1 h at room temperature, hexane (50 ml) was added. The resulting precipitate was filtered off and washed with hexane (3 × 15 ml) to give [Ru{=C=C(C$_6$H$_4$Me-4)-η-C$_5$H$_4$[Ru(PPh$_3$)$_2$(C≡CC$_6$H$_4$Me-4)]}(PPh$_3$)$_2$Cp]PF$_6$ (**21**, 53 mg, 89%) as a brown powder.

(b) The product was obtained similarly from Ru{C≡C(C$_6$H$_4$Me-4)}(PPh$_3$)$_2$Cp (100 mg, 0.12 mmol) and [FeCp$_2$]PF$_6$ (41 mg, 0.12 mmol) and was purified by preparative TLC (1/1 acetone/hexane); the brown band (R_f = 0.81) was collected to give [Ru{=C=C(C$_6$H$_4$Me-4)-η-C$_5$H$_4$[Ru(PPh$_3$)$_2$(C≡CC$_6$H$_4$Me-4)]}(PPh$_3$)$_2$Cp]PF$_6$ (**21**, 16 mg, 17%). IR (Nujol/cm^{-1}): ν(C≡C) 2070, ν(C=C) 1613, ν(PF) 837 cm^{-1}. ^{1}H NMR (d_6-acetone): δ 2.35 (s, 3H, Me), 2.38 (s, 3H, Me), 3.56 (s, 2H, Cp), 4.51 (s, 2H, Cp), 5.38 (s, 5H, Cp), 6.95-7.78 (m, 68H, Ph). ^{13}C NMR (d_6-acetone): δ 20.94 (s, Me), 21.06 (s, Me), 69.34 (s, Ru-C≡*C*), 79.49 (s, C_5H_4), 83.73 (s, C_5H_4), 94.86 (s, Cp), 104.3 (t, $^3J_{CP}$ = 3 Hz, Ru=C=*C*), 114.32 (s, C_5H_4), 121.30 (t, $^2J_{CP}$ = 25 Hz, Ru-*C*≡), 124.56-139.37 (m, Ph), 353.00 (t, $^2J_{CP}$ = 15 Hz, Ru=*C*=). ^{31}P NMR (d_6-acetone): δ 40.8 (s, Ru=C), 49.6 (s, Ru-C≡), -143.1 (septet, $^1J_{PF}$ = 705 Hz, PF_6). ES-MS (*m/z*): calcd for $C_{100}H_{83}P_4Ru_2$ 1611.353, found 1611.319 $[M]^+$.

References

1. Sato, M.; Hayashi, Y.; Tsuda, T.; Katada, M., *Inorg. Chim. Acta* **1997,** *261*, 113-116.
2. (a) Denis, R.; Toupet, L.; Paul, F.; Lapinte, C., *Organometallics* **2000,** *19*, 4240-4251; (b) Paul, F.; Costuas, K.; Ledoux, I.; Deveau, S.; Zyss, J.; Halet, J.-F.; Lapinte, C., *Organometallics* **2002,** *21*, 5229-5235; (c) Paul, F.; Mevellec, J.-Y.; Lapinte, C., *Dalton Trans.* **2002**, 1783–1790; (d) Costuas, K.; Paul, F.; Toupet, L.; Halet, J.-F.; Lapinte, C., *Organometallics* **2004,** *23*, 2053-2068; (e) Paul, F.; Toupet, L.; Thépot, J.-Y.; Costuas, K.; Halet, J.-F.; Lapinte, C., *Organometallics* **2005,** *24*, 5464-5478; (f) Paul, F.; da Costa, G.; Bondon, A.; Gauthier, N.; Sinbandhit, S.; Toupet, L.; Costuas, K.; Halet, J.-F.; Lapinte, C., *Organometallics* **2007,** *26*, 874-896.
3. Paul, F.; Ellis, B. G.; Bruce, M. I.; Toupet, L.; Roisnel, T.; Costuas, K.; Halet, J.-F.; Lapinte, C., *Organometallics* **2006,** *25*, 649-665.
4. Gauthier, N.; Tchouar, N.; Justaud, F.; Argouarch, G.; Cifuentes, M. P.; Toupet, L.; Touchard, D.; Halet, J.-F.; Rigaut, S.; Humphrey, M. G.; Costuas, K.; Paul, F., *Organometallics* **2009,** *28*, 2253-2266.
5. (a) Grime, R. W.; Helliwell, M.; Hussain, Z. I.; Lancashire, H. N.; Mason, C. R.; McDouall, J. J. W.; Mydlowski, C. M.; Whiteley, M. W., *Organometallics* **2008,** *27*, 857-871; (b) Brown, N. J.; Collison, D.; Edge, R.; Fitzgerald, E. C.; Helliwell, M.; Howard, J. A. K.; Lancashire, H. N.; Low, P. J.; McDouall, J. J. W.; Raftery, J.; Smith, C. A.; Yufit, D. S.; Whiteley, M. W., *Organometallics* **2010,** *29*, 1261-1276; (c) Lancashire, H. N.; Brown, N. J.; Carthy, L.; Collison, D.; Fitzgerald, E. C.; Edge, R.; Helliwell, M.; Holden, M.; Low, P. J.; McDouall, J. J. W.; Whiteley, M. W., *Dalton Trans.* **2011,** *40*, 1267-1278.
6. Low, P. J., *Dalton Trans.* **2005**, 2821-2824.
7. (a) Paul, F.; Lapinte, C., Unusual Structures and Physical Properties in Organometallic Chemistry. Gielen, M.; Willem, R.; Wrackmeyer, B., Eds. Wiley: New York, 2002; pp 220-279; (b) Lapinte, C., *J. Organomet. Chem.* **2008,** *693*, 793-801.
8. Powell, C. E.; Humphrey, M. G., *Coord. Chem. Rev.* **2004,** *248*, 725-756.
9. Adams, J. S.; Bitcon, C.; Brown, J. R.; Collison, D.; Cunningham, M.; Whiteley, M. W., *J. Chem. Soc., Dalton Trans.* **1987**, 3049-3053.
10. (a) Le Narvor, N.; Toupet, L.; Lapinte, C., *J. Am. Chem. Soc.* **1995,** *117*, 7129-7138; (b) Bruce, M. I.; Ellis, B. G.; Low, P. J.; Skelton, B. W.; White, A. H., *Organometallics* **2003,** *22*, 3184-3198.
11. Beddoes, R. L.; Bitcon, C.; Ricalton, A.; Whiteley, M. W., *J. Organomet. Chem.* **1989,** *367*, C21-C24.
12. Bruce, M. I.; Burgun, A.; Gendron, F.; Grelaud, G.; Halet, J.-F.; Skelton, B. W., *Organometallics* **2011,** *30*, 2861–2868.
13. Bruce, M. I.; Swincer, A. G., *Adv. Organomet. Chem.* **1983,** *22*, 59.

14. (a) Wisner, J. M.; Bartczk, T. J.; Ibers, J. A., *Inorg. Chim. Acta* **1985,** *100*, 115-123; (b) Bruce, M. I.; Humphrey, M. G.; Snow, M. R.; Tiekink, E. R. T., *J. Organomet. Chem.* **1986,** *314*, 213-225.
15. (a) Bruce, M. I.; Swincer, A. G.; Wallis, R. C., *J. Organomet. Chem.* **1979,** *171*, C5-C8; (b) Bruce, M. I.; Ellis, B. G.; Skelton, B. W.; White, A. H., *J. Organomet. Chem.* **2005,** *690*, 792-801; (c) Le Lagadec, R.; Roman, E.; Toupet, L.; Müller, U.; Dixneuf, P. H., *Organometallics* **1994,** *13*, 5030-5039.
16. (a) Le Narvor, N.; Lapinte, C., *Organometallics* **1995,** *14*, 634-639; (b) Tanaka, Y.; Shaw-Taberlet, J. A.; Justaud, F.; Cador, O.; Roisnel, T.; Akita, M.; Hamon, J.-R.; Lapinte, C., *Organometallics* **2009,** *28*, 4656–4669; (c) de Montigny, F.; Argouarch, G.; Costuas, K.; Halet, J.-F.; Roisnel, T.; Toupet, L.; Lapinte, C., *Organometallics* **2005,** *24*, 4558-4572.
17. Bruce, M. I.; Costuas, K.; Davin, T.; Ellis, B. G.; Halet, J.-F.; Lapinte, C.; Low, P. J.; Smith, M. E.; Skelton, B. W.; Toupet, L.; White, A. H., *Organometallics* **2005,** *24*, 3864-3881.
18. Bruce, M. I.; Hameister, C.; Swincer, A. G.; Wallis, R. C., *Inorg. Synth.* **1982,** *21*, 78-84.
19. Bruce, M. I.; Skelton, B. W.; White, A. H.; Zaitseva, N. N., *J. Organomet. Chem.* **2002,** *650*, 141-150.
20. Connelly, N. G.; Geiger, W. E., *Chem. Rev.* **1996,** *96*, 877-910.

Chapter Four

Reactivity of the 17-Electron Species $[Fe(C{\equiv}CC{\equiv}CR)(dppe)Cp^*]^{\bullet+}$ (R = Ph, Tol)

4.1 Introduction

Although electrochemical studies of diynyl organometallic complexes are known (see Chapter 2) only a few examples of their chemical oxidation are described in the literature. This is probably due to the difficulties of characterising such 17-e species and to their low stability resulting from large delocalisation of the unpaired electron on the butadiynyl bridge. In Chapter 2, 17-e iron and ruthenium diynyl complexes have been characterised by EPR spectroscopy and revealed to be stable at low temperature (-78°C). However, it has been noticed that upon increasing the temperature, the diynyl radical monocations either decomposed or further chemical reactions occurred. This has been shown by simple colour changes and precipitation in the reaction mixture with increasing temperature. When EPR samples were left at room temperature for one hour, the EPR signatures of the 17-e species were no longer present.

4.1.1 Examples of oxidative dimerisation of diynyl complexes

Rigaut et al.[1] published the first example of the dimerisation of diynyl complexes upon chemical oxidation. When the ruthenium complex *trans*-[RuCl(C≡CC≡CSiMe$_3$)(dppe)$_2$] was treated with half an equivalent of ferrocenium salt (Scheme 4.1), a novel deep purple binuclear dimer containing a C_8H_3 bridge and a cyclic four-carbon centre was obtained as the unique product in 45% yield after several crystallisations.

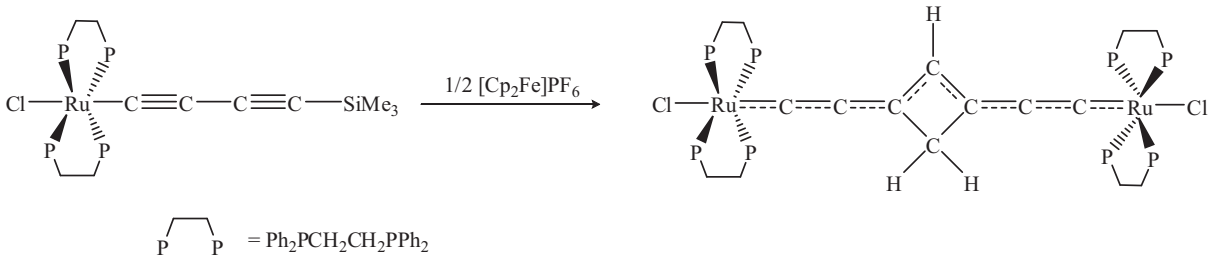

Scheme 4.1

The mechanism of this reaction is unknown but it is assumed that a 17-e species is generated by electron transfer between the diynyl-ruthenium and the ferrocenium cation. This reacts by [2 + 2]-cycloaddition between two C_γ-C_δ bonds (the C_α and C_β atoms being sterically protected by the two bulky dppe ligands) of the electrophilic organoruthenium radical and the neutral diynyl complex. Desilylation and protonation from the solvent (THF) of the organometallic radical intermediates also occurred during this reaction.

Another oxidative dimerisation of diynyl complexes was found by the Bruce group[2] but has not been yet published. The diynyl ruthenium complexes Ru(C≡CC≡CR)(dppe)Cp (R = Ph **23**, Fc **24**) react with one equivalent of ferrocenium salt to afford deep purple products characterised as dimers (Scheme 4.2). The crude mixtures containing the two symmetrical (**25a** and **26a**) and unsymmetrical (**25b** and **26b**) dimers were characterised by the usual spectroscopic methods, the ^{31}P NMR spectra containing three signals with relative intensities 1:2:1, the most intense peak being assigned to the symmetrical dimer and the two others to the asymmetrical dimer. This indicates that the two different isomers are present in the crude mixture in a 50:50 ratio.

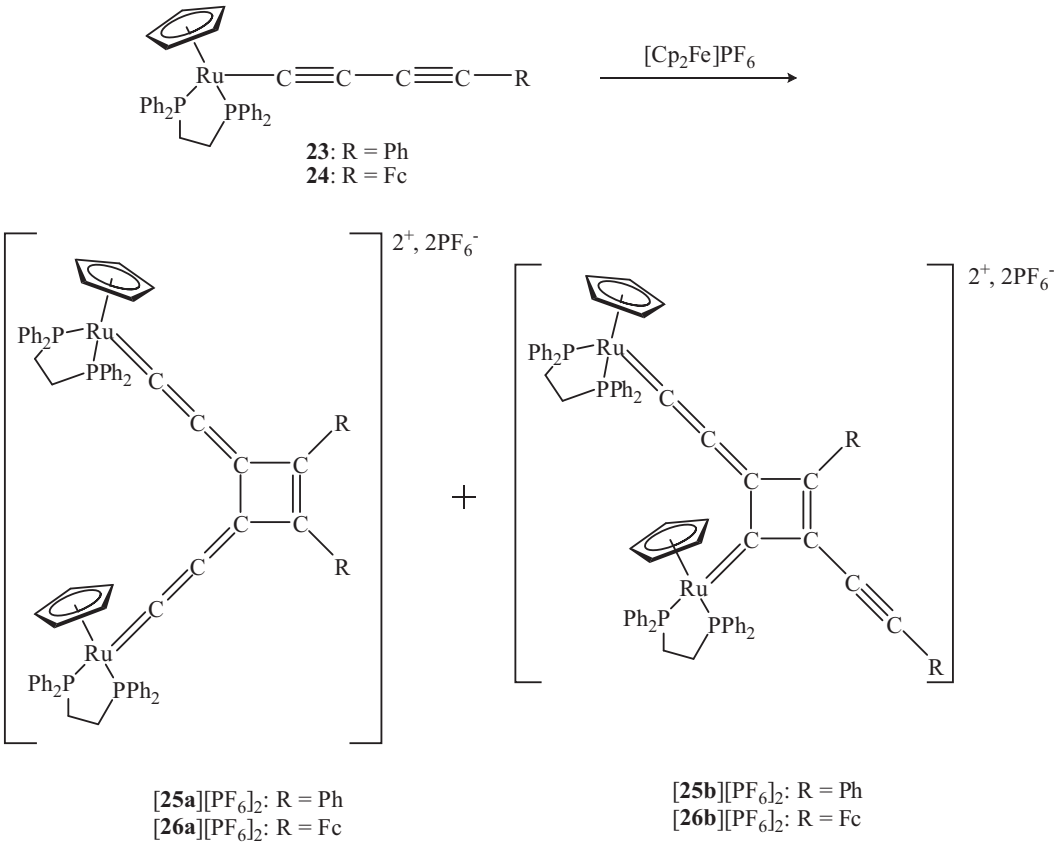

23: R = Ph
24: R = Fc

[**25a**][PF_6]$_2$: R = Ph
[**26a**][PF_6]$_2$: R = Fc

[**25b**][PF_6]$_2$: R = Ph
[**26b**][PF_6]$_2$: R = Fc

Scheme 4.2

The crude mixture has been purified by chromatography for R = Ph, the asymmetric dimer **25b** being obtained pure and its structure confirmed by an X-ray determination while the symmetric dimer **25a** decomposed during preparative t.l.c. For R = Fc, the crude mixture was purified by successive crystallisations affording the pure symmetric dimer **26a** of which the structure was also confirmed by X-ray determination, while the unsymmetrical dimer **26b** could not be obtained pure. These dimers have unique geometries incorporating in both cases, a four-carbon cyclobutene ring. In contrast with the previous example where dimerisation occurred by coupling between one 17-e species and one 18-e neutral, in this reaction, it is assumed that intermolecular radical coupling occurred between two 17-e species. This hypothesis was rationalised by DFT calculations carried out by the Halet group in Rennes. Figure 4.1 shows the atomic spin densities on the carbon chain of the 17-e complex [**23**]PF_6. The atomic spin density is very large on C_2 and C_4 (0.22) and quasi-null on C_1 and C_3 (0.01 and -0.03 respectively) indicating that radical couplings could occur according to three different pathways: C_2-C_2, C_2-C_4 and C_4-C_4. The C_2-C_4 and C_4-C_4 couplings would afford the symmetric and asymmetric dimers, respectively, the C_2-C_2 coupling probably being unfavourable because of steric hindrance.

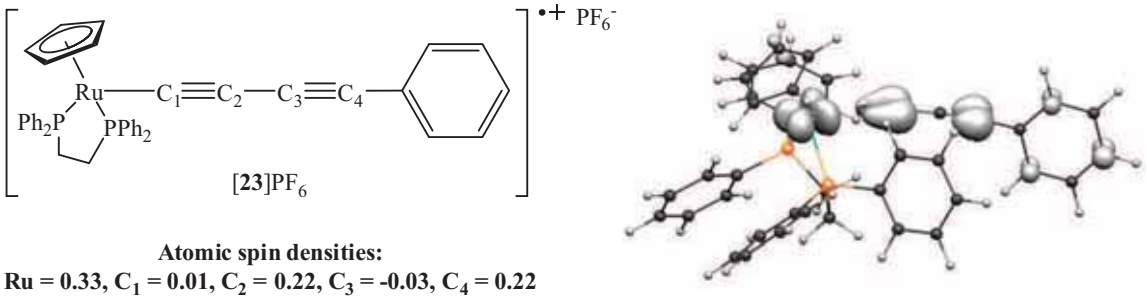

Figure 4.1. *Calculated (left) and representation (right) of the atomic spin densities in [23]PF_6.*

Recently, oxidative dimerisation of diynyl-molybdenum complexes has been reported by Whiteley et al.[3], when the 2,2'-bipyridine ligand of the stable 17-e diynyl complex [Mo(C≡CC≡CSiMe$_3$)(bipy)(η-C_7H_7)]PF_6 (see Section 2.1.6) is replaced by a dppe ligand, the 17-e species is not stable and dimerises to give a unique deep purple dicationic product (Scheme 4.3). In comparison with the previous examples, the mechanism of this dimerisation is similar to the dimerisation of the diynyl-ruthenium complexes [**23**]PF_6 and [**24**]PF_6, radical coupling between two molybdenum 17-e species occuring by C_β-C_β bond formation. However, the molybdenum dimer does not contain a cyclobutene centre as found in the ruthenium dimers.

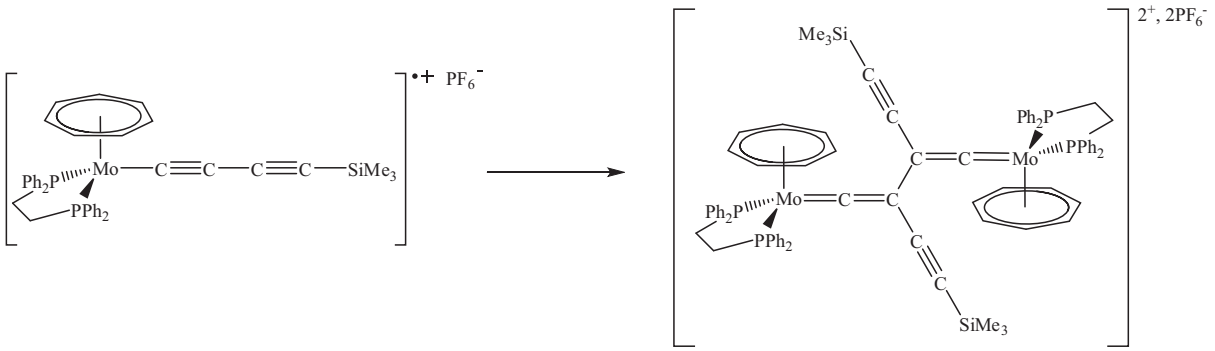

Scheme 4.3

4.1.2 Other examples of dimerisation of diynyl complexes

In 2009, Berke et al.[4] obtained the first crystal structure of a stable organotungsten butatrienylidene complex, W(CO)(dppe)$_2${C=C=C=C(SnMe$_3$)(*p*-C_6H_4*t*Bu)}. However, when left in solution for 24 hours, this compound dimerised to give a biradical species with

two tungsten centres (Scheme 4.4). The authors supposed that the first intermediate of this dimerisation reaction is a dimer with a cyclobutane centre formed by [2 + 2]-cycloaddition between the terminal C_γ=C_δ double bonds of two butatrienylidenes. Then, by stepwise electron transfers, a biradical dimer with a cyclobutene centre is formed which presumably undergoes an electrocyclic ring opening reaction to give the final product.

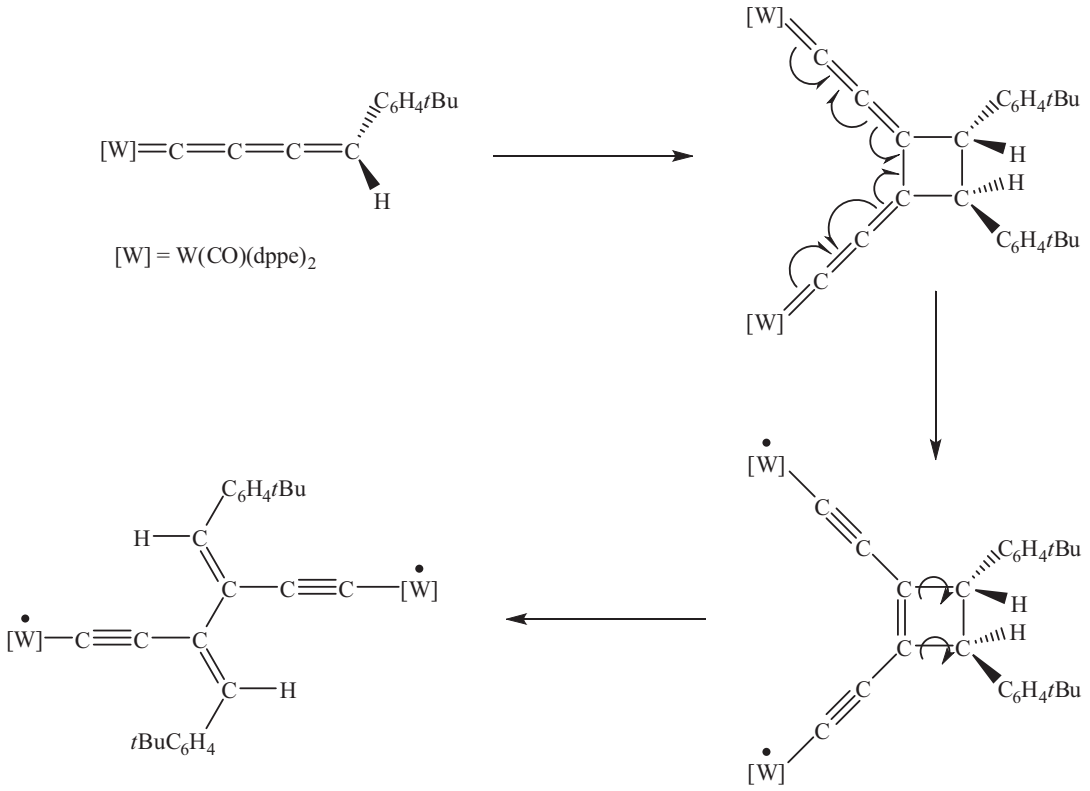

Scheme 4.4

4.2 Aims

Although the 17-e species $[Fe(C{\equiv}CC{\equiv}CR)(dppe)Cp^*]^{\bullet+}$ are sufficiently stable at low temperature (-78°C) to be characterised by EPR spectroscopy, they quickly decompose or further react when the temperature is increased (see Chapter 2). In order to characterise further the products from the chemical oxidation of the neutral butadiynyl-iron complexes and to elucidate their molecular structures, oxidation studies of compounds **2a** and **2b** were carried out. Full characterisation of the products by the usual spectroscopic methods is described in this Chapter. These results are supported by DFT calculations and are compared with the results obtained for the analogous ruthenium examples.

4.3 Results and discussion

4.3.1 Spectro-electrochemistry of Fe(C≡CC≡CPh)(dppe)Cp (2a)*

Before investigating the chemical oxidation reaction of the diynyl-iron species **2a** and **2b**, electrochemical studies were carried out and monitored by UV-Vis and Near-IR spectroscopy. As references, the UV-Vis (Figure 4.2) and Near-IR spectra of the neutral complex **2a** were recorded in dichloromethane; however, the Near-IR range is not shown below because no transitions were observed in this region for **2a**.

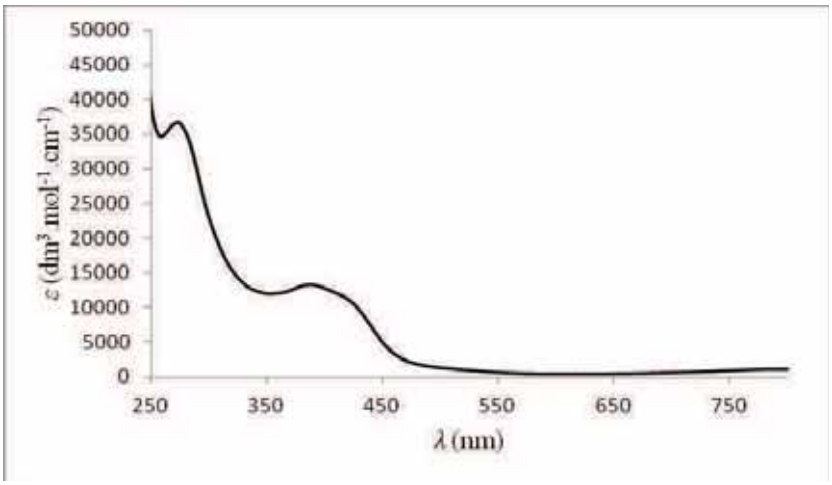

Figure 4.2. *UV-Vis spectrum of **2a** in dichloromethane.*

In the UV-Vis spectrum of **2a**, an intense high energy band is observed at 273 nm which was attributed to $\pi \rightarrow \pi^*$ ligand-centred transitions. A less intense and broader band is observed at 387 nm with a shoulder at 420 nm which was assigned to $d\pi(Fe) \rightarrow \pi^*(C{\equiv}C)$ metal-to-ligand charge transfer (MLCT) transitions. This absorption gives the orange colour to the neutral complex[5]. The UV-Vis spectrum of the analogous complex Fe(C≡CPh)(dppe)Cp* (**11**) containing a shorter carbon chain shows similar absorptions (Table 4.1) to compound **2a**, the MLCT band being higher in energy (350 nm) by 37 nm for **11**. This bathochromic shift of the MLCT band can be ascribed to electronic delocalisation being larger in **2a**, containing a C_4 chain, than in **11**, containing a C_2 chain.

Table 4.1. UV-Vis spectral data for **11** and **2a** in dichloromethane.

Compound	λ/nm (ε × 10^{-3}/dm^3.mol^{-1}.cm^{-1})	Ref
Fe(C≡CPh)(dppe)Cp* (**11**)	277 (14.5), 350 (13.6)	5
Fe(C≡CC≡CPh)(dppe)Cp* (**2a**)	273 (36.7), 387 (13.3)	This work

Initially, electrochemical oxidation of **2a** was carried out until no further changes were observed in the UV-Vis range; selected spectra are shown in Figure 4.3. The $\pi \rightarrow \pi^*$ transitions were not significantly affected during the oxidation process while the MLCT transitions centred at 387 nm totally disappeared with the appearance of new broad and low intense absorptions around 560 nm and 790 nm. These new absorptions can be attributed to ligand-to-metal charge transfer (LMCT) transitions from the oxidised species $\mathbf{2a}^{\bullet+}$, or to new species formed in the electrochemical cell upon oxidation. A single isosbestic point was observed during the oxidation process suggesting that a clean reaction occurred with formation of a unique new product.

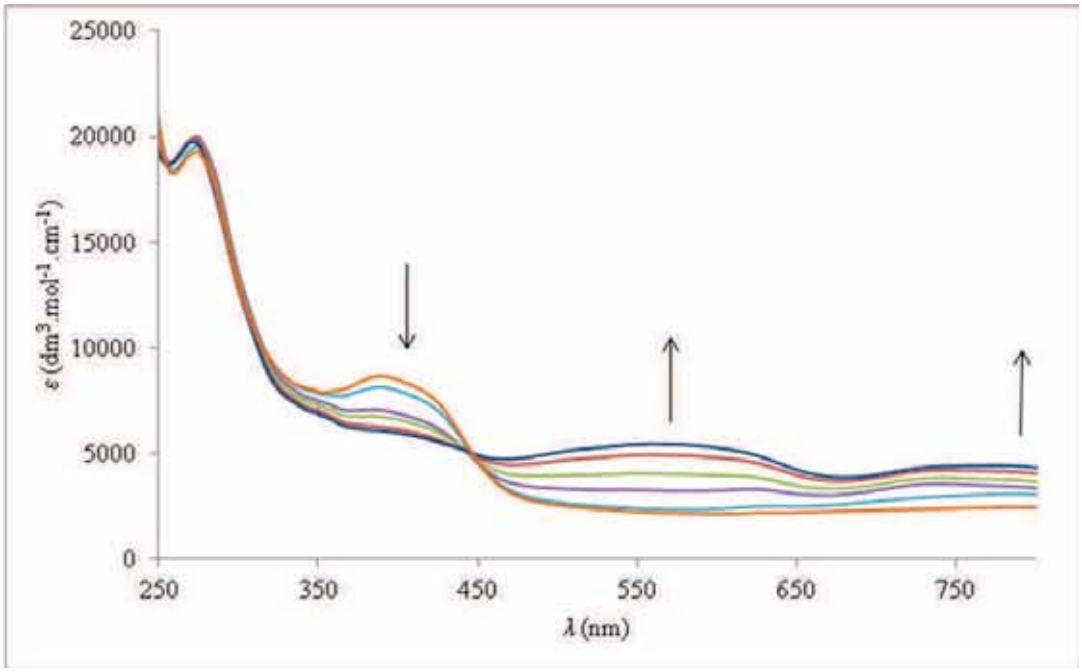

Figure 4.3. *Selected UV-Vis spectra during the oxidation of **2a**.*

In order to investigate the reversibility of the oxidation process in the electrochemical cell, the mixture was then electrochemically reduced. Selected UV-Vis spectra recorded during the reduction process are presented in Figure 4.4. This time, the $\pi \rightarrow \pi^*$ transitions

centred at 273 nm are affected by the electrochemical process and decrease significantly upon reduction while the MLCT band at 387 nm slightly reappears. Besides, low intensity transitions centred at 560 nm disappear and absorptions in the far UV-range at 790 nm increase. In the box (Figure 4.4), traces which do not go through the same point at ca 650 nm are observed; this indicates that new species are formed probably via subsequent reactions.

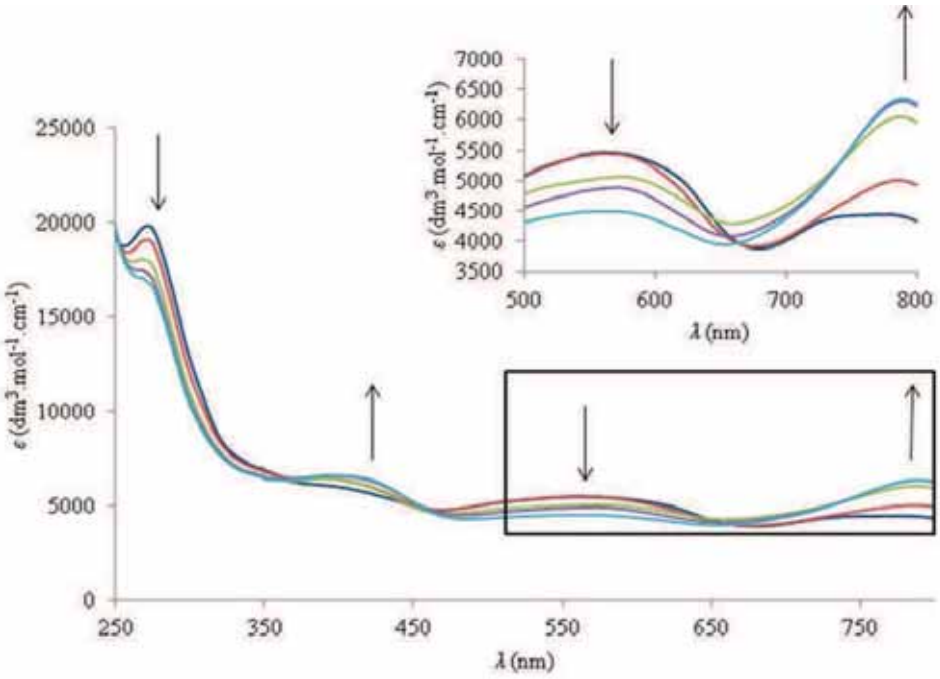

Figure 4.4. *Selected UV-Vis spectra during the reduction of oxidised* ***2a****.*

Spectroelectrochemical analyses were also carried out in the Near-IR region and selected spectra are shown in Figure 4.5. Upon oxidation and then reduction, a low energy and very weak intensity band appears at 5500 cm^{-1} which has been attributed to a forbidden metal-centred ligand field (LF) electronic transition characteristic of Fe(III) complexes[6]. When further reduced, the intensity of this LF transition decreases but it does not totally disappear.

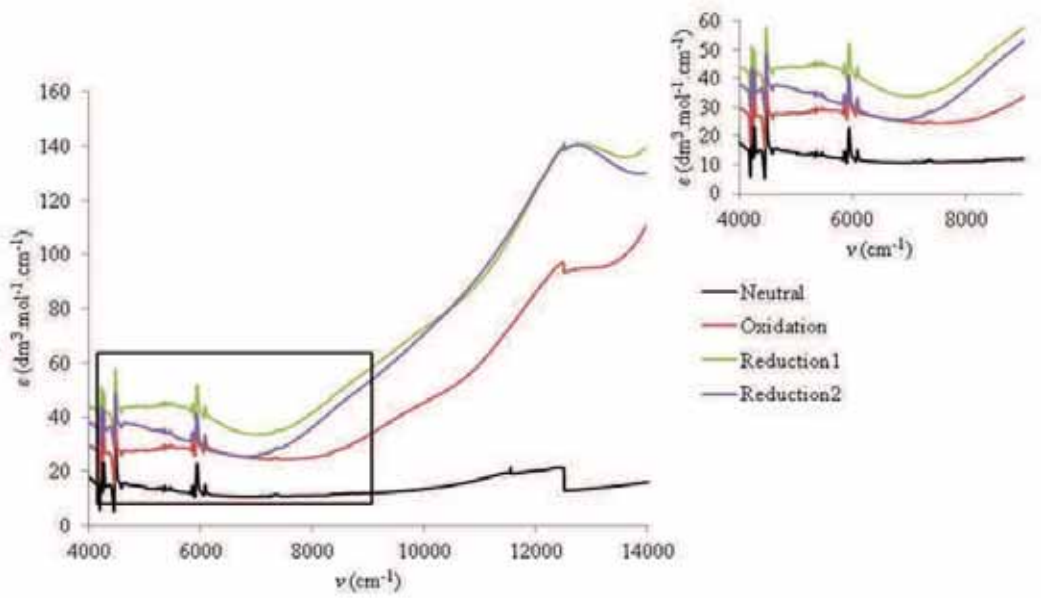

Figure 4.5. *Selected Near-IR spectra of* ***2a*** *during the oxidation and reduction processes.*

Data recorded from the spectroelectrochemistry in the UV-Vis and Near-IR ranges indicate that oxidation of the neutral compound **2a** occurrs to give either the oxidised complex $\mathbf{2a}^{\bullet+}$ or a new species via further reactions. Then, upon reduction, appearance of new absorptions and the lack of isosbestic points in the UV-Vis range suggest that the neutral complex **2a** is only partially recovered and that (a) new species are(is) formed in the electrochemical cell. The generated species $\mathbf{2a}^{\bullet+}$ might slowly react with itself (under the spectro-electrochemical conditions) to afford product(s) **P** (Scheme 4.5), which is(are) probably dimer(s) as found for the ruthenium case. Spectro-electrochemical signatures of this(these) new product(s) **P** together with it(their) oxidised and reduced parents were also partially observed during the oxidation and reduction processes with the appearance of new absorptions.

$$\mathbf{2a} - e^- \rightleftharpoons \mathbf{2a}^{\bullet+} \xrightarrow{\text{"Slow"}} \mathbf{P_1} + \ldots$$

Scheme 4.5

4.3.2 Chemical oxidation of 2a and 2b, characterisations of the products

Guided by the EPR results (Chapter 2) and the spectro-electrochemical analyses carried out on complex **2a**, chemical oxidation reaction of **2a** and **2b** was achieved (using the methyl end-group of **2b** as a NMR probe to help for the characterisation of the products). Formation of the 17-e species $\mathbf{2a}^{\bullet+}$ is expected at low temperature, and as observed by EPR, further reactions occur to give new product(s) which is(are) characterised in this section.

Chemical oxidations were achieved by reacting neutral complexes **2a** or **2b** with one equivalent of ferrocenium salt as the oxidising agent, in THF at -78°C (Scheme 4.6). The colour changed immediately from orange to deep green and after one hour at -78°C, the solution was allowed to warm up slowly to room temperature over five hours. When the temperature reached -35°C, the colour of the solution changed from deep green to deep purple indicating a further chemical reaction had occurred. After one hour at room temperature, pentane was added to the solution in order to precipitate the products. The residue was then washed with pentane to afford a deep purple powder in 61 and 57% yields for **2a** or **2b**, respectively, on the basis of the formulations [**2**][PF_6] or hypothetical [**2**]$_2$[PF_6]$_2$.

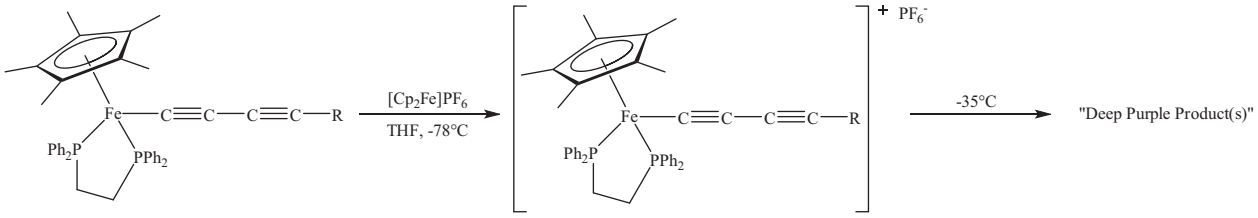

Scheme 4.6

High resolution mass spectra of the mixture from **2a** confirmed the presence of dimers with ions found at *m/z* 714.2274 (z = 2; calculated: 714.2262 for $[M]^{2+}$), 1429.4539 (calculated: 1429.4608 for $[M + H]^+$) and 1573.4097 (calculated: 1573.4172 for $[M + PF_6]^+$). However, the only route to elucidate the exact dimeric structure was to obtain crystals for X-ray analyses.

Molecular structure

After many attempts, small thin purple crystals from the oxidation of **2a** were obtained by slow diffusion of pentane into a concentrated dichloroethane solution of the dimer mixture. Crystals diffracted weakly due to their poor quality, although the X-ray structure was solved with an acceptable R-factor: R = 0.083. An ORTEP view of one cation of the symmetrical dimer [**27a**][PF_6]$_2$ (the PF_6^- anions were squeezed) is presented in Figure 4.6 while selected structural parameters are collected in Table 4.2. The asymmetric unit incorporates half a molecule of [**27a**][PF_6]$_2$ (the symmetry element being a C_2 axis passing through the middle of the cyclobutene ring) and two and a half molecules of dichloroethane. The crystal system is monoclinic *P*2/*c* with unit cell parameters: a = 16.7558(10), b = 12.3342(7), c = 25.7292(12) Å and β = 95.714(2)°.

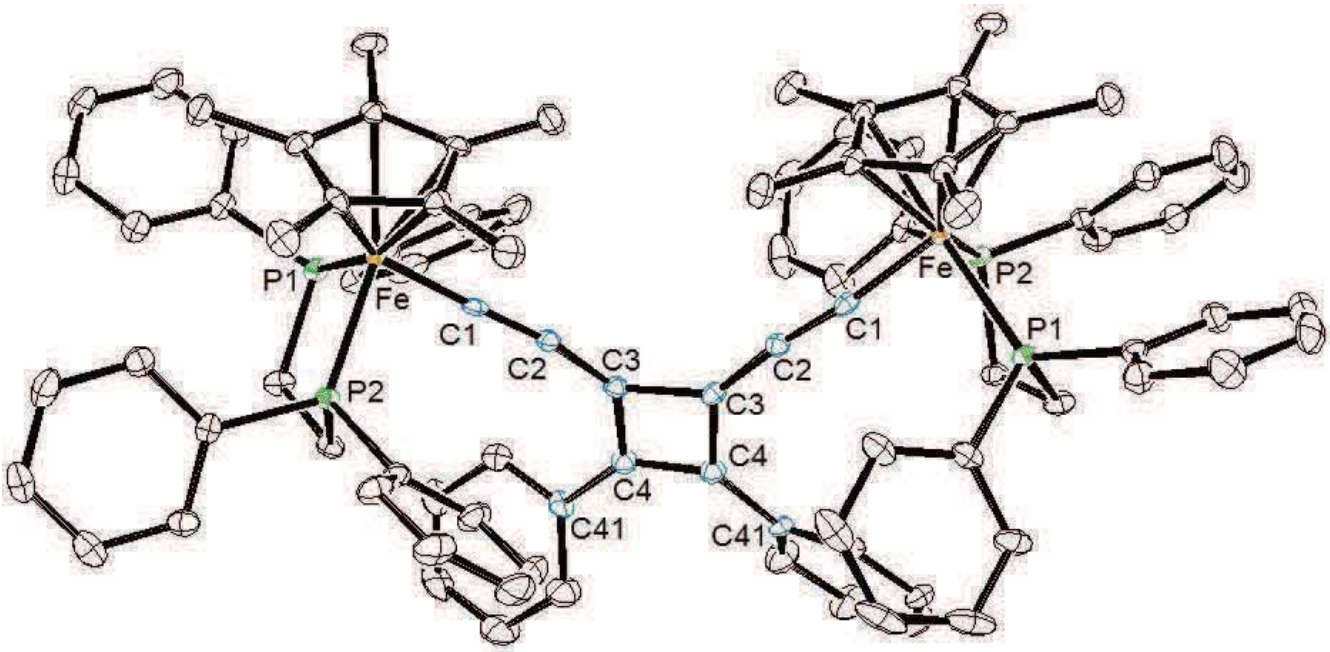

Figure 4.6. *ORTEP view of [{Cp*(dppe)Fe=C=C=}$_2${μ-C_4(Ph)$_2$}][PF_6]$_2$ [**27a**][PF_6]$_2$.*

Table 4.2. Selected structural parameters for [**27a**][PF_6]$_2$.

Bond Distances (Å)		Bond Angles (°)	
Fe-P(1)	2.2332(11)	P(1)-Fe-P(2)	85.11(4)
Fe-P(2)	2.2427(11)	C(1)-Fe-P(1)	90.39(13)
Fe-Cp*$_{cent}$	1.769	C(1)-Fe-P(2)	85.18(13)
Fe-C(1)	1.784(4)	Fe-C(1)-C(2)	174.4(3)
C(1)-C(2)	1.264(6)	C(1)-C(2)-C(3)	170.3(4)
C(2)-C(3)	1.344(6)	C(2)-C(3)-C(4)	134.5(4)
C(3)-C(4)	1.479(6)	C(2)-C(3)-C(3')	137.1(2)
C(3)-C(3')	1.516(8)	C(3)-C(4)-C(41)	130.8(4)
C(4)-C(4')	1.417(8)	C(4)-C(3)-C(3')	88.0(2)
C(4)-C(41)	1.451(6)	C(3)-C(4)-C(4')	91.9(2)
		C(4')-C(4)-C(41)	137.2(2)

Firstly, the X-ray analysis confirmed the structure of [**27a**][PF_6]$_2$ as a symmetrical dimer with two Fe(dppe)Cp* fragments linked by a C_8 ligand bearing a four-carbon cyclobutene centre. The angles in the cyclobutene ring are close to perfect right angles [88.0(2) and 91.9(2)°]; their sum is 360° which indicates that the C_4 ring is planar. As expected, the iron atoms adopt a pseudo-octahedral geometry but the bond lengths in the Fe(dppe)Cp* fragments are significantly different in comparison with the neutral starting material **2a**. The Fe-P(1,2) distances [2.2332(11) and 2.2427(11) Å] are clearly elongated in comparison with the Fe-P(1,2) bond lengths in **2a** [2.1808(4) and 2.1955(4) Å] while the Fe-Cp*$_{cent}$ is also slightly longer [Fe-Cp*$_{cent}$(**2a**) = 1.746, Fe-Cp*$_{cent}$([**27a**][PF_6]$_2$) = 1.769 Å]. The Fe-C(1) bond length significantly decreased [1.784(4) Å] by ca 0.09 Å in comparison with the Fe-C(1) distance in **2a** [1.8733(13) Å] which is consistent with a [Fe=C(dppe)Cp*]$^+$ double-bond formulation. Distances in the [**27a**][PF_6]$_2$ carbon chain [Fe-C(1) = 1.784(4), C(1)-C(2) = 1.264(6) and C(2)-C(3) = 1.344(6) Å] are very close to the distances found in the allenylidene complex [Fe(=C=C=CPh_2)(dppe)Cp*]PF_6 [Fe-C(1) = 1.785(5), C(1)-C(2) = 1.257(7) and C(2)-C(3) = 1.361(7) Å] previously synthesised by Argouarch et al[7]. These bond lengths are characteristic of allenylidene derivatives with the C(1)-C(2) distances being shorter than the C(2)-C(3) distances indicating a contribution from the canonical form [M]{C≡CC$^+$(R)R'}[8]. The Fe-C(1)-C(2)-C(3) chain slightly deviates from linearity with angles at C(1) and C(2) being 174.4(3) and 170.3(4)°. Distances in the cyclobutene ring are consistent with the presence of three single bonds [2 × C(3)-C(4) = 1.479(6) and C(3)-C(3') = 1.516(8) Å] and one C=C double bond [C(4)-

C(4') = 1.417(8) Å]. No short contacts were observed in this structure; however, the two Cp* rings are very close to each other with distances between two methyl groups being ca 3.7 Å.

The difficulties encountered in crystallising dimer [**27a**][PF_6]$_2$ could originate from the presence of several isomers in solution as found in the ruthenium case, only one of which crystallised. Indeed, when the purple powders from the oxidation reactions were analysed by ^{31}P NMR spectroscopy to investigate their composition and purity, the spectra (Figure 4.7) contained four different signals at δ 89.36, 90.06, 90.45 and 91.00 for the purple powder from **2a**, and at δ 89.64, 90.32, 90.76 and 91.25 for the purple powder from **2b** with relative intensities being 16:58:16:10 and 14:64:14:8 (total intensity of 100), respectively. The hexafluorophosphate anions were also observed as septuplets at δ -142.99 ($^1J_{PF}$ = 708 Hz) and -142.94 ($^1J_{PF}$ = 708 Hz) for R = Ph and R = Tol, respectively.

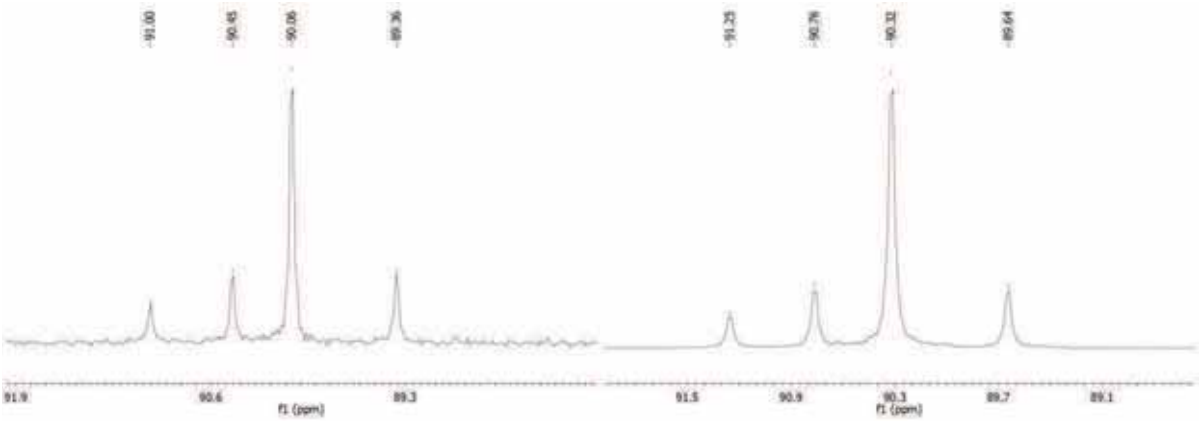

Figure 4.7. *^{31}P NMR spectra of the unknown purple products from the oxidation reactions of **2a** (left) and **2b** (right).*

The ^{31}P NMR spectra in the iron case were very similar to the ones from the ruthenium case[2], so it was assumed that a similar dimerisation of **2**$^{\bullet+}$ had occurred during the oxidation. Indeed, there is a good agreement between the ^{31}P NMR spectra and the dimeric structures proposed in Scheme 4.7: the major peak could correspond to the symmetrical dimer [**27a/b**][PF_6]$_2$ where dimerisation occurred by coupling of the $C_3{\equiv}C_4$ triple bonds of the carbon chain. The two other signals with equal intensities could be attributed to the unsymmetrical dimer [**28a/b**][PF_6]$_2$ where this time, dimerisation occurred by coupling of the $C_1{\equiv}C_2$ and $C_3{\equiv}C_4$ triple bonds. The last peak of low intensity which was not observed in the ruthenium case but is present in both iron examples, could correspond to a

symmetrical dimer [**29a/b**][PF_6]$_2$ where dimerisation occurred by coupling of two $C_1{\equiv}C_2$ triple bonds; its low percentage in the reaction mixture could originate from its unfavoured formation because of steric hindrance. Note that this last symmetrical dimer could also result from a C_2-C_2 coupling as recently reported by Whiteley et al. for related molybdenum complexes (see Scheme 4.3).[3] Additionally, the ^{31}P NMR chemical shifts are consistent with the presence of cationic iron-cumulene fragments[7].

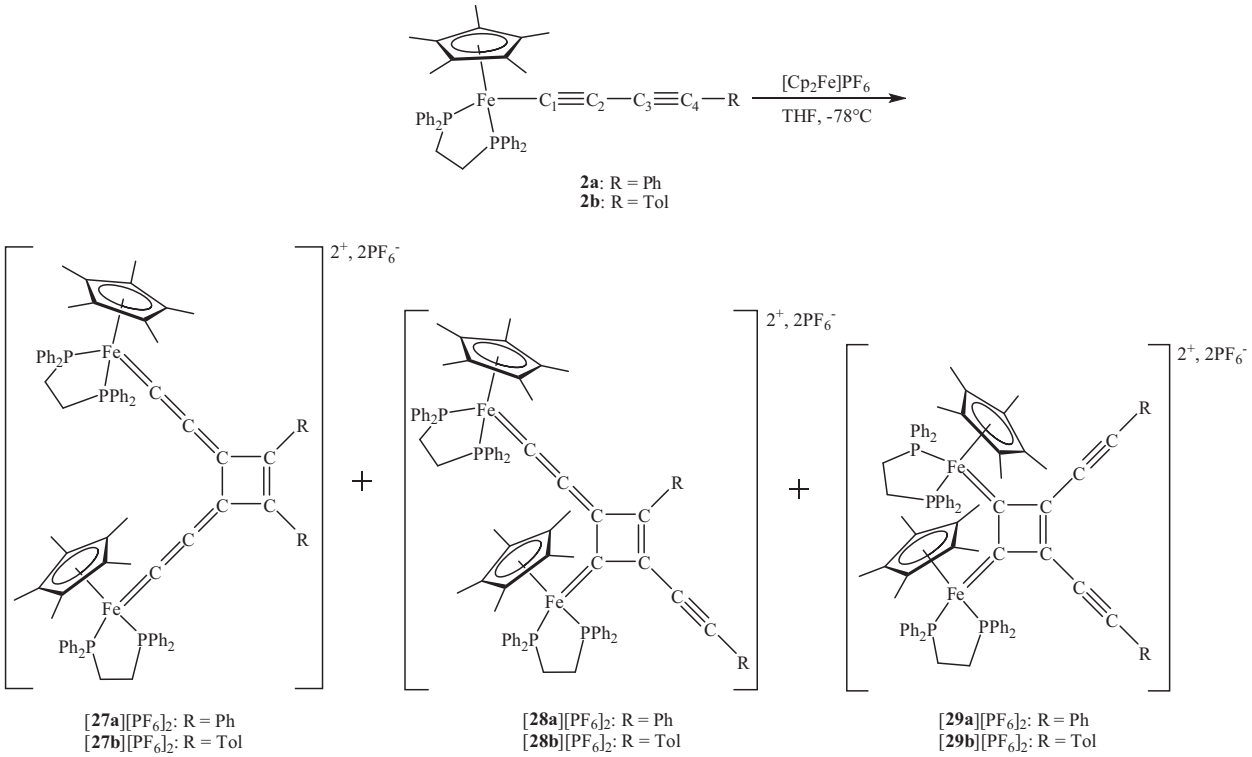

Scheme 4.7. *Hypothetical structures proposed for the oxidative dimerisation of **2a** and **2b**.*

However, this hypothesis was disproved by three different pieces of experimental and theoretical evidence:

i. Attempts to purify the mixtures from **2a** and **2b** were carried out without any success, fractional precipitations or crystallisations always affording exactly the same ratio of dimer signals in the ^{31}P NMR spectra. Even when crystals of the dimer [**27a**][PF_6]$_2$ from X-ray analyses were redissolved for ^{31}P NMR analysis, the spectrum was identical to the ones previously obtained from the starting mixtures (Figure 4.7-left). Unlike the ruthenium dimers which can be purified by chromatography, preparative t.l.c. carried out on the iron dimer mixtures afforded a purple band which, after being collected, was shown by ^{31}P

NMR to be the starting mixture, no noticeable separation of one specific isomer or decomposition being observed.

ii. The C≡C triple bonds characteristic of the hypothetical dimers [**28a/b**][PF_6]$_2$ and [**29a/b**][PF_6]$_2$ were not observed either in the IR or ^{13}C NMR spectra (see Section 4.3.3). In contrast to the ruthenium examples (Scheme 4.2) where the unsymmetrical dimers were characterised by IR [for R = Ph: ν(C≡C) 2169 and ν(CCC) 1933 cm^{-1}][2], no bands were observed in the 2000-2200 cm^{-1} range for the iron cases. No signature resonances of C(*sp*) nuclei (which usually are in the 60-100 ppm range) were found in the ^{13}C NMR spectra of the iron mixtures.

iii. DFT calculations of the three iron dimers (Scheme 4.7) made by Gendron from the Halet group in Rennes disfavour the existence of dimers [**28a/b**][PF_6]$_2$ and [**29a/b**][PF_6]$_2$. Relative energies, molecular orbital diagrams and orbital representations of the [**27a**][PF_6]$_2$ and [**28a**][PF_6]$_2$ ("cis" and "trans") dimers are represented in Figure 4.8. No calculations were carried out for dimer [**29a**][PF_6]$_2$ because it could not be simulated for steric hindrance reasons. The symmetrical dimer [**27a**][PF_6]$_2$ in its optimised geometry (close to the crystal structure geometry in Figure 4.6) was found to be 2.022 eV more stable than the unsymmetrical dimer "cis-[**28a**][PF_6]$_2$", and 1.877 eV more stable than the trans isomer. These values are very large in comparison with the values obtained for the analogous ruthenium dimers [**25a**][PF_6]$_2$ and [**25b**][PF_6]$_2$ (Scheme 4.2) where the symmetrical dimer is more stable than the unsymmetrical dimer by 0.611 eV[9]. This dramatic difference between the iron and ruthenium examples indicates that the formation and existence of the unsymmetrical iron dimer [**28a**][PF_6]$_2$ is largely disfavoured because of the very large energy difference between these dimers, formation of the symmetrical dimer [**29a**][PF_6]$_2$ being totally disfavoured. The stability difference between the iron dimers presumably results from steric hindrance. Note the ruthenium complexes **23** and **24** contain Cp ligands whereas the iron complexes **2a** and **2b** contain Cp* ligands which better sterically protect the C_α of the carbon chain (together with the bulky dppe ligands). Besides, the iron atom is smaller than the ruthenium atom, so that steric protection afforded by the ligands towards C_α is increased in the iron case.

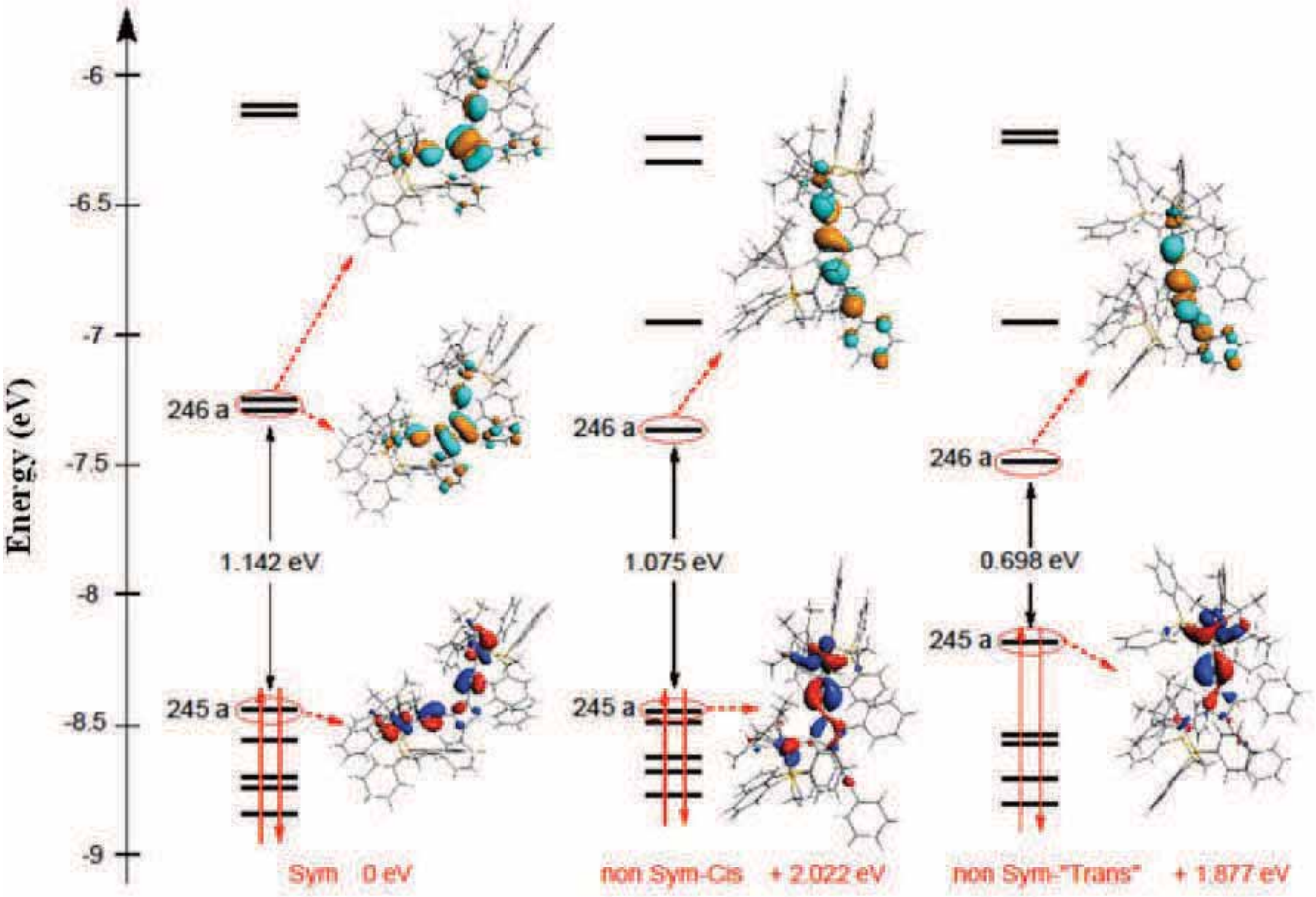

Figure 4.8. *Molecular orbital diagrams and frontier orbital representations of the dimers [**27a**][PF_6]$_2$ and [**28a**][PF_6]$_2$ ("cis" and "trans").*

Theoretical and experimental results thus disprove the proposed hypothesis (Scheme 4.7) for the formation of three different isomeric dimers [**27a/b**][PF_6]$_2$, [**28a/b**][PF_6]$_2$ and [**29a/b**][PF_6]$_2$ upon chemical oxidation of neutral complexes **2a** and **2b**. Based on the crystal structure of the dimer [**27a**][PF_6]$_2$, a new hypothesis was thus formulated: only dimers [**27a/b**][PF_6]$_2$ are formed during the oxidation reaction, however, different *rotamers* of [**27a/b**][PF_6]$_2$ exist due to the rotation of the metallic fragments at the end of the carbon chains. Equilibria or exchange of the different rotamers may explain the difficulties encountered to purify and separate them.

Exchange spectroscopy (EXSY)

In order to validate the rotamer hypothesis, an exchange ^{1}H NMR spectroscopy experiment was carried out. EXSY NMR is a 2D NMR method and pulse sequences used to obtain EXSY spectra are identical to those for NOESY sequences. In the EXSY (or NOESY) experiments, recorded spectra are symmetrical along the diagonal and correlation spots indicate exchange situations (or spatial proximity). The presence of rotamers in the iron case could be confirmed by the measurement of equilibria or exchange between the different conformations of the dimers [**27a/b**][PF_6]$_2$. The EXSY experiment was achieved with the dimer [**27b**][PF_6]$_2$, the protons of Cp* groups being used as probes to observe the exchange processes. Figure 4.9 shows the EXSY spectrum of dimer [**27b**][PF_6]$_2$ in the Cp* region. Circled spots clearly show that exchange occurred in solution between the Cp* signals being in the range of δ 1.34-1.56 (the small peak in the middle being an impurity). Correlation spots are also observed between the Me group of the tolyl and in the aromatic region confirming the exchange phenomenon.

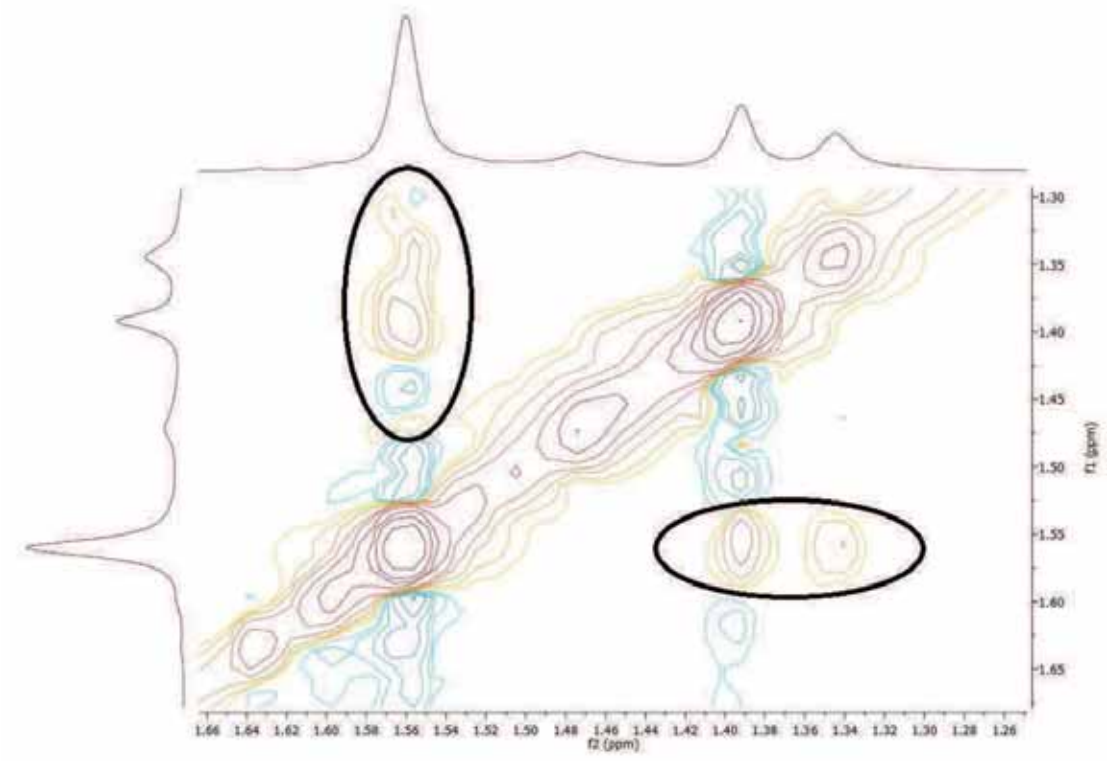

Figure 4.9. *EXSY spectrum of the dimer [**27b**][PF_6]$_2$: Cp* region.*

The exchange processes which were observed using EXSY NMR clearly validate the hypothesis of the formation of only the dimers [**27a/b**][PF_6]$_2$ by oxidative coupling. The dimers from the oxidations of compounds **2a** and **2b** being "pure", they were fully characterised by the usual spectroscopic methods and their physical properties were investigated.

4.3.3 Characterisation of the dimers [27a][PF_6]$_2$ and [27b][PF_6]$_2$

The ^{31}P NMR spectra shown in Figure 4.7 were reinterpreted on the basis that different rotamers were present, and the possible rotamers are presented in Scheme 4.8. The major peak at δ 90.06 in the spectrum of the dimer [**27a**][PF_6]$_2$ (and at δ 90.32 for [**27b**][PF_6]$_2$) probably corresponds to the rotamer [**27a1**][PF_6]$_2$ (and [**27b1**][PF_6]$_2$) which from the X-ray structure is the most stable. The Cp* ligands are on the same side fronting each other. The two equivalent signals at δ 89.36 and 90.45 (and at δ 89.64 and 90.76) could correspond to rotamer [**27a2**][PF_6]$_2$ (and [**27b2**][PF_6]$_2$) where one metal fragment has rotated by 180° making the two dppe ligands inequivalent. The last peak at δ 91.00 (and δ 91.25) could correspond to rotamer [**27a3**][PF_6]$_2$ (and [**27b3**][PF_6]$_2$) where both metal fragments have rotated by 180°, the two dppe ligands now being equivalent. This rotamer is probably slightly disfavoured because of the bulky dppe ligands fronting on the same side which induces large steric hindrance. In the ^{1}H NMR spectra, similar patterns containing the four different peaks with the same relative intensities were observed for the Cp* protons at δ 1.34 (× 2), 1.37 and 1.54 for rotamers [**27a**][PF_6]$_2$, and at δ 1.34, 1.36, 1.38 and 1.54 for rotamers [**27b**][PF_6]$_2$. In these two examples, the dppe-CH_2 protons were found between δ 2.40 and 3.65 as broad signals together with the Me of the tolyl groups (from rotamers [**27b**][PF_6]$_2$) which were found between δ 2.40 and 2.50.

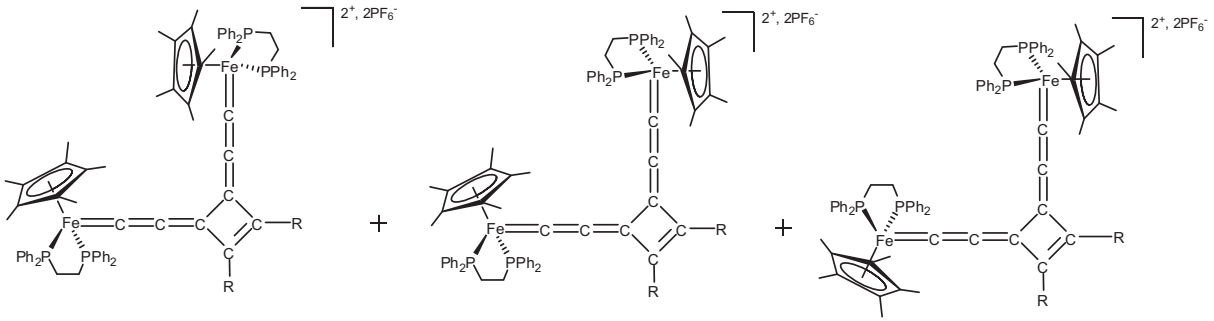

[**27a1**][PF_6]$_2$: R = Ph
[**27b1**][PF_6]$_2$: R = Tol

[**27a2**][PF_6]$_2$: R = Ph
[**27b2**][PF_6]$_2$: R = Tol

[**27a3**][PF_6]$_2$: R = Ph
[**27b3**][PF_6]$_2$: R = Tol

Scheme 4.8. *Selected rotamers of [27a/b][PF_6]$_2$.*

The energies of the different rotamers (in their optimised geometries) in the singlet state have been calculated by Gendron, starting from the energy of the rotamer found in the crystal structure (rotamer [**27a1**][PF_6]$_2$). This lowest energy is -1152.954 eV: successively changing the angle between the two metal fragments by 45, 90 and 180°, the last rotation corresponding to rotamer [**27a2**][PF_6]$_2$, gives energies of -1150.164, -1151.976 and -1152.848 eV, respectively. The energy of rotamer [**27a3**][PF_6]$_2$ where the two metal fragments rotated of 180° in comparison with rotamer [**27a1**][PF_6]$_2$, was calculated to be -1152.652 eV. The theoretical results show that the rotamer energies are considerably dependent on rotation of the metal fragment end-caps, with ΔE values being between 0.106 and 2.790 eV, in comparison with the most stable rotamer [**27a1**][PF_6]$_2$, for the five examples calculated. The smaller gaps of 0.106 and 0.302 eV being between the three proposed rotamers [**27a1**][PF_6]$_2$, [**27a2**][PF_6]$_2$ and [**27a3**][PF_6]$_2$ suggests that the three rotamers observed by ^{31}P NMR spectroscopy might be the most stable conformations.

Dimers [**27a**][PF_6]$_2$ and [**27b**][PF_6]$_2$ were further characterised by IR and ^{13}C NMR spectroscopy. In the IR spectra (Figure 4.10), one strong band was observed at 1888 cm^{-1} together with a medium band at 1968 cm^{-1} for [**27a**][PF_6]$_2$ and [**27b**][PF_6]$_2$ while the P-F bands of the PF_6 anions were observed at ν(PF) 839 cm^{-1} in both cases. In the literature, allenylidene ν(CCC) bands in organometallic complexes [M]{=C=C=C(R)R'} can be found over a large range between 1865 and 2200 cm^{-1}, depending on the metal, the ligands attached to the metal atom and especially the nature of the R and R' end groups[8]. However, the ν(CCC) band in [Fe(=C=C=CPh_2)(dppe)Cp*][PF_6][7] is found at 1896 cm^{-1} which suggests that the band at 1888 cm^{-1} is ν(CCC) of the dimers [**27a/b**][PF_6]$_2$. The medium band at 1968 cm^{-1} may be due to the restricted rotation in the allenylidene fragments giving the different rotamers[10].

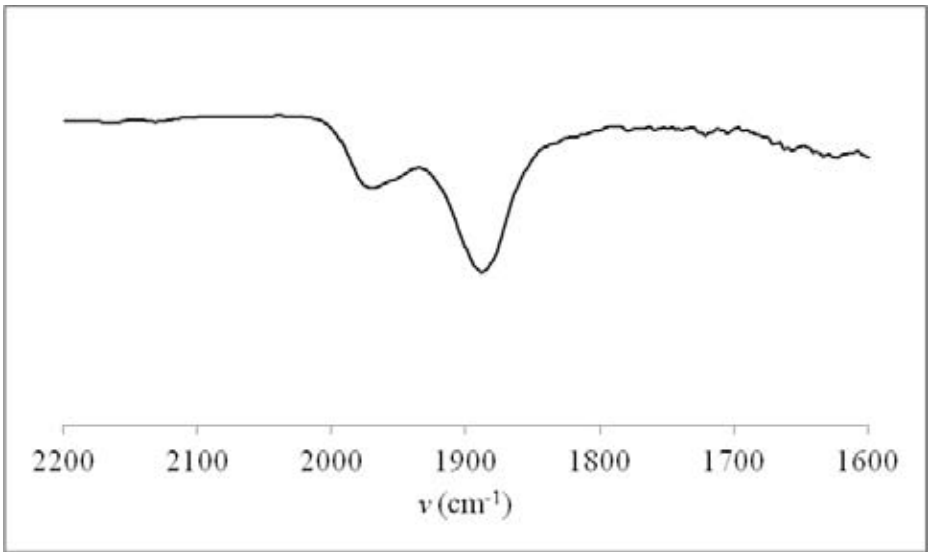

Figure 4.10. *IR spectrum of the dimer [**27a**][PF$_6$]$_2$.*

In the ^{13}C NMR spectrum of dimer [**27a**][PF$_6$]$_2$ (the ^{13}C NMR spectrum of dimer [**27b**][PF$_6$]$_2$ is similar and is not illustrated in this section), patterns analogous to the ^{31}P NMR, containing four signals of specific intensities which are characteristic of the three rotamers, are observed in the entire spectrum. The four signals corresponding to the C$_\alpha$ carbons (Figure 4.11) were found at δ 278.84, 281.05, 283.25 and 283.46 as triplets (the two last triplets being superimposed) with $^2J_{CP}$ = 36 Hz in each case.

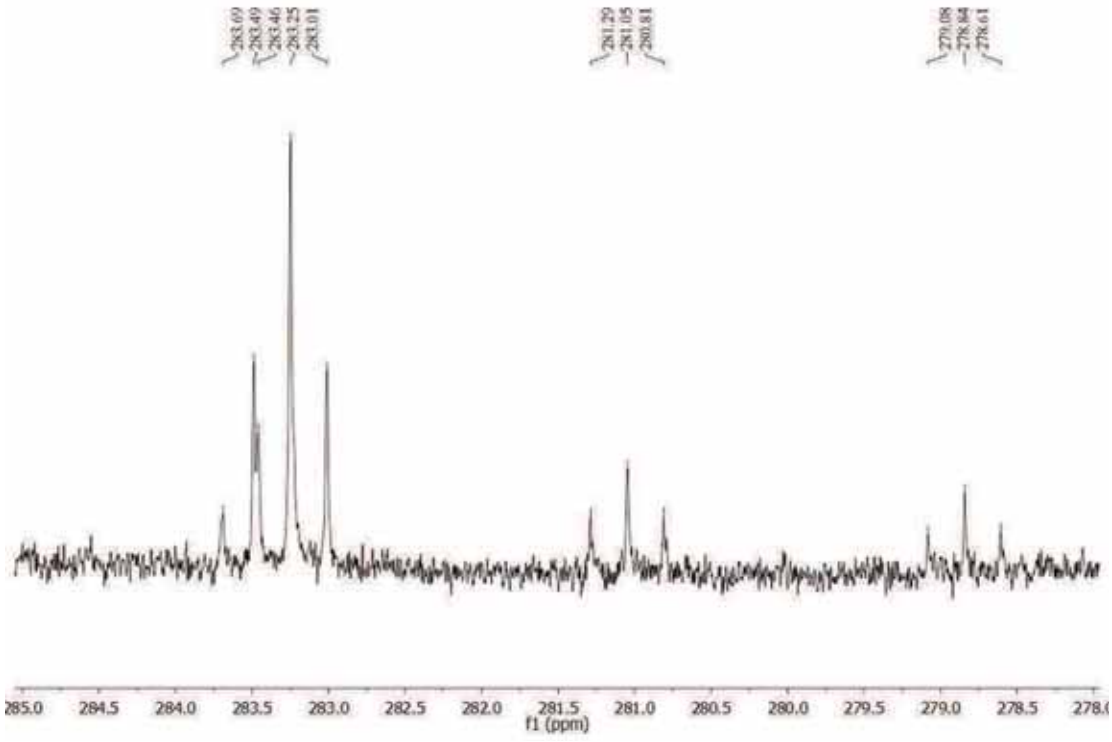

Figure 4.11. *^{13}C NMR spectrum of [**27a**][PF$_6$]$_2$: C$_\alpha$ pattern.*

Two similar patterns of singlets were observed at δ 180.11, 180.63, 181.00, 181.95 and 146.67, 147.51, 147.91, 149.42 ppm (Figure 4.12) always including one intense peak, two medium peaks of similar intensity together with one small peak. These resonances were assigned to the C_γ and a quaternary aromatic carbon (for the patterns centred at 180 and 147 ppm respectively). The pattern corresponding to the C_β resonances was observed around 205 ppm but unfortunately was overlapped by the carbonyl resonance of the deuterated acetone. Chemical shifts observed for the C_α, C_β and C_γ of the allenylidene fragments are consistent with values previously obtained for iron allenylidene complexes[7].

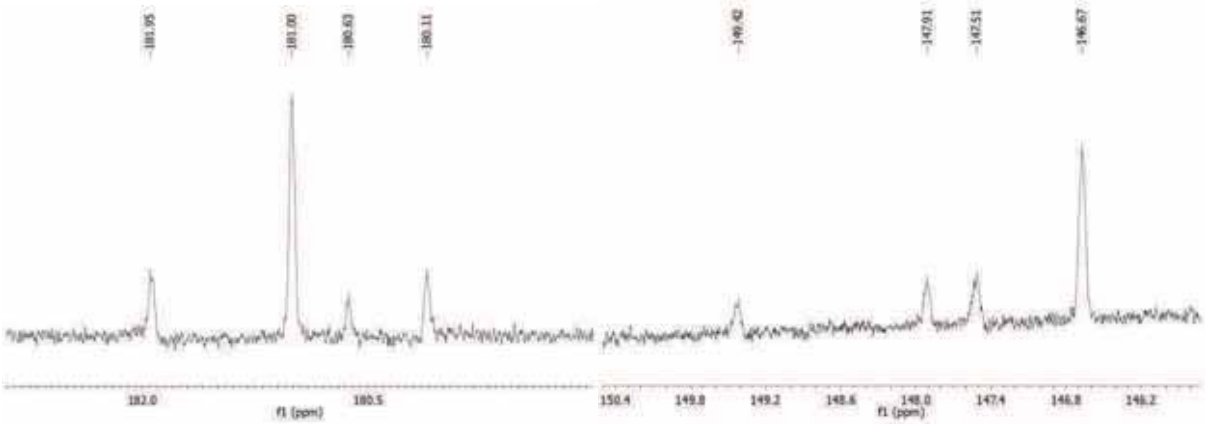

Figure 4.12. *^{13}C NMR spectrum of [**27a**][PF_6]$_2$: C_γ and quaternary aromatic carbon patterns.*

Additionally, resonances of the Cp* ligands were also observed as singlets in patterns (Figure 4.13) at δ 102.39, 102.56, 103.09 and 103.11 for the C_5Me_5 carbon atoms and at δ 10.36, 10.43, 10.64 and 10.78 for the Me carbon atoms. The chemical shifts around 100 ppm for the Cp* ring carbon atoms are characteristic of cationic Fe(II) complexes[11].

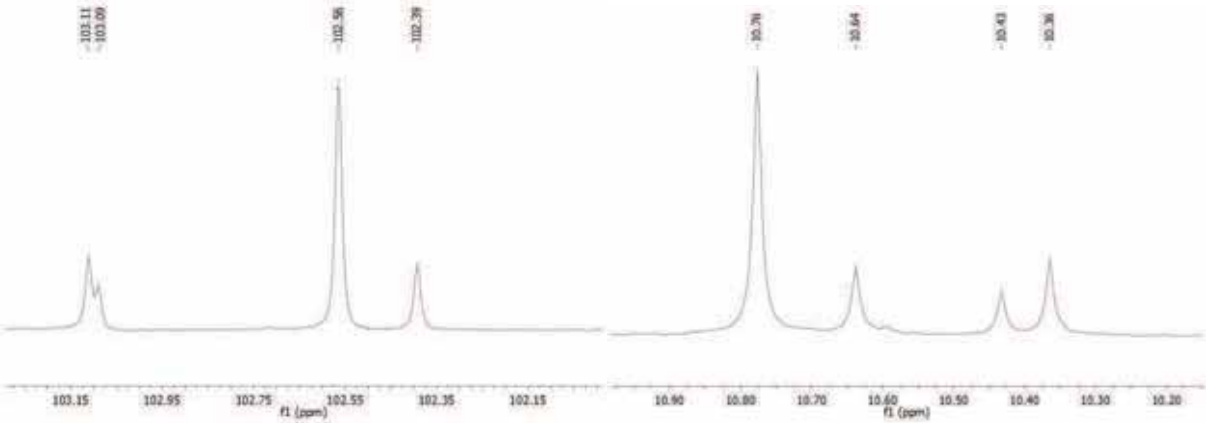

Figure 4.13. *^{13}C NMR spectrum of [**27a**][PF_6]$_2$: $\underline{C}_5Me_5$ (left) and $C_5\underline{Me}_5$(right) patterns.*

In summary, using ^{13}C NMR and IR spectroscopy, the allenylidene fragments in the dimers [**27a**][PF_6]$_2$ and [**27b**][PF_6]$_2$ have been successfully characterised.

4.3.4 Supporting DFT calculations

With the aim of studying and understanding the oxidative coupling reaction affording the iron dimers, DFT calculations were made by Gendron from the Halet group in Rennes. DFT calculations for the ruthenium examples (Section 4.1.1) were extended to the similar iron chemistry described in this Chapter. Atomic spin densities of the 17-e species [Fe(C≡CC≡CPh)(dppe)Cp*]$^{\bullet+}$ (**2a**$^{\bullet+}$) were calculated, the values and representations of the atomic spin densities being shown in Figure 4.14. Very large atomic spin density (0.70) was found on the iron atom and is characteristic of Fe(III) complexes[12]. The atomic spin densities on the C_4 carbon bridge were also surprisingly large on the C_2 (0.20) and C_4 (0.17) atoms, which is very unusual for 17-e iron species. Additionally, the atomic spin densities on the other carbon atoms of the chain were quasi-null (-0.06 and -0.05) whereas small atomic spin density values were found on the *o*- and *p*-carbons of the phenyl end group. In contrast to the [Fe(C≡CR)(dppe)Cp*]$^{\bullet+}$ complexes[6], where the unpaired electron is mostly localised on the iron atom and only weakly on the carbon chain, the unpaired electron is strongly delocalised on the C_4 chain of **2a**$^{\bullet+}$. Comparison with the ruthenium example **23**$^{\bullet+}$ shows no significant changes in the atomic spin densities of the carbon chain, especially on the C_2 and C_4 carbons which conserved quasi-similar values (0.22 to 0.20 for C_2 and 0.22 to 0.17 for C_4). However, the atomic spin density on the metal atom is considerably increased when ruthenium is replaced by iron (0.33 to 0.70).

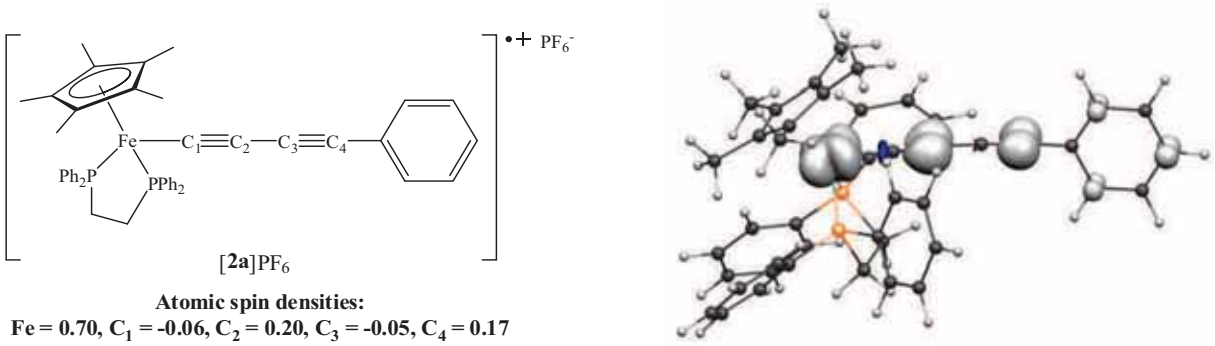

Figure 4.14. *Calculated (left) and representation (right) of the atomic spin densities in [2a]PF_6.*

These theoretical calculations support the experimental results obtained in this Chapter and contribute to the proposed mechanism (Scheme 4.9) for the formation of the dimer [**27a**][PF_6]$_2$ (and thus [**27b**][PF_6]$_2$). The first step is a radical coupling between C_4 of two molecules of **2a**$^{\bullet+}$. Considering the atomic spin densities, the C_4-C_4 radical coupling is not the most favoured compared with the C_2-C_2 and C_2-C_4 couplings. However, steric hindrance from the bulky dppe and Cp* ligands prevent the C_2-C_2 and C_2-C_4 couplings, leaving the C_4-C_4 coupling as the most facile route. In comparison with the ruthenium examples where both C_2-C_4 and C_4-C_4 couplings occurred, the Cp* ligand in the iron cases (which is replaced by Cp in the ruthenium examples), plays an important role in protecting C_2 from radical coupling. After the C_4-C_4 coupling, formation of a bis-butatrienylidene intermediate is proposed; this species is highly unstable, intramolecular cyclisation occurring instantaneously to form the cyclobutene centre in dimer [**27a**][PF_6]$_2$.

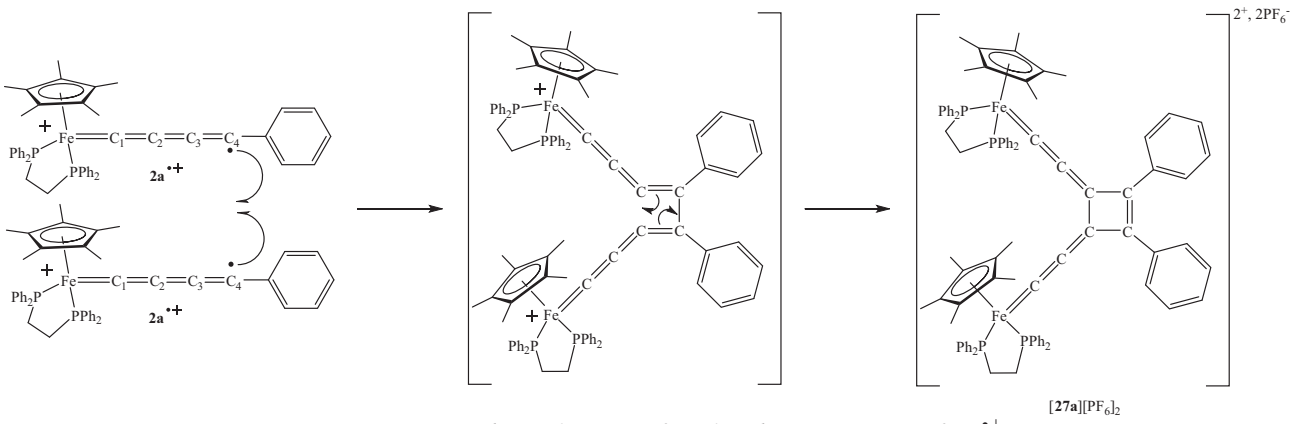

Scheme 4.9. *Proposed mechanism for the dimerisation of* ***2a***$^{\bullet+}$.

DFT calculations were also carried out on dimer [**27a**][PF_6]$_2$ of which the energy diagram is shown in Figure 4.8 (Section 4.3.2) with selected frontier orbital representations in Figure 4.15. Atomic percentages of the frontier molecular orbitals on the different atoms in [**27a**][PF_6]$_2$ are collected in Table 4.3. As expected, these indicate that the HOMOs (245a, 244a and 243a) mostly have a metallic character with large percentages on the iron atoms. In contrast, the LUMOs (246a and 247a) mostly have an organic character, especially localised on the cyclobutene ring: the atomic percentages on four carbons C_5, C_6, C_7 and C_8 sum to 39 and 37% for 246a and 247a, respectively.

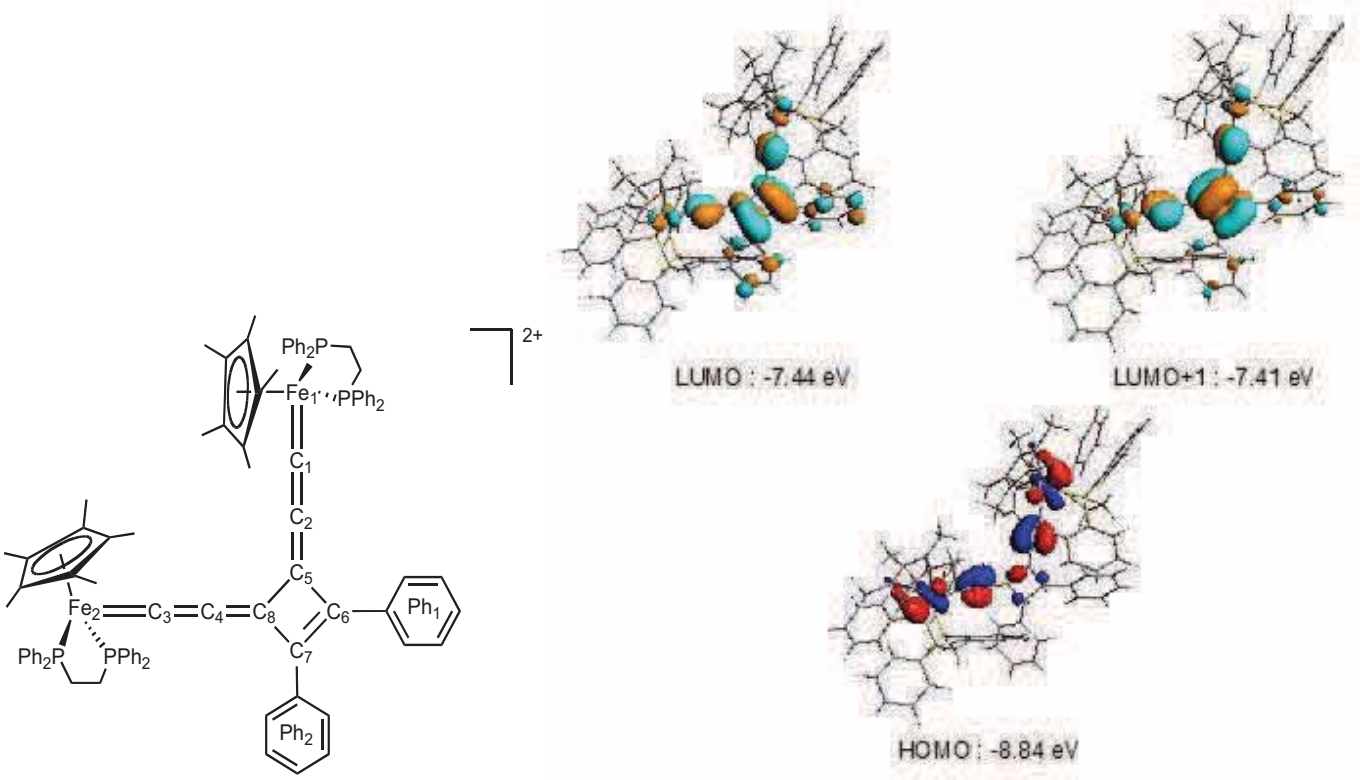

Figure 4.15. *Selected frontier orbital representations of dimer [27a][PF$_6$]$_2$.*

Table 4.3. Atomic percentage (%) in molecular orbitals of [**27a**][PF$_6$]$_2$.

	Frontier orbitals for dimer [**27a**][PF$_6$]$_2$				
	247a	246a	245a	244a	243a
E	7.26	-7.28	-8.45	-8.57	-8.70
occ	0	0	2	2	2
% Fe_1	11	7	29	33	33
% Fe_2	10	7	29	33	33
% Cp^*	0	0	1	3	2
% C_1	9	6	1	0	0
% C_2	0	0	8	2	2
% C_3	9	6	1	0	0
% C_4	0	0	7	2	2
% C_5	12	5	0	0	0
% C_6	6	13	0	0	0
% C_7	7	13	0	0	0
% C_8	12	8	0	0	0
%Ph_1	2	6	0	0	0
%Ph_2	4	6	0	0	0

4.3.5 Electrochemistry

The cyclic voltammogram of the dimer [**27b**][PF_6]$_2$ was recorded (using similar conditions to section 2.3.4) in order to determine its redox potentials and to investigate electronic communication in the molecule. Redox potentials of dimer [**27b**][PF_6]$_2$ are collected in Table 4.4.

Table 4.4. Electrochemical potentials of [**27b**][PF_6]$_2$.

	E^0_1 (V)	E^0_2 (V)	E^0_3 (V)	E^0_4 (V)
[**27b**][PF_6]$_2$	-0.94	-0.59	+1.07	+1.25

In the CV of [**27b**][PF_6]$_2$, four redox processes were observed, with two oxidation waves and two reduction waves. The reversibility of the two oxidation waves at E^0_3 = +1.07 and E^0_4 = +1.25 V could not be determined because of their positions relative to the solvent front while the two reduction waves centred at E^0_1 = -0.94 and E^0_2 = -0.59 V were fully reversible (i_a/i_c = 1). As the HOMOs have very strong metallic character, the two oxidation waves are attributed to the two $Fe(II)^+ \rightarrow Fe(III)^{2+}$ processes at the metal centres, the species **27b**$^{3+}$ and **27b**$^{4+}$ being formed successively. The separation of two waves (ΔE = 0.18 V) indicates that some electronic communication exists between the two metal centres. The two reduction processes were attributed to the reduction of the carbon chain and more especially of the cyclobutene ring, due to the large contribution to the LUMO character. Upon reduction, the monocationic and neutral dimers are successively formed at the electrode surface. Fast decomposition of the dimer [**27b**][PF_6]$_2$ was observed during the electrochemical experiment as indicated by the appearance of weak redox processes which increased in intensity in successive runs.

4.3.6 EPR spectroscopy

The electronic behaviour of the iron dimer [**27a**][PF_6]$_2$ (dimer [**27b**][PF_6]$_2$ was not examined by EPR) was investigated by EPR studies. The species intermediate between the different rotamer conformations during the exchange could be a triplet state which would be EPR-active. Surprisingly, dimer [**27a**][PF_6]$_2$, which was fully characterised by NMR spectroscopy, was EPR-active, as illustrated in Figure 4.16.

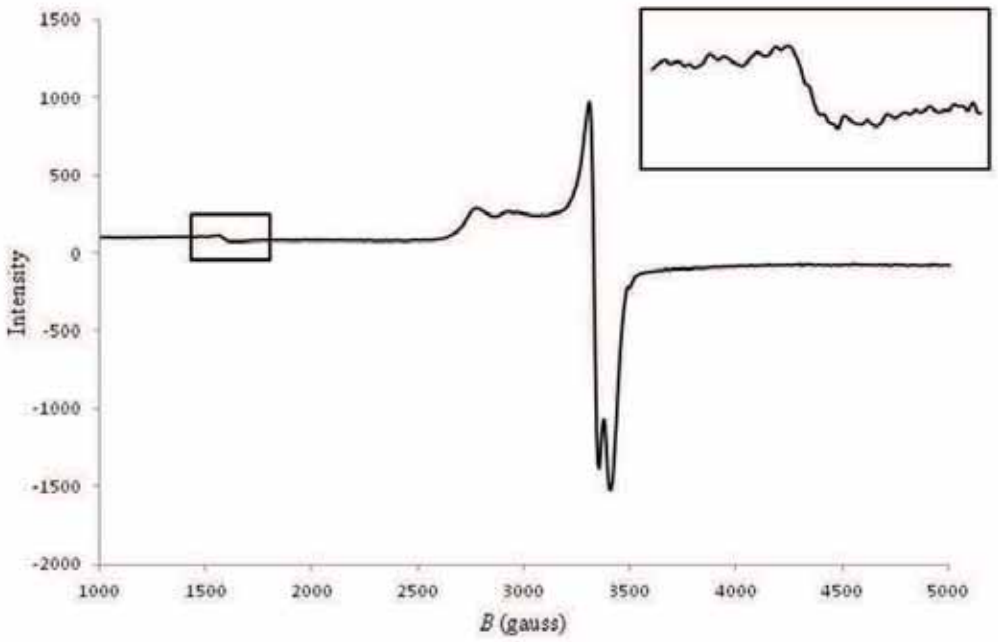

Figure 4.16. *EPR spectrum of the dimer [**27a**][PF_6]$_2$ in CH_2Cl_2 at 67 K.*

In the EPR spectrum, an intense signal characteristic of Fe(III) was observed with the three g-tensors being at g_1 = 2.443, g_2 = 2.035 and g_3 = 1.989 (Δg = 0.454 and g_{iso} = 2.156). Additionally, the anisotropy Δg = 0.454 is very large indicating strong metallic character of the SOMOs (because the unpaired electrons are mostly localised on the metallic atoms). The half-field signal centred at g = 4.263 indicates the presence of a biradical which is consistent with the structure of dimer [**27a**][PF_6]$_2$ having a triplet state (Figure 4.17). This triplet state could possibly be the intermediate in the equilibria between the different rotamers, and has been trapped by freezing the dichloromethane solution at 67 K; however, its stability might be low due to the unstable cyclobutadiene ring formally present in this mesomer. The triplet state could also exist as an open structure similar as the

structure of the intermediate compound in Scheme 4.9, which might be more stable than with a cyclobutadiene ring.

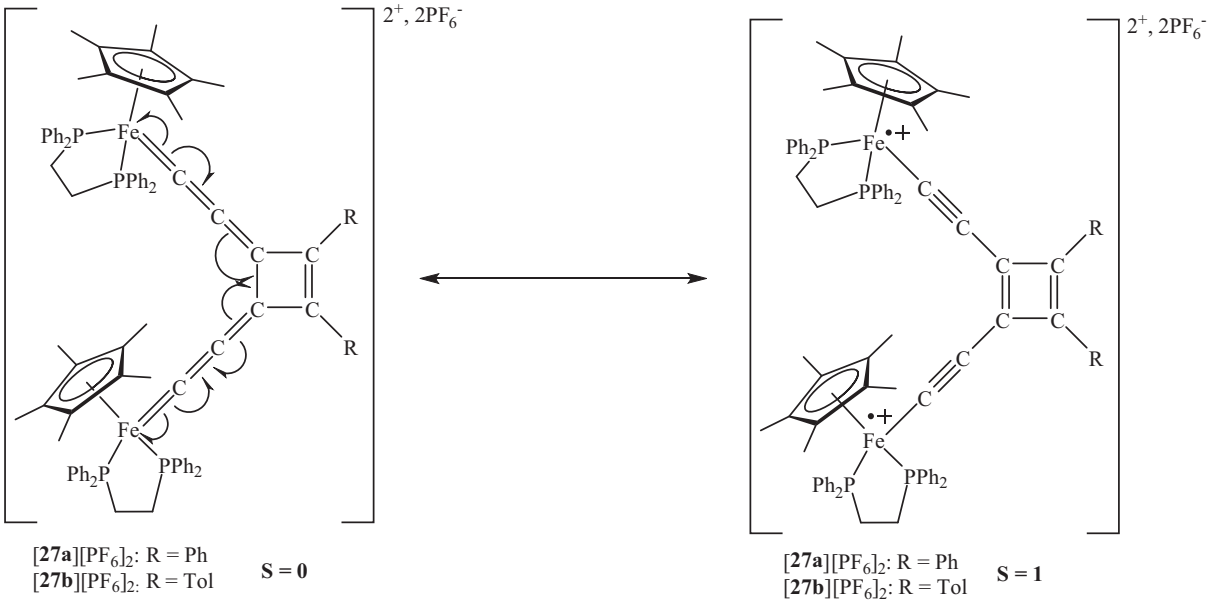

Figure 4.17. *Possible limit resonance structures for the singlet and triplet states in dimer [27a/b][PF$_6$]$_2$.*

In order to investigate the stability of the triplet state of dimer [**27a**][PF_6]$_2$, the energy of the triplet state of rotamer [**27a1**][PF_6]$_2$ (which is the most stable in the singlet state [*E*(singlet) = -1152.954 eV]) was computed by Gendron. The triplet state was found to be 0.952 eV less stable [*E*(triplet) = -1152.002 eV] than the singlet state, which is a large difference. However, energies of other conformations (rotations of the end-capped metal fragments) in the triplet state have not been calculated yet. Thus, the triplet state could be more stable with energies close to the singlet state in other conformations as it has been observed previously that the energies are strongly dependent on the orientations of the metal fragments.

4.3.7 Conclusion

Investigations have been carried out on the oxidation of the new diynyl complexes **2a** and **2b** synthesised in Chapter 2. These reactions afforded the new iron dimers [**27a/b**][PF_6]$_2$ containing two allenylidene fragments linked to a cyclobutene centre. Unlike the ruthenium examples, where oxidation gave two different dimers, one symmetrical and one unsymmetrical, only one symmetrical dimer resulting from C_4-C_4 radical coupling is

formed in the iron cases. However, an equilibrium mixture of three rotamers was observed and characterised, their interconversion being slow on the ^{1}H NMR time scale. The original dimers [**27a/b**][PF_6]$_2$ also showed good electronic communication between the two iron sites (K_c = 1.3 × 10^3). Surprisingly, replacing the metal atoms (Ru by Fe) in the diynyl 17-e species does not significantly change the atomic spin densities on the carbon chain. In contrast, replacing the Cp ligand by a bulkier Cp* dramatically changes the reactivity of the diynyl 17-e species which is sterically protected from couplings to C_2.

Structures for the rotamers were proposed and their relative stabilities are largely dependent on the orientations of the metal end-caps. Additionally, a possible intermediate in the rotamer exchange processes may be the triplet state which has been characterised by EPR spectroscopy.

Other diynyl complexes of general formula M(C≡CC≡CR)(dppe)Cp* with M = Fe, Ru and R = $SiMe_3$, H, $AuPPh_3$ were also chemically oxidised in order to obtain dimers with different R groups. However, in these reactions fast decomposition of the 17-e species was observed and no products could be isolated and characterised.

Most of the results described in this Chapter were rationalised by DFT calculations achieved by Gendron from the Halet group at the Université de Rennes 1.

Experimental

General experimental conditions are detailed in Chapter 2, Experimental section.

Spectro-electrochemistry: Spectro-electrochemistry of complex **2a** was carried out in dichloromethane at room temperature with 0.2 M of $[NBu^n_4]PF_6$ (0.1 M for the Near-IR range) as the supporting electrolyte using a platinum grid as the working electrode, one platinum wire as the counter electrode and one silver wire as the reference electrode.
Reagent: $[FeCp_2]PF_6$[13] was prepared using the cited methods.

Synthesis of [{Cp*(dppe)Fe=C=C=}$_2${μ-C_4Ph_2}][PF_6]$_2$ ([27a][PF_6]$_2$)

Fe(C≡CC≡CPh)(dppe)Cp* **2a** (100 mg, 0.14 mmol) and $[FeCp_2]PF_6$ (46 mg, 0.14 mmol) were dissolved in THF (10 ml) at -78°C when the colour changed immediately from orange to deep green. After stirring 1 h at -78°C, the solution was slowly allowed to warm up to room temperature over a period of 5 h. When the temperature reached -35°C, the colour of the solution changed from deep green to deep purple. After stirring 1 h at room temperature, pentane (60 ml) was added to the solution and the resulting precipitate was filtered off and washed with pentane (3 × 10 ml) to afford [{Cp*(dppe)Fe=C=C=}$_2${μ-C_4Ph_2}][PF_6]$_2$ [**27a**][PF_6]$_2$ (74 mg, 61%) as a deep purple powder. Anal. Calcd for $C_{92}H_{88}F_{12}P_6Fe_2.CH_2Cl_2$: C, 61.91; H, 5.03. Found: C, 62.02; H, 5.24. IR (KBr): ν(CCC) 1968, 1888; ν(P-F) 839 cm^{-1}. ^{1}H NMR (d_6-acetone, 600 MHz): δ 1.34, 1.37 (2 × s, 13H, Cp*), 1.54 (s, 17H, Cp*), 2.51, 2.94, 3.44, 3.65 (4 × s (br), 8H, PCH_2), 6.93-7.69 (m, 50H, Ph). ^{13}C NMR (d_6-acetone, 150 MHz): δ 10.36, 10.43, 10.64, 10.78 (4 × s, C_5Me_5), 29.57-32.33 (m, dppe), 102.39, 102.56, 103.09, 103.11 (4 × s, C_5Me_5), 126.75-135.52 (m, Ph), 146.67, 147.51, 147.91, 149.42 (4 × s, Ph), 180.11, 180.63, 181.00, 181.95 (4 × s, C_γ), 202.59, 205.46, 205.62 (3 × s, C_β), 278.84, 281.05, 283.25, 283.46 (4 × t, 4 × $^2J_{CP}$ = 36 Hz, C_α). ^{31}P NMR (d_6-acetone, 121 MHz): δ 89.36, 90.06, 90.45, 91.00 (4 × s), -142.99 (septet, $^1J_{PF}$ = 708 Hz, PF_6). ES-MS (*m/z*): calcd for $C_{92}H_{88}P_4Fe_2$ 714.2262, found 714.2274 $[M]^{2+}$; calcd for $C_{92}H_{89}P_4Fe_2$ 1429.4608, found 1429.4539 $[M + H]^+$; calcd for $C_{92}H_{88}F_6P_5Fe_2$ 1573.4172, found 1573.4097 $[M + PF_6]^+$.

Synthesis of [{Cp*(dppe)Fe=C=C=}$_2${μ-$C_4(C_6H_4Me)_2$}][PF_6]$_2$ ([27b][PF_6]$_2$)

Similarly, from Fe(C≡CC≡CC_6H_4Me)(dppe)Cp* **2b** (100 mg, 0.14 mmol) and [$FeCp_2$]PF_6 (45 mg, 0.14 mmol) was obtained [{Cp*(dppe)Fe=C=C=}$_2${μ-$C_4(C_6H_4Me)_2$}][PF_6]$_2$ [**27b**][PF_6]$_2$ (70 mg, 57%). IR (KBr): ν(CCC) 1968, 1888; ν(P-F) 839 cm^{-1}. ^{1}H NMR (d_6-acetone, 400 MHz): δ 1.34 (s, 4H, Cp*), 1.36 (s, 4H, Cp*), 1.38 (s, 3H, Cp*), 1.54 (s, 19H, Cp*), 2.08, 2.28, 2.38 (3 × s, 6H, C_6H_4*Me*), 2.48, 2.97, 3.45, 3.64 (4 × m, 8H, PCH_2), 6.84-7.67 (m, 48H, Ph). ^{13}C NMR (d_6-acetone, 100 MHz): δ 10.23, 10.27, 10.41, 10.55 (4 × s, C_5*Me*$_5$), 21.91(m, C_6H_4*Me*), 29.27-32.61 (m, dppe), 101.99, 102.14, 102.71, 102.75 (4 × s, *C*$_5$Me$_5$), 126.77-135.65 (m, Ph), 140.99, 143.32, 143.42, 143.64 (4 × s, Ph), 180.37, 180.62, 181.98, 181.70 (4 × s, C_γ), 200.10, 203.10, 203.16, 203.73 (4 × s, C_β), 278.07, 280.45, 282.58 (3 × t, 3 × $^2J_{CP}$ = 36 Hz, C_α). ^{31}P NMR (d_6-acetone, 121 MHz): δ 89.64, 90.32, 90.76, 91.25 (4 × s), -142.94 (septet, $^1J_{PF}$ = 708 Hz, PF_6).

References

1. Rigaut, S.; Le Pichon, L.; Daran, J.-C.; Touchard, D.; Dixneuf, P. H., *Chem. Commun.* **2001**, 1206-1207.
2. Bruce, M. I.; Jevric, M., *unpublished results*.
3. Brown, N. J.; Collison, D.; Edge, R.; Fitzgerald, E. C.; Low, P. J.; Helliwell, M.; Ta, Y. T.; Whiteley, M. W., *Chem. Commun.* **2010,** *46*, 2253-2255.
4. Semenov, S. N.; Blacque, O.; Fox, T.; Venkatesan, K.; Berke, H., *Angew. Chem. Int. Ed.* **2009,** *48*, 5203 –5206.
5. Denis, R.; Toupet, L.; Paul, F.; Lapinte, C., *Organometallics* **2000,** *19*, 4240-4251.
6. Paul, F.; Toupet, L.; Thépot, J.-Y.; Costuas, K.; Halet, J.-F.; Lapinte, C., *Organometallics* **2005,** *24*, 5464-5478.
7. Argouarch, G.; Thominot, P.; Paul, F.; Toupet, L.; Lapinte, C., *C. R. Chimie* **2003,** *6*, 209-222.
8. Bruce, M. I., *Chem. Rev.* **1998,** *98*, 2797-2858.
9. Gendron, F.; Costuas, K.; Halet, J.-F., *personal communication*.
10. Guillaume, V.; Thominot, P.; Coat, F.; Mari, A.; Lapinte, C., *J. Organomet. Chem.* **1998,** *565*, 75-80.
11. Bitcon, C.; Whiteley, M. W., *J. Organomet. Chem.* **1987,** *336*, 385-392.
12. Paul, F.; Ellis, B. G.; Bruce, M. I.; Toupet, L.; Roisnel, T.; Costuas, K.; Halet, J.-F.; Lapinte, C., *Organometallics* **2006,** *25*, 649-665.
13. Connelly, N. G.; Geiger, W. E., *Chem. Rev.* **1996,** *96*, 877-910.

Chapter Five

Syntheses, Characterisation and Properties of $[\{Cp'(dppe)M\}(C{\equiv}CC{\equiv}CC{\equiv}C)\{M(dppe)Cp'\}]^{n+}$ (n = 0, 1, 2; M = Fe, Ru; Cp' = Cp, Cp*)

5.1 Introduction

Mixed-valence complexes containing transition metals linked by organic bridges have attracted much attention over the last few decades. In order to study and understand electron transfer over nanometer distances, molecules with many different organic bridges and different transition metal fragments have been studied. It has been demonstrated that the strength of the electronic coupling is dependent on the organic bridges and the nature of the transition metal fragments. The "C≡C" units are one of the most widely used motifs for the construction of rigid-carbon bridges, and often play the role of connectors between the metal centres and organic or organometallic R groups (Scheme 5.1).

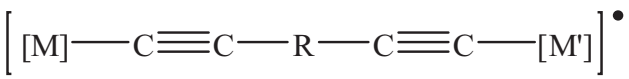

Scheme 5.1

For symmetrical complexes (M = M'), many kinds of R groups have been studied, including such aromatic groups as benzene (*para*-[1] or *meta*-substituted[2]), thiophene[3], naphthalene[4], anthracene[5], biphenyl[6] and dithienylethene[7] which, together with the ethynyl fragments, form good electron-conducting bridges and typically afford class II or class III mixed-valence systems. Less conducting R groups such as saturated hydrocarbon bridges[8], silicon chains[9] and carboranes[10] have also been studied, most of the time affording weakly coupled class II mixed-valence systems. A wide range of organometallic R groups have also been studied such as ferrocene[11], biferrocene[12], $Pd(PEt_3)_2$[13], Hg[14] and other more complex fragments[15]; these systems have most of the time been described as class I (when the organometallic R group acts as an insulator) or class II mixed-valence systems. A few unsymmetrical mixed-valence complexes containing two different end-capping metal fragments (M ≠ M') with R = 1,4-C_6H_4 have also been reported[16], and have been described as class II mixed-valence systems. However, pure polyyne bridges are well known as one of the most efficient linkers in promoting electronic interactions between two metal fragments, the electronic coupling decreasing when the number of "C≡C" units increases.

5.1.1 Mixed-valence complexes containing C_2 and C_4 chains

Only a few examples of symmetrical mixed-valence complexes containing a C_2 bridge have been prepared, fully characterised and studied. One of them, the dimanganese complex $[\{(MeC_5H_4)(dmpe)Mn\}_2(\mu\text{-}C_2)]PF_6$, has been described by Berke et al.[17]. Extremely strong electronic coupling of the manganese end groups has been measured by electrochemistry ($K_c = 8.6 \times 10^{16}$), which is consistent with $[\{(MeC_5H_4)(dmpe)Mn\}_2(\mu\text{-}C_2)]PF_6$ being a class III delocalised mixed-valence system. In contrast, the ruthenium mixed-valence complex $[\{Cp(dppe)Ru\}_2(\mu\text{-}C_2)]PF_6$, which has been described by Bruce et al.[18], also exhibits strong electronic interactions by electrochemistry ($K_c = 7 \times 10^{13}$); however, the low energy band observed in the Near-IR range was attributed to a Ru(d)-[Ru(d)/$C_2(\pi)$]* transition rather than an intervalence charge transfer (IVCT) transition on the basis of DFT calculations. Therefore, electron transfer in $[\{Cp(dppe)Ru\}_2(\mu\text{-}C_2)]PF_6$ has not been interpreted based on Hush theory[19] due to the non-innocent redox character of the ethyndiyl ligand[2c, 20].

Symmetrical mixed-valence complexes containing a butadiyndiyl bridge of general formula $[\{M\}_2(\mu\text{-}C{\equiv}CC{\equiv}C)]^{\bullet+}$ (Scheme 5.2) have been widely studied with a large range

of metal fragments such as $Re(NO)(PPh_3)Cp^*$[21], $Fe(dppe)Cp^*$[22], $Ru(PP)Cp'$ [PP = $(PPh_3)_2$, dppe, dppm; Cp' = Cp, Cp*][23], $Mn(dmpe)_2I$[24] and $W(dppe)_2I$[25]. Depending on the nature of the metal, the butadiyndiyl unit is a more or less efficient bridge in promoting electronic interactions between metal centres. These mixed-valence complexes generally exhibit characteristic intense low energy bands in the Near-IR range which were attributed to IVCT transitions. Most of these complexes were classified as class III delocalised mixed-valence complexes where the unpaired electron is fully delocalised between the two metal centres, giving very large electronic coupling parameters, especially in the ruthenium and rhenium cases ($V_{ab} \approx 0.7$ eV). Exceptions were observed for mixed-valence complexes containing the $Mn(dmpe)_2I$ and $W(dppe)_2I$ fragments, which were classified as class II mixed-valence systems. Electron localisation was observed on the very fast IR time scale in both cases (10^{-13} s).

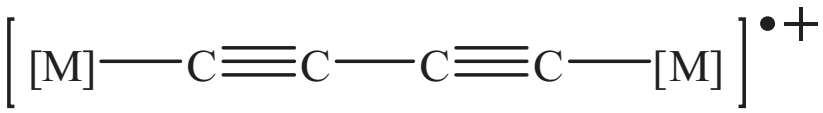

Scheme 5.2

Unsymmetrical mixed-valence complexes of general formula $[\{M\}(C{\equiv}CC{\equiv}C)\{M'\}]^{\bullet+}$ with Fe, Ru and Re metal fragments[26] have also been studied, affording weakly-coupled class II mixed-valence complexes as predicted by the Hush model for unsymmetrical systems[19a].

5.1.2 Mixed-valence complexes containing long polyyne carbon chains

Characterised mixed-valence complexes containing a carbon chain longer than C_4 are extremely rare. To date, the mixed-valence complex containing the longest elemental carbon chain is $[\{Cp^*(dppe)Fe\}_2(\mu\text{-}C{\equiv}CC{\equiv}CC{\equiv}CC{\equiv}C)]^{\bullet+}$ (**42**$^{\bullet+}$) synthesised by Lapinte et al.[27] (Scheme 5.3). It contains a C_8 bridge and the distance between the two iron centres is 12.6 Å. Unfortunately, no crystal structure has been obtained. Even over a distance as great as the C_8 bridge, a large electronic coupling has been measured and **42**$^{\bullet+}$ has been classified as a class III mixed-valence system.

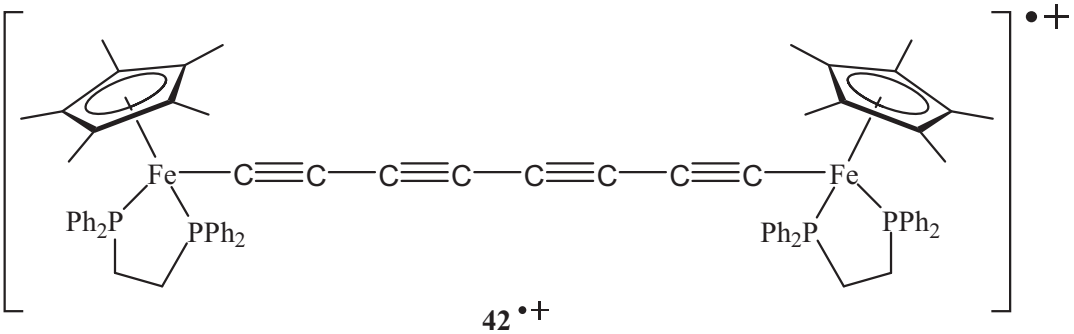

42$^{\bullet+}$

Scheme 5.3

The syntheses of mixed-valence complexes with C_6 and C_8 chains linking Re(NO)(PPh_3)Cp* end groups were attempted by Gladysz et al.[28]. However, they were unsuccessful; mixed-valence species have been detected by IR spectroscopy [ν(NO) bands were consistent with the presence of radical cations], but these were unstable at low temperature and quickly decomposed. The authors proposed that the radical cations are much more susceptible to intermolecular reactions (with increasing length of the carbon chain) and that a possible carbon-carbon radical coupling could occur to afford dimers.

Finally, an unsymmetrical mixed-valence complex containing a C_6 chain, with the two metal fragments Re(NO)(PPh_3)Cp* and Fe(dppe)Cp* has been reported[29]. Unfortunately, the [{Cp*(PPh_3)(NO)Re}(C≡CC≡CC≡C){Fe(dppe)Cp*}]$^{\bullet+}$ radical cation has only been characterised by IR and EPR spectroscopy, no further measurements, especially in the Near-IR range, being achieved. However, the EPR results suggest that the g-values are typical for an iron-centred radical.

5.2 Aims

As described above, mixed-valence complexes containing a C_4 bridge have been widely studied, together with, in the Fe(dppe)Cp* series, the mixed-valence system containing a C_8 chain (**42**$^{\bullet+}$). However, studies on mixed-valence complexes containing odd number of C≡C motifs have been missing (apart from some complexes with a C_2 bridge) and especially of compounds with a C_6 bridge. Properties intermediate between analogous C_4 and C_8 complexes might be expected for a mixed-valence complex containing a C_6 bridge, however, it could also have novel properties due to the C_6 ligand containing an odd number of C≡C triple bonds.

Syntheses and characterisation of new bimetallic hexatriynyl complexes containing the metal fragments Fe(dppe)Cp*, Ru(dppe)Cp* and Ru(dppe)Cp are described in this Chapter. In order to investigate electronic interactions between the two end-capping metal fragments through the C_6 bridge and the thermodynamic stability of the mixed-valence states, electrochemical studies of the novel complexes were carried out. Chemical oxidation of the new complexes was also carried out to generate novel radical cations, of which some were stable enough to be isolable. The new stable mixed-valence complexes were fully characterised and their physical properties investigated in order to study the strength of electron transfer over such distances, for which EPR and Near-IR spectroscopy were the most efficient methods.

Two-electron chemical oxidation was also investigated to give new dicationic species with unusual magnetic properties. Finally, tetracyanoethene (TCNE) reacted with some of the neutral hexatriynyl complexes to afford new compounds, which exhibited interesting physical properties.

5.3 Results and discussion

5.3.1 Syntheses of {Cp'(dppe)M}(C≡CC≡CC≡C){M(dppe)Cp'} (M = Fe, Ru; Cp' = Cp, Cp)*

In the literature, few methods are available for the preparation of symmetrical hexatriynyl complexes; the most widely used is the reaction between a metal halide and the TMS-protected triyne $Me_3Si(C{\equiv}C)_3SiMe_3$[1c, 30] in the presence of a desilylating agent such as KF (Scheme 5.4). This method is very efficient because the bimetallic complex $[M]_2(\mu\text{-}C{\equiv}CC{\equiv}CC{\equiv}C)$ generally precipitates out of solution and no further purification is needed. The second method consists of a Cu(I)-catalysed cross-coupling reaction between a metal diynyl [M](C≡CC≡CH) and the ethynyl [M](C≡CH) (Scheme 5.4)[31]. The advantage of this method is that unsymmetrical complexes [M](C≡CC≡CC≡C)[M'] can be synthesised. However, the hexatriynyl complex is not the only product: homocoupling of the ethynyl or diynyl complexes afford binuclear compounds containing C_4 and C_8 chains, respectively, so that separation and purification of the different products may be very difficult or even impossible.

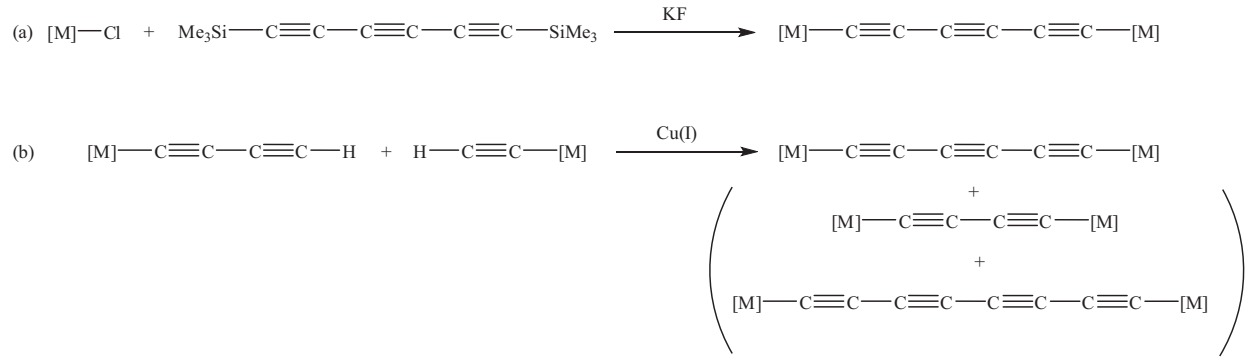

Scheme 5.4. *Methods for the preparation of $[M]_2(\mu\text{-}C{\equiv}CC{\equiv}CC{\equiv}C)$.*

Syntheses of the symmetrical complexes $\{Cp^*(dppe)Fe\}_2(\mu\text{-}C{\equiv}CC{\equiv}CC{\equiv}C)$ (**30**) and $\{Cp(dppe)Ru\}_2(\mu\text{-}C{\equiv}CC{\equiv}CC{\equiv}C)$ (**31**) were achieved via method (a) (Scheme 5.5). For **30**, two equivalents of **1** react with one equivalent of the silylated triyne $Me_3Si(C{\equiv}C)_3SiMe_3$ in the presence of KF in MeOH. After stirring one night at room temperature, the resulting orange precipitate was filtered off and washed with methanol to afford **30** as a fine orange powder in 75% yield. As with the ruthenium analogue $\{Cp^*(dppe)Ru\}_2(\mu\text{-}C{\equiv}CC{\equiv}CC{\equiv}C)$ (**32**)[32], complex **30** was insoluble or poorly soluble in all solvents tested (from apolar to very polar). A similar synthesis was used for **31**; instead of **1**, the organoruthenium precursor RuCl(dppe)Cp **33** was used and the mixture was heated under reflux during one

hour. The resulting yellow precipitate was collected and washed with methanol to give the biruthenium complex **31** in 80% yield as a yellow powder. In the ruthenium case, the mixture was heated because the reactivity of RuCl(dppe)Cp is less than FeCl(dppe)Cp*, as a result of the stronger Ru-Cl bond.

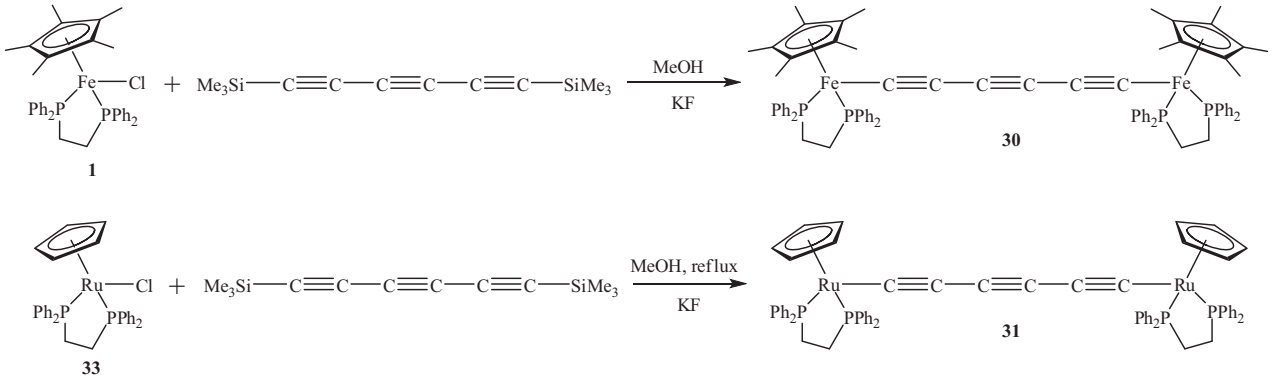

1 + Me_3Si—C≡C—C≡C—C≡C—C≡C—$SiMe_3$ → **30**

33 + Me_3Si—C≡C—C≡C—C≡C—C≡C—$SiMe_3$ → **31**

Scheme 5.5

Mixed iron-ruthenium bimetallic complexes [M](C≡CC≡CC≡C)[M'] **34** and **35** (Scheme 5.6) were prepared by reacting the mononuclear TMS-protected hexatriynyl complex with a metal chloride precursor in the presence of KF as the desilylating agent[29]. {Cp*(dppe)Fe}(C≡CC≡CC≡C){Ru(dppe)Cp*} **34** was thus made from the ruthenium hexatriynyl complex Ru(C≡CC≡CC≡C$SiMe_3$)(dppe)Cp* (**10**) with 1.1 equivalents of organoiron precursor **1** in the presence of KF in a 1:1 THF/MeOH mixture. After one night at room temperature the orange precipitate was collected and washed with methanol to give **34** as a fine orange powder in 61% yield. Similar solubility behaviour was observed for **30**, **32** and **34**. The bimetallic complex {Cp*(dppe)Fe}(C≡CC≡CC≡C){Ru(dppe)Cp} **35** was prepared via the same method but starting from the TMS-protected organoiron complex **9** and the organoruthenium precursor **33** in a 1:5 THF/MeOH mixture. After stirring one night, the resulting precipitate was collected and purified on a basic alumina column, eluting with a CH_2Cl_2/NEt_3 (5:1) mixture, when **35** was obtained as an orange powder in 30% yield.

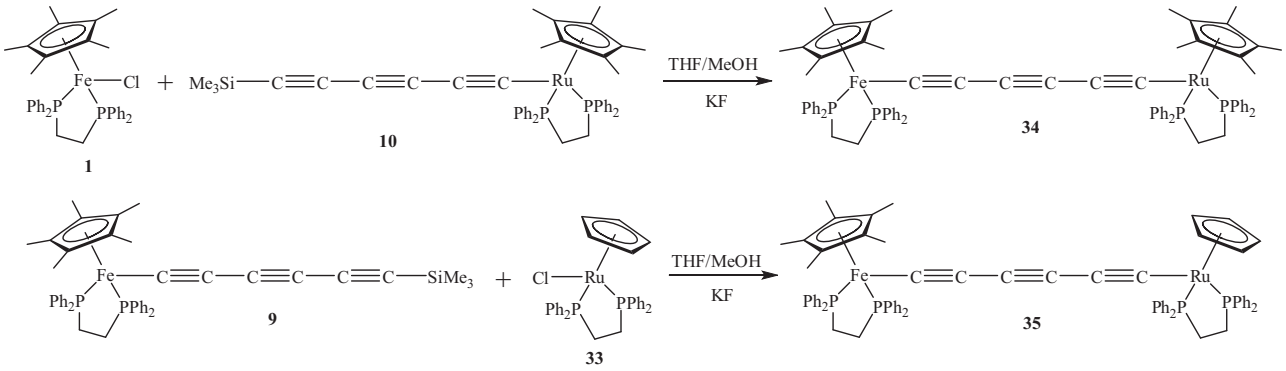

Scheme 5.6

Mixtures of THF/MeOH were used for the syntheses of the mixed bimetallic complexes **34** and **35** because no reaction occurred in pure MeOH, while THF increases the solubility of the protected hexatriynyl complexes **9** and **10**. In the preparation of **35**, the minimum of THF was used to facilitate the precipitation of the product, which is unnecessary for **34** because of its poor solubility.

5.3.2 Characterisation of compounds 30, 31, 34 and 35

Unfortunately, characterisation of **30** and **34** has been complicated because of their extremely poor solubility which makes NMR studies impossible; however, the IR spectra in the solid state (powder or KBr) have been recorded. One single ν(C≡C) band was observed at 2040 cm^{-1} for **30** reflecting the symmetry of the complex, whereas in **34**, three ν(C≡C) bands were observed at 2110, 2050 and 1969 cm^{-1}. The most efficient method to confirm the molecular formula of compounds **30** and **34** has been high resolution ES-mass spectra, which displayed $[M]^+$ at *m/z* 1250.3952 (calculated: 1250.3753) and 1296.3453 (calculated: 1296.3447) for complexes **30** and **34,** respectively.

Bimetallic complexes **31** and **35** were also characterised by the usual spectroscopic methods. For the diruthenium complex **31** in CH_2Cl_2, the IR spectrum showed one ν(C≡C) band at 2063 cm^{-1}. In the ^1H NMR spectrum, the Cp resonance was observed at δ 4.56 (s) while the dppe-CH_2 groups gave multiplets at δ 1.84-1.87 and 2.43-2.46. The Ru(dppe)Cp fragment was also observed in the ^{13}C NMR spectrum, with Cp at δ 83.16 (s), CH_2 of the dppe between δ 28.23-28.53 as a multiplet and C_α of the carbon chain as a triplet coupling to the two phosphorus atoms of the dppe at δ 102.64 ($^2J_{CP}$ = 28 Hz). The ^{31}P NMR

spectrum displayed one peak at δ 85.8 corresponding to the four equivalent phosphorus atoms of the molecule.

The IR spectrum of the unsymmetrical compound **35** which contains Fe(dppe)Cp* and Ru(dppe)Cp end-groups displayed ν(C≡C) bands at 2048 and 1920 cm^{-1}. The expected resonances were observed for the two organometallic fragments in the NMR spectra with the Cp* at δ 1.45 (^{1}H NMR) and δ 10.37, 88.25 (^{13}C NMR), and the Cp at δ 4.66 (^{1}H NMR) and δ 83.26 (^{13}C NMR). Besides, resonances of the two C_{α} atoms were found as triplets at δ 102.32 ($^{2}J_{CP}$ = 26 Hz) and 124.91 ($^{2}J_{CP}$ = 41 Hz) corresponding to the Ru-*C* and Fe-*C* atoms, respectively. In the ^{31}P NMR spectrum, singlets from the two dppe ligands were observed at δ 84.8 and 99.6 for the ruthenium and iron respectively. The high resolution ES-mass spectrum displayed $[M]^{+}$ at *m/z* 1226.2653 (calculated: 1226.2664).

Compounds **30** and **34** being poorly soluble, crystals could not be obtained and thus, no X-ray studies have been achieved. However, to confirm their molecular structures, reactions with a well-known reagent such as TCNE have been investigated and adduct X-ray crystal structures determined.

Reactions of 30 and 34 with TCNE

The rich chemistry of TCNE has been extensively studied[33]. TCNE is a useful reagent which is very electron-deficient; thus it can be used as an oxidising agent, for example, with Fe(C≡C-ant-C≡N)(dppe)Cp* (ant = $C_{14}H_8$) to give [Fe(C≡C-ant-C≡N)(dppe)Cp*][TCNE], which contains a 17-e cation and the $[TCNE]^{\bullet-}$ radical anion[34]. TCNE also undergoes [2 + 2]-cycloaddition reactions with transition-metal alkynyl complexes to give interesting products with polarised conjugated π systems[35]. These products generally crystallise easily allowing X-ray investigations which can be used to confirm the structure of the parent alkynyl complex. Addition of TCNE to the hexatriynyl complex $\{Cp(PPh_3)_2Ru\}_2(\mu\text{-}C{\equiv}CC{\equiv}CC{\equiv}C)$ has already been described[1c] (Scheme 5.7), TCNE reacting with the central C≡C triple bond to give a 1,2-bis(ethynyl)buta-2,3-diene derivative, probably by ring-opening (retro-cyclisation) of an intermediate 1,2-bis(ethynyl)cyclobutene. Here, TCNE reacts with the poorly soluble and incompletely characterised complexes **30** and **34** to give similar ring-opened [2 + 2]-cycloadducts which

could be fully characterised, thereby confirming the structures of the parent triyndiyl complexes.

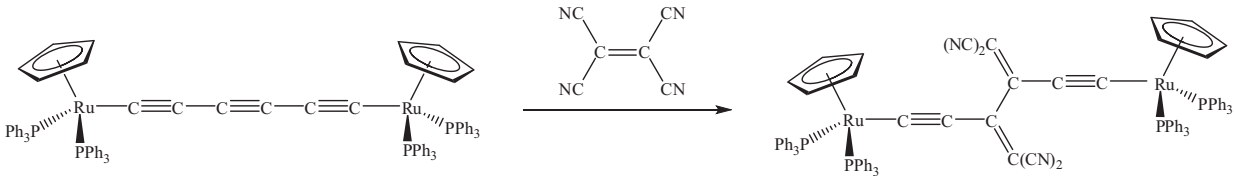

Scheme 5.7

When one equivalent of TCNE reacts with one equivalent of the Fe_2 complex **30** or the Fe-Ru complex **34** in dichloromethane (Scheme 5.8), the colour of the solution changed immediately from orange to deep purple. At the same time the insoluble precursor dissolved. After purification by precipitating the purple product and successive washes with hexane, $\{Cp^*(dppe)Fe\}_2\{\mu\text{-}C{\equiv}CC[{=}C(CN)_2]C[{=}C(CN)_2]C{\equiv}C\}$ (**36**) and $\{Cp^*(dppe)Fe\}\{C{\equiv}CC[{=}C(CN)_2]C[{=}C(CN)_2]C{\equiv}C\}\{Ru(dppe)Cp^*\}$ (**37**) were isolated as deep purple powders in 82 and 87% yields, respectively. It is assumed that the first product in this reaction is a TCNE salt which immediately undergoes a [2 + 2]-cycloaddition to form a cyclobutenyl complex, which in turn, opens to give the butadienyl adducts **36** or **37**[33] (Scheme 5.8).

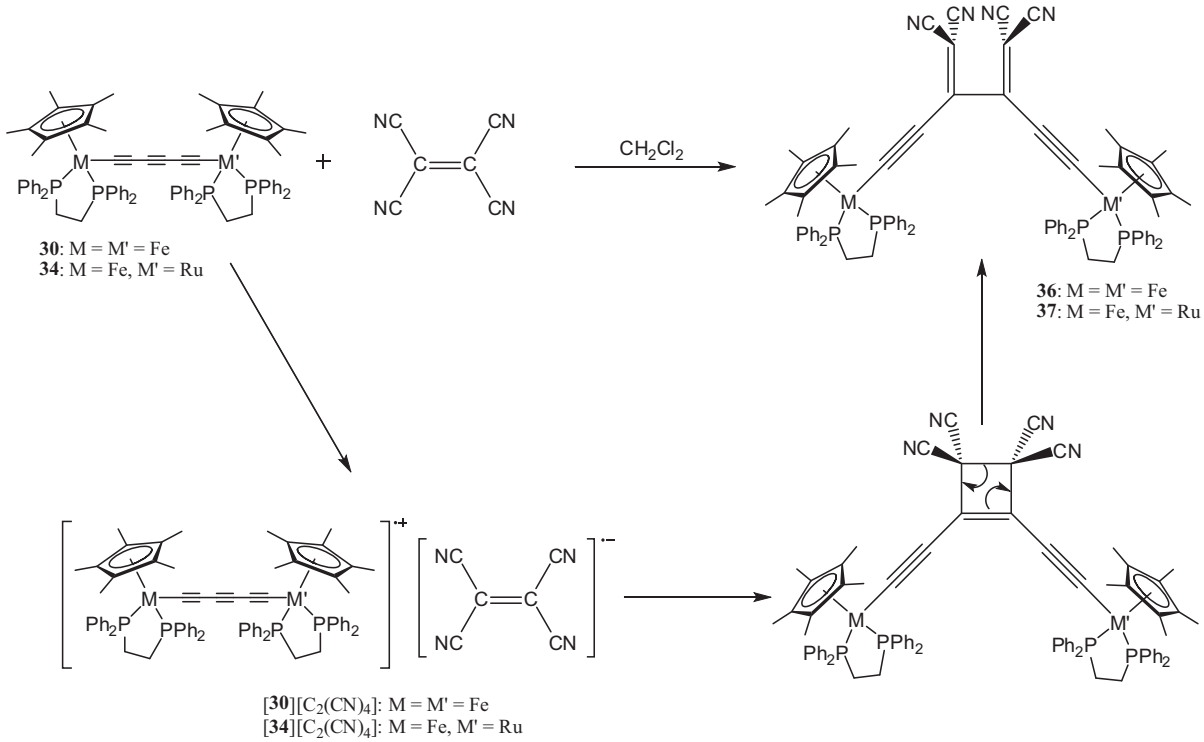

Scheme 5.8

The TCNE adduct **37** has been characterised by the usual spectroscopic methods while **36** has only been partially characterised as yet (IR, ^{31}P NMR, mass and X-ray analysis). In the IR spectrum of **36**, ν(C≡N) and ν(C≡C) bands were observed at 2206 and 1950 cm^{-1} respectively, while the ^{31}P NMR spectrum (Figure 5.1) displayed two well-separated broad doublets at δ 97.7 ($^{2}J_{PP}$ = 7 Hz) and 92.9 ($^{2}J_{PP}$ = 7 Hz). The two phosphorus atoms of each dppe ligand are no longer equivalent because of twisting of the cyanocarbon fragment about the central C-C bond, and form an AB quartet. In the high resolution ES-mass spectrum, $[M]^{+}$ was found at *m/z* 1378.3873 (calculated: 1378.3870).

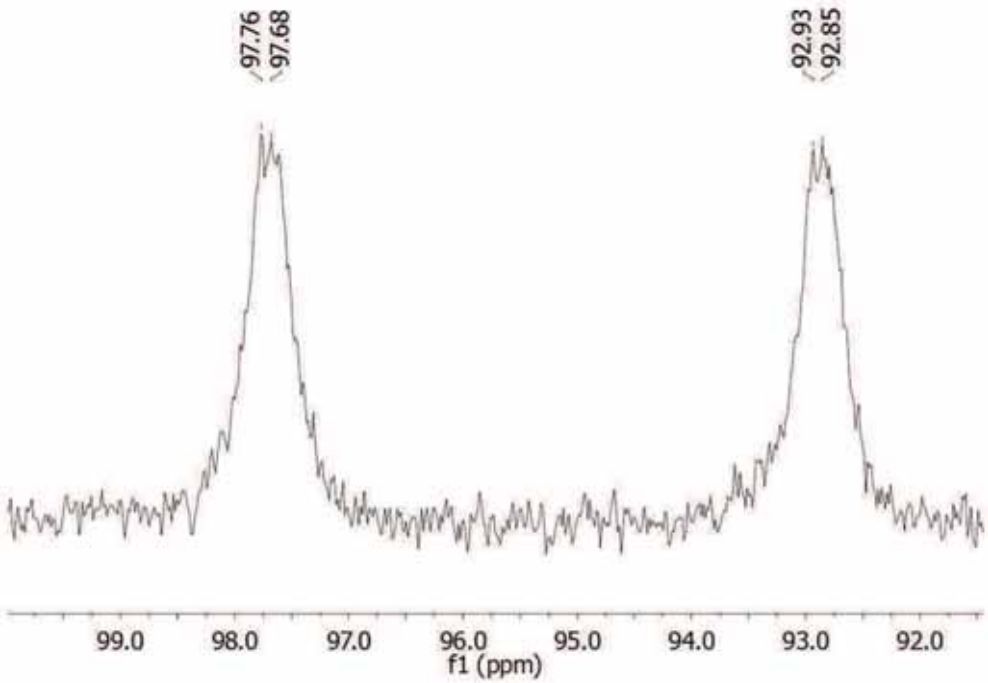

Figure 5.1. *^{31}P NMR spectrum of **36**.*

For **37**, the IR spectrum displayed a ν(C≡N) band at 2209 cm^{-1} together with a strong ν(C≡C) band at 1956 cm^{-1}. The two fragments Fe(dppe)Cp* and Ru(dppe)Cp* were observed by NMR spectroscopy: in the ^{1}H NMR spectrum: two Cp* singlet resonances were found at δ 1.07 (FeCp*) and 1.26 (RuCp*) [Figure 5.2 (b)] while the CH_2 groups of the dppe ligands were observed between δ 1.95-2.14 and at δ 2.52 and 2.59 as multiplets. The ^{13}C NMR spectrum showed very interesting features, indeed, Cp* resonances were observed at δ 10.32, 10.40 [Figure 5.2 (c)] for the methyl groups and at δ 96.26, 96.46 [Figure 5.2 (d)] for the ring carbons with signals corresponding to the Fe(dppe)Cp* fragment being broad with low intensity. Three CN resonances were observed at δ 114.19,

115.68 and 117.02, the second peak being broad and probably including two CN groups. Unfortunately, only one C_α resonance was found at δ 205.64 as a very broad signal which precluded determination of $^2J_{CP}$. In the ^{31}P NMR spectrum [Figure 5.2 (a)], an AB quartet was observed at δ 79.3 (d, $^2J_{PP}$ = 14 Hz) and 74.2 (d, $^2J_{PP}$ = 14 Hz) which was attributed to the dppe ligand of the Ru(dppe)Cp* fragment, the first signal being broad. No signals were found for the Fe(dppe)Cp* fragment between δ 90-100 ppm range, as expected in comparison with **36**.

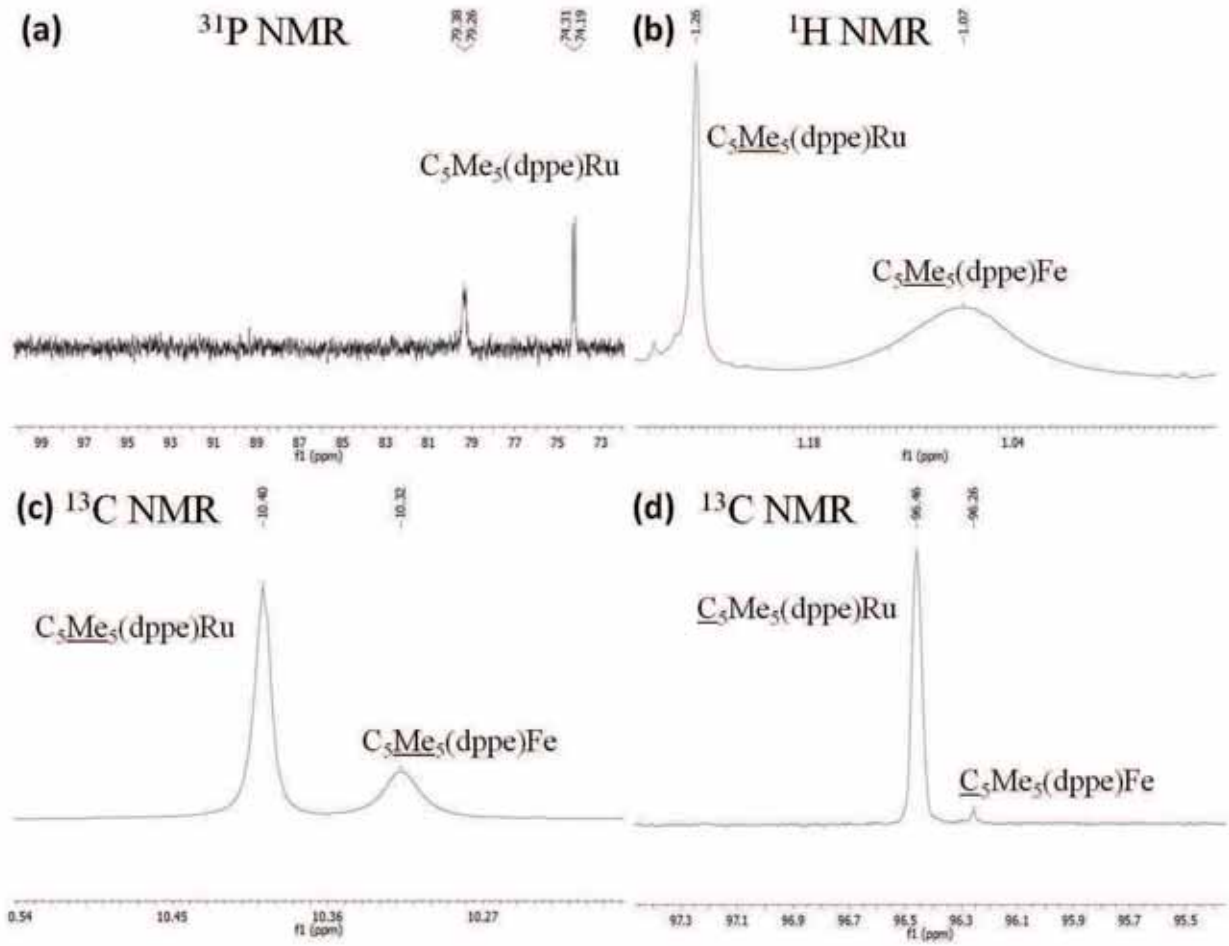

Figure 5.2. *Selected NMR spectra of **37**.*

Significant chemical shifts in the NMR spectra of the TCNE adducts in comparison with related neutral Fe(II) and Ru(II) complexes are observed in the ^{31}P NMR spectra [δ{Fe(II)(dppe)Cp*} ≈ 100 vs δ{Fe(dppe)Cp*(**36**)} = 97.7 , 92.9 and δ{Ru(II)(dppe)Cp*} ≈ 80 vs δ{Ru(dppe)Cp*(**37**)} = 79.3, 74.2 ppm] and in the ^{1}H NMR spectra [δ{Cp*(dppe)M(II)} ≈ 1.50 vs δ{Fe(dppe)Cp*(**37**)} = 1.07 and δ{Ru(dppe)Cp*(**37**)} = 1.26 ppm]. This is due to the strong electron-withdrawing ability of the cyanocarbon

fragment which dramatically affects the electron-rich metal fragments through the C≡C triple bonds. However, it seems that this electron-withdrawing ability affects the metal centres in **36** and **37** differently. In the symmetrical compound **36**, the ^{31}P NMR resonances suggest that intramolecular charge transfer occurs between the electron-rich Fe(dppe)Cp* moieties and the electron-poor cyanocarbon centre, which indicates that the mesomeric form **36B** (Scheme 5.9) has a strong contribution to the formulation of **36**.

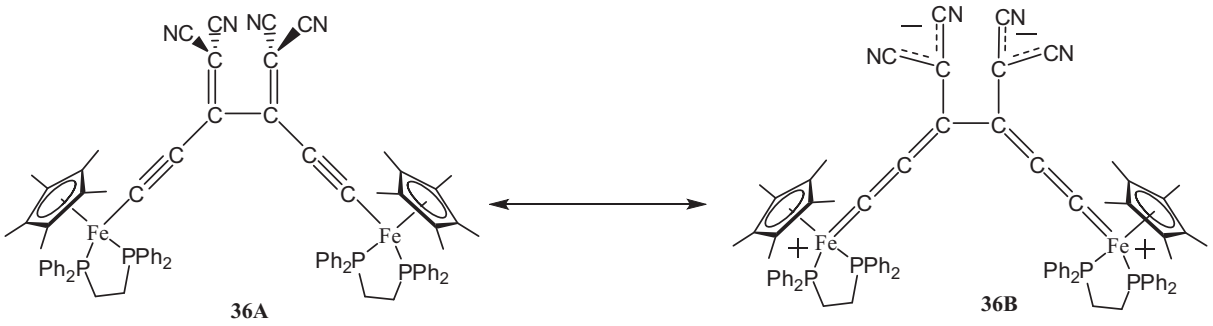

Scheme 5.9

The same phenomenon probably results in the broadening and decrease in intensity of all the NMR resonances from the Fe(dppe)Cp* moiety in comparison with the resonances of the Ru(dppe)Cp* fragment in **37** (Figure 5.2). Indeed, NMR signals of the Fe(dppe)Cp* fragment were not observed in the ^{31}P NMR spectrum while in the ^{1}H and ^{13}C NMR spectra, Cp* resonances were found to be very broad and abnormally weak, especially for the quaternary carbons [Figure 5.2 (d)]. These observations also suggest that the only C_α resonance found in the ^{13}C NMR spectrum corresponds to Ru-C_α whereas that of Fe-C_α cannot be observed. As the Fe(dppe)Cp* moiety is more electron-rich than its ruthenium analogue [Fe(dppe)Cp* is easier to oxidise than Ru(dppe)Cp*], the electron-withdrawing effect of the cyanocarbon has more effect on the iron than on the ruthenium centre. The very low intensity of some of the Fe(dppe)Cp* NMR signals also suggests that **37** is slightly paramagnetic, perhaps as a result of intramolecular electron transfer between Fe and the cyano ligand (Scheme 5.10). However, this intramolecular electron transfer has not been further characterised, molecule **37** being silent in EPR at 67K while no absorptions were observed in the Near-IR range (see Sections 5.3.6 and 5.3.8).

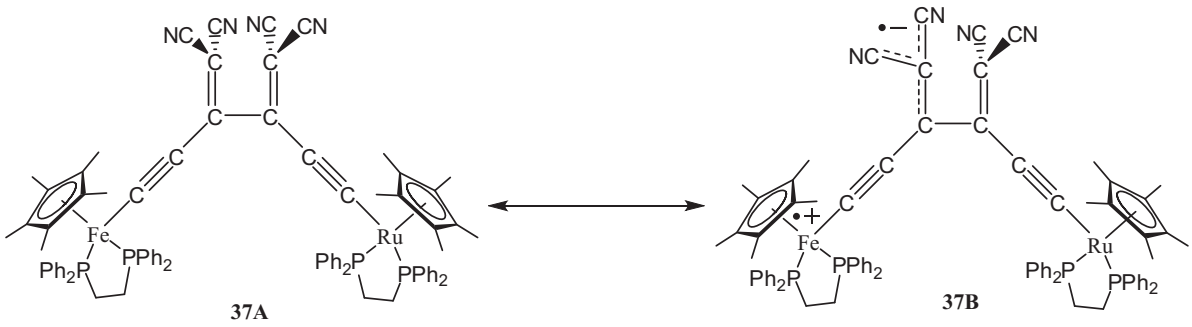

Scheme 5.10

Finally, when the bimetallic complex **34** was reacted with a large excess of TCNE (10 equivalents) in dichloromethane (Scheme 5.11), the salt [**37**][$C_3(CN)_5$] was obtained as a dark brown solid in 51% yield after purification by preparative TLC. Compound [**37**][$C_3(CN)_5$] is formed by oxidation of **37** with concomitant formation of pentacyanopropenide anion $C_3(CN)_5^-$. Decomposition of the $[TCNE]^{\bullet-}$ radical anion to form the $C_3(CN)_5^-$ anion in the presence of dioxygen is well known[36]. The proposed mechanism for the formation of [**37**][$C_3(CN)_5$] is illustrated in Scheme 5.11, excess of TCNE oxidising **37** to give [**37**][$C_2(CN)_4$] salt, which in the presence of dioxygen (during purification on silica gel) is converted into air-stable [**37**][$C_3(CN)_5$]. The added C(CN) group might come from the large excess of TCNE. However, the oxidation of **37** by TCNE should not be favoured: TCNE potentials are at E^0_1 = -0.83 and E^0_2 = +0.26 V whereas **37** oxidation potentials are at E^0_1 = +0.35 and E^0_2 = +0.88 V (see Section 5.3.3). Therefore, the key step of this synthesis is the reaction of the $[TCNE]^{\bullet-}$ radical anion with dioxygen which drags the reaction coordinate towards the final product [**37**][$C_2(CN)_4$].

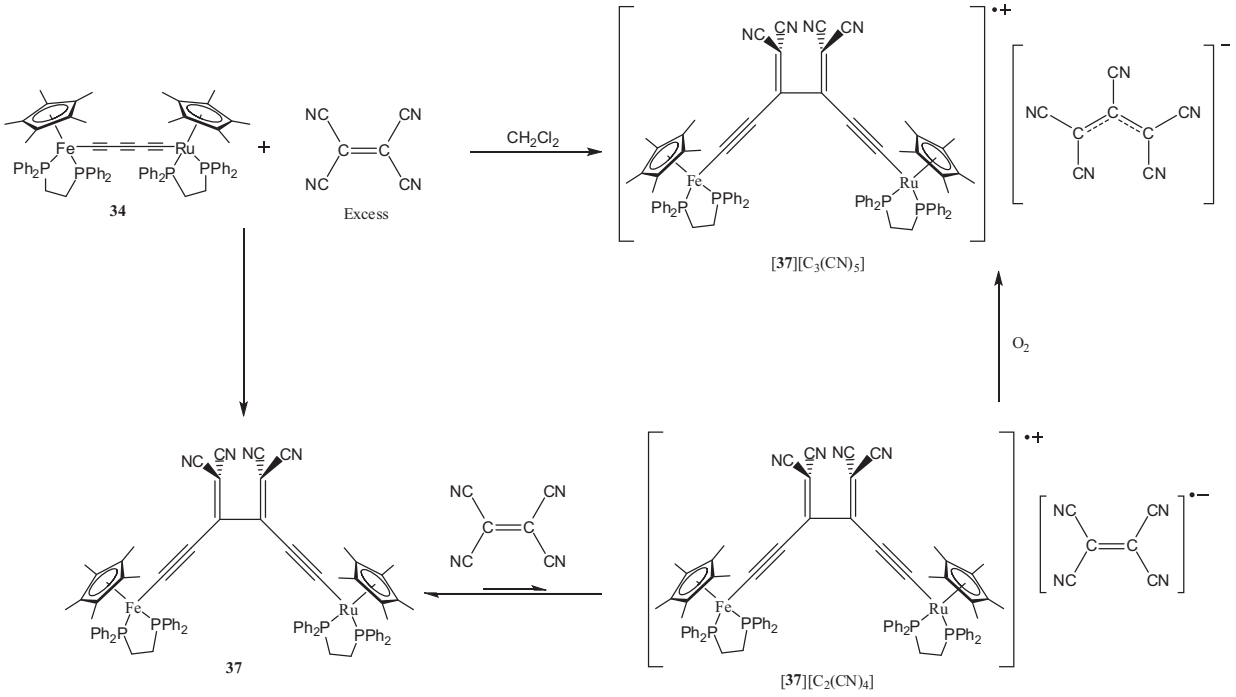

Scheme 5.11

Compound [**37**][$C_3(CN)_5$] is paramagnetic and difficult to characterise. However, the IR spectrum displayed ν(C≡N) and ν(C≡C) bands at 2199 and 1957 cm^{-1}, respectively, while the ν(CCC) band characteristic of the pentacyanopropenide anion[36] was found at 1506 cm^{-1}. In the high resolution ES-mass spectrum, $[M]^+$ was found at *m/z* 1424.3601 (calculated: 1424.3570). Paramagnetic [**37**][$C_3(CN)_5$] has also been characterised by EPR and Near-IR spectroscopy (see Sections 5.3.6 and 5.3.8).

The IR ν(C≡C) bands of the compounds synthesised in this section are summarised in Table 5.1. As expected, the two symmetrical complexes **30** and **31** displayed only one ν(C≡C) band corresponding to the M-C≡C triple bonds, the central ν(C≡C) vibration being IR-inactive. For the unsymmetrical complexes **34** and **35**, the three different ν(C≡C) vibrations are found in the range of 1920-2110 cm^{-1}, overlapping with each other in the case of compound **35** where only two bands are observed. When the C_6 bridge is modified by cycloaddition of TCNE to the central C≡C triple bond, reduction of bond order for the M-C≡C triple bonds is observed. In the symmetrical examples **30** and **36**, the ν(C≡C) vibrations decrease by 90 cm^{-1} whereas in the unsymmetrical examples **34** and **37**, reduction of bond order is also observed with the strong and broad ν(C≡C) band in **37** being at 1956 cm^{-1}, which probably contains the two M-C≡C vibrations. Upon oxidation of the TCNE adduct **37**, no changes were observed in the ν(C≡C) stretches with a strong and

broad band found at 1957 cm^{-1} in [**37**][$C_3(CN)_5$]. This broad band might also incorporate the two different ν(C≡C) vibrations existing in [**37**][$C_3(CN)_5$].

Table 5.1. IR ν(C≡C) bands for the neutral complexes and [**37**][$C_3(CN)_5$] synthesised in this section.

Compound	$\nu_{C\equiv C}$ (cm^{-1})
{Cp*(dppe)Fe}$_2$(C≡CC≡CC≡C) **30**	2040[a]
{Cp(dppe)Ru}$_2$(C≡CC≡CC≡C) **31**	2063[b]
{Cp*(dppe)Fe}(C≡CC≡CC≡C){Ru(dppe)Cp*} **34**	2110, 2050, 1969[c]
{Cp*(dppe)Fe}(C≡CC≡CC≡C){Ru(dppe)Cp} **35**	2048, 1920[b]
{Cp*(dppe)Fe}$_2$[μ-C≡CC{=C(CN)$_2$}C{=C(CN)$_2$}C≡C] **36**	1950[b]
{Cp*(dppe)Fe}C≡CC{=C(CN)$_2$}C{=C(CN)$_2$}C≡C-{Ru(dppe)Cp*} **37**	1956[b]
[{Cp*(dppe)Fe}C≡CC(=C(CN)$_2$)C(=C(CN)$_2$)C≡C{Ru(dppe)Cp*}][$C_3(CN)_5$] [**37**][$C_3(CN)_5$]	1957[b]

[a]KBr. [b]CH_2Cl_2. [c]Powder

Molecular structures

Suitable crystals of **31** for X-ray analyses were obtained by slow diffusion of hexane into a benzene solution. An ORTEP view of **31** is illustrated in Figure 5.3 and key structural parameters are collected in Table 5.2. The crystal structure of **31** was difficult to solve because finding a lower symmetry space group than $P4_2/n$ (tetragonal system) was unsuccessful, resulting in an *R*-factor of 0.072. The unit cell contains one molecule of **31** and half a molecule of benzene with parameters: a = 35.6390(18), b = 35.6390(18), c = 9.3223(8) Å.

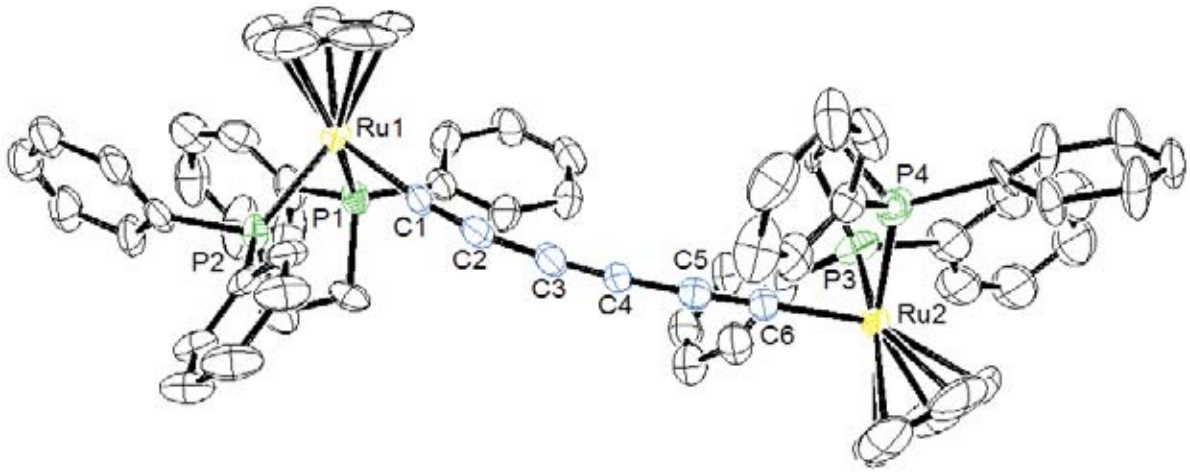

Figure 5.3. *ORTEP view of {Cp(dppe)Ru}$_2$(μ-C≡CC≡CC≡C)* ***31****.*

Table 5.2. Selected structural parameters for **31**.

Bond Distances (Å)		**Bond Angles (°)**	
Ru(1,2)-P(1,3)	2.2460(18), 2.247(2)	P(1,3)-Ru(1,2)-P(2,4)	81.75(7), 82.38(8)
Ru(1,2)-P(2,4)	2.2563(19), 2.261(2)	C(1,6)-Ru(1,2)-P(1,3)	84.98(19), 83.9(2)
Ru(1,2)-Cp(1,2)$_{cent}$	1.883, 1.895	C(1,6)-Ru(1,2)-P(2,4)	88.81(18), 86.6(2)
Ru(1,2)-C(1,6)	1.991(6), 1.996(7)	Ru(1)-C(1)-C(2)	171.8(6)
C(1)-C(2)	1.217(9)	C(1)-C(2)-C(3)	168.3(7)
C(2)-C(3)	1.385(9)	C(2)-C(3)-C(4)	172.8(8)
C(3)-C(4)	1.213(9)	C(3)-C(4)-C(5)	175.7(7)
C(4)-C(5)	1.376(10)	C(4)-C(5)-C(6)	178.0(8)
C(5)-C(6)	1.221(9)	C(5)-C(6)-Ru(2)	177.5(6)

As expected, bond lengths in the Ru(dppe)Cp fragment are typical while angles confirm the pseudo-octahedral geometry of the metal atoms. Distances along the carbon chain confirm its hexatriynyl nature with C≡C triple bond lengths being between 1.213(9)-1.221(9) Å and C-C single bond distances being 1.385(9) and 1.376(10) Å. However, the Ru-C_6-Ru chain deviates significantly from linearity with the angle between the Ru(1)-C(1) and C(6)-Ru(2) bonds being 34° as illustrated in Figure 5.3.

Crystals of **35** suitable for X-ray analysis were difficult to obtain, although slow evaporation of a dichloromethane/triethylamine solution afforded poor quality material which gave a large *R*-factor: $R = 0.118$. Complex **35** crystallises with two independent molecules in the asymmetric unit, the crystals being monoclinic $P2_1/c$ with unit cell

parameters: a = 30.502(3), b = 16.4366(8), c = 26.640(2) Å, β = 106.197(8)°. An ORTEP view of a molecule of **35** is shown in Figure 5.4 while selected structural parameters of the two independent molecules are collected in Table 5.3.

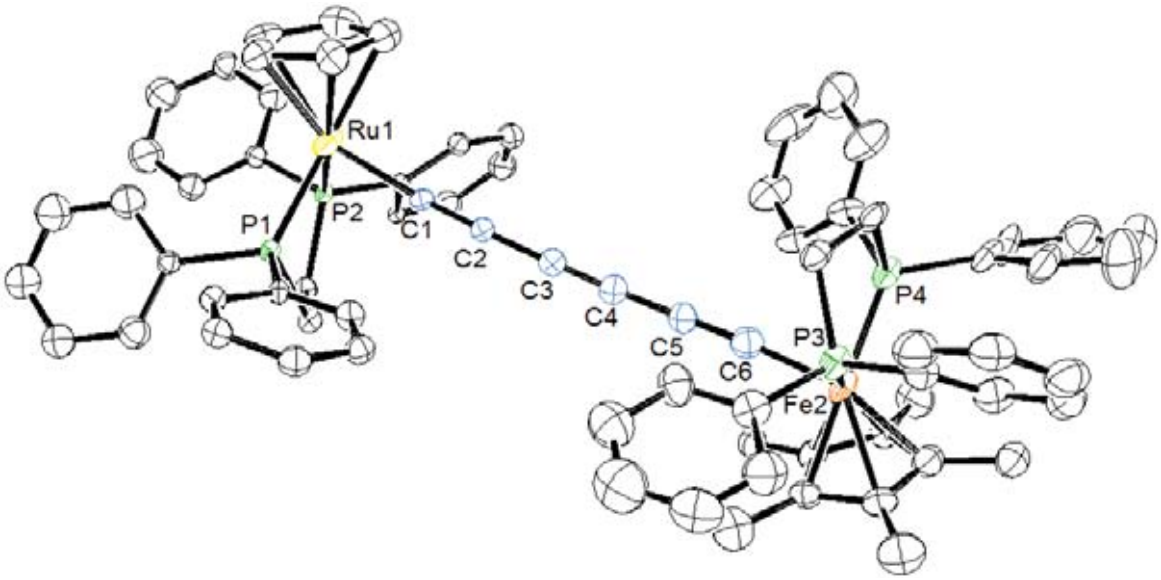

Figure 5.4. *ORTEP view of {Cp*(dppe)Fe}(C≡CC≡CC≡C){Ru(dppe)Cp}* ***35****.*

Table 5.3. Selected structural parameters for **35** (Italicised values refer to the second molecule).

Bond Distances (Å)		**Bond Angles (°)**	
Ru(1)-P(1)	2.262(3), *2.239(5)*	P(1)-Ru(1)-P(2)	81.92(10), *83.28(15)*
Ru(1)-P(2)	2.249(3), *2.235(4)*	C(1)-Ru(1)-P(1)	85.5(3), *85.6(4)*
Ru(1)-Cp_{cent}	1.887, *1.898*	C(1)-Ru(1)-P(2)	84.2(3), *87.5(3)*
Ru(1)-C(1)	1.990(10), *2.007(11)*	P(3)-Fe(2)-P(4)	85.28(13), *85.34(13)*
Fe(2)-P(3)	2.194(3), *2.177(3)*	C(6)-Fe(2)-P(3)	86.3(4), *85.5(4)*
Fe(2)-P(4)	2.173(4), *2.185(4)*	C(6)-Fe(2)-P(4)	86.1(4), *83.3(4)*
Fe(2)-Cp^*_{cent}	1.735*, 1.745*	Ru(1)-C(1)-C(2)	175.1(10), *177.1(11)*
Fe(2)-C(6)	1.888(12), *1.891(12)*	C(1)-C(2)-C(3)	178.4(13), *175.7(15)*
C(1)-C(2)	1.221(13), *1.211(15)*	C(2)-C(3)-C(4)	179.0(15), *178.4(15)*
C(2)-C(3)	1.390(14), *1.352(17)*	C(3)-C(4)-C(5)	177.0(14), *177.8(14)*
C(3)-C(4)	1.201(14), *1.259(16)*	C(4)-C(5)-C(6)	176.4(13), *177.1(13)*
C(4)-C(5)	1.355(15), *1.360(16)*	C(5)-C(6)-Fe(2)	175.4(11), *177.7(11)*
C(5)-C(6)	1.232(15), *1.214(14)*		

The Ru(dppe)Cp and Fe(dppe)Cp* fragments show expected bond lengths and angles for neutral Ru(II) and Fe(II) complexes, both metal atoms adopting a pseudo-octahedral geometry with M-P, M-C(1,6) bond distances being in the usual ranges for iron [Fe(2)-P(3,4): 2.173(4)-2.194(3); Fe(2)-C(6): 1.888(12) and 1.891(12) Å] and ruthenium [Ru(1)-P(1,2): 2.235(4)-2.262(3); Ru(1)-C(1): 1.990(10) and 2.007(11) Å]. In contrast to **31** where the C_6 chain is significantly bent, the carbon chain in compound **35** is close to linear with angles being between 175.1(10)-179.0(15)°.

X-ray diffraction studies have also been carried out on crystals of **36**, **37** and [**37**][$C_3(CN)_5$] confirming their structures and that TCNE has added to the central C≡C triple bond to form the ring-opened products. These X-ray studies also support the structure assignments of the insoluble parent complexes **30** and **34**. Complex **36** crystallised from a dichloromethane/pentane solution, the unit cell incorporating one molecule of **36** together with one molecule of CH_2Cl_2 and half a molecule of 1,2-bis(diphenylphosphino)ethane oxide, formed during work-up as an impurity, but in this case also helping with the crystallisation process. The crystal is triclinic *P*-1 and an ORTEP view of **36** is given in Figure 5.5 while important parameters are collected in Table 5.4.

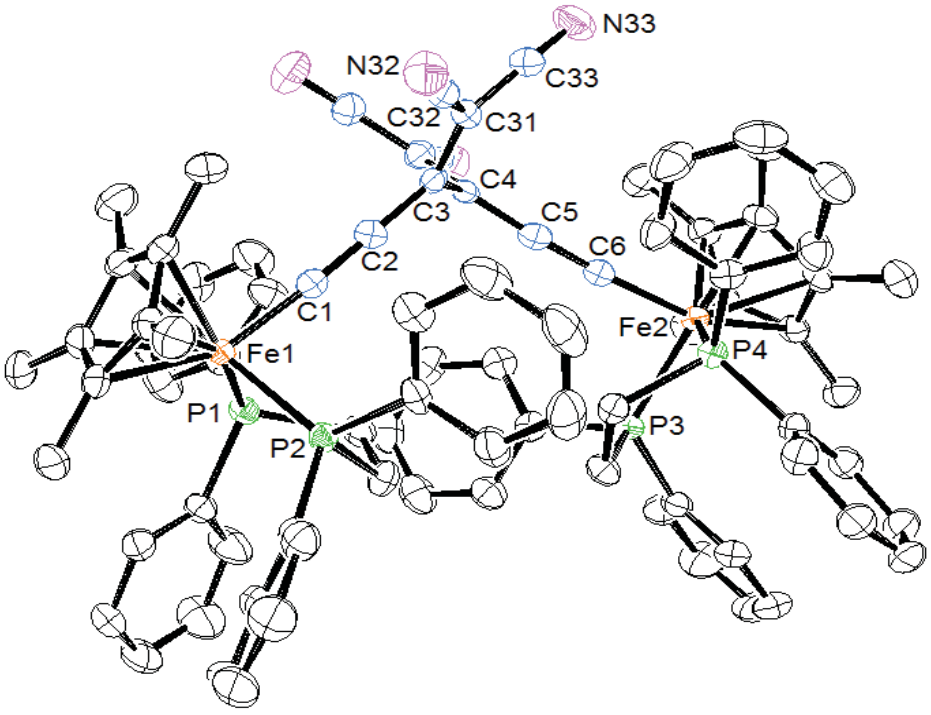

Figure 5.5. *ORTEP view of {Cp*(dppe)Fe}$_2${μ-C≡CC[=C(CN)$_2$]C[=C(CN)$_2$]C≡C}* ***36****.*

Table 5.4. Selected structural parameters for **36**.

Bond Distances (Å)		Bond Angles (°)	
Fe(1)-P(1,2)	2.1966(7), 2.2012(8)	P(1,3)-Fe(1,2)-P(2,4)	85.27(3), 85.54(3)
Fe(2)-P(3,4)	2.2140(8), 2.1909(7)	C(1,6)-Fe(1,2)-P(1,3)	87.15(8), 89.51(8)
Fe(1,2)-Cp*(1,2)$_{cent}$	1.750, 1.756	C(1,6)-Fe(1,2)-P(2,4)	86.76(8), 85.33(8)
Fe(1,2)-C(1,6)	1.840(3), 1.840(3)	Fe(1,2)-C(1,6)-C(2,5)	174.3(2), 174.6(2)
C(1,6)-C(2,5)	1.242(4), 1.243(4)	C(1,6)-C(2,5)-C(3,4)	174.2(3), 177.0(3)
C(2,5)-C(3,4)	1.392(4), 1.385(4)	C(2,5)-C(3,4)-C(4,3)	117.4(2), 118.8(2)
C(3)-C(4)	1.509(3)	C(2,5)-C(3,4)-C(31,41)	126.3(2), 125.6(2)
C(3,4)-C(31,41)	1.386(4), 1.388(4)		
C(31,41)-C(32,42)	1.432(4), 1.436(4)		
C(31,41)-C(33,43)	1.443(4), 1.431(4)		

The electron-withdrawing cyanocarbon group significantly affects bond lengths around the metal centres, Fe-P [2.1909(7)-2.2140(8) Å] distances being longer than in typical neutral Fe(II)(dppe)Cp* fragments while the Fe-C(1,6) distances [1.840(3) Å] are slightly shorter. The C≡C triple bonds are also slightly longer [1.242(4) and 1.243(4) Å]. These changes in the bond lengths suggest a contribution from mesomer **36B** to the molecular structure (Scheme 5.9). For the organic part of the chain, C(3)-C(4) [1.509(3) Å] and C(3,4)-C(31,41) [1.386(4) and 1.388(4) Å] distances are consistent with single and double bonds, respectively. It is interesting to note that the dihedral angle between the two planes containing the C=C(CN)$_2$ fragments is very close to a right-angle with a value of 89.80°.

Crystals of complex **37** were obtained from a saturated dichloromethane solution, and by slow diffusion of hexane into a concentrated benzene solution for [**37**][$C_3(CN)_5$]. Compound **37** crystallised with one molecule of **37** and one molecule of dichloromethane in the unit cell and is orthorhombic $P2_12_12_1$. The unit cell of [**37**][$C_3(CN)_5$] contains one molecule of [**37**][$C_3(CN)_5$] and is monoclinic $P2_1/c$. ORTEP views of the two complexes are given in Figure 5.6 while selected structural parameters are collected in Table 5.5.

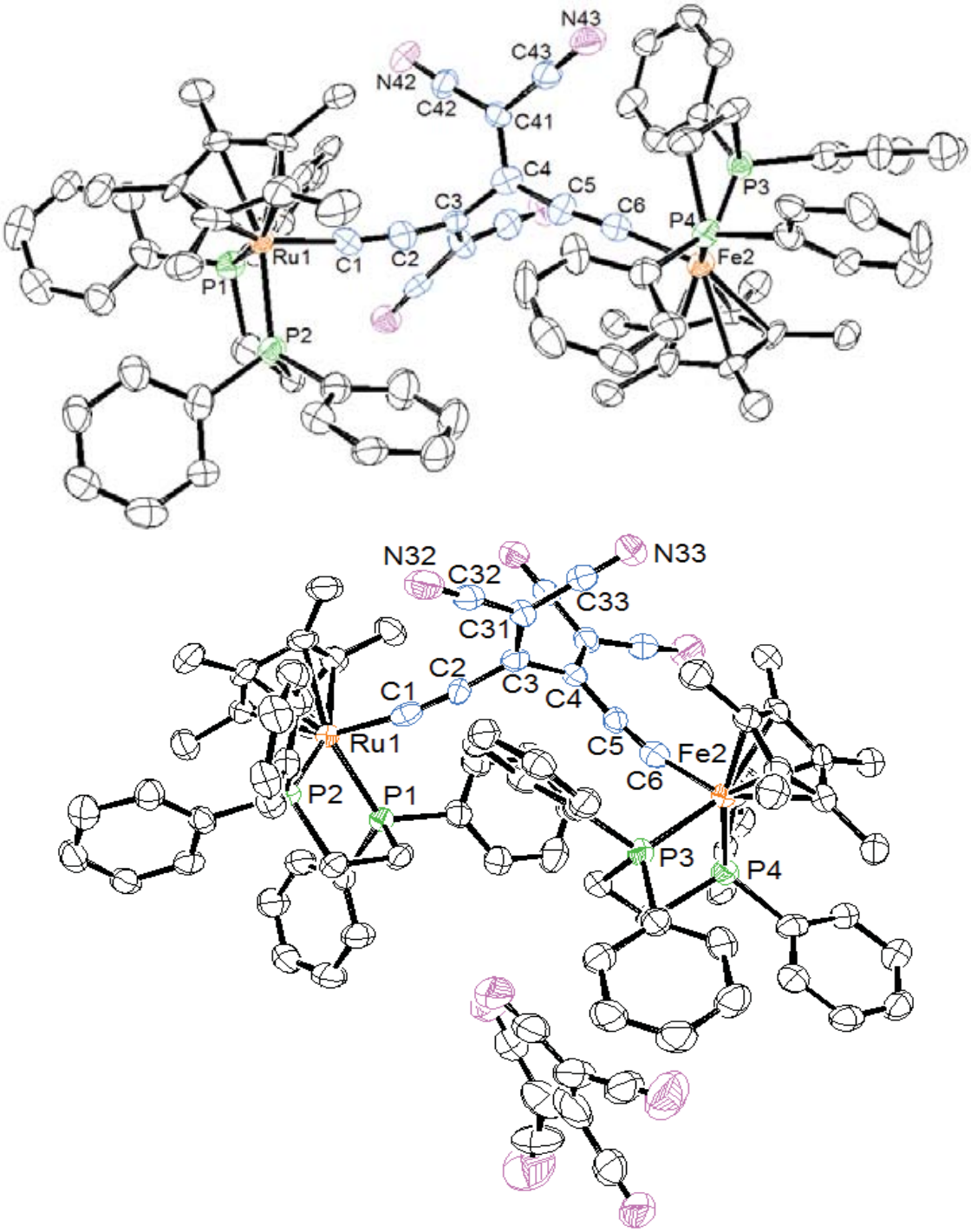

Figure 5.6. *ORTEP views of {Cp*(dppe)Fe}{C≡CC[=C(CN)$_2$]C[=C(CN)$_2$]C≡C}{Ru(dppe)Cp*}* ***37*** *(top) and [{Cp*(dppe)Fe}{C≡CC[=C(CN)$_2$]C[=C(CN)$_2$]C≡C}{Ru(dppe)Cp*}][C$_3$(CN)$_5$] [**37**][C$_3$(CN)$_5$] (bottom).*

Table 5.5. Selected structural parameters for **37** and [**37**][$C_3(CN)_5$].

	37	[**37**][$C_3(CN)_5$]
Bond Distances (Å)		
M(1)-P(1)	2.262(3)	2.2985(12)
M(1)-P(2)	2.233(3)	2.2866(12)
M(1)-Cp*$_{cent}$	1.846	1.895
M(1)-C(1)	1.882(9)	1.924(5)
M(2)-P(3)	2.247(3)	2.2517(13)
M(2)-P(4)	2.220(3)	2.2752(12)
M(2)-Cp*$_{cent}$	1.820	1.801
M(2)-C(6)	1.900(9)	1.895(5)
C(1,6)-C(2,5)	1.257(13), 1.215(12)	1.248(6), 1.229(6)
C(2,5)-C(3,4)	1.396(13), 1.393(13)	1.372(6), 1.391(6)
C(3)-C(4)	1.517(14)	1.516(6)
C(3,4)-C(31,41)	1.367(13), 1.389(13)	1.376(6), 1.370(6)
C(31,41)-C(32,42)	1.448(14), 1.442(14)	1.431(5), 1.439(6)
C(31,41)-C(33,43)	1.405(14), 1.408(13)	1.429(7), 1.432(7)
Bond Angles (°)		
P(1)-M(1)-P(2)	84.00(10)	81.74(4)
C(1)-M(1)-P(1)	86.7(3)	83.12(13)
C(1)-M(1)-P(2)	87.1(3)	95.55(13)
M(1)-C(1)-C(2)	174.4(8)	168.0(4)
P(3)-M(2)-P(4)	84.02(10)	83.11(4)
C(6)-M(2)-P(3)	87.5(3)	85.29(14)
C(6)-M(2)-P(4)	87.5(3)	93.79(13)
M(2)-C(6)-C(5)	170.7(9)	169.4(4)
C(1,6)-C(2,5)-C(3,4)	167.8(10), 168.4(10)	172.1(5), 170.3(5)
C(2,5)-C(3,4)-C(4,3)	117.4(9), 118.6(9)	118.7(4), 117.0(4)
C(2,5)-C(3,4)-C(31,41)	123.9(9), 122.0(10)	125.3(4), 125.0(4)

In the molecule of **37**, the ruthenium and iron atoms are equally disordered between the two metal sites and distances about the metal atoms are similar, so that it is not possible to differentiate between the iron and ruthenium atoms. In the cation of [**37**][$C_3(CN)_5$], the metal atoms are also disordered, site occupancies for M(1) and M(2) refining to 0.790(2) for Ru(1) and Fe(2), with those for Fe(1) and Ru(2) being the complement. The major metal contribution in both Cp*(dppe)M fragments can be deduced from the bond lengths (M-P, M-C and M-Cp*$_{cent}$) at the major iron site being slightly shorter than at the major ruthenium site. However, the structural parameters of the neutral and oxidised compounds **37** and [**37**][$C_3(CN)_5$] are not significantly different, although in both cases the average M-

P distances (Fe and Ru) are elongated in comparison with typical M(II)-P average distances. Average M-C(1,6) bond lengths are shorter, due to the electron-withdrawing cyanocarbon ligand as found for **36**. In the two structures, the metal atoms have a pseudo-octahedral geometry with the C(1,6)-M-P(2,4) angles [95.55(13) and 93.79(13)°] in [**37**][$C_3(CN)_5$] being larger than the usual values (87°). Similarly to **36**, the C(3)-C(4) [1.517(14) and 1.516(6) Å] and C(3,4)-C(31,41) [1.367(13), 1.389(13) and 1.376(6), 1.370(6) Å] distances are consistent with single and double bonds, respectively. Finally, the dihedral angles between the two C=C$(CN)_2$ planes are significantly different in the neutral and oxidised species, at 86.57 and 77.8(1)°, respectively.

5.3.3 Electrochemistry

Cyclic voltammograms of the novel hexatriynyl complexes were recorded under conditions similar to those described earlier in Chapter 2 (Section 2.3.4) and compared with some related complexes in Table 5.6. The electronic interaction between the metal end-groups has been measured for the symmetrical bimetallic complexes by calculation of ΔE and the comproportionation constants K_c which determine the thermodynamic stability of the mixed-valence species. However the use of ΔE and K_c values to assess the degree of electronic communication between metals must be approached very judiciously[37]. For example, K_c for {Cp*(dppe)Fe}$_2$(μ-C≡CC≡C) **38** (1.6×10^{12}) is larger than K_c for the ruthenium analogue {Cp*(dppe)Ru}$_2$(μ-C≡CC≡C) **39** (9.7×10^{10}), but the electronic coupling parameter is larger in [**39**]PF_6 (V_{ab} = 0.63 eV) than in [**38**]PF_6 (V_{ab} = 0.47 eV), which indicates that electronic communication between metals is better in the ruthenium complex than in the iron system. CVs of the bimetallic complexes {Cp*(dppe)Fe}$_2$(μ-C≡CC≡CC≡C) **30** and {Cp*(dppe)Fe}(C≡CC≡CC≡C){Ru(dppe)Cp*} **34** were recorded using their oxidised forms [**30**]PF_6 and [**34**]PF_6 synthesised in Section 5.3.4, because the very poor solubility precluded electrochemical investigations of the neutral complexes.

Table 5.6. Electrochemical data for {Cp'(dppe)M}(C≡CC≡CC≡C){M(dppe)Cp'} (M = Fe, Ru; Cp' = Cp, Cp*) and related complexes.

Compound	E^0_1 (V)	E^0_2 (V)	ΔE (V)	K_c	E^0_3 (V)	Ref
$\{Cp^*(dppe)Fe\}_2(\mu\text{-}C{\equiv}CC{\equiv}C)$ **38**	-0.67	+0.04	0.72	1.6×10^{12}	+0.95	22b
$\{Cp^*(dppe)Ru\}_2(\mu\text{-}C{\equiv}CC{\equiv}C)$ **39**	-0.43	+0.22	0.65	9.7×10^{10}	+1.04	23c
$\{Cp^*(dppe)Fe\}(C{\equiv}CC{\equiv}C)\{Ru(dppe)Cp^*\}$ **40**	-0.59	+0.18	0.77	1.1×10^{13}	+0.99	26c
$\{Cp(dppe)Ru\}_2(\mu\text{-}C{\equiv}CC{\equiv}C)$ **41**	-0.24	+0.35	0.59	1.0×10^{10}	+1.08	38
$Fe\{C{\equiv}C\text{-}C{\equiv}C\text{-}C{\equiv}C\text{-}SiMe_3\}(dppe)Cp^*$ **9**	+0.08					This work
$Ru\{C{\equiv}C\text{-}C{\equiv}C\text{-}C{\equiv}C\text{-}SiMe_3\}(dppe)Cp^*$ **10**	+0.41					39
$[\{Cp^*(dppe)Fe\}_2(\mu\text{-}C{\equiv}CC{\equiv}CC{\equiv}C)]PF_6$ [**30**]PF_6	-0.42	+0.13	0.55	2.1×10^{9}	+1.00	This work
$\{Cp^*(dppe)Ru\}_2(\mu\text{-}C{\equiv}CC{\equiv}CC{\equiv}C)$ **32**	-0.15	+0.33	0.48	1.4×10^{8}	+1.05	32
$\{Cp(dppe)Ru\}_2(\mu\text{-}C{\equiv}CC{\equiv}CC{\equiv}C)$ **31**	+0.01	+0.45	0.44	2.9×10^{7}	+1.11	This work
$[\{Cp^*(dppe)Fe\}(C{\equiv}CC{\equiv}CC{\equiv}C)\{Ru(dppe)Cp^*\}]PF_6$ [**34**]PF_6	-0.32	+0.27	0.59	1.0×10^{10}	+1.01	This work
$\{Cp^*(dppe)Fe\}(C{\equiv}CC{\equiv}CC{\equiv}C)\{Ru(dppe)Cp\}$ **35**	-0.28	+0.36	0.64	7.0×10^{10}	+1.03	This work
$\{Cp^*(dppe)Fe\}_2(\mu\text{-}C{\equiv}CC{\equiv}CC{\equiv}CC{\equiv}C)$ **42**	-0.23	+0.20	0.43	2.0×10^{7}		27
$\{Cp^*(dppe)Fe\}_2[\mu\text{-}C{\equiv}CC\{{=}C(CN)_2\}C\{{=}C(CN)_2\}C{\equiv}C]$ **36**	+0.28	+0.48	0.20	2.4×10^{3}		This work
$\{Cp^*(dppe)Fe\}C{\equiv}CC\{{=}C(CN)_2\}C\{{=}C(CN)_2\}C{\equiv}C\{Ru(dppe)Cp^*\}$ **37**	+0.35	+0.88	0.53	9.6×10^{8}		This work

CVs of the two symmetrical complexes **30** and **31** each contained three well-separated and fully reversible 1-e processes (Figure 5.7). The large separations of the two first oxidation waves [ΔE(**30**) = 0.55 and ΔE(**31**) = 0.44 V], and the very large comproportionation constants (K_c = 2.1 × 10^9 for **30** and 2.9 × 10^7 for **31**) reveal strong electronic interactions between the two metal centres through the hexatriynyl bridge in each complex. The ΔE values are considerably larger than 250 mV, so that the 35-e species $\mathbf{30}^{\bullet+}$ and $\mathbf{31}^{\bullet+}$ can be considered as class III delocalised mixed-valence complexes[40].

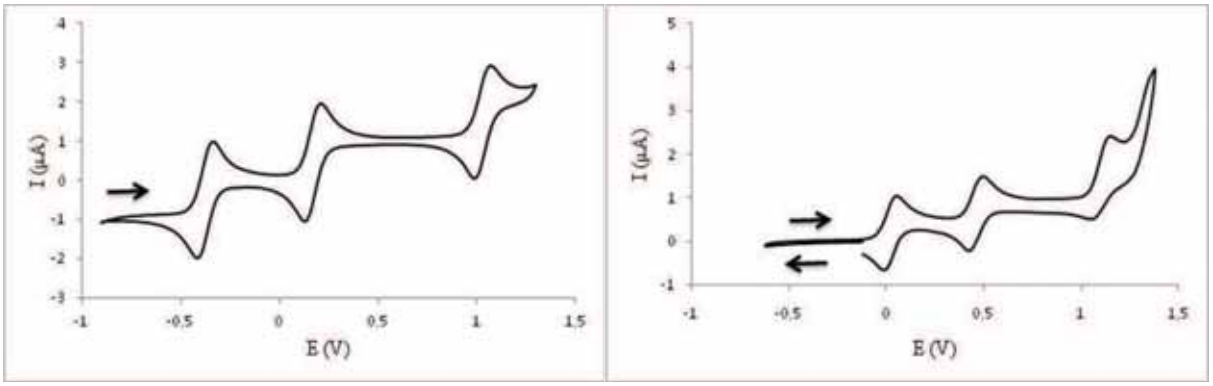

Figure 5.7. *Cyclic voltammograms of **30** (left) and **31** (right).*

Mixed-metal complexes **34** and **35** also show three fully reversible oxidation waves (Figure 5.8) in their respective cyclic voltammograms. The first oxidation waves at E^0_1 = -0.32 and -0.28 V are attributed to the Fe(dppe)Cp* fragments while the second oxidation waves at E^0_2 = +0.27 and +0.36 V correspond to the Ru(dppe)Cp* and Ru(dppe)Cp fragments, respectively. Unfortunately, as these compounds are unsymmetrical, electronic interactions between metal centres cannot be approximated with the use of the K_c values, which are relatively large (K_c = 1.0 × 10^{10} for **34** and 7.0 × 10^{10} for **35**) and indicate that the mixed-valence targets are thermodynamically very stable. However, electronic interactions between metal centres can be approximated by comparing the oxidation potential of the Fe(dppe)Cp* unit in the bimetallic compounds **34** and **35** with the monometallic complex **9** (E^0_1 = +0.08) containing a $SiMe_3$ end-group instead of a ruthenium fragment. Bimetallic complexes **34** and **35** are easier to oxidise than the monometallic complex **9** by approximately 0.38 V, indicating that the ruthenium centres are strong electron-donating groups in comparison to $SiMe_3$, and also reveals that electronic communication between the two metal fragments in complexes **34** and **35** exists.

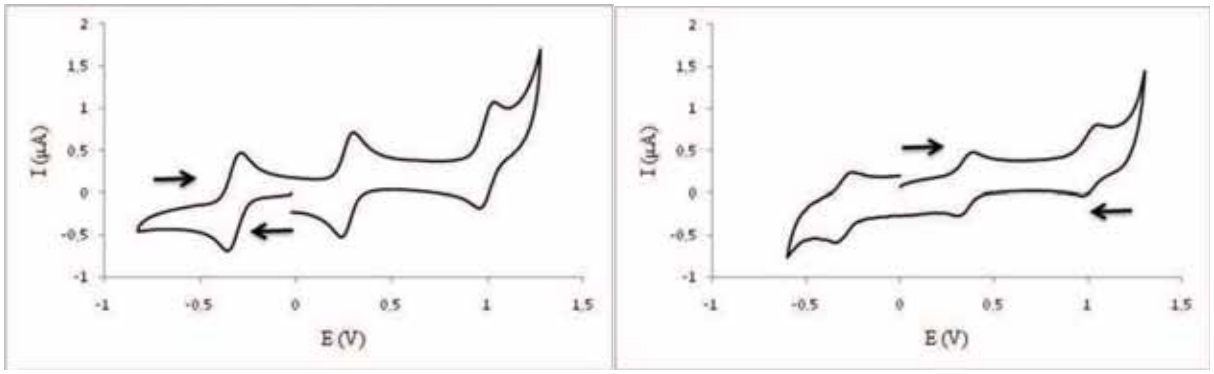

Figure 5.8. *Cyclic voltammograms of **34** (left) and **35** (right).*

The electrochemical behaviour of the TCNE adducts **36**, **37** and [**37**][$C_3(CN)_5$] was investigated (Figure 5.9) to measure the effects of the cyanocarbon group cyclo-added to the carbon chain. As expected, the CVs of **37** and [**37**][$C_3(CN)_5$] were identical; although pentacyanopropenide anion is electrochemically active (E^0_{red} = -1.82 and E^0_{pox} = +1.18 V)[41], it was not observed in the studied range. For the symmetrical complex **36**, two 1-e oxidation processes are observed at E^0_1 = +0.28 and E^0_2 = +0.48 V, with the separation between the two waves being ΔE = 0.20 V, giving $K_c = 2.4 \times 10^3$. Cycloaddition of TCNE to the central C≡C triple bond of the C_6 chain thus significantly changes the electrochemistry. The cyanocarbon group, which is strongly electron-withdrawing, captures some electron density from the electron-rich Fe(dppe)Cp* units, so that **36** is harder to oxidise than **30** (by 0.70 V). This indicates a strong contribution of the mesomeric form **36B**, the positively charged Fe(dppe)Cp* moiety being more difficult to oxidise than in the neutral configuration. Strong decreases of ΔE [ΔE(**30**) = 0.55 *vs* ΔE(**36**) = 0.20 V] and the comproportionation constant ($K_c = 2.1 \times 10^9$ for **30** *vs* 2.4×10^3 for **36**) values are observed, suggesting that the mixed-valence species is thermodynamically very much less stable for **36** than for **30**. It can also be suggested that electronic communication through the modified C_6 bridge in **36** does not completely disappear and is still significant (the two waves are well-separated). Comparison of **34** and **37** shows a similar result: complex **34** is easier to oxidise than **37** (by 0.67 V) which also suggests a strong contribution from the mesomeric form **37B**, and the K_c value slightly decreasing ($K_c = 1.0 \times 10^{10}$ for **34** *vs* 9.6×10^8 for **37**). In the CV of **37**, a third wave close to the solvent front was observed at -1.31 V, although its reversibility could not be measured. This 1-e process was attributed to reduction of the cyanocarbon fragment on the bridge, the $C(CN)_2$ groups stabilising the resulting anionic species. This process was not observed in compound **36**, probably because it was masked by the solvent front.

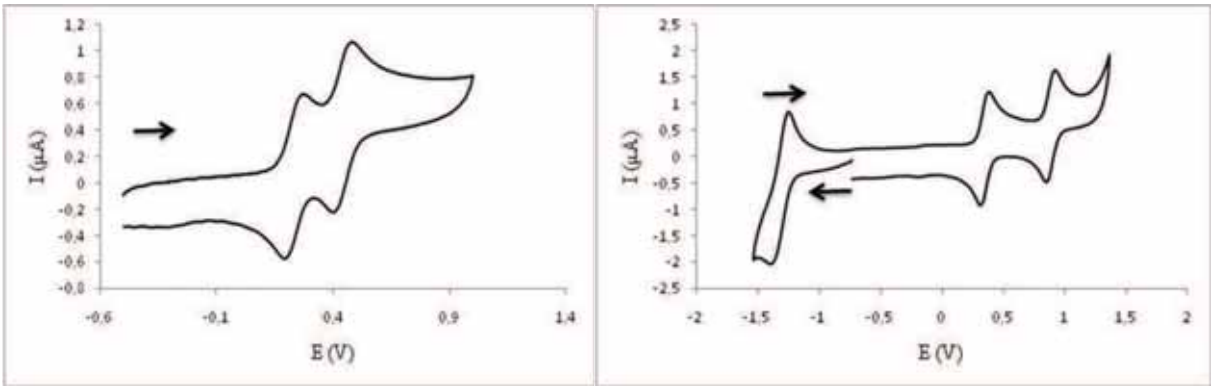

Figure 5.9. *Cyclic voltammograms of* ***36*** *(left) and* ***37*** *(right).*

Comparisons of electrochemical properties of the different bimetallic hexatriynyl complexes synthesised in this Chapter with other related complexes suggest that when the length of the carbon chain increases, the ΔE and the K_c values decrease, which indicates that the thermodynamical stability of the mixed-valence species decreases (possibly together with the electronic communication between metal fragments). This observation is also true for unsymmetrical bimetallic complexes; for example, diynyl complex {Cp*(dppe)Fe}(C≡CC≡C){Ru(dppe)Cp*} **40** is easier to oxidise than hexatriynyl complex **34** by 0.27 V, ΔE decreasing by 0.18 V. Additionally, when an organic unit such as $SiMe_3$ is replaced by an electron-rich metal fragment, the oxidation potentials decrease considerably. Metal fragments can be ranked by ease of oxidation: Fe(dppe)Cp* > Ru(dppe)Cp* > Ru(dppe)Cp which is consistent with iron being easier to oxidise than ruthenium, and an increase in electron donor power of the Cp* ligand over Cp. Finally, when the organic C_6 bridge is modified by addition of TCNE, the oxidation potentials increase significantly by ca 0.7 V as a result of the strong electron-withdrawing properties of the cyanocarbon.

5.3.4 Synthesis and characterisation of [{Cp'(dppe)M}(C≡CC≡CC≡C){M(dppe)Cp'}]$^{n+}$ (M = Fe, Ru; Cp' = Cp, Cp; n = 1, 2)*

Guided by the electrochemical data and with the aim of studying the behaviour and physical properties of mixed-valence complexes containing two metal fragments linked by a C_6 chain, 35-e species have been generated by simple chemical oxidation using $[FeCp_2]PF_6$ as the oxidising agent. A symmetrical dication containing a C_6 chain bridging two Fe(dppe)Cp* fragments has also been synthesised and studied.

Syntheses of the mixed-valence complexes [**30**]PF_6, [**31**]PF_6, [**34**]PF_6 and [**35**]PF_6 were achieved via the same method in each case (Scheme 5.12). Neutral bimetallic complexes were reacted with one equivalent of $[FeCp_2]PF_6$ in a THF or dichloromethane solution at -78°C. After stirring during one hour, the temperature was allowed to warm up slowly to room temperature. During this warming process, the deep red mixed-valence complexes [**31**]PF_6 and [**35**]PF_6 further reacted to give other products (as shown by a colour change from deep red to deep blue or purple) (see Chapter Six). The two other salts [**30**]PF_6 and [**34**]PF_6 were more stable and could be isolated by precipitation with pentane or hexane. Then, after several washes with the precipitating solvents, the mixed-valence complexes [**30**]PF_6 and [**34**]PF_6 were obtained as dark brown powders in 77% yield in both cases.

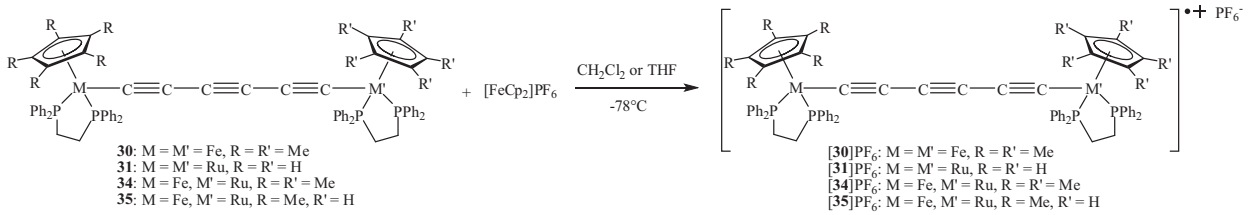

30: M = M' = Fe, R = R' = Me
31: M = M' = Ru, R = R' = H
34: M = Fe, M' = Ru, R = R' = Me
35: M = Fe, M' = Ru, R = Me, R' = H

[**30**]PF_6: M = M' = Fe, R = R' = Me
[**31**]PF_6: M = M' = Ru, R = R' = H
[**34**]PF_6: M = Fe, M' = Ru, R = R' = Me
[**35**]PF_6: M = Fe, M' = Ru, R = Me, R' = H

Scheme 5.12

The stable paramagnetic mixed-valence complexes were characterised by IR spectroscopy with the ν(C≡C) bands at 2005, 1818 and 2014, 1881, 1824 cm^{-1} for [**30**]PF_6 and [**34**]PF_6, respectively (IR data are described in more detail in Section 5.3.5). In the high resolution ES-mass spectra, $[M]^+$ ions were found at *m/z* 1250.3755 (calculated: 1250.3753) for [**30**][PF_6] and 1296.3596 (calculated: 1296.3447) for [**34**][PF_6].

A second oxidation affording the dicationic salt [**30**][PF_6]$_2$ was achieved by reacting the monocationic salt [**30**]PF_6 with one equivalent of $[FeCp_2]PF_6$ in dichloromethane at -78°C (Scheme 5.13). When reaction was complete and after purification, [**30**][PF_6]$_2$ was obtained as a dark green powder in 83% yield.

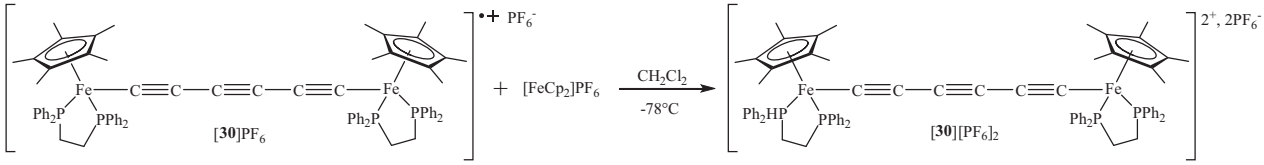

[**30**]PF_6 [**30**][PF_6]$_2$

Scheme 5.13

The IR spectrum of [**30**][PF_6]$_2$ is complex and displayed several bands in the ν(C≡C) region at 2162, 2062, 2008, 1947 and 1826 cm^{-1} (see Section 5.3.5). However, NMR data displayed original features: in the ^{31}P NMR spectrum resonances of the four equivalent phosphorus atoms of the dppe ligands were surprisingly found as a broad singlet at δ 11.1 (Figure 5.10) and the PF_6 anion as a septuplet at δ -145.4 ($^1J_{PF}$ = 710 Hz). In the ^1H NMR spectrum, the Cp* protons were observed at δ 0.78 (s) while the dppe-CH_2 were multiplets at δ 2.76 and 4.32. These NMR chemical shifts are unusual for the Fe(dppe)Cp* fragment, neutral or not, indicating that compound [**30**][PF_6]$_2$ exhibits paramagnetic behaviour. Magnetic studies of the dication [**30**][PF_6]$_2$ are described in Section 5.3.9.

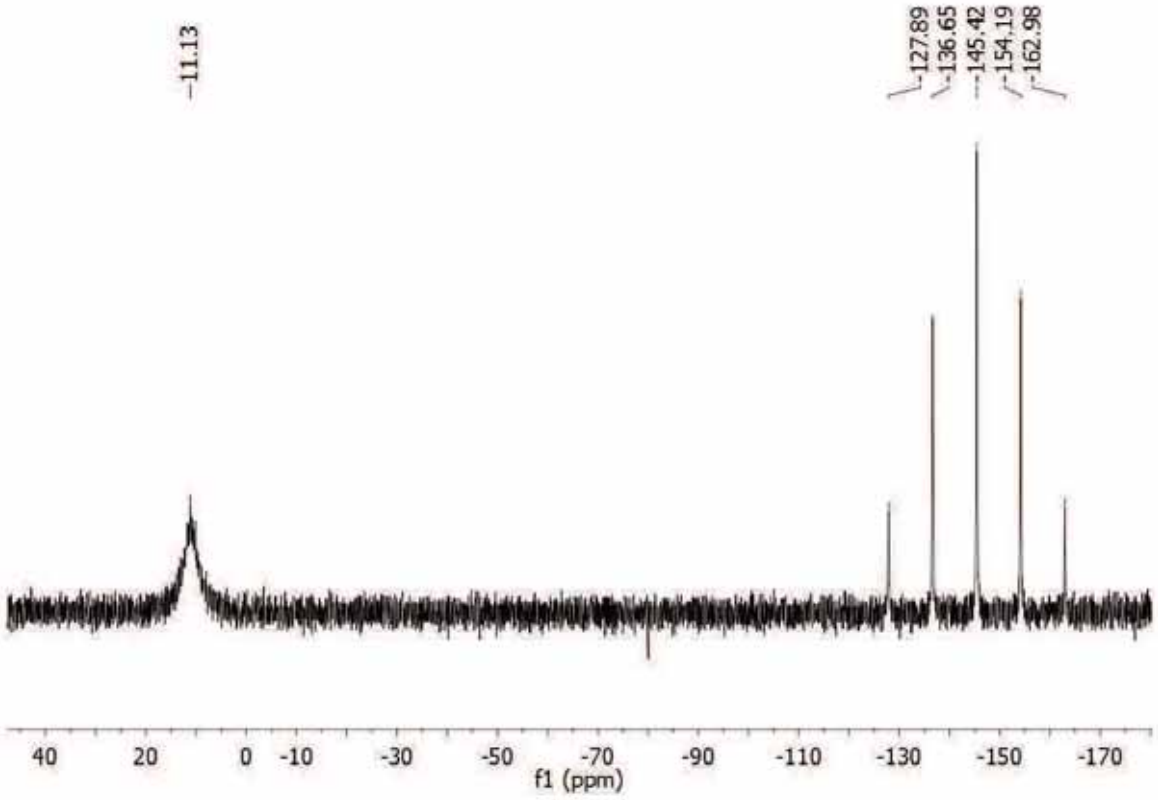

Figure 5.10. *^{31}P NMR of [30][PF_6]$_2$.*

Indeed, in the dication [**30**][PF_6]$_2$ an equilibrium may exist between the singlet and triplet states (Figure 5.11), the unpaired electrons being spin-opposed (singlet, s = 0, [**30A**][PF_6]$_2$ and [**30B**][PF_6]$_2$) or spin-aligned (triplet, s = 1, [**30C**][PF_6]$_2$). A singlet-triplet equilibrium can exist if the singlet-triplet energy gap (ΔG_{ST}) is small enough. As the NMR spectra were recorded at room temperature, this suggests that the singlet-triplet exchange rate might be fast on the NMR time scale. The diamagnetic form [**30A**][PF_6]$_2$ probably makes only a small contribution to the electronic configuration of [**30**][PF_6]$_2$, the ^{31}P NMR

of such diamagnetic dicationic species being at ca 90 ppm[6, 22b]. Other related dicationic complexes such as [{Cp*(dppe)Fe}$_2$(μ-C≡CC≡C)][PF$_6$]$_2$[22b], [{Cp*(dppe)Fe}(C≡CC≡C){RuL$_2$Cp'}][PF$_6$]$_2$ (L$_2$ = 2PPh$_3$, dppe; Cp' = Cp, Cp*)[26c] and [{Cp*(dppe)Fe}(C≡CC≡C){Re(NO)(PPh$_3$)Cp*}][PF$_6$]$_2$[26b] show similar paramagnetic behaviour.

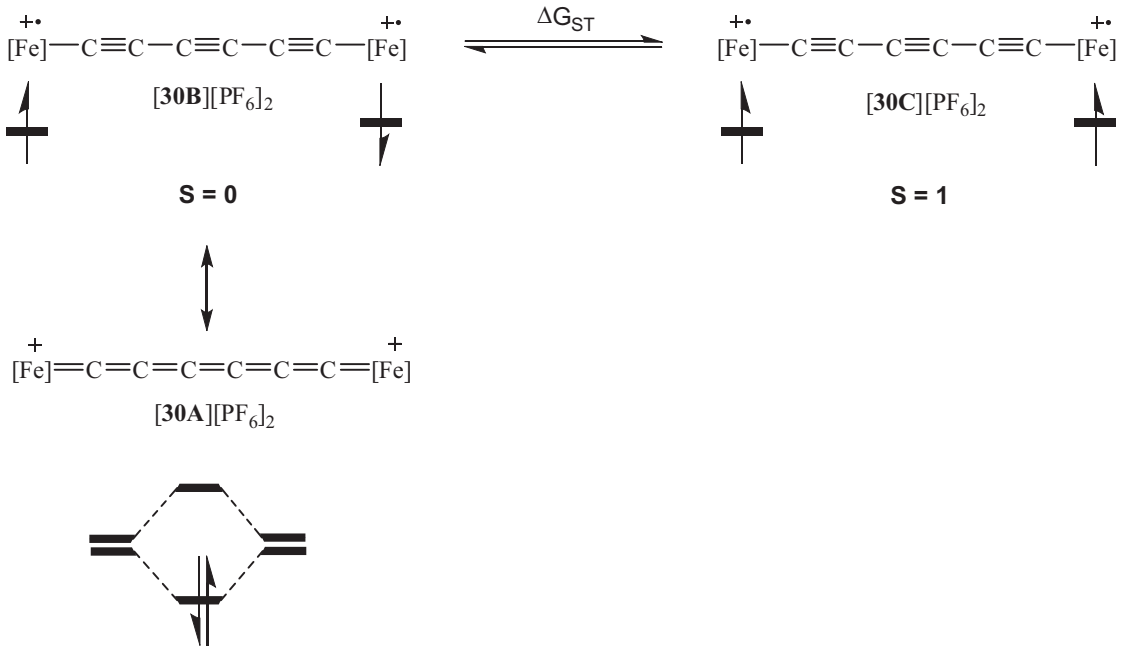

Figure 5.11. *Singlet-triplet states equilibrium for [30][PF$_6$]$_2$.*

Molecular structures

X-ray studies were carried out on the two stable mixed-valence complexes [**30**]PF$_6$ and [**34**]PF$_6$ together with the stable dicationic species [**30**][PF$_6$]$_2$. Complex [**30**]PF$_6$ crystallised by slow diffusion of pentane into a concentrated solution in dichloromethane. The asymmetric unit contains half a molecule of [**30**]PF$_6$ and 2.5 molecules of dichloromethane (the symmetry element is a C$_2$ axis passing through the central carbon-carbon bond). The crystal is monoclinic *P*2/*c*. Crystallisation of [**30**][PF$_6$]$_2$ was achieved via the same method as for [**30**]PF$_6$ but using toluene instead of pentane. Similarly, the unit cell incorporates half a molecule of [**30**][PF$_6$]$_2$ and crystals are monoclinic *P*2$_1$/*n* (the symmetry element is an inversion centre in the middle of the central carbon-carbon bond). ORTEP representations of [**30**]PF$_6$ and [**30**][PF$_6$]$_2$ are given in Figure 5.12 and key parameters are collected in Table 5.7.

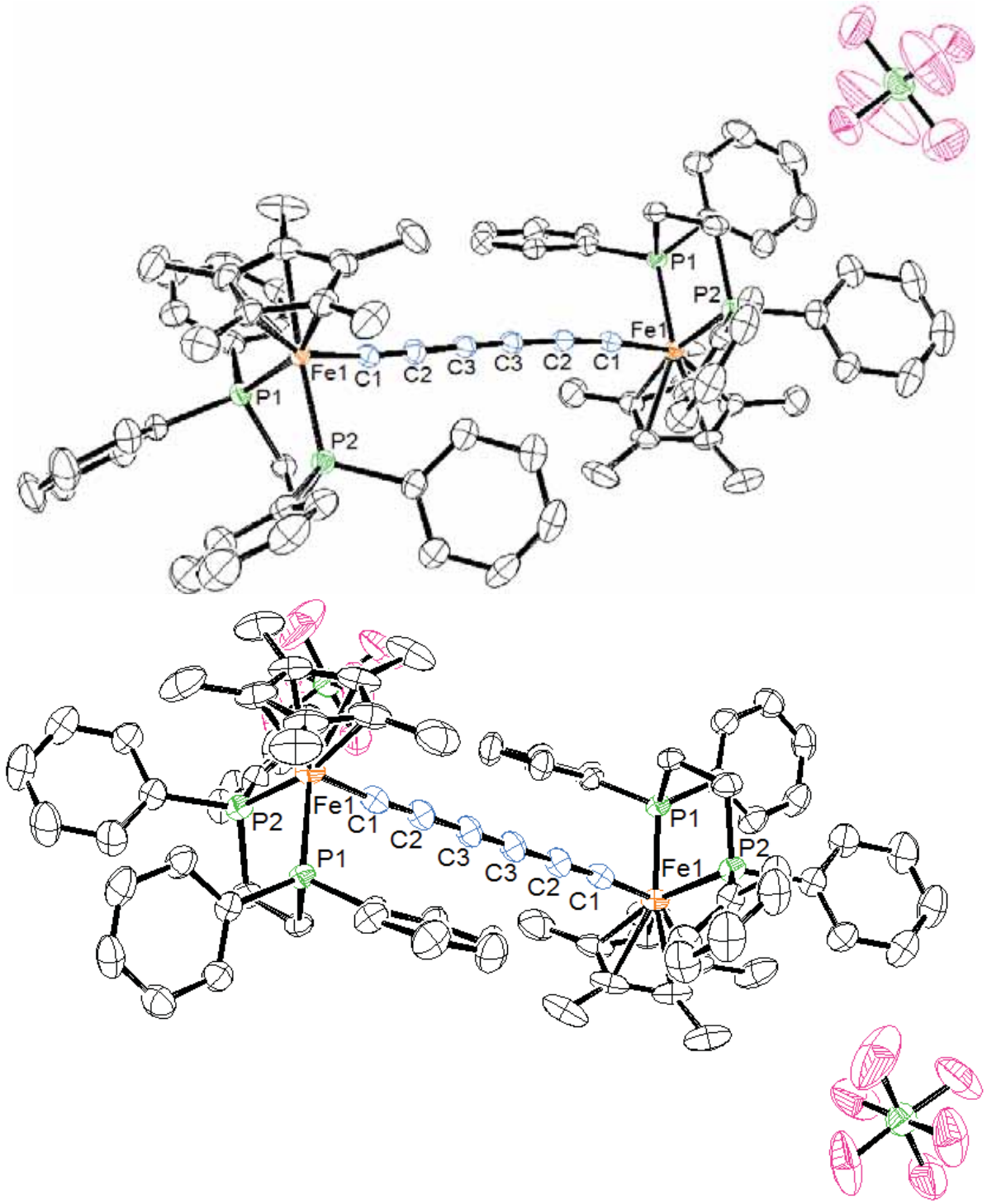

Figure 5.12. *ORTEP view of [{Cp*(dppe)Fe}$_2$(μ-C≡CC≡CC≡C)]PF_6 [**30**]PF_6 (top) and [{Cp*(dppe)Fe}$_2$(μ-C≡CC≡CC≡C)][PF_6]$_2$ [**30**][PF_6]$_2$ (bottom).*

Table 5.7. Selected structural parameters for [**30**]PF_6 and [**30**][PF_6]$_2$.

	[**30**][PF_6]	[**30**][PF_6]$_2$
Bond Distances (Å)		
Fe-P(1)	2.2114(7)	2.2331(6)
Fe-P(2)	2.2251(8)	2.2514(7)
Fe-Cp*$_{cent}$	1.767	1.778
Fe-C(1)	1.822(3)	1.811(2)
C(1)-C(2)	1.251(4)	1.255(3)
C(2)-C(3)	1.342(3)	1.325(3)
C(3)-C(3)	1.237(5)	1.246(5)
Bond Angles (°)		
P(1)-Fe-P(2)	84.97(3)	82.54(2)
C(1)-Fe-P(1)	85.72(8)	87.07(8)
C(1)-Fe-P(2)	87.09(8)	89.35(8)
Fe-C(1)-C(2)	174.1(2)	175.6(2)
C(1)-C(2)-C(3)	177.0(3)	179.1(3)
C(2)-C(3)-C(3)	176.47(18)	179.8(4)

The iron fragments have the expected pseudo-octahedral geometry and the carbon chains between the two metallic centres are close to linear for both structures. Bond lengths in the two oxidised species are significantly different in comparison with typical neutral Fe(II) distances, with Fe-P and Fe-Cp*$_{cent}$ distances increasing while the Fe-C(1) distances decrease. The character of the carbon chain is also affected after chemical oxidation, the single and triple bonds being shortened and lengthened, respectively, which indicates that the contribution of the cumulenic form is more important upon oxidation. Possible resonance forms of the radical cation in [**30**]PF_6 are represented in Scheme 5.14. Small differences in bond lengths in the monocation [**30**]PF_6 and the dication [**30**][PF_6]$_2$ are also observed, the cumulenic character being slightly larger in [**30**][PF_6]$_2$. However, these slight differences in the structures of [**30**]PF_6 and [**30**][PF_6]$_2$ are hardly significant. As expected, these observations are consistent with changes occurring in the electronic structure of Cp*(dppe)Fe-C_6-Fe(dppe)Cp* upon oxidation. The electron density is weaker at the metal centres resulting in less back-bonding to the phosphorus atoms (M-P distances increase) and an increase of the cumulenic contribution, confirmed by the shortening of the M-C and C-C bond lengths and the elongation of the C≡C triple bonds in the bridge.

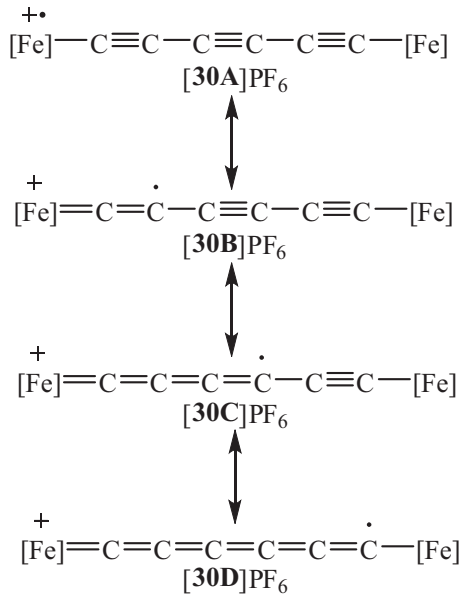

Scheme 5.14. *Selected resonance structures for [**30**]PF_6.*

Crystals of the mixed iron-ruthenium complex [**34**]PF_6 were obtained by slow diffusion of hexane into a dichloromethane solution. It crystallised with two half-molecules in the asymmetric unit (the symmetry element being a C_2 axis passing through the central C≡C triple bond) in which the iron and ruthenium atoms are disordered 50:50, the hexafluorophosphate anion also being heavily disordered, resulting in a high resolution parameter R = 0.082. The unit cell is monoclinic $C2/c$. A molecule of [**34**]PF_6 is shown in Figure 5.13 while selected structural parameters are collected in Table 5.8.

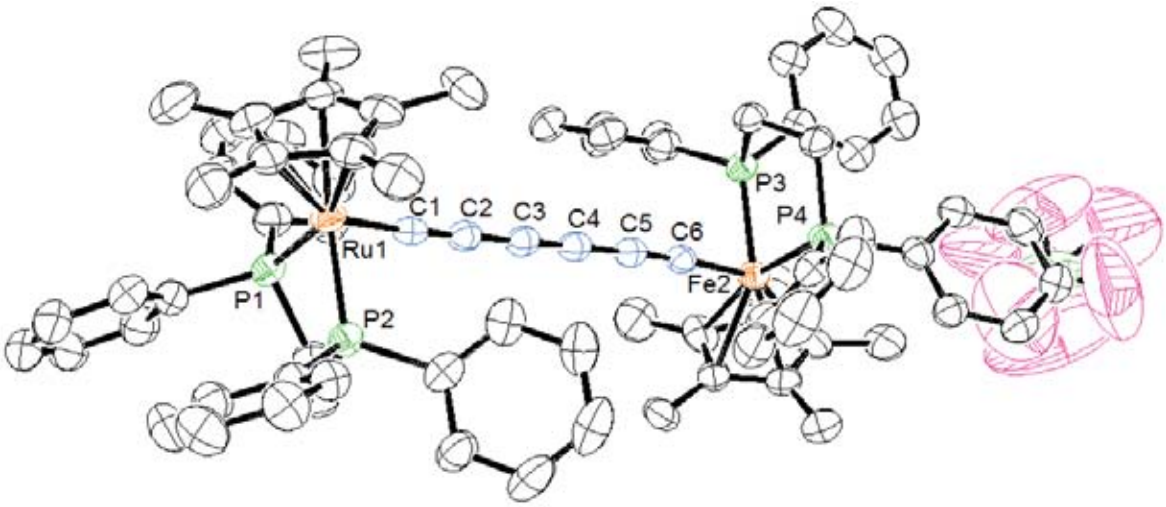

Figure 5.13. *ORTEP view of [{Cp*(dppe)Fe}(C≡CC≡CC≡C){Ru(dppe)Cp*}]PF_6 [**34**]PF_6.*

Table 5.8. Selected structural parameters for [**34**]PF_6 (Italicised values refer to the second half molecule).

Bond Distances (Å)		**Bond Angles (°)**	
M-P(1,3)	2.2393(13), *2.2491(12)*	P(1,3)-M-P(2,4)	84.38(5), *84.60(4)*
M-P(2,4)	2.2497(13), *2.2521(12)*	C(1,6)-M-P(1,3)	84.51(14), *83.51(13)*
M-Cp*(1,2)$_{cent}$	1.821, *1.829*	C(1,6)-M-P(2,4)	87.45(14), *87.39(13)*
M-C(1,6)	1.871(5), *1.853(4)*	M-C(1,6)-C(2,5)	175.7(4), *176.2(4)*
C(1,6)-C(2,5)	1.227(6), *1.231(6)*	C(1,6)-C(2,5)-C(3,4)	177.4(5), *177.7(5)*
C(2,5)-C(3,4)	1.340(6), *1.333(6)*	C(2,3)-C(3,4)-C(4,3)	177.9(7), *179.2(3)*
C(3)-C(4)	1.239(9), *1.225(9)*		

As expected, the metal sites adopt a pseudo-octahedral geometry while the carbon bridges are close to linear with angles in the range 175.7(4)-179.2(3)°. As described above, bond lengths are affected by the oxidation process: M-P and M-Cp*$_{cent}$ distances are longer and M-C(1,6) distances shorter than typical neutral M(II) bond lengths. However, bond lengths around the metal atoms are the average of iron and ruthenium distances and generally longer than those in the analogous diiron complex [**30**]PF_6, where the Fe-C(1,6) are shorter [1.822(3) and 1.811(2) versus 1.871(5) and 1.853(4) Å].

5.3.5 IR spectroscopy

IR spectroscopy, used as a probe, is known to be an efficient method to measure the extent of the electron delocalisation in mixed-valence systems. Indeed, if the IR stretching mode for a given mixed-valence compound occurs at a frequency intermediate between those of the corresponding unoxidized and dioxidized species, then it can be concluded that the intramolecular electron transfer rate is fast on the IR time scale (10^{-13} s)[22b]. The ν(C≡C) bands of the hexatriynyl-bimetallic complexes and their oxidised species synthesised in this Chapter are summarised in Table 5.9.

Table 5.9. IR ν(C≡C) band stretchings for [{Cp'(dppe)M}(C≡CC≡CC≡C){M(dppe)Cp'}]$^{n+}$ (M = Fe, Ru; Cp' = Cp, Cp*; n = 0, 1, 2).

Compound	$\nu_{C\equiv C}$ (cm^{-1})
{Cp*(dppe)Fe}$_2$(μ-C≡CC≡CC≡C) **30**	2040[a]
{Cp(dppe)Ru}$_2$(μ-C≡CC≡CC≡C) **31**	2063[b]
{Cp*(dppe)Fe}(C≡CC≡CC≡C){Ru(dppe)Cp*} **34**	2110, 2050, 1969[c]
{Cp*(dppe)Fe}(C≡CC≡CC≡C){Ru(dppe)Cp} **35**	2048, 1920[b]
[{Cp*(dppe)Fe}$_2$(μ-C≡CC≡CC≡C)]PF_6 [**30**]PF_6	2005, 1818[d] 2008, 1829[b]
[{Cp*(dppe)Fe}(C≡CC≡CC≡C){Ru(dppe)Cp*}]PF_6 [**34**]PF_6	2014, 1881, 1824[b]
[{Cp*(dppe)Fe}$_2$(μ-C≡CC≡CC≡C)][PF_6]$_2$ [**30**][PF_6]$_2$	2162, 2062, 2008, 1947, 1826[d]

[a]KBr. [b]CH_2Cl_2. [c]Powder. [d]Grind crystals in KBr.

IR spectra of the three redox states of [{Cp*(dppe)Fe}$_2$(μ-C≡CC≡CC≡C)][PF_6]$_n$ (n = 0, 1,2) **30**, [**30**]PF_6 and [**30**][PF_6]$_2$, respectively, are compared in Figure 5.14. As expected, the IR spectrum of the neutral complex {Cp*(dppe)Fe}$_2$(μ-C≡CC≡CC≡C) **30** exhibits only one strong ν(C≡C) band which is assigned to the two M-C≡C triple bonds, the central ν(C≡C) vibration being forbidden by symmetry. Upon 1-e oxidation of **30**, if the mixed-valence complex **30**$^{\bullet+}$ is fully delocalised on the IR time scale, the symmetry should be conserved and only one ν(C≡C) band should be observed. However, if the system is localised on the IR time scale (the electron transfer rate is slow on the IR time scale), the symmetry would be broken and three ν(C≡C) bands should be observed: the Fe-C≡C, [Fe-C≡C]$^{\bullet+}$ and the central ν(C≡C) vibration are all allowed and should all appear[25, 42]. The mixed-valence complex [**30**]PF_6 which has been characterised as fully delocalised on the X-ray time scale (structure centro-symmetric) exhibits two strong ν(C≡C) vibrations at 2008 and 1829 cm^{-1} in the IR spectrum (in CH_2Cl_2). Observation of two ν(C≡C) bands in the IR spectrum of [**30**]PF_6 is unexpected as it has been predicted that either one or three ν(C≡C) bands should be observed for the delocalised or localised systems, respectively. These two ν(C≡C) bands could be due to different conformations in solution; however, the IR spectrum recorded in KBr using powdered crystals is similar [ν(C≡C) at 2005 and 1818 cm^{-1}], so this hypothesis can be dismissed. The strong symmetric ν(C≡C) vibration at 1829

cm^{-1} could be assigned to both Fe-C≡C triple bonds and the higher energy ν(C≡C) band at 2008 cm^{-1} to the forbidden central ν(C≡C) vibration. The apparent removal of the degeneracy might be explained by the observation of a vibronic coupling[43] between the intramolecular electron transfer and some of the molecular vibrational states. This hypothesis can be confirmed or not by observation of the vibronic coupling in absorption spectroscopy (see Section 5.3.7 and 5.3.8).

The IR analysis of the dication [**30**][PF_6]$_2$, recorded in KBr using powdered crystals, displayed a complex spectrum [Figure 5.14 (c)] with many ν(C≡C) bands of different intensities at 2162, 2062, 2008, 1947 and 1826 cm^{-1}. This unexpected and complex IR ν(C≡C) spectrum is difficult to interpret. However, the two strong bands at 2162 and 1947 cm^{-1}, together with others in the 1826-2162 region, seem to indicate that there is no reduction in the C≡C bond order in comparison with [**30**]PF_6. An identical phenomenon has been described for the dication [{Cp*(dppe)Fe}$_2$(μ-C≡CC≡C)][PF_6]$_2$[22b], which suggests that there is no or only a weak contribution from the cumulenic resonance structure [**30A**][PF_6]$_2$ (Figure 5.11), in contrast with the related ruthenium[23c] and rhenium[21a] examples.

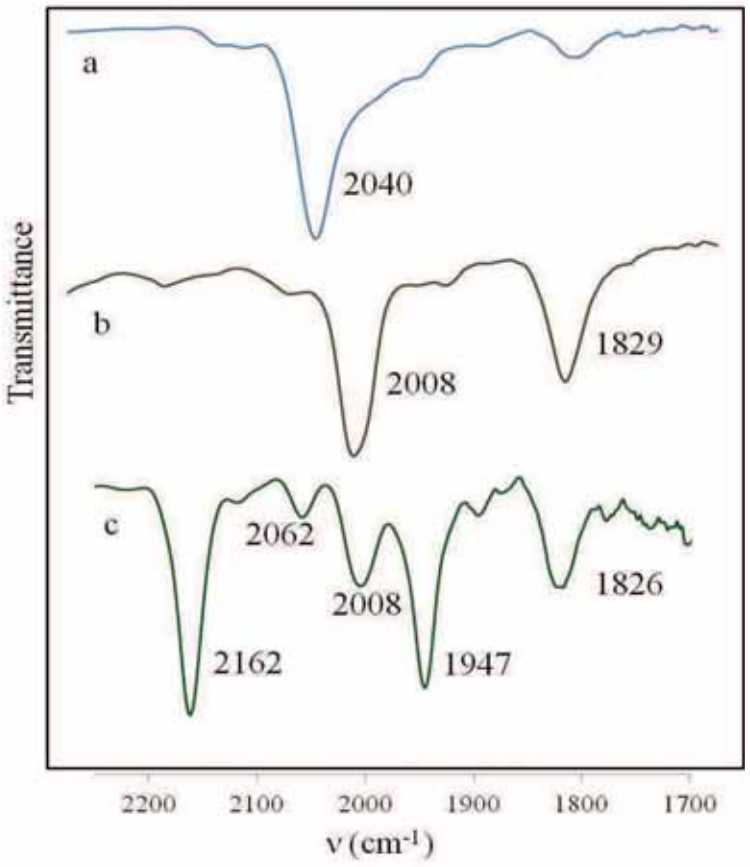

Figure 5.14. *IR spectra for [{Cp*(dppe)Fe}$_2$(μ-C≡CC≡CC≡C)][PF$_6$]$_n$ {(a) n = 0, **30** in KBr; (b) n = 1, [**30**]PF$_6$ in CH$_2$Cl$_2$; (c) n = 2, [**30**][PF$_6$]$_2$ in KBr (the spectrum in CH$_2$Cl$_2$ was flat)} in the 1800-2250 cm^{-1} region.*

As expected, in the IR spectrum of the unsymmetrical neutral complex **34**, where the symmetry is broken in comparison with the diiron complex **30**, three ν(C≡C) bands corresponding to the three different C≡C triple bonds in the molecule are observed. The ν(C≡C) band at 2110 cm^{-1} can probably be assigned to the central C≡C triple bond due to its high vibrational energy in comparison with the other two at 2050 and 1969 cm^{-1}, which might correspond to the two M-C≡C triple bonds. Upon oxidation, in [**34**]PF$_6$, reduction of bond order is observed for the three C≡C triple bonds which are found at 2014, 1881 and 1824 cm^{-1}, the first one being assigned to the central C≡C triple bond. This suggests that IR spectroscopy does not reveal charge localisation on one or the other metallic site on the IR time scale, which is unexpected for an unsymmetrical mixed-valence system.

5.3.6 EPR spectroscopy

The paramagnetic behaviour of the 35-e species described in this Chapter was investigated by EPR spectroscopy, which by measuring the signal anisotropy in these cases, is a very useful method to approximate the degree of delocalisation of the unpaired electron in the mixed-valence complexes. EPR spectroscopic data for the stable and isolable mixed-valence complexes [**30**]PF_6, [**34**]PF_6 and [**37**][$C_3(CN)_5$], together with the mixed-valence complex [{Cp*(dppe)Ru}$_2$(μ-C≡CC≡CC≡C)]PF_6 [**32**]PF_6 and some related complexes, are shown in Table 5.10. Data for the unstable mixed-valence complexes [**31**]PF_6 and [**35**]PF_6 were also collected by generating the EPR-active species "in-situ" at -78°C in dichloromethane; however, when the samples were left at room temperature for one hour, the colour of the solutions changed and the mixed-valence complex signals were no longer present. All the EPR spectra were recorded in frozen dichloromethane solutions at 67K.

Table 5.10. EPR spectroscopic data for [{M(dppe)Cp'}$_2$(μ-C≡CC≡CC≡C)]PF_6 (M = Fe, Ru; Cp' = Cp, Cp*), [**37**][$C_3(CN)_5$] and related complexes measured at 67K in CH_2Cl_2 glass.

Compound	g_1	g_2	g_3	Δg[a]	g_{iso}[b]	Ref
[{Cp*(dppe)Fe}$_2$(μ-C≡CC≡C)]PF_6 [**38**]PF_6	2.139	2.089	2.079	0.060	2.102	26c
[{Cp*(dppe)Fe}$_2$(μ-C≡CC≡CC≡C)]PF_6 [**30**]PF_6	2.133	2.133	1.996	0.137	2.087	This work
[{Cp(dppe)Ru}$_2$(μ-C≡CC≡CC≡C)]PF_6 [**31**]PF_6	2.253	2.047	1.985	0.268	2.095	This work
[{Cp*(dppe)Ru}$_2$(μ-C≡CC≡CC≡C)]PF_6 [**32**]PF_6	2.153	2.153	1.981	0.172	2.096	This work
[{Cp*(dppe)Fe}(C≡CC≡C){Ru(dppe)Cp*}]PF_6 [**40**]PF_6	2.186	2.082	1.999	0.187	2.089	26c
[{Cp*(dppe)Fe}(C≡CC≡CC≡C){Ru(dppe)Cp*}]PF_6 [**34**]PF_6	2.158	2.158	1.994	0.164	2.103	This work
[{Cp*(dppe)Fe}(C≡CC≡CC≡C){Ru(dppe)Cp}]PF_6 [**35**]PF_6	2.263	2.055	1.991	0.272	2.103	This work
[{Cp*(dppe)Fe}C≡CC(=C$(CN)_2$)C(=C$(CN)_2$)C≡C{Ru(dppe)Cp*}][$C_3(CN)_5$] [**37**][$C_3(CN)_5$]	2.480	2.023	1.974	0.506	2.159	This work

[a]$\Delta g = g_1 - g_3$. [b]$g_{iso} = (g_1 + g_2 + g_3)/3$.

Surprisingly, the EPR spectra of [**30**]PF_6, [**32**]PF_6 and [**34**]PF_6 were very similar in shape and values. For example, the EPR spectra of the diiron complex [**30**]PF_6 is shown in Figure 5.15. In the three spectra, very intense signals with a unique shape (which has never been observed before for this kind of complex) are displayed, where $g_1 = g_2$. These g-tensor values are unexpected because usually it is observed that $g_1 \neq g_2$ and the g_2 and g_3 values are very close. These special features for the mixed-valence complexes [**30**]PF_6, [**32**]PF_6 and [**34**]PF_6 seem to be due to the presence of the C_6 bridge coupling with M(dppe)Cp* fragments, as shown by comparison with other related complexes in Table 5.10. The very weak signal anisotropies (Δg = 0.137, 0.172 and 0.164 for [**30**]PF_6, [**32**]PF_6 and [**34**]PF_6, respectively) suggest that these mixed-valence systems have a large electronic delocalisation. The anisotropy in the diiron complex [**30**]PF_6 (Δg = 0.137) is larger than in the C_4 compound [**38**]PF_6 (Δg = 0.060), but is also surprisingly larger than that found in the C_8 mixed-valence complex [**42**]PF_6, where Δg = 0.109[44]. This indicates that electron delocalisation in [**30**]PF_6 does not have the anticipated average value of complexes [**38**]PF_6 and [**42**]PF_6, which contain shorter (C_4) and longer (C_8) carbon chains, respectively. In contrast, the anisotropy in the unsymmetrical complex [**34**]PF_6 (Δg = 0.164) is weaker than in the related complex containing a C_4 chain [**40**]PF_6 (Δg = 0.187), suggesting there is larger electron delocalisation in the C_6 complex [**34**]PF_6. Additionally, the anisotropy found for [**34**]PF_6 is between those of the diiron [**30**]PF_6 (smaller) and the diruthenium [**32**]PF_6 (larger). However, the signal anisotropy, which reflects delocalisation of the unpaired electron, should be larger in an unsymmetrical system such as [**34**]PF_6 in comparison with its symmetrical analogues [**30**]PF_6 and [**32**]PF_6. On the other hand, these anisotropy values are also unexpected because Δg ([**30**]PF_6) < Δg ([**32**]PF_6) (0.137 < 0.172), which contradicts the fact that electronic coupling in ruthenium should be larger than in iron analogue complexes[26c, 37].

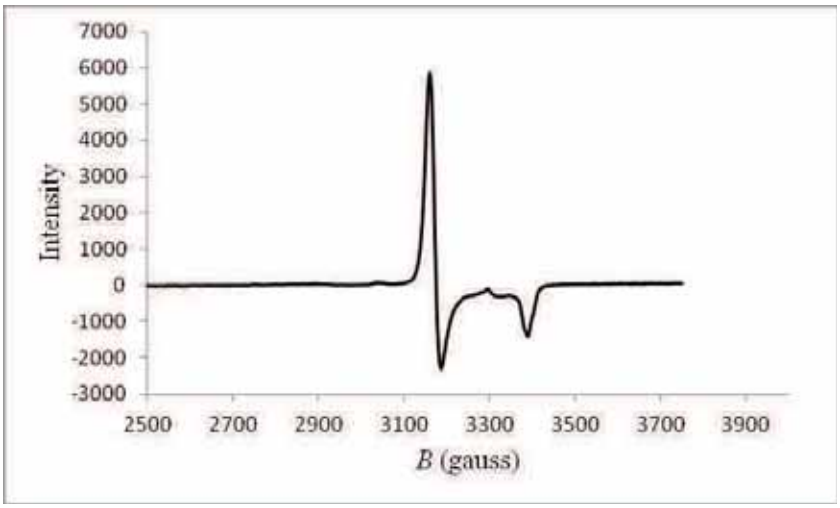

Figure 5.15. *EPR spectrum of [**30**]PF_6 measured at 67K in CH_2Cl_2 glass.*

The EPR spectrum of the symmetrical mixed-valence complex [**31**]PF_6 is shown in Figure 5.16 and exhibits an intense signal characteristic of Ru(III) species, with $g_1 = 2.253$, $g_2 = 2.047$, $g_3 = 1.985$ and $\Delta g = 0.268$. The weak signal anisotropy suggests strong delocalisation of the unpaired electron between the two metal centres. However, the anisotropy of the analogous complex [**32**]PF_6, containing Cp* instead of Cp, is weaker which is probably due to the more electron-donating Cp* groups increasing the electronic delocalisation in the molecule.

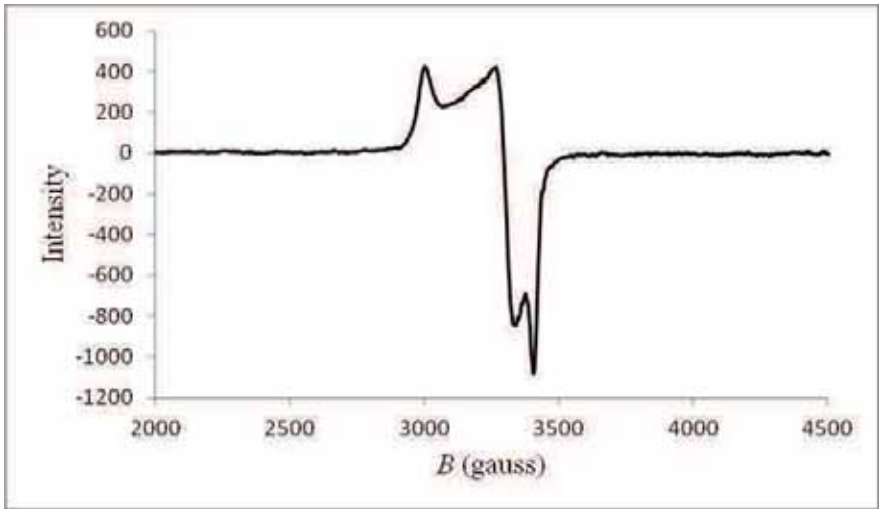

Figure 5.16. *EPR spectrum of [**31**]PF_6 measured at 67K in CH_2Cl_2 glass.*

The mixed-valence complex [**35**]PF_6 displayed an EPR signal which is more characteristic of an Fe(III) species with parameters $g_1 = 2.263$, $g_2 = 2.055$ and $g_3 = 1.991$ suggesting that the unpaired electron is more localised on the iron atom. However, the

anisotropy $\Delta g = 0.272$ is relatively small, which indicates that there is good electron delocalisation in [**35**]PF_6.

In contrast, the EPR spectrum of the unsymmetrical mixed-valence complex [**37**][$C_3(CN)_5$] (Figure 5.17), containing a modified C_6 bridge, is dramatically different from the spectra of the mixed-valence complexes described above. Indeed, the EPR signal is characteristic of an Fe(III) species with parameters $g_1 = 2.480$, $g_2 = 2.023$ and $g_3 = 1.974$. The anisotropy $\Delta g = 0.506$ is very large and can be compared with the anisotropy of mononuclear iron complexes such as Fe(C≡CPh)(dppe)Cp* (**11**) where $\Delta g = 0.489$[45]. The large anisotropy suggests that the unpaired electron is mostly localised on the iron site and that electron delocalisation in [**37**][$C_3(CN)_5$] is very weak. EPR investigations were also carried out on the neutral TCNE adduct **37** which showed a slight paramagnetic behaviour in the NMR studies but, unfortunately, **37** is EPR silent at 67K which could be due to the relaxation time; EPR measurements at 4K will be made on **37** in the future.

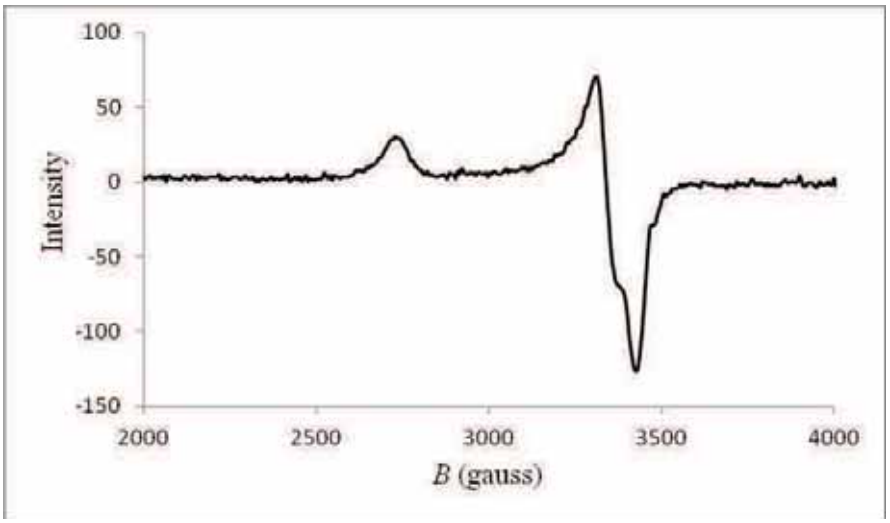

Figure 5.17. *EPR spectrum of [37][$C_3(CN)_5$] measured at 67K in CH_2Cl_2 glass.*

EPR investigations showed that electron delocalisation in the mixed-valence complexes studied in this section (apart from [**37**][$C_3(CN)_5$]) and for the unsymmetrical complexes such as [**34**]PF_6 and [**35**]PF_6 is strong. Replacing Cp* by Cp increases the signal anisotropy as seen in diruthenium complexes [**32**]PF_6 and [**31**]PF_6, and the mixed-metal complexes [**34**]PF_6 and [**35**]PF_6. Surprisingly, successive replacement of an iron by a ruthenium atom in [**30**]PF_6, [**32**]PF_6 and [**34**]PF_6 slightly increases the anisotropy.

EPR study of a single crystal of [30]PF_6

In order to investigate further the EPR characteristics of the mixed-valence complex [**30**]PF_6 and to understand the unusual g-tensor values where $g_1 = g_2$, EPR measurements on a single crystal of [**30**]PF_6 were carried out with the collaboration of Dr. Cador, to determine the orientations and values of the three g-tensors. This experiment was carried out by recording EPR spectra of the single crystal over 10° rotations using a goniometer and along the three a, b and c axes of the crystal unit cell. Figure 5.18 shows the EPR spectra obtained during a full rotation (360°) along one axis, while Figure 5.19 is a plot of values of the g-tensors (actually g^2) in the three different planes against the rotation angles. The g values have a sinusoidal relation to the rotation angles.

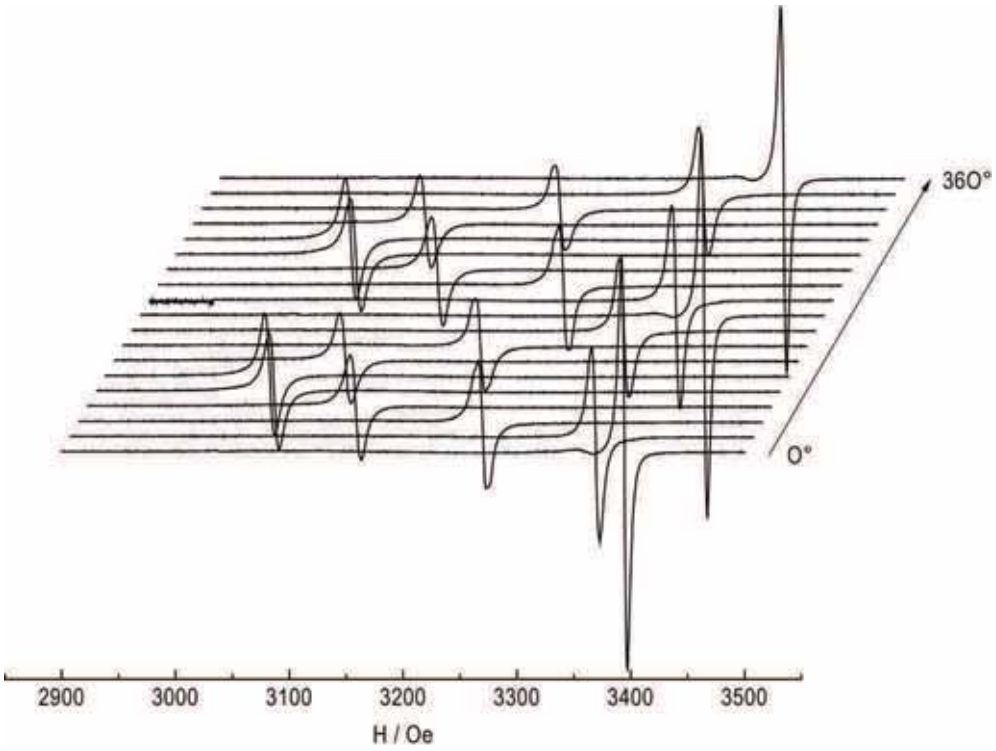

Figure 5.18. *EPR spectra of the [30]PF_6 single crystal, full rotation (0 to 360°) along one axis.*

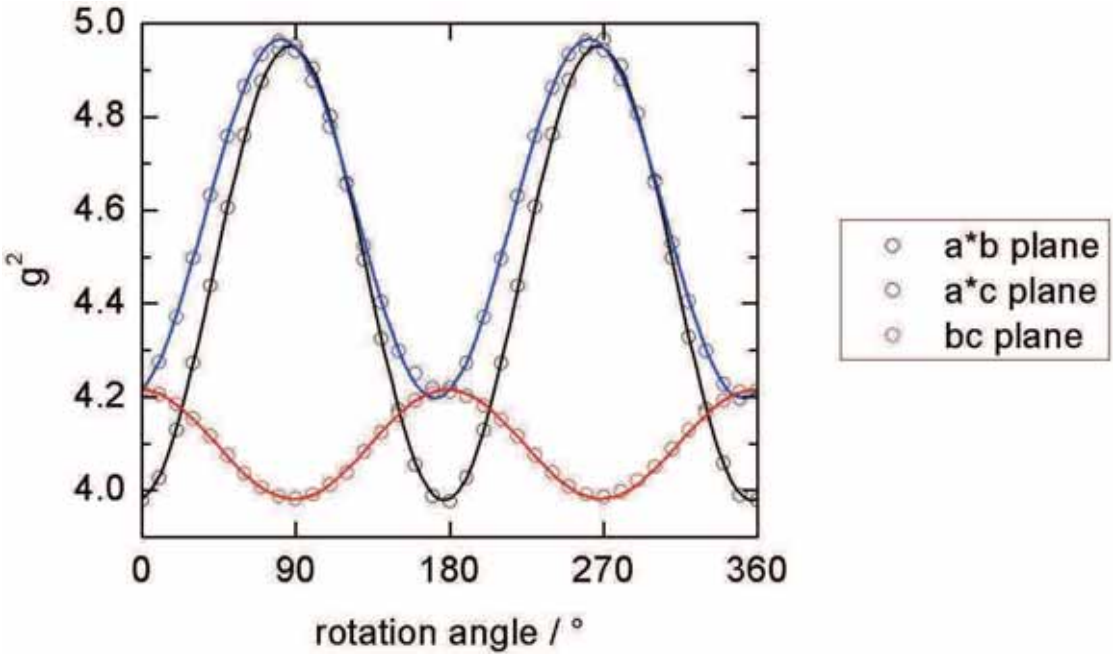

Figure 5.19. *Summary of the EPR orientation experiment.*

Afterwards, the three g-tensors were calculated using the following equations[46]:

In the a*b plane (considered as the xy plane):

$$g^2 = (gg)_{xx}\sin^2\phi + 2(gg)_{xy}\sin\phi\cos\phi + (gg)_{xx}\cos^2\phi$$

In the a*c plane (considered as the xz plane):

$$g^2 = (gg)_{xx}\sin^2\theta + 2(gg)_{xz}\sin\theta\cos\theta + (gg)_{zz}\cos^2\theta$$

In the bc plane (considered as the yz plane):

$$g^2 = (gg)_{yy}\sin^2\theta + 2(gg)_{xz}\sin\theta\cos\theta + (gg)_{zz}\cos^2\theta$$

The values of the three g-tensors are: g_1 = 2.229, g_2 = 2.040 and g_3 = 1.990 with Δg = 0.239 and g_{iso} = 2.081. These values are significantly different from the g-tensors found for [**30**]PF_6 in dichloromethane glass where $g_1 = g_2$ = 2.133 and g_3 = 1.996 (Δg = 0.137 and g_{iso} = 2.087). Such a difference between the EPR data in frozen solution and in the single crystal state is unusual. However, it seems that g_1 and g_2 have become averaged in the frozen solution [(2.229 + 2.040)/2 = 2.134] whereas g_3 did not significantly change [1.996 (in CH_2Cl_2 glass) vs 1.990 (single crystal)]. Indeed, the g_{iso} values in CH_2Cl_2 glass: 2.087, and in the single crystal state: 2.081, are almost identical. In order to rationalise the EPR

data, DFT calculations on [**30**]PF_6 were carried out by Gendron, giving values of the g-tensors of g_1 = 2.241 g_2 = 2.030 and g_3 = 1.979 (Δg = 0.262 and g_{iso} = 2.083). These theoretical values are in very good agreement with the g values obtained with the single crystal, but contrast with the g values obtained for the CH_2Cl_2 glass measurement (apart for the g_3 and g_{iso} values). At this stage, a satisfactory explanation for these differences is not available.

Orientations of the three g-tensors in the [**30**]PF_6 molecule were determined in the EPR experiment with the single crystal and are illustrated in Figure 5.20. The larger tensor g_1 deviates slightly from the Fe-Cp*$_{cent}$ axis.

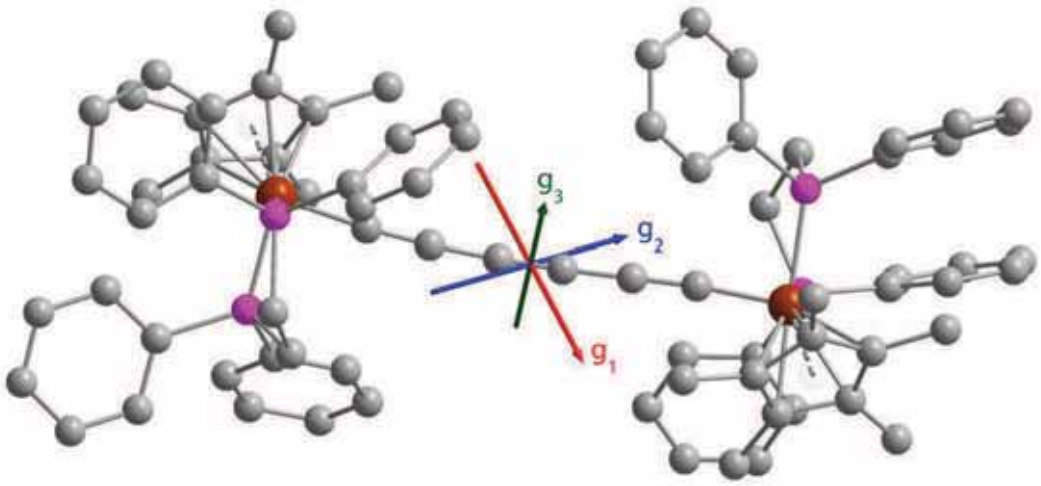

Figure 5.20. *Orientations of the three g-tensors in [30]PF_6.*

5.3.7 UV-Vis spectroscopy

The stable mixed-valence complexes [**30**]PF_6 and [**34**]PF_6 together with the stable dicationic [**30**][PF_6]$_2$ have also been studied by UV-Vis spectroscopy. Spectra recorded in dichloromethane are shown in Figure 5.21 while absorption values are collected in Table 5.11. Unfortunately, spectra of the neutral species **30** and **34** could not be recorded for comparison because of their very poor solubility.

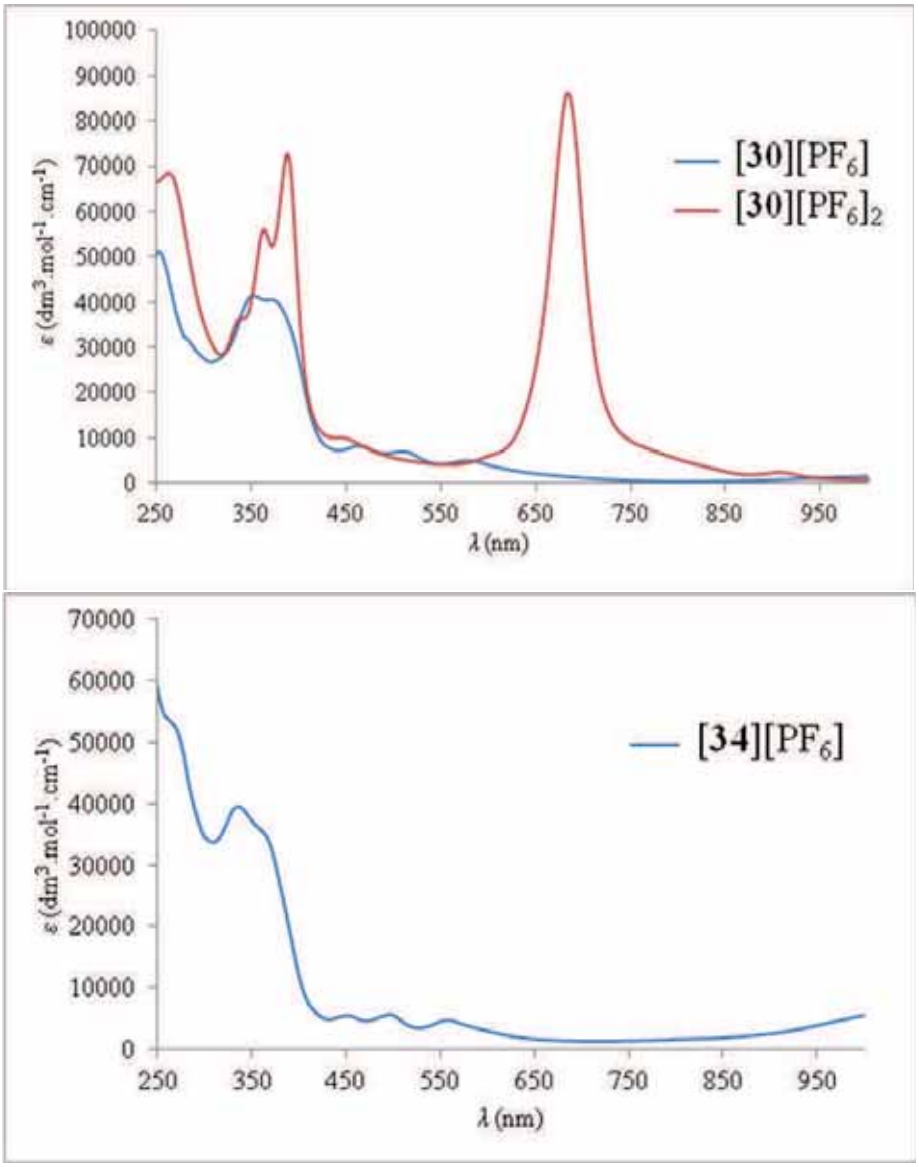

Figure 5.21. *UV-Vis spectra of [**30**]PF_6 and[**30**]$[PF_6]_2$ (top) and [**34**]PF_6 (bottom) in CH_2Cl_2.*

Table 5.11. UV-Vis data for [**30**]PF_6, [**30**]$[PF_6]_2$ and [**34**]PF_6 in CH_2Cl_2.

Compound	λ/nm (ε × 10^{-3}/dm^3.mol^{-1}.cm^{-1})
[{Cp*(dppe)Fe}$_2$(μ-C≡CC≡CC≡C)]PF_6 [**30**]PF_6	254 (51.1), 352 (41.5), 378 (40.1), 464 (8.3), 510 (7.0), 578 (5.0)
[{Cp*(dppe)Fe}$_2$(μ-C≡CC≡CC≡C)]$[PF_6]_2$ [**30**]$[PF_6]_2$	264 (68.4), 364 (55.9), 388 (72.7), 684 (86.1)
[{Cp*(dppe)Fe}(C≡CC≡CC≡C){Ru(dppe)Cp*}] PF_6 [**34**]PF_6	270 (52.3), 338 (39.4), 368 (34.0), 452 (5.4), 496 (5.5), 558 (4.6)

The UV-Vis spectra of [**30**]PF_6 and [**34**]PF_6 are very similar in shape and consist of related absorptions. Firstly, intense high energy bands are observed at 254 and 270 nm for [**30**]PF_6 and [**34**]PF_6 respectively, and are assigned to $\pi \rightarrow \pi^*$ transitions. Intense absorptions are also observed at 352, 378 and 338, 368 nm for [**30**]PF_6 and [**34**]PF_6 respectively, which are assigned to metal-to-ligand charge transfer MLCT transitions. Finally, three absorptions are found at 464, 510, 578 for [**30**]PF_6 and at 452, 496, 558 nm for [**34**]PF_6, and are assigned to ligand-to-metal charge transfer LMCT transitions. It is interesting to note that these three medium absorptions in both mixed-valence complexes [**30**]PF_6 and [**34**]PF_6, are separated by ca 2100 cm^{-1} (Figure 5.22). This value of 2100 cm^{-1} is very close to the ν(C≡C) values observed in the IR spectra of [**30**]PF_6 and [**34**]PF_6 (see Section 5.3.5), and it is tempting to suggest that these three absorptions could arise by vibronic coupling as described previously[43].

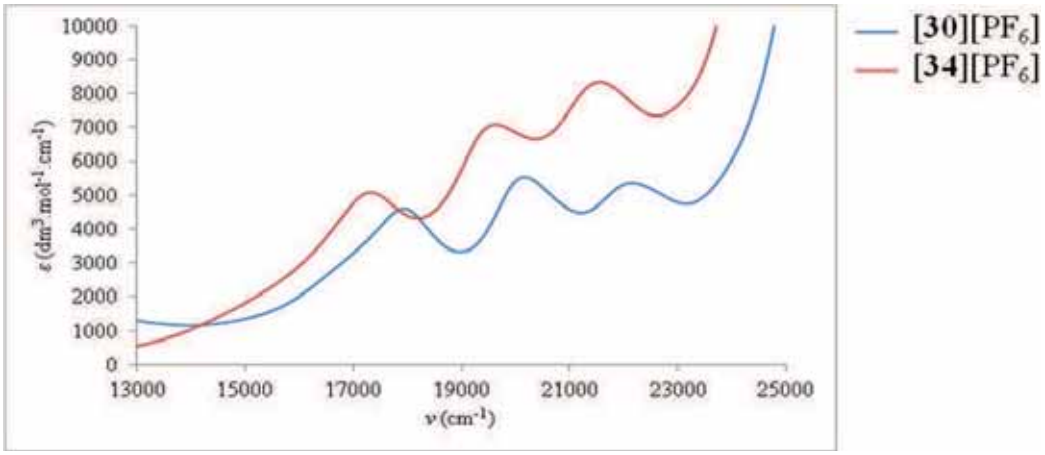

Figure 5.22. *UV-Vis spectra of [30]PF_6 and [34]PF_6 in CH_2Cl_2: 13000-25000 cm^{-1} region.*

Additionally, rather small (between 10-20 nm) hypsochromic shifts of the mixed-valence complex absorptions (apart for the $\pi \rightarrow \pi^*$ transitions at high energies) are observed when one iron atom in [**30**]PF_6 is replaced by ruthenium in [**34**]PF_6. In comparison, the spectrum of [**30**][PF_6]$_2$ presents similar absorptions in the high energy range at 264 and 364, 388 nm which are more intense than the ones found in the spectra of the mixed-valence complexes. These are assigned to $\pi \rightarrow \pi^*$ and MLCT transitions, respectively. However, a very intense band (ε = 86100 $dm^3.mol^{-1}.cm^{-1}$) is observed at lower energy (684 nm) which gives the deep green colour to the complex, is assigned to LMCT transitions. In comparison with the UV-Vis spectrum of the monocation [**30**]PF_6,

small bathochromic shifts (ca 10 nm) of the $\pi \rightarrow \pi^*$ and MLCT transitions are observed in the spectrum of [**30**][PF_6]$_2$.

UV-Vis spectra of **37** and its oxidized form [**37**][$C_3(CN)_5$] were also recorded, details being given in Figure 5.23 and Table 5.12. In both spectra, the intense high energy band at 266 nm is attributed to the $\pi \rightarrow \pi^*$ transitions. Then, three bands forming a major part of each spectrum are observed at 436, 488, 550 for **37**and at 424, 448, 594 for [**37**][$C_3(CN)_5$]. The two first high energy absorptions in both cases were attributed to MLCT transitions, while the low energy absorptions at 550 and 594 nm (for **37** and [**37**][$C_3(CN)_5$], respectively), were attributed to LMCT transitions. Upon oxidation, the MLCT transitions centred at 436 and 488 nm in **37** are shifted toward higher energies to give, in [**37**][$C_3(CN)_5$], the two bands at 424 and 448 nm, which are also slightly more intense. In contrast, a bathochromic shift of the LMCT band from 550 in **37** to 594 nm in [**37**][$C_3(CN)_5$] is found upon oxidation, together with a decrease in band intensity.

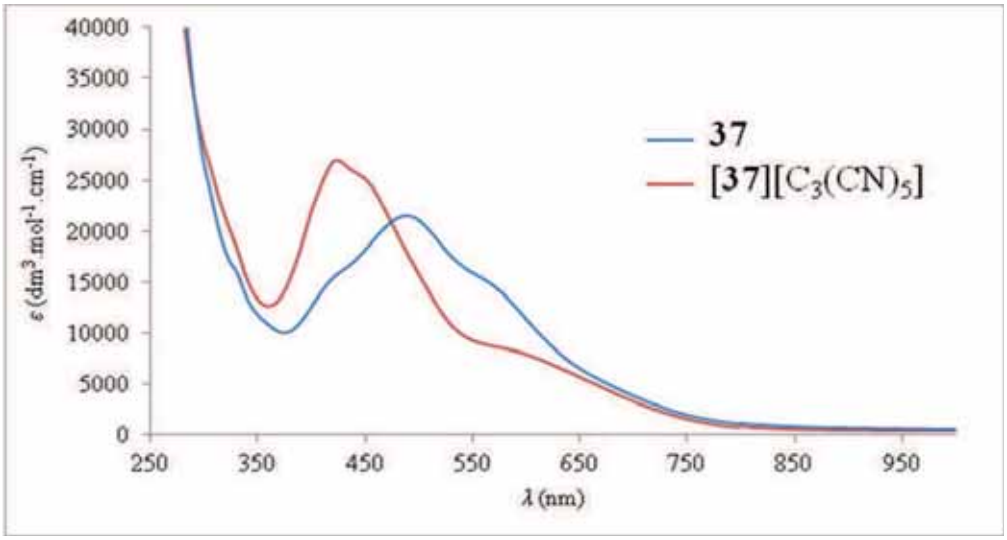

Figure 5.23. *UV-Vis spectra of 37 and [37][$C_3(CN)_5$] in CH_2Cl_2.*

Table 5.12. UV-Vis data for **37** and [**37**][$C_3(CN)_5$] in CH_2Cl_2.

Compound	λ/nm (ε × 10^{-3}/dm^3.mol^{-1}.cm^{-1})
{Cp*(dppe)Fe}C≡CC(=C(CN)$_2$)C(=C(CN)$_2$) C≡C{Ru(dppe)Cp*} **37**	266 (61.4), 436 (16.8), 488 (21.6), 550 (16.0)
[{Cp*(dppe)Fe}C≡CC(=C(CN)$_2$)C(=C(CN)$_2$) C≡C{Ru(dppe)Cp*}][$C_3(CN)_5$] [**37**][$C_3(CN)_5$]	266 (50.8), 424 (27.1), 448 (25.4), 594 (8.1)

5.3.8 Near-IR spectroscopy

Mixed-valence complexes such as [**30**]PF_6 and [**34**]PF_6 have typical signatures in the Near-IR region, the spectra generally exhibiting low-energy bands of varying intensity corresponding to the inter-valence charge-transfer (IVCT) transitions, from which the electronic coupling V_{ab} can be measured. The Near-IR spectra of [**30**]PF_6 and [**34**]PF_6, recorded in dichloromethane at room temperature, are shown in Figure 5.24. The two experimental spectra display very intense absorptions with a complex shape (several transitions) which can be deconvoluted to several Gaussian functions.

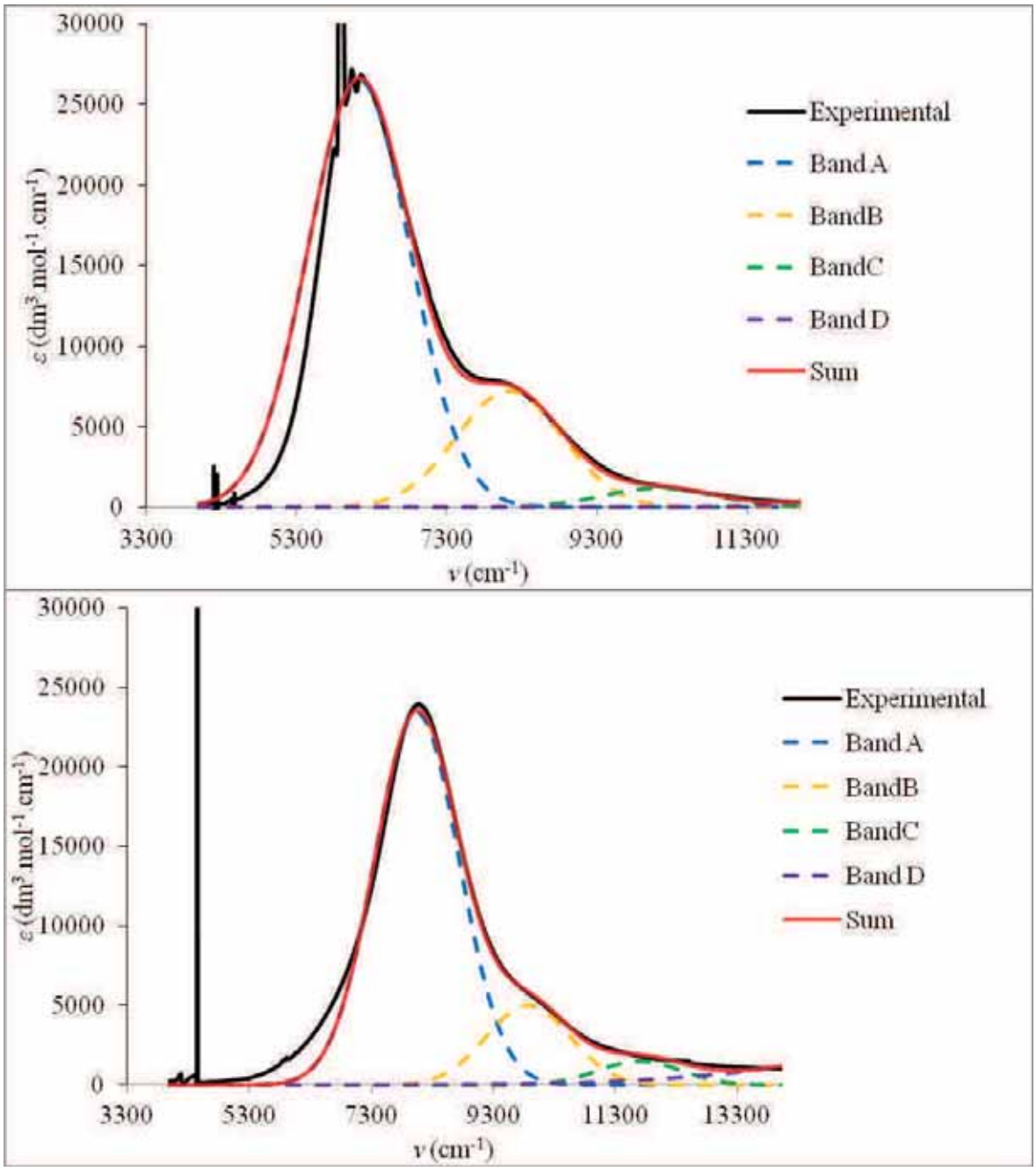

Figure 5.24. *Near-IR spectra of [**30**]PF_6 (top) and [**34**]PF_6 (bottom) in CH_2Cl_2.*

In the two spectra, the experimental curves fit well with the simulated curves which are the sum of three Gaussian functions: Bands A, B and C in both cases. Another Gaussian, Band D, was used in both simulated spectra to give a better fit in the high energy region; however, Band D originates from the Visible range and is not considered to be a Near-IR transition. Characteristic values of the different Gaussian functions are collected in Table 5.13.

Table 5.13. Near-IR data for [**30**]PF_6 and [**34**]PF_6 in CH_2Cl_2.

Compound	Band	ν_{max}/cm^{-1} ($\varepsilon \times 10^{-3}/dm^3.mol^{-1}.cm^{-1}$)	$(\Delta\nu_{1/2})_{exp}$ (cm^{-1})	R_{MM},[a] (Å)	$(\Delta\nu_{1/2})_{theo}$[b] (cm^{-1})
[**30**][PF_6]	A	6130 (26.5)	960	10.01	3763
	B	8135 (7.2)	1000		4335
	C	10140 (1.2)	1050		4840
[**34**][PF_6]	A	8050 (23.4)	980	10.01	4312
	B	9874 (5.0)	980		4776
	C	11698 (1.4)	980		5198

[a]Evaluated from X-ray structures. [b]Values calculated from Equation 5.1.

In both cases, the lower energy and very intense bands (Band A) at ν_{max} 6130 and 8050 cm^{-1} for [**30**]PF_6 and [**34**]PF_6, respectively, are attributed to the IVCT transitions. The observed full widths at half-height are $(\Delta\nu_{1/2})_{exp}$ [**30**]PF_6 = 960 and $(\Delta\nu_{1/2})_{exp}$ [**34**]PF_6 = 980 cm^{-1}, which are significantly narrower than the values calculated from Hush's theory[19] (Equation 5.1): $(\Delta\nu_{1/2})_{theo}$ [**30**]PF_6 = 3766 and $(\Delta\nu_{1/2})_{theo}$ [**34**]PF_6 = 4318 cm^{-1}.

$$\Delta\nu_{1/2} = (2310\nu_{max})^{1/2} \qquad \textbf{Equation 5.1}$$

This clearly confirms that the interpretation of the results based on class II mixed-valence systems cannot apply to [**30**]PF_6 and [**34**]PF_6, an interpretation based on class III delocalised mixed-valence systems being more likely. However, for [**34**]PF_6, this contrasts with the Hush theory where for unsymmetrical mixed-valence systems, the redox centres are weakly coupled and class II model should apply.

From a first interpretation, it was thought that the two other bands, B and C, might originate from coupling with the ligand-field (LF) transitions. However, considering the hypothesis of the vibronic coupling[43, 47] between the electron transfer and the vibrational states of the molecule which might have been observed by IR and UV-Vis spectroscopies, the Near-IR spectra have been deconvoluted with Bands B and C originating from the vibronic coupling, the separations between the three bands A, B and C in the calculated spectra being 2005 and 1824 cm^{-1} for [**30**]PF_6 and [**34**]PF_6, respectively, and correlating

with the selected ν(C≡C) bands observed in the IR spectra (Table 5.9). For the diiron complex [**30**]PF_6, the vibration centred at 2008 cm^{-1} in the IR spectrum thus originates from vibronic coupling. The only remaining ν(C≡C) band at 1829 cm^{-1} can be assigned to the two equivalent Fe-C≡C triple bonds, which indicates that [**30**]PF_6 is delocalised on the IR time scale. This is in good agreement with the Near-IR observations where the IVCT is very intense and $(\Delta\nu_{1/2})_{exp}$ is significantly narrower than $(\Delta\nu_{1/2})_{theo}$, thus mixed-valence [**30**]PF_6 can definitely be considered as a class III system.

In the spectrum of [**30**]PF_6, the experimental Band A is narrower than the Gaussian one, this kind of low-energy cut-off being characteristic of borderline class II-III mixed-valence systems and may suggest a strong electronic coupling in the mixed-valence system[48]. However, this low-energy cut-off could also arise from vibrational progressions or other band overlaps and cannot be used a priori as an indicator of strong coupling[49].

In contrast, the experimental spectrum of [**34**]PF_6 is slightly larger in the low energies than the simulated one. This could be attributed to a fifth low-intensity band at ca 6500 cm^{-1}, which could arise from the presence of another redox isomer[16c] in solution such as [**34B**]$^+$ represented in Scheme 5.15 (considering that [**34A**]$^+$ is the major redox isomer in solution).

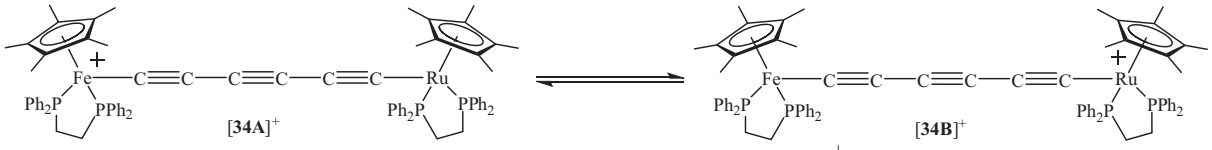

Scheme 5.15. *Redox isomers of [34]*$^+$.

The electronic coupling parameters for the mixed-valence complexes [**30**]PF_6 and [**34**]PF_6 were calculated and are listed in Table 5.14 together with literature data from related mixed-valence complexes containing shorter (C_4) or longer (C_8) carbon chains. For [**30**]PF_6, the electronic coupling term was calculated from Equation 5.2, which applies to class III mixed-valence systems, as V_{ab} = 0.38 eV. This result correlates well with V_{ab} of the related diiron complexes [**38**]PF_6 containing a C_4 chain (V_{ab} = 0.47 eV), and [**42**]PF_6 containing a C_8 chain (V_{ab} = 0.32 eV). Indeed, electronic coupling should exponentially decay with increasing chain length between the two metal sites[50].

$$V_{ab} = \nu_{max}/2 \qquad \textbf{Equation 5.2}$$

In contrast, the case of [**34**]PF_6 is more complicated because typically, in non-symmetric mixed-valence systems, the redox centres are only weakly coupled and the Hush model should apply. In this case, the electronic coupling V_{ab} should be calculated from Equation 5.3 which applies to class II mixed-valence complexes.

$$V_{ab} = 0.0205(\varepsilon_{max}\nu_{max}\Delta\nu_{1/2})^{1/2}/R_{MM'} \qquad \textbf{Equation 5.3}$$

However, since the IR data (Section 5.3.5), the very large IVCT extinction coefficient (ε_{max} = 23300) of the mixed-valence complex [**34**]PF_6 and the band width at half-height, which is narrower than Hush theory predicts, are all consistent with strong electron delocalisation, the results obtained using Equation 5.3 should be regarded with caution. Indeed, none of the unsymmetrical mixed-valence C_4 complexes based on Fe, Ru or Re[26] show such an intense IVCT transition. The electronic coupling for [**34**]PF_6 calculated from Equation 5.3, where $R_{MM'}$ is the through-space metal-metal distance of 10.096 Å (assuming that the electron-transfer distance is approximately the same as the crystallographic M···M through-space distance), gives a value of 872 cm^{-1} (0.11 eV). When the electronic coupling parameter is calculated from Equation 5.2 (in the case of a class III system), a very large value of 0.50 eV is found. These electronic coupling values are very large for an unsymmetrical complex and are significantly higher than the value found for the analogous complex [**40**]PF_6 (V_{ab} = 0.038 eV) which contains a C_4 bridge. Besides, in [**40**]PF_6, the IVCT band width at half-height $(\Delta\nu_{1/2})_{exp} \approx 1400$ cm^{-1}, is larger than the one observed in the hexatriynyl complex [**34**]PF_6, where $(\Delta\nu_{1/2})_{exp}$ = 980 cm^{-1}.

The Near-IR results obtained for the unsymmetrical mixed-valence complex [**34**]PF_6 are unexpected: the IVCT transition is very intense and the strength of the electronic coupling does not seem to obey the electronic coupling decay as a function of chain length: V_{ab}([**34**]PF_6) > V_{ab}([**40**]PF_6). By comparing the $(\Delta\nu_{1/2})_{exp}$ and V_{ab} values, which in both cases are greater for [**34**]PF_6, the Near-IR studies show that the electronic coupling in [**34**]PF_6 is stronger than that in its C_4 analogue [**40**]PF_6. This unexpected result is supported by the EPR observations: Δg ([**34**]PF_6) < Δg ([**40**]PF_6) and by IR spectroscopy where [**34**]PF_6 was shown to be delocalised on the very fast IR time scale. Further Near-IR investigations on the mixed-valence complex [**34**]PF_6 are in progress in order to clarify this result with more precision (class II or III) by studying solvent effects on the IVCT bands.

Table 5.14. IVCT transition parameters for [{Cp'(dppe)M}(C≡CC≡CC≡C){M(dppe)Cp'}]PF_6 (M = Fe, Ru; Cp' = Cp, Cp*) and related complexes.

Compound	ν_{max} (cm^{-1})	ε_{max} ($dm^3.mol^{-1}.cm^{-1}$)	V_{ab} (eV)	Ref
[{Cp*(dppe)Fe}$_2$(μ-C≡CC≡C)]PF_6 [**38**]PF_6	7541	12000	0.47[a]	22b
[{Cp*(dppe)Ru}$_2$(μ-C≡CC≡C)]PF_6 [**39**]PF_6	10195	9850	0.63[a]	23c
[{Cp*(dppe)Fe}$_2$(μ-C≡CC≡CC≡C)]PF_6 [**30**]PF_6	6130	26500	0.38[a]	This work
[{Cp*(dppe)Fe}$_2$(μ-C≡CC≡CC≡CC≡C)]PF_6 [**42**]PF_6	5107	31000	0.32[a]	27
[{Cp*(dppe)Fe}(C≡CC≡C){Ru(dppe)Cp*}]PF_6 [**40**]PF_6	7700	----	0.038[b]	26c
[{Cp*(dppe)Fe}(C≡CC≡CC≡C){Ru(dppe)Cp*}]PF_6 [**34**]PF_6	8050	23300	0.50[a] 0.11[b]	This work

[a]Value calculated from Equation 5.2. [b]Value calculated from Equation 5.3.

Near-IR studies were also carried out on the TCNE adducts **37** and [**37**][$C_3(CN)_5$] with the aim of observing electron transfer between the cyano-ligands and the metal sites. This was also probed by NMR spectroscopy for **37**. Unfortunately, **37** is silent in the Near-IR range and no transitions were observed. However, it cannot be concluded that this type of transition does not exist in **37**; it might be of very low intensity and could be hidden.

In the Near-IR spectrum of the unsymmetrical mixed-valence complex [**37**][$C_3(CN)_5$] (Figure 5.25), a very weak and broad low-energy band was observed around 8000 cm^{-1}. This band was deconvoluted using two Gaussian functions: bands A and B, with the parameters listed in Table 5.15. Band A, which is very low in intensity and energy is assigned to a LF transition, whereas the broad Band B, which is also low in intensity and centred at 8000 cm^{-1}, is assigned to the IVCT transition. The observed and calculated full widths at half-height $(\Delta\nu_{1/2})_{exp}$ = 3500 and $(\Delta\nu_{1/2})_{theo}$ = 4299 of the IVCT band are not significantly different, which is in good agreement with Hush's theory for class II mixed-valence systems. Therefore, the electronic coupling parameter of [**37**][$C_3(CN)_5$] was calculated from Equation 5.3 which applies to class II mixed-valence systems to give V_{ab} = 0.030 eV. This value is consistent with [**37**][$C_3(CN)_5$] being a weakly-coupled class II mixed-valence complex, which is to be expected for an unsymmetrical molecule. The cyanocarbon bridge also disfavours the electronic coupling in comparison with the all-carbon C_6 bridge in [**34**]PF_6, where V_{ab} = 0.11 eV (using Equation 5.3).

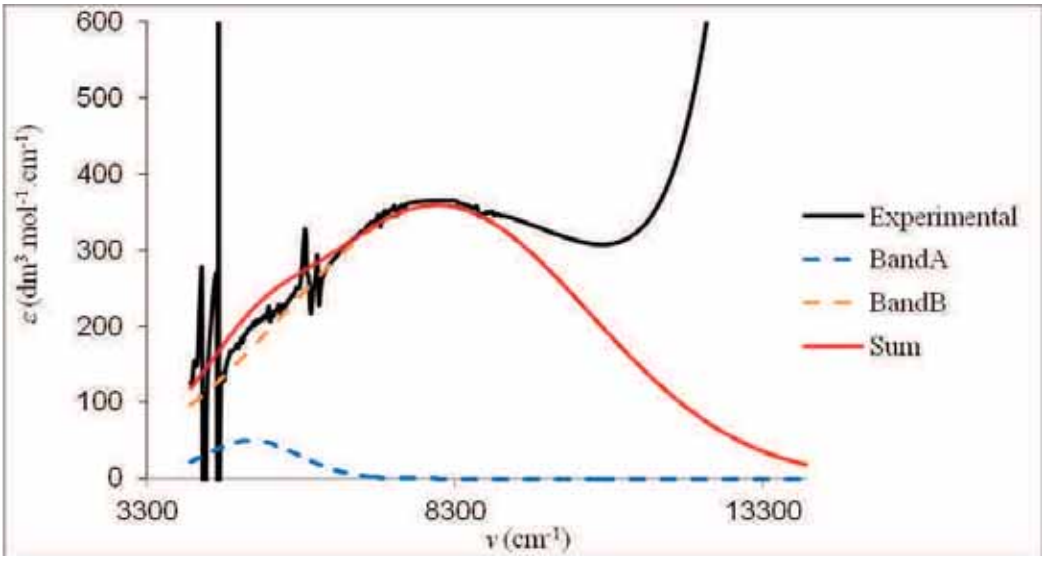

Figure 5.25. *Near-IR spectrum of [37][$C_3(CN)_5$] in CH_2Cl_2.*

Table 5.15. Near-IR data for [**37**][$C_3(CN)_5$] in CH_2Cl_2.

Compound	Band	ν_{max}/cm^{-1} (ε/dm^3.mol^{-1}.cm^{-1})	$(\Delta\nu_{1/2})_{exp}$ (cm^{-1})	R_{MM},[a] (Å)	$(\Delta\nu_{1/2})_{theo}$[b] (cm^{-1})	V_{ab} eV
[**37**][$C_3(CN)_5$]	A	5000 (50)	1100	8.613	3398	
	B	8000 (360)	3500		4299	0.030[c]

[a]Evaluated from X-ray structures. [b]Values calculated from Equation 5.1. [c]Value calculated from Equation 5.3.

Near-IR investigations allowed the determination of the electronic coupling parameters of the mixed-valence complexes described in this Chapter. The bridge types (pure carbon or chemically modified by addition of TCNE) and the nature of the metals (Fe or Ru) considerably affect the electronic coupling parameter V_{ab}, which is larger in the ruthenium complexes than in the iron analogues. The unsymmetrical mixed-valence complex [**34**]PF_6 showed an unexpectedly large V_{ab} (0.11 from Equation 5.3 and 0.50 from Equation 5.2), indicating that strong electronic delocalisation exists in this complex.

5.3.9 Magnetic behaviour of the dicationic complex [30][PF$_6$]$_2$

Guided by the NMR studies (Section 5.3.4) which revealed the paramagnetism of [**30**][PF_6]$_2$, the magnetic properties of the dicationic diiron complex [**30**][PF_6]$_2$ were investigated by EPR spectroscopy in collaboration with Dr. Cador, and rationalised by DFT calculations carried out by Gendron. An EPR experiment at 67K was first carried out in the solid state with the single crystal used for the X-ray structure determination and no signals were observed. However, when the crystal was dissolved in a few drops of dichloromethane and the solution frozen at 67K, an intense signal was observed in the EPR spectrum (Figure 5.26). This signal is characteristic of a Fe(III) species with parameters g_1 = 2.224 g_2 = 2.045 and g_3 = 1.992 (Δg = 0.232 and g_{iso} = 2.087), the half-field signal centred at g = 4.259 indicating the presence of a biradical species which confirms that the EPR-active species is in the triplet state (Figure 5.11). The signal at g* = 2.139 was attributed to paramagnetic impurities. Unlike the analogous dicationic complex [{Cp*(dppe)Fe}$_2$(μ-C≡CC≡C)][PF_6]$_2$ [**38**][PF_6]$_2$, which is EPR silent[22b], [**30**][PF_6]$_2$ is EPR-active at 67K in a CH_2Cl_2 glass but not in the single crystalline phase. This

observation is very unexpected for this type of compound and DFT calculations were carried out in order to obtain the relative energies of the singlet and triplet states, and to determine whether exchange between the two states is possible (small ΔG_{ST}).

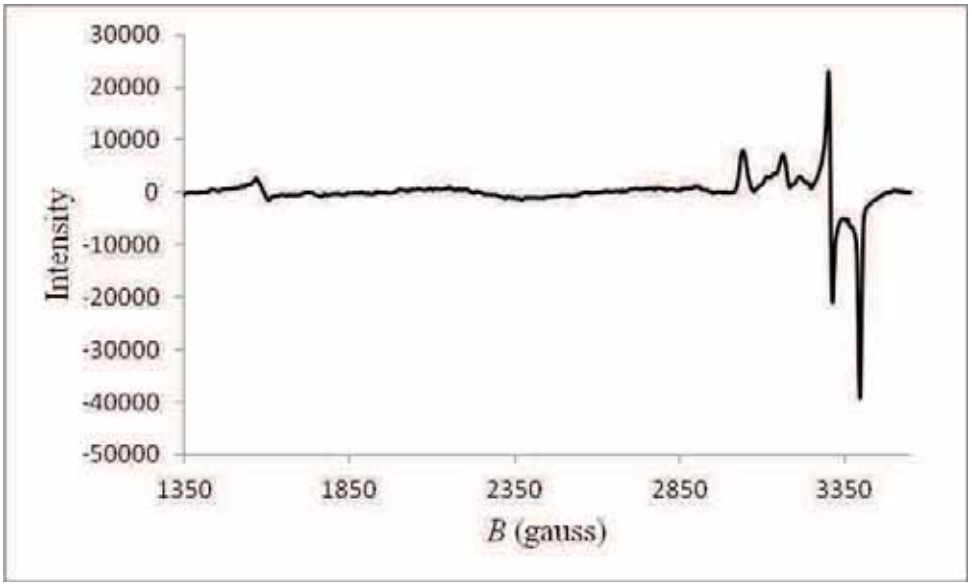

Figure 5.26. *EPR spectrum of [**30**][PF_6]$_2$ measured at 67K in CH_2Cl_2 glass.*

Figure 5.27 presents the energy diagrams and frontier orbitals of the singlet and triplet states (with the angle between the two iron sites τ = 180°, which is similar to the X-ray structure geometry). The calculated energy difference found between the singlet and triplet states when the angle between the metal fragments is τ = 180° is ΔE = 0.03 eV in favour of the triplet state which signifies that the singlet and triplet states have almost the same energies in this configuration.

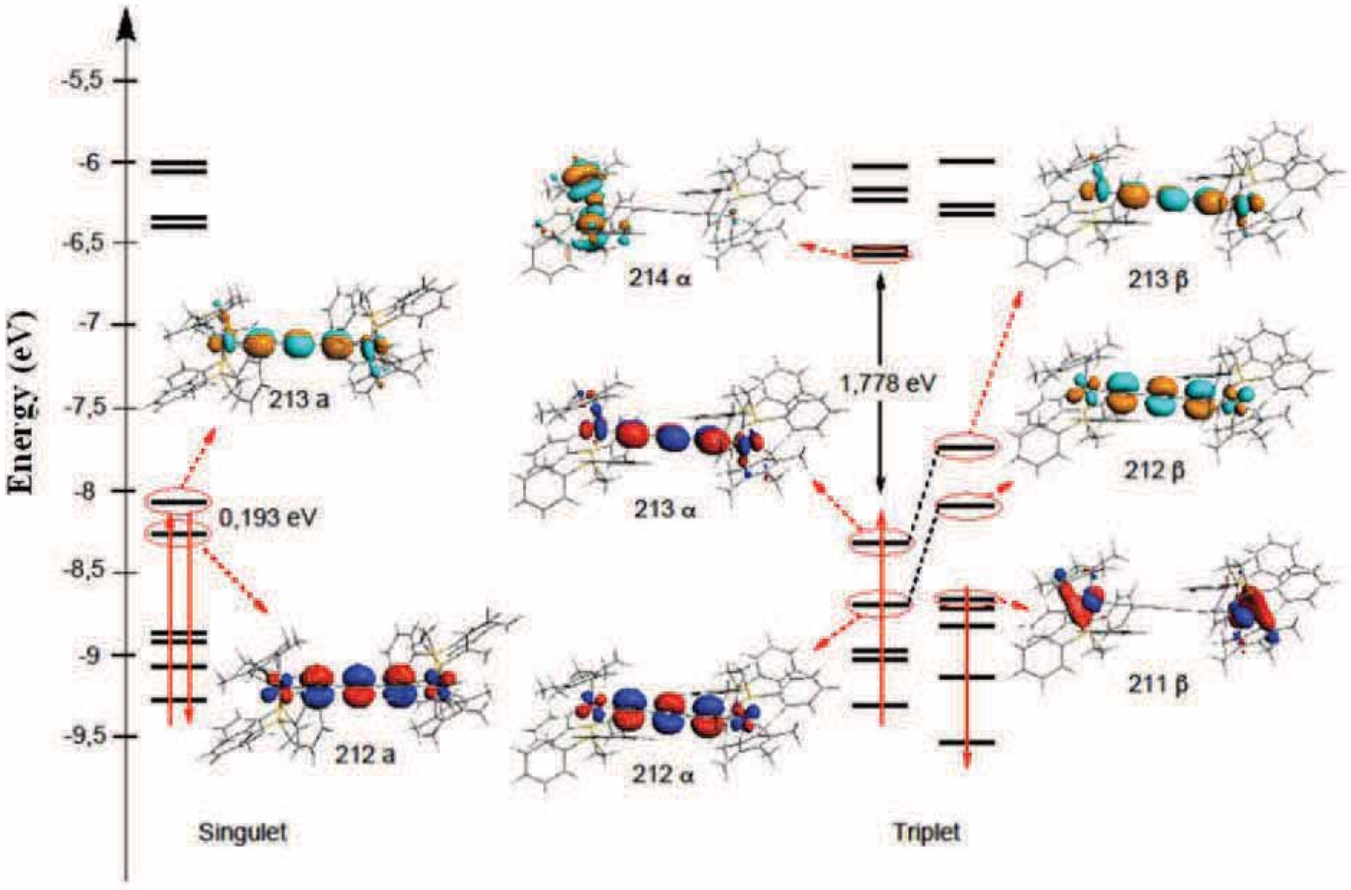

Figure 5.27. *Energy diagrams and frontier orbital representations of the [**30**][PF_6]$_2$ singlet and triplet states (τ = 180°).*

However, the energy difference between the singlet and triplet states dramatically changes with relative orientation of the metal fragments, as found for the rotamers of [**27**][PF_6]$_2$ (see Chapter 4). For example, when the angle between the two metal fragments is τ = 45°, the energy difference is ΔE = 0.15 eV in favour of the triplet state, which is significantly different to ΔE = 0.03 eV for τ = 180°. In this configuration, the triplet state is much more stable than the singlet state. On the basis of these theoretical results, we propose that the single crystal is EPR-silent because [**30**][PF_6]$_2$ is in the singlet state (the singlet state presumably being the only configuration to crystallise). However, when the crystal is dissolved in dichloromethane, the end-capping metal fragments can rotate about the C_6 axis to give different conformations (different τ) which, when the solution was frozen at 67K, are EPR-active because the triplet state is now accessible. Therefore, the EPR signal of the solution arises from the triplet state. While this hypothesis has not yet

been verified, it is presently the only viable explanation of the difference between the EPR spectra obtained in solution and from a single crystal.

5.4 Conclusion

New symmetrical and unsymmetrical bimetallic complexes containing C_6 chains have been synthesised and characterised (Scheme 5.16). The symmetric diiron complex {Cp*(dppe)Fe}$_2$(μ-C≡CC≡CC≡C) **30** and the asymmetric mixed iron-ruthenium complex {Cp*(dppe)Fe}(C≡CC≡CC≡C){Ru(dppe)Cp*} **34** both have poor solubility and therefore could not be fully characterised. However, they react with the electron-deficient cyano-alkene TCNE to afford the ring-opened adducts **36** and **37**, together with the mixed-valence complex [**37**][$C_3(CN)_5$], which was obtained when a large excess of TCNE was used. These products were fully characterised by the usual spectroscopic methods which in turn allowed confirmation of the structures of the parent complexes.

The electrochemical behaviour of these new hexatriynyl complexes was investigated and revealed that their mixed-valence states were thermodynamically stable, as shown by the very large K_c values (from 2.9×10^7 for **31** to 7.0×10^{10} for **35**). The diiron system **36** containing the C_6 bridge modified by addition of one TCNE molecule to the central C≡C triple bond also exhibits two well-separated waves with $K_c = 2.4 \times 10^3$, indicating that electronic interactions between the two metallic sites, through the cyanocarbon bridge, exist.

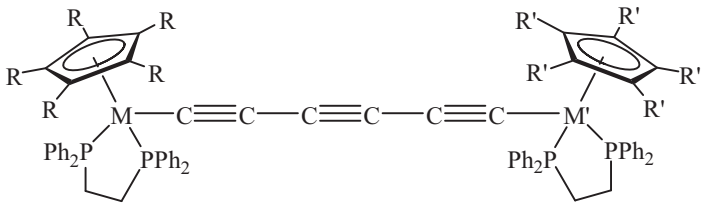

30: M = M' = Fe, R = R' = Me
31: M = M' = Ru, R = R' = H
34: M = Fe, M' = Ru, R = R' = Me
35: M = Fe, M' = Ru, R = Me, R' = H

Scheme 5.16

Guided by the electrochemical observations, 1-e chemical oxidations were carried out on the new bimetallic complexes to afford novel mixed-valence complexes which were all characterised by EPR spectroscopy. The EPR analyses showed weak anisotropy (Δg

between 0.137-0.272) in all mixed-valence complexes (apart from [**37**][$C_3(CN)_5$]) suggesting good electron delocalisation between the two metal fragments through the C_6 bridge. Surprisingly, the EPR spectra of the complexes [**30**]PF_6, [**32**]PF_6 and [**34**]PF_6, exhibit very similar shapes which are characteristic of the C_6 chain bridging two Cp*(dppe)M fragments (M = Fe, Ru). However, in the case of [**30**]PF_6, different spectra were obtained depending on whether a single crystal or a CH_2Cl_2 glass was used for data collection. Unfortunately, no explanation for this interesting difference is available yet.

The first crystal structures of mixed-valence complexes containing a chain longer than C_4 were obtained for [**30**]PF_6 and [**34**]PF_6, the two other mixed-valence complexes containing the Ru(dppe)Cp motif [**31**]PF_6 and [**35**]PF_6 being unstable above -10°C. Complexes [**30**]PF_6 and [**34**]PF_6 were fully characterised by the usual spectroscopic methods which suggested that very strong electronic couplings exist between the metal centres. As expected, the symmetrical complex [**30**]PF_6 was determined to be a class III delocalised mixed-valence system. The electronic coupling parameter V_{ab} correlates well with those of the previously described analogues [**38**]PF_6 and [**42**]PF_6, which contain a shorter C_4 chain and a longer C_8 chain, respectively. However, the low-energy cut-off of the IVCT band characteristic of borderline class II-III mixed-valence systems, and the larger EPR anisotropy value of [**30**]PF_6 than found for both [**38**]PF_6 and [**42**]PF_6, slightly contradict the previous observation. New features which have not been observed in the mixed-valence systems [**38**]PF_6 and [**42**]PF_6 are also found in the novel [**30**]PF_6 complex containing an odd number of C≡C triple bonds: a vibronic coupling between the intramolecular electron transfer and some of the molecular vibrational states was characterised, together with induced changes in the [**30**]PF_6 properties (IR, UV-Vis and Near-IR).

Unexpected results were also observed for the unsymmetrical complex [**34**]PF_6, which was expected to be a weakly coupled class II mixed-valence system, but behaved as a class III mixed-valence complex. All the spectroscopic data collected on the mixed-valence complex [**34**]PF_6: IR (no charge localisation on the IR time scale), Near-IR (large V_{ab}) and EPR (weak anisotropy) are consistent with strong electronic delocalisation existing in this molecule. The most surprising observation is that electronic coupling in [**34**]PF_6 is stronger than in the analogous [**40**]PF_6 containing a C_4 chain, this feature strongly contrasting with the electronic coupling decay as a function of chain length. As found for the diiron

complex [**30**]PF_6, vibronic coupling has also been observed in [**34**]PF_6. Additionally, the unsymmetrical TCNE adduct [**37**][$C_3(CN)_5$] exhibits a large, weak intensity IVCT band at low energies, which is in good agreement with Hush's theory. Compound [**37**][$C_3(CN)_5$] is thus classified as a weakly-coupled class II mixed-valence complex with V_{ab} = 0.030 eV.

Finally, the novel dicationic complex [{Cp*(dppe)Fe}$_2$(μ-C≡CC≡CC≡C)][PF_6]$_2$ [**30**][PF_6]$_2$ was synthesised by chemically oxidising [**30**]PF_6 and was structurally characterised by X-ray analysis. This complex showed interesting paramagnetic behaviour, being EPR-silent as a single crystal but EPR-active in a CH_2Cl_2 glass. In order to explain this new phenomenon, it is proposed that only the singlet state crystallised, but after dissolving the crystal in dichloromethane, rotation of the end-capping metal fragments around the C_6 axis occurred, different conformations having a more stable triplet state, resulting in an EPR-active sample. This hypothesis was supported by DFT calculations carried out by Gendron on the singlet-triplet energy differences in two different orientations.

Experimental

General experimental conditions are detailed in Chapter 2, Experimental section.

Reagents: Tetracyanoethene (Aldrich) was used as received. $Me_3Si(C{\equiv}C)_3SiMe_3$[51] and RuCl(dppe)Cp[52] were prepared using the cited methods.

Synthesis of {Cp*(dppe)Fe}$_2$(μ-C≡CC≡CC≡C) (30)

To a solution of FeCl(dppe)Cp* **1** (300 mg, 0.48 mmol) and KF (28 mg, 0.48 mmol) in MeOH (25 ml) was added $Me_3SiC{\equiv}CC{\equiv}CC{\equiv}CSiMe_3$ (53 mg, 0.24 mmol). After stirring at room temperature overnight, the orange precipitate was filtered off and washed with cold MeOH (3 × 10 ml), acetone (3 × 10 ml), and then hexane (20 ml) to afford {Cp*(dppe)Fe}$_2$(μ-C≡CC≡CC≡C) **30** (224 mg, 75%) as a very poorly soluble orange powder. IR (KBr): ν(C≡C) 2040 cm^{-1}. ES-MS (*m/z*): calcd for $C_{78}H_{78}Fe_2P_4$ 1250.3753, found 1250.3952 $[M]^+$.

Synthesis of {Cp(dppe)Ru}$_2$(μ-C≡CC≡CC≡C) (31)

A methanolic (25 ml) suspension of RuCl(dppe)Cp **33** (200 mg, 0.33 mmol), $Me_3SiC{\equiv}CC{\equiv}CC{\equiv}CSiMe_3$ (73 mg, 0.33 mmol) and KF (39 mg, 0.67 mmol) was heated under reflux for 1 h, after which the mixture was allowed to cool. The yellow precipitate was filtered off and washed with cold MeOH (3 × 10 ml) to give {Ru(dppe)Cp}$_2$(μC≡CC≡CC≡C) **31** (158 mg, 80%). X-ray quality crystals were obtained from benzene/hexane. Anal.Calcd ($C_{68}H_{58}P_4Ru_2.0.5C_6H_6$): C, 68.76; H, 4.96. Found: C, 68.97; H, 5.16. IR (CH_2Cl_2): ν(C≡C) 2063 cm^{-1}. ^{1}H NMR (C_6D_6): δ 1.84-1.87, 2.43-2.46 (2 × m, 2 × 2H, 2 × CH_2), 4.56 (s, 5H, Cp), 6.85-7.90 (m, 40H, Ph). ^{13}C NMR (C_6D_6): δ 28.23-28.53 (m, dppe), 83.16 (s, C_5H_5), 96.93 (s), 102.64 (t, Ru-C≡, $^2J_{CP}$ = 28 Hz), 127.55-142.91 (m, Ph). ^{31}P NMR (C_6D_6): δ 85.8. ES-MS (positive ion mode, MeOH-NaOMe, *m/z*): 1202 $[M]^+$.

Synthesis of {Cp*(dppe)Fe}(C≡CC≡CC≡C){Ru(dppe)Cp*} (34)

Ru(C≡CC≡CC≡CSiMe$_3$)(dppe)Cp* **10** (92 mg, 0.12 mmol), FeCl(dppe)Cp* **1** (81 mg, 0.13 mmol) and KF (7 mg, 0.12 mmol) were dissolved in a 1:1 mixture of THF / MeOH (10 ml). After stirring at room temperature overnight, the orange precipitate was filtered off and washed with cold MeOH (3 × 5 ml), acetone (3 × 5 ml), and then hexane (10 ml) to afford {Cp*(dppe)Fe}(C≡CC≡CC≡C){Ru(dppe)Cp*} **34** (94 mg, 61%) as a very poorly soluble orange powder. IR (Powder): ν(C≡C) 2110, 2050, 1969 cm^{-1}. ES-MS (*m/z*): calcd for $C_{78}H_{78}P_4FeRu$ 1296.3447, found 1296.3453 $[M]^+$.

Synthesis of {Cp*(dppe)Fe}(C≡CC≡CC≡C){Ru(dppe)Cp} (35)

To a solution of Fe(C≡CC≡CC≡CSiMe$_3$)(dppe)Cp* **9** (22 mg, 0.030 mmol) in THF (1 ml) was added MeOH (5 ml). Immediately after, RuCl(dppe)Cp **33** (20 mg, 0.033 mmol) and KF (2 mg, 0.030 mmol) were added. After stirring at room temperature overnight, the brown precipitate was filtered off, washed with cold MeOH (3 × 5 ml), dissolved in a 5:1 CH_2Cl_2/NEt_3 mixture and passed through a basic alumina column eluting with the same solvent. The orange band was collected and the solvent removed to afford {Cp*(dppe)Fe}(C≡CC≡CC≡C){Ru(dppe)Cp} **35** (11 mg, 30%) as an orange powder. Anal. Calcd ($C_{73}H_{68}FeP_4Ru$): C, 71.51; H, 5.59. Found: C, 71.08; H, 5.96. IR (CH_2Cl_2): ν(C≡C) 2048, 1920 cm^{-1}. ^{1}H NMR (C_6D_6): δ 1.45 (s, 15H, Cp*), 1.75, 1.93 (2 × m, 4H, PCH_2), 2.55 (m, 4H, PCH_2), 4.66 (s, 5H, Cp), 6.90-8.01 (m, 40H, Ph). ^{13}C NMR (C_6D_6): δ 10.37 (s, $C_5\mathit{Me}_5$), 28.33-28.64 (m, dppe), 30.24-31.29 (m, dppe), 54.00, 56.7 (s, C≡C), 83.26 (s, C_5H_5), 88.25 (s, C_5Me_5), 97.34, 103.86 (s, M-C≡*C*), 102.32 (t, Ru-*C*≡, $^2J_{CP}$ = 26 Hz), 124.91 (t, Fe-*C*≡, $^2J_{CP}$ = 41 Hz), 127.30-143.00 (m, Ph). ^{31}P NMR (C_6D_6): δ 84.8 (s, Ru(dppe)Cp), 99.6 (s, Fe(dppe)Cp*). ES-MS (*m/z*): calcd for $C_{73}H_{68}FeP_4Ru$ 1226.2664, found 1226.2653 $[M]^+$.

Synthesis of {Cp*(dppe)Fe}$_2${μ-C≡CC[=C(CN)$_2$]C[=C(CN)$_2$]C≡C} (36)

{Cp*(dppe)Fe}$_2$(μ-C≡CC≡CC≡C) **30** (50 mg, 0.040 mmol) and TCNE (5 mg, 0.040 mmol) were dissolved in dichloromethane (5 ml). After stirring for 2 h at room temperature, pentane (50 ml) was added to the solution. The resulting precipitate was filtered off and washed with pentane (3 × 5 ml) to afford {Cp*(dppe)Fe}$_2${μ-C≡CC[=C(CN)$_2$]C[=C(CN)$_2$]C≡C} **36** (45 mg, 82%) as a deep purple powder. IR (CH_2Cl_2): ν(C≡N) 2206, ν(C≡C) 1950, ν(C=C) 1599 cm^{-1}. ^{31}P NMR ($CDCl_3$, 121 MHz): δ

97.7 (d (br), $^2J_{PP}$ = 7 Hz) and 92.9 (d (br), $^2J_{PP}$ = 7 Hz). ES-MS (*m/z*): calcd for $C_{84}H_{78}Fe_2N_4P_4$ 1378.3870, found 1378.3873 $[M]^+$.

Synthesis of {Cp*(dppe)Fe}{C≡CC[=C(CN)$_2$]C[=C(CN)$_2$]C≡C}{Ru(dppe)Cp*} (37)

{Cp*(dppe)Fe}(C≡CC≡CC≡C){Ru(dppe)Cp*} **34** (44 mg, 0.034 mmol) and TCNE (4 mg, 0.034 mmol) were dissolved in dichloromethane (5 ml). After stirring for 2 h at room temperature, hexane (50 ml) was added to the solution. The resulting precipitate was filtered off and washed with hexane (3 × 10 ml) to afford {Cp*(dppe)Fe}{C≡CC[=C(CN)$_2$]C[=C(CN)$_2$]C≡C}{Ru(dppe)Cp*} **37** (42 mg, 87%) as a deep purple powder. Anal.Calcd ($C_{84}H_{78}FeN_4P_4Ru$): C, 70.83; H, 5.52; N, 3.93. Found: C, 71.14; H, 6.00; N, 3.77. IR (CH_2Cl_2): ν(C≡N) 2209, ν(C≡C) 1956, ν(C=C) 1604 cm^{-1}. ^{1}H NMR ($CDCl_3$): δ 1.07 (s, 15H, Cp*Fe), 1.26 (s, 15H, Cp*Ru), 1.95-2.14 (m, 4H, 2 × CH_2), 2.52, 2.59 (2m, 4H, 2 × CH_2), 6.78-7.74 (m, 40H, Ph). ^{13}C NMR ($CDCl_3$): δ 10.32 (s, C_5*Me$_5$*), 10.40 (s, C_5*Me$_5$*), 29.07-30.46 (m, dppe), 96.26 (s, *C*$_5$Me$_5$), 96.46 (s, *C*$_5$Me$_5$), 114.19, 117.02 (2 x s, 2 x CN), 115.68 (s(br), 2 x CN), 122.51 (s), 127.33-139.41 (m, Ph), 205.64 [t(br), M-*C*≡]. ^{31}P NMR ($CDCl_3$): δ 79.3 [d (br), $^2J_{PP}$ = 14 Hz, Ru(dppe)], 74.2 [d, $^2J_{PP}$ = 14 Hz, Ru(dppe)]. ES-MS (*m/z*): calcd for $C_{84}H_{78}FeN_4P_4Ru$ 1424.3570, found 1424.5621 $[M]^+$.

Synthesis of [{Cp*(dppe)Fe}{μ-C≡CC[=C(CN)$_2$]C[=C(CN)$_2$]C≡C}{Ru(dppe)Cp*}] [C$_3$(CN)$_5$] [37][C$_3$(CN)$_5$]

{Cp*(dppe)Fe}(C≡CC≡CC≡C){Ru(dppe)Cp*} **34** (41 mg, 0.032 mmol) and TCNE (40 mg, 0.32 mmol) were dissolved in dichloromethane (8 ml). After stirring for 2 h at room temperature, the solvent was removed under reduced pressure. The residue was then purified by preparative TLC (acetone/hexane, 1:1) and the brown band (R_f = 0.50) was collected to afford [{Cp*(dppe)Fe}{C≡CC[=C(CN)$_2$]C[=C(CN)$_2$]C≡C}{Ru(dppe)Cp*}][C$_3$(CN)$_5$] [**37**][C$_3$(CN)$_5$] (26 mg, 51%) as a dark brown powder. IR (CH_2Cl_2): ν(C≡N) 2199, ν(C≡C) 1957, ν(C=C) 1592, ν(CCC) 1506 cm^{-1}. ES-MS (*m/z*): calcd for $C_{84}H_{78}FeN_4P_4Ru$ 1424.3570, found 1424.3601 $[M]^+$.

Synthesis of [{Cp*(dppe)Fe}$_2$(μ-C≡CC≡CC≡C)]PF_6 ([30]PF_6)

When {Cp*(dppe)Fe}$_2$(μ-C≡CC≡CC≡C) **30** (180 mg, 0.144 mmol) and [Cp_2Fe]PF_6 (47 mg, 0.144 mmol) were dissolved in dichloromethane (15 ml) at -78°C, the colour changed immediately from orange to dark brown. After stirring 1 h at -78°C, the solution was allowed to slowly warm up to room temperature over 5 h. Then, pentane (60 ml) was added to the solution; the resulting precipitate was filtered off and washed with toluene (3 × 10 ml). The residue was dissolved in dichloromethane (10 ml), the solution was filtered via cannula and the solvent removed under reduced pressure to afford [{Cp*(dppe)Fe}$_2$(μ-C≡CC≡CC≡C)]PF_6 [**30**]PF_6 (154 mg, 77%) as a dark brown powder. Anal. Calcd ($C_{78}H_{78}F_6Fe_2P_5.CH_2Cl_2$): C, 64.07; H, 5.44. Found: C, 63.89; H, 5.65. IR (KBr): ν(C≡C) 2005, 1818, ν(P-F) 839 cm^{-1}. ES-MS (*m/z*): calcd for $C_{78}H_{78}Fe_2P_4$ 1250.3753, found 1250.3755 $[M]^+$.

Synthesis of [{Cp*(dppe)Fe}(C≡CC≡CC≡C){Ru(dppe)Cp*}]PF_6 ([34]PF_6)

{Cp*(dppe)Fe}(C≡CC≡CC≡C){Ru(dppe)Cp*} **34** (44 mg, 0.034 mmol) and [Cp_2Fe]PF_6 (11 mg, 0.034 mmol) were dissolved in dichloromethane (6 ml) at -78°C, the colour changed immediately from orange to dark brown. After stirring 1 h at -78°C, the solution was removed from the cold bath and allowed to slowly warm up to room temperature over 5 h. Then, hexane (60 ml) was added to the solution and the resulting precipitate was filtered off and washed with hexane (3 × 5 ml). The residue was dissolved in dichloromethane (10 ml), the solution was filtered via cannula and the solvent removed under reduced pressure to afford [{Cp*(dppe)Fe}(C≡CC≡CC≡C){Ru(dppe)Cp*}]PF_6 [**34**]PF_6 (32 mg, 77%) as a dark brown powder. Anal.Calcd ($C_{78}H_{78}F_6FeP_5Ru.CH_2Cl_2$): C, 62.17; H, 5.28. Found: C, 62.65; H, 5.69. IR (CH_2Cl_2): ν(C≡C) 2014, 1881, 1824 cm^{-1}. ES-MS (*m/z*): calcd for $C_{78}H_{78}FeP_4Ru$ 1296.3447, found 1296.3596 $[M]^+$.

Synthesis of [{Cp*(dppe)Fe}$_2$(μ-C≡CC≡CC≡C)][PF_6]$_2$ ([30][PF_6]$_2$)

When [{Cp*(dppe)Fe}$_2$(μ-C≡CC≡CC≡C)]PF_6 [**30**]PF_6 (120 mg, 0.086 mmol) and [Cp_2Fe]PF_6 (28 mg, 0.086 mmol) were dissolved in dichloromethane (10 ml) at -78°C, the colour changed immediately from dark brown to dark green. After stirring 1 h at -78°C, the solution was allowed to slowly warm up to room temperature over 5 h. Then, pentane (60 ml) was added to the solution; the resulting precipitate was filtered off and washed with toluene (3 × 10 ml) to afford [{Cp*(dppe)Fe}$_2$(μ-C≡CC≡CC≡C)][PF_6]$_2$ [**30**][PF_6]$_2$ (110 mg, 83%) as a dark green powder. Anal.Calcd ($C_{78}H_{78}F_{12}Fe_2P_6$): C, 60.80; H, 5.10. Found:

C, 61.08; H, 5.21. IR (KBr): ν(C≡C) 2162, 1947, ν(PF) 839 cm^{-1}. ^{1}H NMR (CD_2Cl_2): δ 0.78 (s, 30H, Cp*), 2.76 (m, 4H, 2 × CH_2), 4.32 (m, 4H, 2 × CH_2), 6.48-7.60 (m, 40H, Ph). ^{31}P NMR (CD_2Cl_2): δ 11.1 [s (br)], -145.4 (septet, J_{PF} = 710 Hz, PF_6).

References

1. (a) Field, L. D.; George, A. V.; Laschi, F.; Malouf, E. Y.; Zanello, P., *J. Organomet. Chem.* **1992,** *435*, 347-356; (b) Le Narvor, N.; Lapinte, C., *Organometallics* **1995,** *14*, 634-639; (c) Bruce, M. I.; Hall, B. C.; Kelly, B. D.; Low, P. J.; Skelton, B. W.; White, A. H., *J. Chem. Soc., Dalton Trans.* **1999**, 3719–3728; (d) Armitt, D. J.; Bruce, M. I.; Gaudio, M.; Zaitseva, N. N.; Skelton, B. W.; White, A. H.; Le Guennic, B.; Halet, J.-F.; Fox, M. A.; Roberts, R. L.; Hartl, F.; Low, P. J., *Dalton Trans.* **2008**, 6763-6775; (e) Pevny, F.; Piazza, E. D.; Norel, L.; Drescher, M.; Winter, R. F.; Rigaut, S., *Organometallics* **2010,** *29*, 5912–5918.
2. (a) Weyland, T.; Costuas, K.; Mari, A.; Halet, J.-F.; Lapinte, C., *Organometallics* **1998,** *17*, 5569-5579; (b) Weyland, T.; Lapinte, C.; Frapper, G.; Calhorda, M. J.; Halet, J.-F.; Toupet, L., *Organometallics* **1997,** *16*, 2024-2031; (c) Fox, M. A.; Farmer, J. D.; Roberts, R. L.; Humphrey, M. G.; Low, P. J., *Organometallics* **2009,** *28*, 5266-5269.
3. Le Stang, S.; Paul, F.; Lapinte, C., *Organometallics* **2000,** *19*, 1035-1043.
4. Tanaka, Y.; Shaw-Taberlet, J. A.; Justaud, F.; Cador, O.; Roisnel, T.; Akita, M.; Hamon, J.-R.; Lapinte, C., *Organometallics* **2009,** *28*, 4656–4669.
5. de Montigny, F.; Argouarch, G.; Costuas, K.; Halet, J.-F.; Roisnel, T.; Toupet, L.; Lapinte, C., *Organometallics* **2005,** *24*, 4558-4572.
6. Ghazala, S. I.; Paul, F.; Toupet, L.; Roisnel, T.; Hapiot, P.; Lapinte, C., *J. Am. Chem. Soc.* **2006,** *128*, 2463-2476.
7. Liu, Y.; Lagrost, C.; Costuas, K.; Tchouar, N.; Le Bozec, H.; Rigaut, S., *Chem. Commun.* **2008**, 6117-6119.
8. Roué, S.; Lapinte, C.; Bataille, T., *Organometallics* **2004,** *23*, 2558-2567.
9. Hamon, P.; Justaud, F.; Cador, O.; Hapiot, P.; Rigaut, S.; Toupet, L.; Ouahab, L.; Stueger, H.; Hamon, J.-R.; Lapinte, C., *J. Am. Chem. Soc.* **2008,** *130*, 17372–17383.
10. Brown, N. J.; Lancashire, H. N.; Fox, M. A.; Collison, D.; Edge, R.; Yufit, D. S.; Howard, J. A. K.; Whiteley, M. W.; Low, P. J., *Organometallics* **2011,** *30*, 884-894.
11. Bruce, M. I.; Low, P. J.; Hartl, F.; Humphrey, P. A.; de Montigny, F.; Jevric, M.; Lapinte, C.; Perkins, G. J.; Roberts, R. L.; Skelton, B. W.; White, A. H., *Organometallics* **2005,** *24*, 5241-5255.
12. (a) Lohan, M.; Ecorchard, P.; Rüffer, T.; Justaud, F.; Lapinte, C.; Lang, H., *Organometallics* **2009,** *28*, 1878-1890; (b) Lohan, M.; Justaud, F.; Roisnel, T.; Ecorchard, P.; Lang, H.; Lapinte, C., *Organometallics* **2010,** *29*, 4804-4817.
13. Weng, W.; Bartik, T.; Brady, M.; Bartik, B.; Ramsden, J. A.; Arif, A. M.; Gladysz, J. A., *J. Am. Chem. Soc.* **1995,** *117*, 11922-11931.
14. Bruce, M. I.; Halet, J.-F.; Guennic, B. L.; Skelton, B. W.; Smith, M. E.; White, A. H., *Inorg. Chim. Acta* **2003,** *350*, 175-181.

15. (a) Ghazala, S. I.; Gauthier, N.; Paul, F.; Toupet, L.; Lapinte, C., *Organometallics* **2007,** *26*, 2308-2317; (b) Malvolti, F.; Le Maux, P.; Toupet, L.; Smith, M. E.; Man, W. Y.; Low, P. J.; Galardon, E.; Simonneaux, G.; Paul, F., *Inorg. Chem.* **2010,** *49*, 9101-9103.
16. (a) Wong, K. M.-C.; Lam, S. C.-F.; Ko, C.-C.; Zhu, N.; Roué, S.; Lapinte, C.; Fathallah, S.; Costuas, K.; Kahlal, S.; Halet, J.-F., *Inorg. Chem.* **2003,** *42*, 7086-7097; (b) Gauthier, N.; Olivier, C.; Rigaut, S.; Touchard, D.; Roisnel, T.; Humphrey, M. G.; Paul, F., *Organometallics* **2008**, 1063–1072; (c) Fitzgerald, E. C.; Ladjarafi, A.; Brown, N. J.; Collison, D.; Costuas, K.; Edge, R.; Halet, J.-F.; Justaud, F.; Low, P. J.; Meghezzi, H.; Roisnel, T.; Whiteley, M. W.; Lapinte, C., *Organometallics* **2011,** *30*, 4180-4195.
17. Kheradmandan, S.; Venkatesan, K.; Blacque, O.; Schmalle, H. W.; Berke, H., *Chem.– Eur. J.* **2004,** *10*, 4872-4885.
18. Bruce, M. I.; Costuas, K.; Ellis, B. G.; Halet, J.-F.; Low, P. J.; Moubaraki, B.; Murray, K. S.; Ouddaï, N.; Perkins, G. J.; Skelton, B. W.; White, A. H., *Organometallics* **2007,** *26*, 3735-3745.
19. (a) Hush, N. S., *Prog. Inorg. Chem.* **1967,** *8*, 391; (b) Hush, N. S., *Coord. Chem. Rev.* **1985,** *64*, 135-157.
20. Costuas, K.; Rigaut, S., *Dalton Trans.* **2011,** *40*, 5643-5658.
21. (a) Seyler, J. W.; Weng, W.; Zhou, Y.; Gladysz, J. A., *Organometallics* **1993,** *12*, 3802-3804; (b) Brady, M.; Weng, W.; Zhou, Y.; Seyler, J. W.; Amoroso, A. J.; Arif, A. M.; Böhme, M.; Frenking, G.; Gladysz, J. A., *J. Am. Chem. Soc.* **1997,** *119*, 775-788.
22. (a) Le Narvor, N.; Lapinte, C., *J. Chem. Soc., Chem Commun.* **1993**, 357-359; (b) Le Narvor, N.; Toupet, L.; Lapinte, C., *J. Am. Chem. Soc.* **1995,** *117*, 7129-7138.
23. (a) Bruce, M. I.; Denisovich, L. I.; Low, P. J.; Peregudova, S. M.; Ustynyuk, N. A., *Mendeleev Commun.* **1996,** *6*, 200-201; (b) Bruce, M. I.; Low, P. J.; Costuas, K.; Halet, J.-F.; Best, S. P.; Heath, G. A., *J. Am. Chem. Soc.* **2000,** *122*, 1949-1962; (c) Bruce, M. I.; Ellis, B. G.; Low, P. J.; Skelton, B. W.; White, A. H., *Organometallics* **2003,** *22*, 3184-3198.
24. Kheradmandan, S.; Heinze, K.; Schmalle, H. W.; Berke, H., *Angew. Chem., Int. Ed. Engl.* **1999,** *38*, 2270-2273.
25. Semenov, S. N.; Blacque, O.; Fox, T.; Venkatesan, K.; Berke, H., *J. Am. Chem. Soc.* **2010,** *132*, 3115-3127.
26. (a) Coat, F.; Guillevic, M.-A.; Toupet, L.; Paul, F.; Lapinte, C., *Organometallics* **1997,** *16*, 5988-5998; (b) Paul, F.; Meyer, W. E.; Toupet, L.; Jiao, H.; Gladysz, J. A.; Lapinte, C., *J. Am. Chem. Soc.* **2000,** *122*, 9405-9414; (c) Bruce, M. I.; Costuas, K.; Davin, T.; Ellis, B. G.; Halet, J.-F.; Lapinte, C.; Low, P. J.; Smith, M. E.; Skelton, B. W.; Toupet, L.; White, A. H., *Organometallics* **2005,** *24*, 3864-3881.
27. Coat, F.; Lapinte, C., *Organometallics* **1996,** *15*, 477-479.
28. Dembinski, R.; Bartik, T.; Bartik, B.; Jaeger, M.; Gladysz, J. A., *J. Am. Chem. Soc.* **2000,** *122*, 810-822.

29. Szafert, S.; Paul, F.; Meyer, W. E.; Gladysz, J. A.; Lapinte, C., *C. R. Chimie* **2008,** *11*, 693-701.
30. (a) Zheng, Q.; Bohling, J. C.; Peters, T. B.; Frisch, A. C.; Hampel, F.; Gladysz, J. A., *Chem. Eur. J.* **2006,** *12*, 6486–6505; (b) Bruce, M. I.; Kramarczuk, K. A.; Skelton, B. W.; White, A. H., *J. Organomet. Chem.* **2010,** *695*, 469–473.
31. (a) Brady, M.; Weng, W.; Gladysz, J. A., *J. Chem. Soc., Chem. Commun.* **1994**, 2655-2656; (b) Paul, F.; Lapinte, C., *Coord. Chem. Rev.* **1998,** *178-180*, 431-509.
32. Ellis, B. Ph.D. thesis, University of Adelaide, 2003.
33. Bruce, M. I., *Aust. J. Chem.* **2011,** *64*, 77–103.
34. de Montigny, F.; Argouarch, G.; Roisnel, T.; Toupet, L.; Lapinte, C.; Lam, S. C.-F.; Tao, C.-H.; Yam, V. W.-W., *Organometallics* **2008,** *27*, 1912–1923.
35. (a) Bruce, M. I.; Hambley, T. W.; Snow, M. R.; Swincer, A. G., *Organometallics* **1985,** *4*, 501-508; (b) Bruce, M. I.; de Montigny, F.; Jevric, M.; Lapinte, C.; Skelton, B. W.; Smith, M. E.; White, A. H., *J. Organomet. Chem.* **2004,** *689*, 2860–2871; (c) Bruce, M. I.; Jevric, M.; Parker, C. R.; Patalinghug, W.; Skelton, B. W.; White, A. H.; Zaitseva, N. N., *J. Organomet. Chem.* **2008,** *693*, 2915–2920.
36. Miller, J. S.; Calabrese, J. C.; Rommelmann, H.; Chittipeddi, S. R.; Zhang, J. H.; Reiff, W. M.; Epstein, A. J., *J. Am. Chem. Soc.* **1987,** *109*, 769-781.
37. Lapinte, C., *J. Organomet. Chem.* **2008,** *693*, 793-801.
38. Smith, M. Ph.D. thesis, University of Adelaide, 2002.
39. Bruce, M. I.; Cole, M. L.; Parker, C. R.; Skelton, B. W.; White, A. H., *Organometallics* **2008,** *27*, 3352–3367.
40. Astruc, D., *Electron Transfer and Radical Processes in Transition-Metal Chemistry*. VCH: New York, 1995.
41. Duclos, S.; Conan, F.; Triki, S.; Le Mest, Y.; Liu Gonzalez, M.; Sala Pala, J., *Polyhedron* **1999,** *18*, 1935-1939.
42. Demadis, K. D.; El-Samanody, E.-S.; Coia, G. M.; Meyer, T. J., *J. Am. Chem. Soc.* **1999,** *121*, 535-544.
43. Bailey, S. E.; Zink, J. I.; Nelsen, S. F., *J. Am. Chem. Soc.* **2003,** *125*, 5939-5947.
44. Lapinte, C., *personal communication*.
45. Paul, F.; Toupet, L.; Thépot, J.-Y.; Costuas, K.; Halet, J.-F.; Lapinte, C., *Organometallics* **2005,** *24*, 5464-5478.
46. Weil, J. A.; Bolton, J. R., *Electron Paramagnetic Resonance: Elementary Theory and Practical Applications, Second Edition*. Wiley Interscience, John Wiley & Sons, Inc. : Hoboken, New Jersey, 2007.
47. D'Alessandro, D. M.; Keene, F. R., *Chem. Soc. Rev.* **2006,** *35*, 424–440.
48. Brunschwig, B. S.; Creutz, C.; Sutin, N., *Chem. Soc. Rev.* **2002,** *31*, 168-184.
49. Low, P.; Brown, N., *J. Clust. Sci.* **2010,** *21*, 235-278.
50. (a) Closs, G. L.; Miller, J. R., *Science* **1988,** *240*, 440; (b) Ribou, A.-C.; Launay, J.-P.; Sachtleben, M. L.; Li, H.; Spangler, C. W., *Inorganic Chemistry* **1996,** *35*, 3735-3740.
51. Rubin, Y.; Lin, S. S.; Knobler, C. B.; Anthony, J.; Boldi, A. M.; Diederich, F., *J. Am. Chem. Soc.* **1991,** *113*, 6943-6949.

52. Alonso, A. G.; Reventós, L. B., *J. Organomet. Chem.* **1988,** *338*, 249-254.

Chapter Six

Synthesis of New Tetrametallic Complexes with a Square Core by Oxidative Dimerisation of {M(dppe)Cp'(C≡CC≡CC≡C){M(dppe)Cp'} (M = Fe, Ru; Cp' = Cp, Cp*): Potential QCA Models

6.1 Introduction

Over the last decade, the synthesis and study of square complexes containing four metal centres linked by conjugated π systems have attracted much interest. In these higher dimensional systems, the metal centres and conjugated π bridges might be considered as quantum dots and tunnelling junctions, respectively, of molecular QCA devices (similar to a pair of identical mixed-valence complexes; see Section 1.4.1). However, even if the synthesis of such complexes is most of the time very challenging[1], many examples of square molecules containing four metal centres have been reported. Some of these have already been identified as possible candidates for the construction of QCA devices[2] due to their redox-active metal centres. Examples are complexes synthesised by Cotton et al.[3] containing four dimolybdenum units [Figure 6.1 (a)] and by Lau et al.[4], who proposed a tetranuclear analogue of the well-known and often studied Creutz-Taube complex[5] [Figure 6.1 (b)].

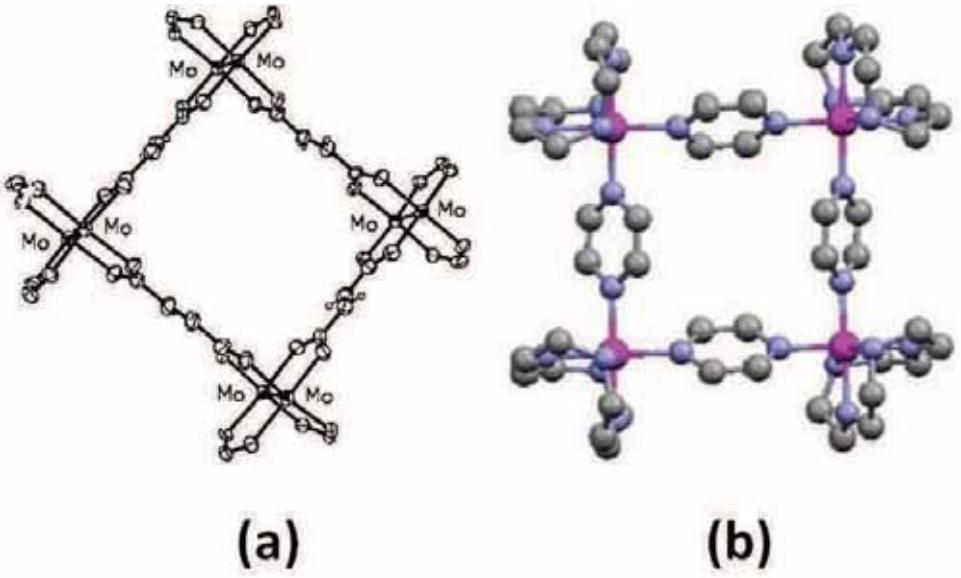

Figure 6.1. *Possible QCA molecules: (a) with dimolybdenum centres: [cis-Mo_2(N,N'-di-p-anisylformamidinate)$_2$]$_4$(trans-$O_2CCH=CHCO_2$)$_4$ and (b) the Creutz-Taube square [(cyclen)$_4$$Ru_4(pz)_4$]$^{9+}$ cation.*

However, there are only a few examples where electron transfer has been studied: in most cases the comproportionation constant K_c of the different mixed-valence states is too small to allow their generation[1]. Rare examples of electron transfer investigations in square molecules have been published by Oshio et al., who used cyanide anions to bridge $Fe(bpy)_2$[6] and/or $Ru(bpy)_2$[7] metal centres. The homo- and hetero-, mono- and di-oxidised mixed-valence species $[Fe(II)_3Fe(III)]^{5+}$, $[Fe(II)_2Fe(III)_2]^{6+}$, $[Ru(II)_2Fe(II)Fe(III)]^{5+}$ and $[Ru(II)_2Fe(III)_2]^{6+}$ have been generated under spectroelectrochemical conditions to probe intramolecular electron transfer by Near-IR spectroscopy. These complexes exhibited average IVCT transitions and the Hush model applies[8]; therefore, they have been classified as class II mixed-valence-systems. Interestingly, electronic coupling in the iron and ruthenium heterometallic system $[Ru(II)_2Fe(III)_2]^{6+}$ was found to be stronger than that in the homometallic system $[Fe(II)_2Fe(III)_2]^{6+}$, which is unexpected[9]. The authors proposed that this might be due to the asymmetric bridging ligands CN^-, which have the potential to propagate not only magnetic but also electronic interactions.

To our knowledge, only two examples of isolated square four-metal, mixed-valence complexes containing two mobile electrons have been published to date. These were studied as potential candidates for QCA devices. Both contain four ferrocene centres, that studied by Jiao et al.[10] incorporating a $Co(\eta^4\text{-}C_4)(\eta^5\text{-}C_5H_5)$ core [Figure 6.2 (a)] whereas the complex studied by Nemykin et al.[11] contains a porphyrin centre [Figure 6.2 (b)].

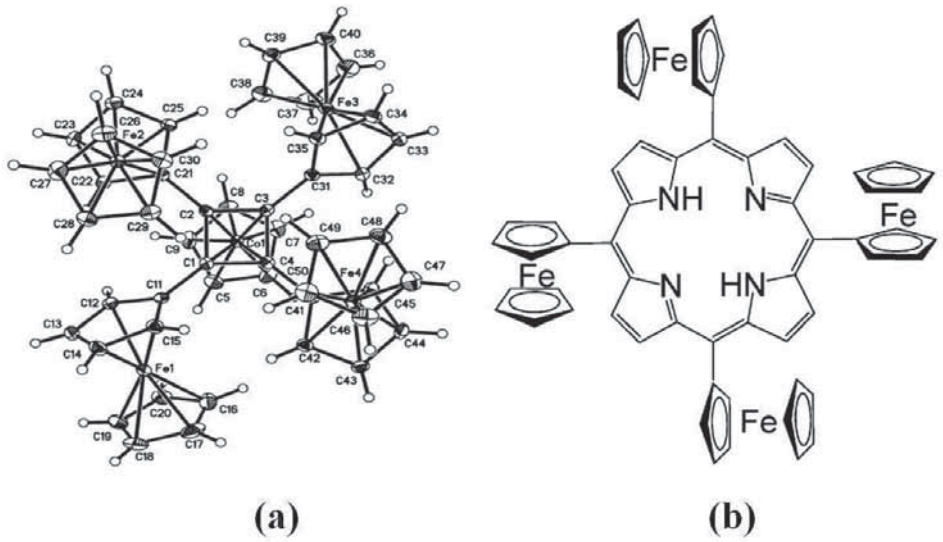

Figure 6.2. *Candidates for molecular QCA cells (neutral species): (a) $\{(\eta^5\text{-}C_5H_5)Fe(\eta^5\text{-}C_5H_4)\}_4(\eta^4\text{-}C_4)Co(\eta^5\text{-}C_5H_5)$. (b) 5,10,15,20-tetraferrocenylporphyrin(2-).*

Both $[\{(\eta^5\text{-}C_5H_5)Fe(\eta^5\text{-}C_5H_4)\}_4(\eta^4\text{-}C_4)Co(\eta^5\text{-}C_5H_5)]^{2+}$ and [5,10,15,20-tetraferrocenyl-porphyrin(2-)]$^{2+}$ mixed-valence systems have been synthesised by chemical oxidation of the neutral parent complexes and characterised. Charge localisation has been probed by IR and Mössbauer spectroscopy while in the Near-IR range, IVCT transitions were observed. The IVCT bands were analysed using Hush theory and the dioxidised tetraferrocenyl complexes were classified as characteristic class II mixed-valence systems. Therefore, the authors concluded that these square systems were excellent candidates for molecular QCA devices. However, the behaviour of such complexes on surfaces has not yet been studied, the challenge probably resulting from difficulties in deposition on surfaces[2a].

The synthesis of bimetallic molecules containing a planar square cyclobutene centre by chemical oxidation of their monometallic butadienyl parents has been described in Chapter 4. The square geometry of these complexes and their charge configurations (+2) are very attractive features for possible QCA models. On this basis, we proposed to synthesise tetrametallic complexes such as those illustrated in Figure 6.3, containing a cyclobutene centre for the square geometry and two positive charges either partially or fully delocalised, for the binary information unit of the QCA cell. In such complexes, the metal atoms are formally in the M(II) state and are expected to be more stable than the above mixed-valence examples, the binary information being encoded by the charge configuration. Further investigation of their physical properties would then determine if they are candidates for molecular QCA devices.

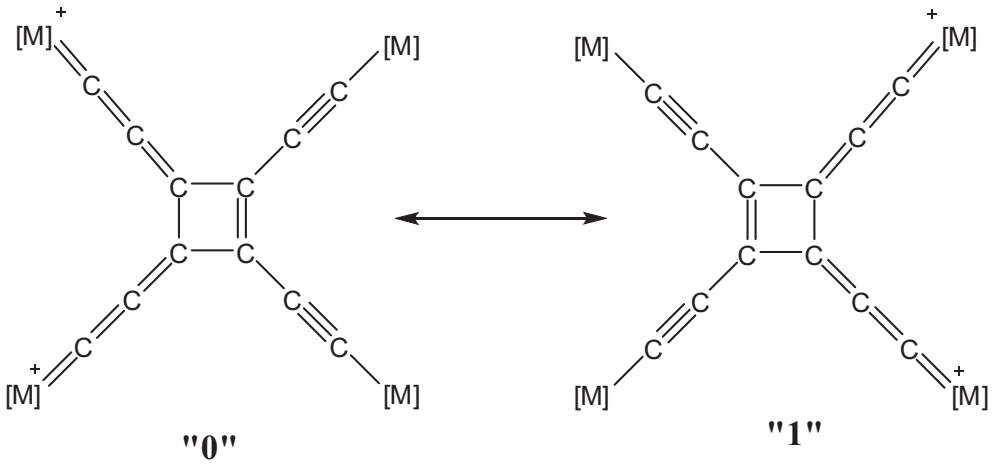

[M] = Ru(dppe)Cp, Fe(dppe)Cp*

Figure 6.3. *Possible molecular QCA models.*

6.2 Aims

The aim of the work described in this Chapter was to synthesise new tetranuclear complexes for possible QCA models. Guided by the results obtained in Chapter 4 on the radical coupling of the 17-e diynyl species which gave dimers containing a cyclobutene core, we thought that similar coupling of the mixed-valence complexes synthesised in Chapter 5 might occur. Indeed, the mixed-valence complexes [**31**]PF_6 and [**35**]PF_6 are unstable above -10°C, further reaction occurring (see Chapter 5); the analogous complexes [**30**]PF_6 and [**34**]PF_6 were

stable and isolable at room temperature. Intermolecular radical coupling between two mixed-valence molecules could afford the symmetrical tetrametallic target complexes needed for possible molecular QCA applications (Scheme 6.1).

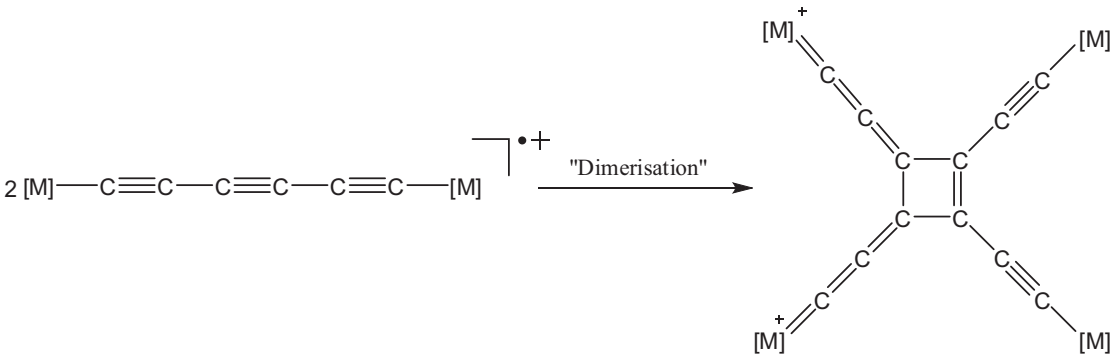

Scheme 6.1. *Expected product from the dimerisation of {Cp'(dppe)M}(C≡CC≡CC≡C){M(dppe)Cp'} (M = Fe, Ru; Cp' = Cp, Cp*): application for QCA models.*

The products resulting from the reactions of the mixed-valence complexes [**31**]PF_6 and [**35**]PF_6 occurring above -10°C are characterised in this Chapter, their physical properties also being investigated. The experimental results were rationalised by DFT calculations carried out by Gendron from the Halet group.

6.3 Results and discussion

6.3.1 Syntheses and structures of the tetranuclear complexes [43][PF_6]$_2$ and [44][PF_6]$_2$

In order to obtain the tetranuclear complexes, the neutral parent complexes **31** and **35** were treated with one equivalent of [$FeCp_2$]PF_6 in THF at -78°C to give unstable mixed-valence complexes [**31**]PF_6 and [**35**]PF_6 (Scheme 6.2). The colour changed immediately from yellow (**31**) or orange (**35**) to deep red which indicated

the formation of the mixed-valence species [**31**]PF_6 and [**35**]PF_6. After one hour at -78°C, the solution was allowed to warm up to room temperature over five hours. When the temperature reached -10°C, the colour of the solution changed from deep red to deep blue (**31**) or purple (**35**) indicating that a further reaction had occurred. After one hour at room temperature, hexane was added to the solution to precipitate the products, which were washed with hexane to afford deep blue {[**31**]PF_6}$_2$ (92% yield) and purple {[**35**]PF_6}$_2$ (65%) powders.

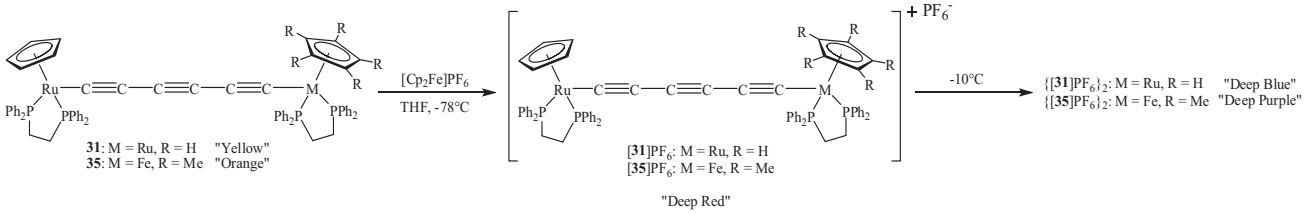

Scheme 6.2

The dimeric formulations were confirmed by high resolution mass spectrometry of the dications at *m/z* 1201.740 (z = 2; calculated: 1201.661 for $[M]^{2+}$) and *m/z* 1226.2818 (z = 2; calculated: 1226.2664 for $[M]^{2+}$) for {[**31**]PF_6}$_2$ and {[**35**]PF_6}$_2$ mixtures, respectively. Well-resolved ion clusters were obtained (Figure 6.4).

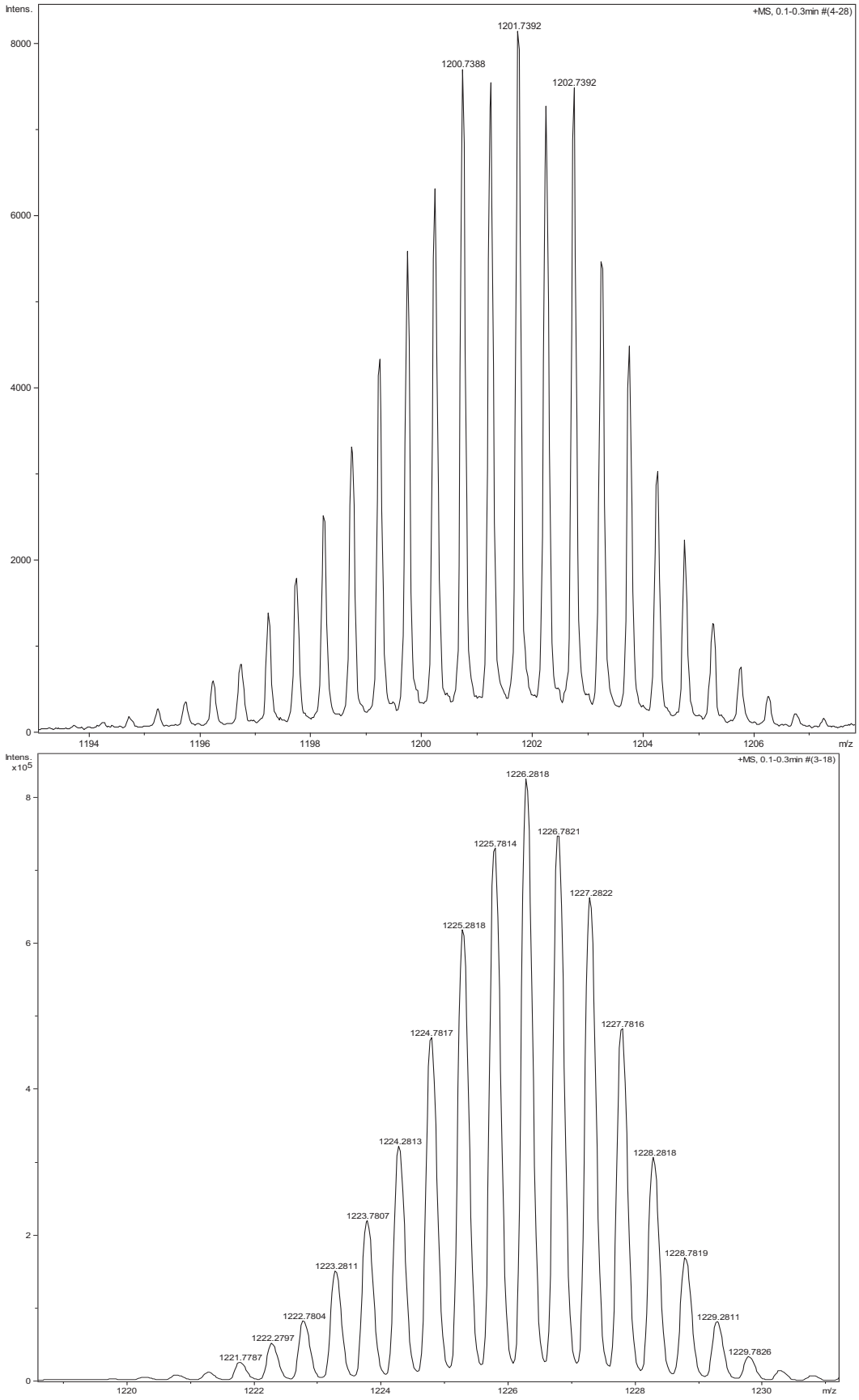

Figure 6.4. *Mass spectra: $[M]^{2+}$ patterns for {[**31**]PF_6}$_2$ (top) and {[**35**]PF_6}$_2$ (bottom).*

Molecular structures

After many attempts, deep blue crystals of $\{[\mathbf{31}]AsF_6\}_2$ were obtained by slow diffusion of benzene into a concentrated solution in dichloromethane, the more bulky $[AsF_6]^-$ anions facilitating crystallisation. The crystals obtained were very prone to desolvation when out of the mother liquor, although the X-ray structure was solved with a R-factor of 0.077. An ORTEP view of the unsymmetrical dication $[\mathbf{43}][AsF_6]_2$ is presented in Figure 6.5 (the phenyl rings of the dppe and the AsF_6^- anions have been omitted for clarity) while selected key parameters are collected in Table 6.1. The unit cell incorporates one molecule of $[\mathbf{43}][AsF_6]_2$, two molecules of dichloromethane and four and half molecules of benzene. The crystal system is triclinic *P*-1 with unit cell parameters: a = 17.2467(7), b = 20.2846(7), c = 22.0628(9) Å, α = 98.452(3), β = 94.541(4) and γ = 95.517(3)°.

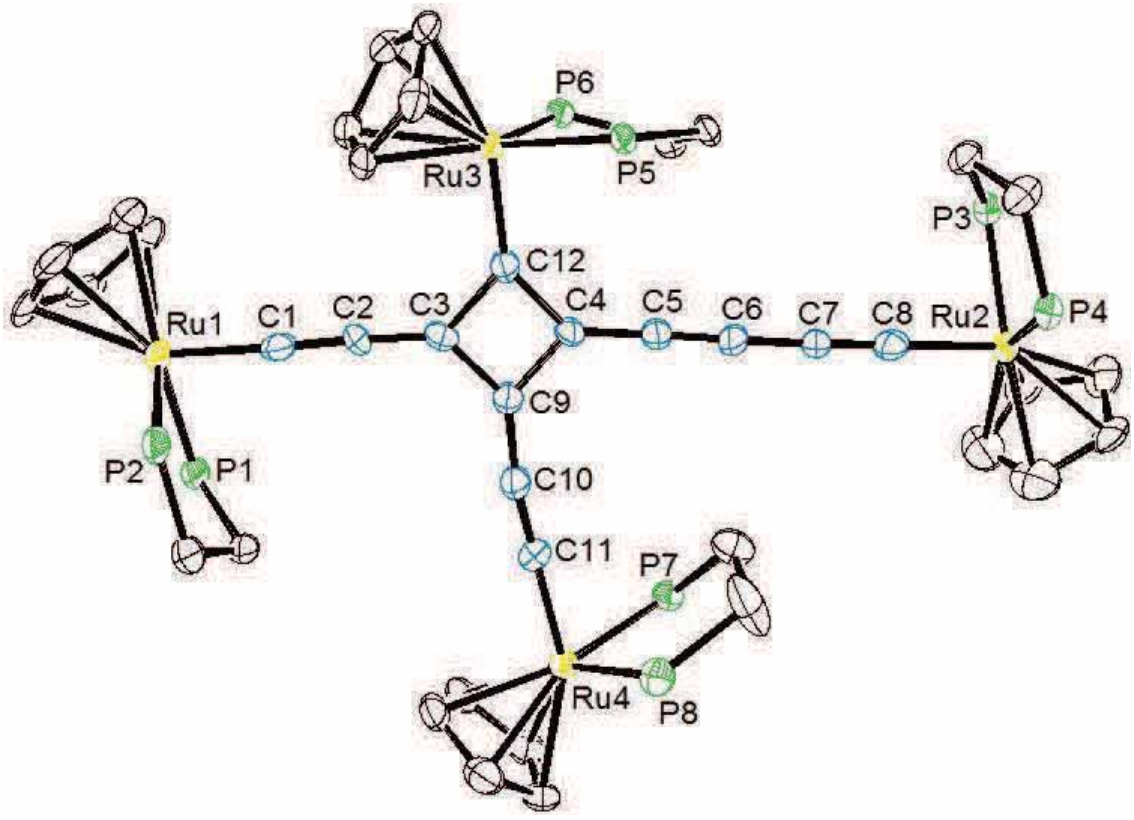

Figure 6.5. *ORTEP view of [{Ru(dppe)Cp}$_4${μ-C$_{12}$}][AsF$_6$]$_2$ [**43**][AsF$_6$]$_2$ (phenyl groups have been omitted for clarity).*

Table 6.1. Selected structural parameters for [**43**][AsF_6]$_2$.

Bond Distances (Å)		**Bond Angles (°)**	
Ru(1,2,3,4)-P(1,3,5,7)	2.269(2), 2.256(2), 2.2675(17), 2.2715(19)	P(1,3,5,7)-Ru(1,2,3,4)-P(2,4,6,8)	83.00(8), 83.96(7), 84.36(7), 82.72(8)
Ru(1,2,3,4)-P(2,4,6,8)	2.293(2), 2.261(2), 2.2594(19), 2.258(2)	C(1,8,12,11)-Ru(1,2,3,4)-P(1,3,5,7)	82.0(2), 83.9(2), 91.6(2), 83.3(2)
Ru(1,2,3,4)-Cp(1,2,3,4)$_{cent}$	1.911, 1.907, 1.911, 1.907	C(1,8,12,11)-Ru(1,2,3,4)-P(2,4,6,8)	86.6(3), 87.3(2), 90.0(2), 88.5(2)
Ru(1,2,3,4)-C(1,8,12,11)	1.916(8), 1.936(8), 1.948(7), 1.933(7)	Ru(1)-C(1)-C(2)	177.0(7)
C(1)-C(2)	1.254(11)	C(1)-C(2)-C(3)	176.7(8)
C(2)-C(3)	1.343(10)	C(2)-C(3)-C(9)	133.8(6)
C(3)-C(9)	1.456(10)	C(2)-C(3)-C(12)	134.8(7)
C(3)-C(12)	1.507(10)	C(9)-C(3)-C(12)	91.4(6)
C(4)-C(5)	1.382(10)	C(5)-C(4)-C(9)	130.6(7)
C(4)-C(9)	1.452(10)	C(5)-C(4)-C(12)	136.0(6)
C(4)-C(12)	1.464(10)	C(9)-C(4)-C(12)	93.3(6)
C(5)-C(6)	1.229(10)	C(6)-C(5)-C(4)	176.4(8)
C(6)-C(7)	1.343(10)	C(5)-C(6)-C(7)	176.5(9)
C(7)-C(8)	1.234(11)	C(8)-C(7)-C(6)	176.8(9)
C(9)-C(10)	1.372(10)	C(7)-C(8)-Ru(2)	177.0(7)
C(10)-C(11)	1.240(11)	C(10)-C(9)-C(4)	132.6(7)
		C(10)-C(9)-C(3)	138.5(7)
		C(4)-C(9)-C(3)	88.8(6)
		C(11)-C(10)-C(9)	170.1(8)
		C(10)-C(11)-Ru(4)	177.5(7)
		C(4)-C(12)-C(3)	86.4(5)
		C(4)-C(12)-Ru(3)	142.2(5)
		C(3)-C(12)-Ru(3)	131.1(5)

As expected, the X-ray analysis confirmed that [**43**][AsF_6]$_2$ contains four Ru(dppe)Cp fragments and one cyclobutene centre. However, the unsymmetrical geometry of the molecule is surprising: two metal fragments are attached to the cyclobutene ring through C_2 chains, while the two others are connected either through a C_4 chain or directly to the cyclobutene centre. The C_4 ring slightly deviates from a perfect square, with angles in the range of 86.4(5)-93.3(6)° (sum of angles = 360°) and C-C bond lengths between 1.452(10)-1.507(10) Å. The three carbon chains Ru(1)-C(1-3), Ru(2)-C(8-4) and Ru(4)-C(11-9) are close to linear, with angles being between 170.1(8)-177.5(7)°, apart from the small bending at the end of the C_4 chain. The C_{12} ligand is approximately planar, with the major bending at C(8): a plane through the atoms C(1-5) and C(9-12) shows deviations of the other atoms C(6), C(7), C(8) of 0.05(1), 0.17(1), 0.34(1) Å, respectively. As expected, each ruthenium atom adopts a pseudo-octahedral geometry; however, the angles C(12)-Ru(3)-P(5) = 91.6(2) and C(12)-Ru(3)-P(6) = 90.0(2)° at the Ru(3) atom are larger than in the other Ru(dppe)Cp fragments which is probably due to steric hindrance [the Ru(3)(dppe)Cp fragment is directly attached to the C_4 ring]. Distances in the four Ru(dppe)Cp fragments are very similar, the Ru-P bond lengths being in the range 2.256(2)-2.293(2) Å, somewhat longer than in typical neutral Ru(II)(dppe)Cp complexes such as **31** (see Chapter 5), and shorter than those found in typical cationic [Ru(II)(dppe)Cp]$^+$ complexes (Ru-P ≈ 2.30 Å)[12]. Similarly, the Ru-C(chain) bond lengths are between 1.916(8)-1.948(7) Å, which is between typical Ru(II)-C(dppe)Cp (≈ 2.00 Å) and [Ru(II)=C(dppe)Cp]$^+$ (≈ 1.85 Å) distances. The C-C distances within the carbon chains (two C_2 and one C_4) of the C_{12} ligand are also very similar, the formal C≡C triple bonds are slightly elongated [1.229(10)-1.254(11) Å] while the formal C-C single bonds are slightly shortened [1.343(10)-1.382(10) Å]. Distances in the cyclobutene ring [range 1.452(10)-1.507(10) Å] are also between C=C double and C-C single bonds, C(3)-C(12) = 1.507(10) Å being a C-C single bond. The distances in the Ru(dppe)Cp fragments being between typical Ru(II)(dppe)Cp and [Ru(II)(dppe)Cp]$^+$ bond lengths, together with the distances found in the C_{12} ligand indicate that the positive charges are not localised on two metal centres, as it might be expected for an unsymmetrical complex, but are delocalised on the whole molecule at the X-ray time scale. This last observation makes it difficult to represent the bonding of

[**43**][PF_6]$_2$ with a single Lewis formula; thus it has been drawn as fully delocalised (Scheme 6.3).

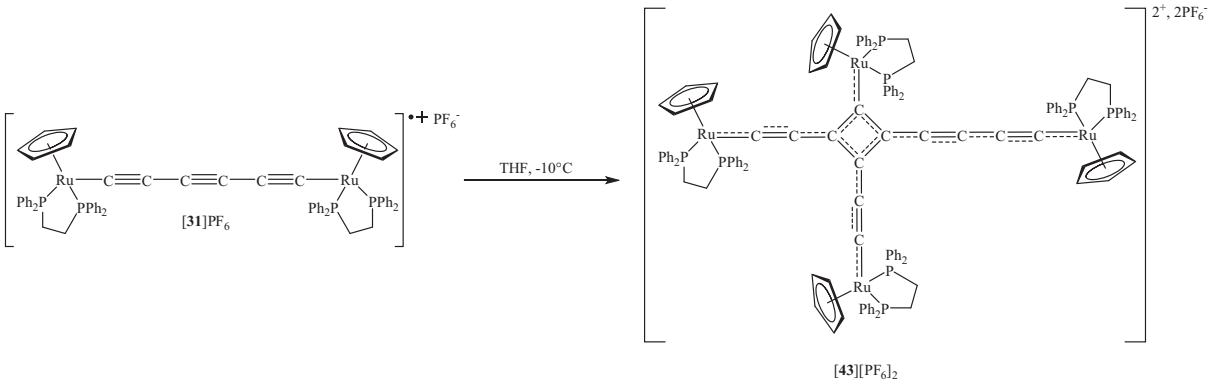

Scheme 6.3

Initially, it was thought that, similar to the dimerisation of the Ru(C≡CC≡CR)(dppe)Cp (R = Ph **23**, Fc **24**) (see Section 4.1.1), two isomers might result from the dimerisation of [**31**]PF_6. Beside the unsymmetrical compound [**43**][PF_6]$_2$, a symmetric dimer, which would be more appropriate for possible molecular QCA applications, could be formed (Scheme 6.4). However, this hypothesis was quickly ruled out by the NMR characterisation (see Section 6.3.2) and the clean electrochemistry (see Section 6.3.4) which confirmed that only the unsymmetrical dimer [**43**][PF_6]$_2$ is formed upon thermal evolution of [**31**]PF_6.

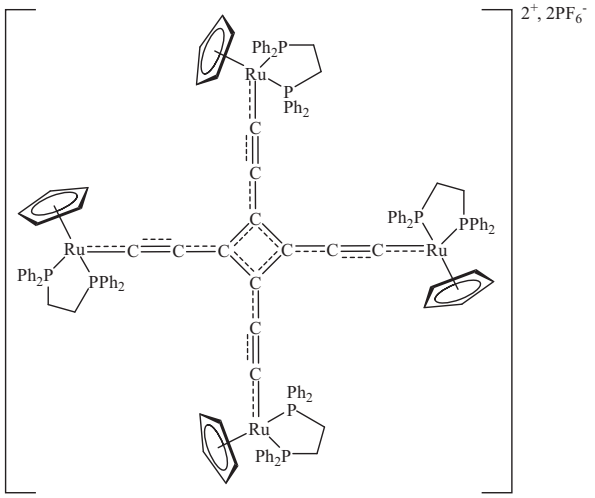

Scheme 6.4. *Formula of the symmetric dimer which was not formed upon oxidative dimerisation of **31***

The product which results from the dimerisation of the mixed-iron and -ruthenium complex [**35**]PF_6 also provided small deep purple crystals by slow diffusion of hexane into a concentrated solution in dichloromethane. Figure 6.6 is an ORTEP view of the tetranuclear complex [**44**][PF_6]$_2$ while selected structural parameters are collected in Table 6.2. The asymmetric unit incorporates one molecule of [**44**][PF_6]$_2$ and four molecules of dichloromethane. One PF_6^- anion is disordered, although the X-ray structure was solved with a respectable R-factor of 0.079. The crystal system is triclinic *P*-1 with unit cell parameters: a = 13.5399(5), b = 18.4682(8), c = 29.2517(12) Å, α = 87.561(3), β = 88.318(3) and γ = 79.960(3)°.

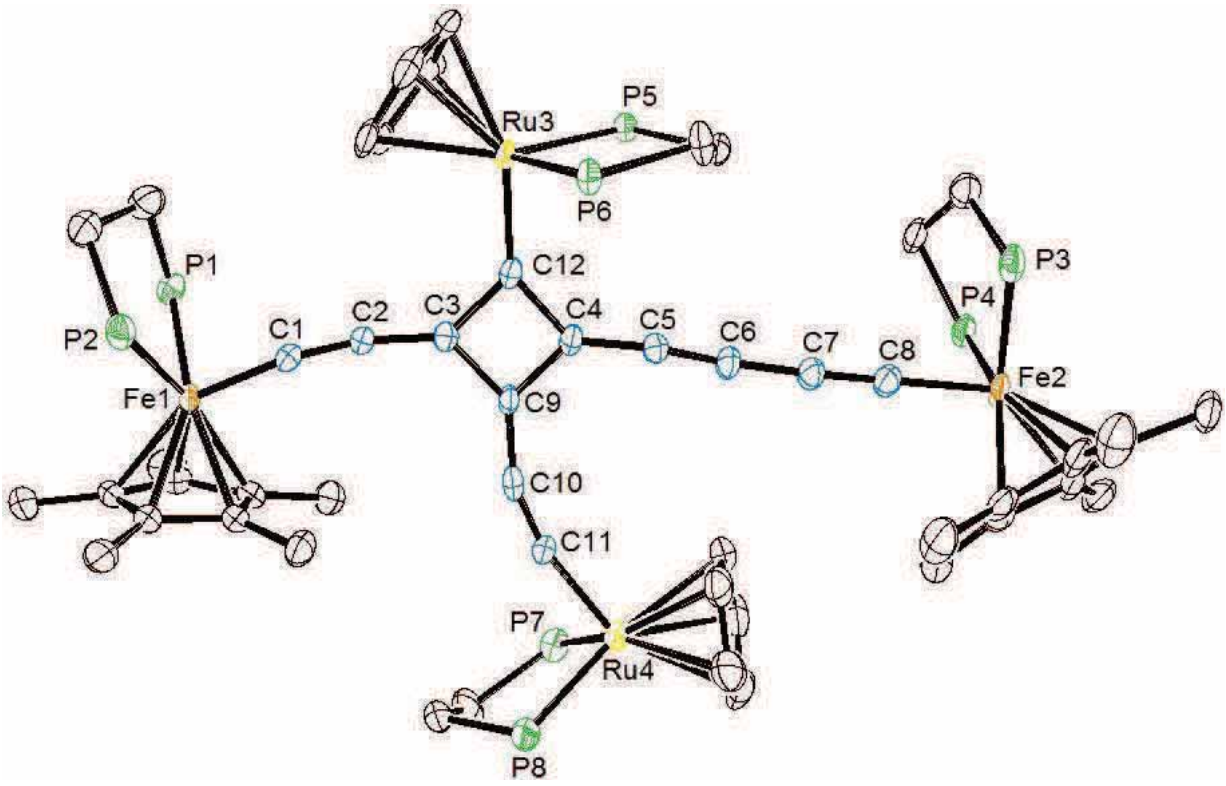

Figure 6.6. *ORTEP view of [{Fe(dppe)Cp*}$_2${Ru(dppe)Cp}$_2${μ-C_{12}}][PF_6]$_2$ [**44**][PF_6]$_2$ (phenyl groups have been omitted for clarity).*

Table 6.2. Selected structural parameters for [**44**][PF_6]$_2$.

Bond Distances (Å)		Bond Angles (°)	
Fe(1,2)-P(1,3)	2.2194(17), 2.196(2)	P(1,3)-Fe(1,2)-P(2,4)	86.46(7), 86.27(7)
Fe(1,2)-P(2,4)	2.2429(18), 2.1956(18)	C(1,8)-Fe(1,2)-P(1,3)	87.88(18), 86.9(2)
Fe(1,2)-Cp*(1,2)$_{cent}$	1.764, 1.754	C(1,8)-Fe(1,2)-P(2,4)	92.77(19), 82.22(19)
Fe(1,2)-C(1,8)	1.813(6), 1.837(6)	P(5,7)-Ru(3,4)-P(6,8)	84.14(5), 82.44(6)
Ru(3,4)-P(5,7)	2.2613(15), 2.2722(17)	C(12,11)-Ru(3,4)-P(5,7)	94.21(16), 90.85(17)
Ru(3,4)-P(6,8)	2.2839(15), 2.2795(17)	C(12,11)-Ru(3,4)-P(6,8)	89.38(16), 92.14(17)
Ru(3,4)-Cp(3,4)$_{cent}$	1.923, 1.903	Fe(1)-C(1)-C(2)	169.5(5)
Ru(3,4)-C(12,11)	1.950(6), 1.942(6)	C(1)-C(2)-C(3)	167.8(6)
C(1)-C(2)	1.244(7)	C(2)-C(3)-C(9)	132.1(5)
C(2)-C(3)	1.365(7)	C(2)-C(3)-C(12)	137.6(5)
C(3)-C(9)	1.465(7)	C(9)-C(3)-C(12)	90.2(4)
C(3)-C(12)	1.495(7)	C(5)-C(4)-C(9)	130.6(5)
C(4)-C(5)	1.384(8)	C(5)-C(4)-C(12)	136.5(5)
C(4)-C(9)	1.427(7)	C(9)-C(4)-C(12)	92.5(4)
C(4)-C(12)	1.475(8)	C(6)-C(5)-C(4)	173.5(6)
C(5)-C(6)	1.213(8)	C(5)-C(6)-C(7)	176.1(6)
C(6)-C(7)	1.359(8)	C(8)-C(7)-C(6)	173.1(7)
C(7)-C(8)	1.246(8)	C(7)-C(8)-Fe(2)	178.1(6)
C(9)-C(10)	1.375(8)	C(10)-C(9)-C(4)	131.1(5)
C(10)-C(11)	1.237(8)	C(10)-C(9)-C(3)	138.6(5)
		C(4)-C(9)-C(3)	90.1(4)
		C(11)-C(10)-C(9)	158.0(6)
		C(10)-C(11)-Ru(4)	165.2(5)
		C(4)-C(12)-C(3)	87.1(4)
		C(4)-C(12)-Ru(3)	140.3(4)
		C(3)-C(12)-Ru(3)	132.0(4)

As for the dimer [**43**][PF_6]$_2$, the X-ray analysis showed [**44**][PF_6]$_2$ to be the unsymmetrical dimer containing two Fe(dppe)Cp* and two Ru(dppe)Cp fragments, together with a cyclobutene centre. The two Fe(dppe)Cp* fragments are connected to the cyclobutene centre through C_2 and C_4 chains, opposed to each other, similar to the Ru(dppe)Cp fragments which are straight or through a C_2 chain attached to the cyclobutene ring. The sum of the angles in the cyclobutene ring is 360° and the C_{12} ligand is quasi-planar, the C_4 chain being slightly bent and out of the cyclobutene plane. As expected, the iron and ruthenium atoms each adopt a pseudo-octahedral geometry. In the Fe(dppe)Cp* fragments, the Fe-P distances being between 2.2194(17)-2.2429(18) Å are slightly longer and the Fe(1,2)-C(1,8) [1.813(6) and 1.837(6) Å] are shorter than in the neutral starting material **35** (see Chapter 5). Similar changes are observed for the Ru(dppe)Cp fragments: the Ru-P distances are longer [being between 2.2613(15)-2.2839(15) Å] and the Ru(3,4)-C(12,11) [1.950(6) and 1.942(6) Å] are shorter compared with **35**. In comparison with the tetraruthenium complex [**43**][PF_6]$_2$, the average Ru-P and Ru-C_α distances in [**44**][PF_6]$_2$ [Ru-P(average) = 2.274; Ru-C_α(average) = 1.946 Å] are not significantly different than in [**43**][PF_6]$_2$ [Ru-P(average) = 2.267; Ru-C_α(average) = 1.933Å]. Therefore, as for [**43**][PF_6]$_2$, we conclude that the positive charges in [**44**][PF_6]$_2$ are delocalised over the whole molecule, even with the presence of the two Fe(dppe)Cp* fragments where the positive charges could be expected to be more localised. This is in good agreement with the formal C≡C triple bonds [range 1.213(8)-1.246(8) Å], being slightly longer [apart for C(5)-C(6) = 1.213(8) Å which is closer to a C≡C triple bond], and the C-C single bonds of the carbon chains [range 1.359(8)-1.384(8) Å] being slightly shorter. As in [**43**][PF_6]$_2$, bond lengths in the cyclobutene ring are between 1.427(7)-1.495(7) Å, between C=C double and C-C single bonds, with the C(3)-C(12) distance also being the longest. As described above, the carbon chains of the molecule [**44**][PF_6]$_2$ are in the cyclobutene plane apart from the Fe(2)-C_4 chain which is slightly out of the plane; however, both M(1,4)-C_2 chains are significantly bent in the cyclobutene plane with angles being in the 158.0(6)-169.5(5)° range, which can be seen in Figure 6.6. The difference between [**43**][PF_6]$_2$ and [**44**][PF_6]$_2$ is probably due to steric hindrance caused by the Cp* of the Fe(dppe)Cp* fragments in [**44**][PF_6]$_2$ which are bulkier than the Cp in the Ru(dppe)Cp fragments.

Aside from the hypothesis of the presence of "symmetrical" dimers (containing four C_2 chains) with geometry similar to that of the dimer drawn in Scheme 6.4, which has been eliminated by comparison with the dimer [**43**][PF_6]$_2$, another unsymmetrical dimer [**45**][PF_6]$_2$ (Scheme 6.5) could be formed during the oxidative coupling of **35**. Hypothetical dimer [**45**][PF_6]$_2$ differs by having two mutually *cis* Fe (or Ru) fragments. Further work is in progress to determine whether other isomers are formed in the dimerisation reactions described above.

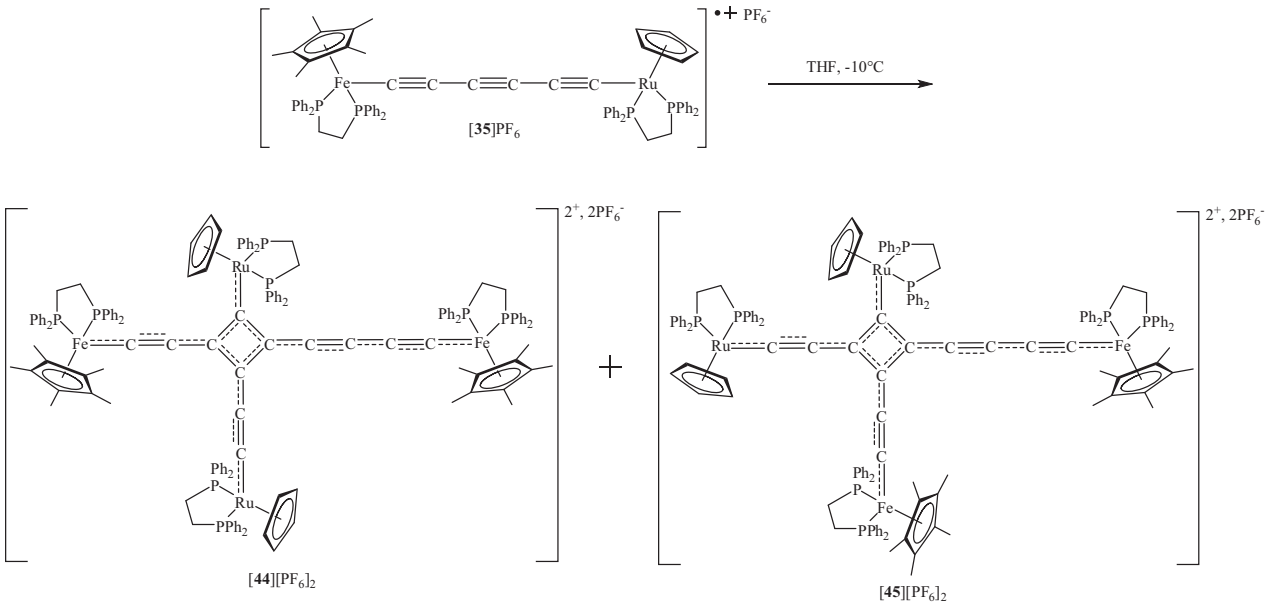

Scheme 6.5. *Oxidative dimerisation of **35**: formation of dimer [**44**][PF_6]$_2$ and an hypothetical dimer [**45**][PF_6]$_2$.*

6.3.2 Characterisation of the tetraruthenium complex [43][PF_6]$_2$

The ^{31}P NMR spectrum of [**43**][PF_6]$_2$ contains only one unresolved, very broad and weak signal between δ 80 and 95 at room temperature. In contrast, the signal of the PF_6^- anions was observed as a very well resolved septuplet ($^1J_{PF}$ = 710 Hz) centred at δ -143.2. In order to improve the resolution in the δ 80-95 region, low temperature ^{31}P NMR spectra were measured. The ^{31}P NMR spectrum of [**43**][PF_6]$_2$ recorded at -80°C is shown in Figure 6.7 and contains three broad peaks at δ 80.7, 85.3 and 94.8 (relative intensity 1:2:1), consistent with the presence of only one product. The signal at δ 85.3, with a relative intensity of 2, is assigned to the dppe phosphorus atoms of the two similar -C_2-Ru(dppe)Cp fragments. The peak centred at δ 94.8 is assigned to the Ru(dppe)Cp directly attached to the C_4

ring; ^{31}P NMR chemical shifts of the dppe phosphorus atoms of similar ruthenium complexes being substituted on the C_α, are centred in the δ 90-100 region[13]. De facto, the last signal at δ 80.7 is assigned to the fourth Ru(dppe)Cp fragment, attached to the cyclobutene ring through the C_4 chain.

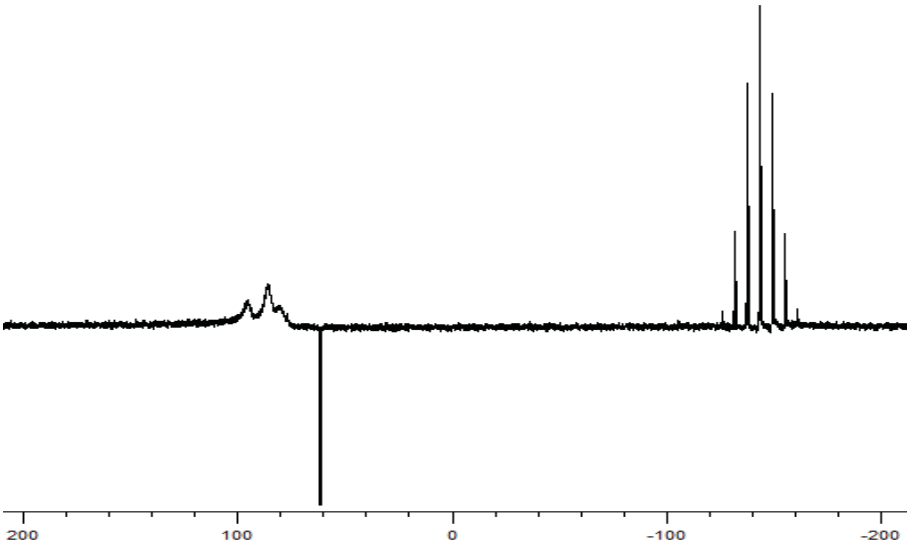

Figure 6.7. *^{31}P NMR spectrum of [**43**][PF_6]$_2$ in acetone-d_6 at -80°C.*

In the room temperature ^{1}H NMR spectrum, the CH_2 and aromatic protons of the dppe ligand were found between δ 2.62-3.08 and δ 7.01-8.01, respectively. The protons of the four different Cp ligands (Figure 6.8) were observed at δ 4.86 [s(br)], 5.15 (s), 5.20 (s) and 5.64 [s(br)], which also indicates that [**43**][PF_6]$_2$ is clearly the only product from the oxidative dimerisation of **31**. As the chemical shifts of the Cp protons were very close to each other, no signal could be assigned with exactitude to a selected Ru(dppe)Cp fragment.

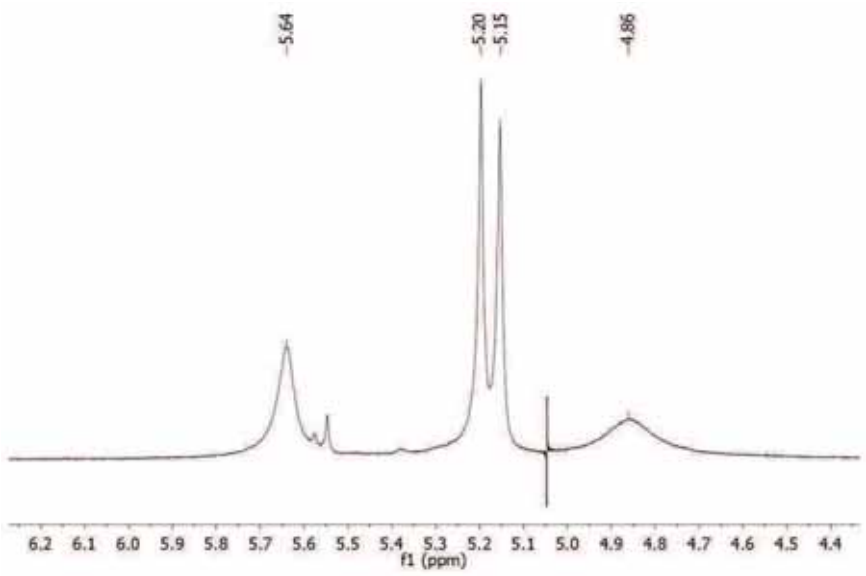

Figure 6.8. *^{1}H NMR spectrum of [**43**][PF_6]$_2$ in acetone-d_6 at room temperature.*

In the ^{13}C NMR spectrum, also recorded at room temperature, very weak and broad unresolved signals were observed at δ 227.81, 258.64, 226.10, 187.15 and 159.69, which could be assigned to the C_α atoms directly attached to the Ru(dppe)Cp centre, together with some *sp* carbons of the chains. Other signals were found in the aromatic region as multiplets between δ 125.59-143.39, which could be assigned to the phenyl groups of the dppe ligands and some carbons of the C_{12} ligand. The Cp carbons were observed as four singlets (three well-resolved) at δ 86.62, 87.04, 88.26 (br) and 89.49 for the four different Ru(dppe)Cp fragments. The chemical shifts of the Cp carbons are between those of neutral Ru(II)(dppe)Cp and cationic [Ru(II)(dppe)Cp]$^+$ moieties. Finally, the CH_2 groups of the dppe ligand were observed, as expected, as multiplets between δ 27.70-31.46. Additionally, no *sp* carbon resonances were observed in the usual C≡C triple bond range.

The new tetranuclear dimer [**43**][PF_6]$_2$ was further characterised by IR spectroscopy in solution (CH_2Cl_2) and in the solid state (Nujol) in order to observe and hopefully assign the different multiple bonds in the molecule. In the IR spectrum recorded in Nujol, two ν(CC) vibrations were observed at 2069(m) and 1941(s) cm^{-1} while the ν(PF) band was displayed at 836 cm^{-1}. The IR spectrum of a dichloromethane solution is shown in Figure 6.9, where two signals are observed in the multiple carbon-carbon bond region: a medium band was found at 2071 cm^{-1}

while a second strong band is centred at 1928 cm^{-1} with two shoulders at 1983 and 1960 cm^{-1}. The solution and solid state spectra are very similar overall, but the strong and large band at 1941 cm^{-1} in the Nujol spectrum, is split into three closely separated bands at 1983, 1960 and 1928 cm^{-1} in the solution spectrum. The higher energy band at 2071 cm^{-1} (in CH_2Cl_2) was initially assigned to a ν(C≡C) vibration, but could also be assigned to a vibration from a cumulenic form of the C_4 chain although this has never been identified before for this kind of molecule. Similarly, the bands at 1983, 1960 and 1928 cm^{-1} (in CH_2Cl_2) could either be assigned to allenylidene ν(C=C=C) or to low energy ν(C≡C) vibrations. Deduction of the proper Lewis formulas for [**43**][PF_6]$_2$ from the IR observations is thus very difficult because of the uncertain attributions of the ν(CC) vibrations.

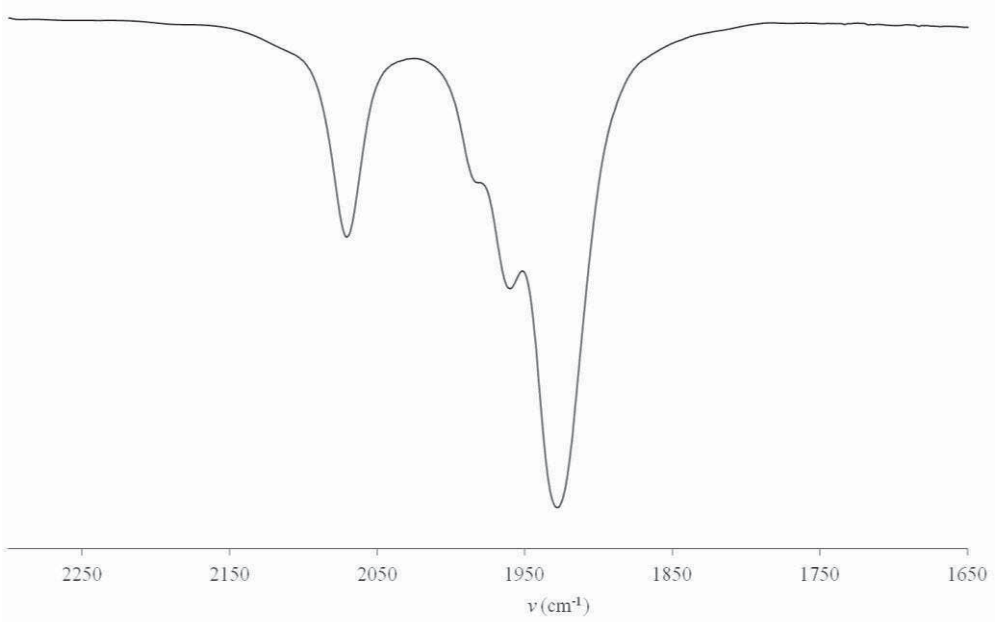

Figure 6.9. *IR spectrum of [43][PF_6]$_2$ in CH_2Cl_2.*

From the IR and NMR analyses of [**43**][PF_6]$_2$, no exact conformation with localised charges on selected metal centres can be proposed, the configuration where positive charge is fully delocalised (Scheme 6.3) being the most appropriate.

6.3.3 Supporting DFT calculations

In order to understand why some of the mixed-valence complexes synthesised in Chapter 5 were stable and isolable ([**30**]PF_6 and [**34**]PF_6) whereas some others

were not ([**31**]PF_6 and [**35**]PF_6), dimerising to afford the tetrametallic complexes [**43**][PF_6]$_2$ and [**44**][PF_6]$_2$, DFT calculations were carried out by Gendron. These calculations also allow mechanisms for the formation of dimers [**43**][PF_6]$_2$ and [**44**][PF_6]$_2$ to be proposed. Additionally, DFT calculations were also performed on the tetrametallic complexes synthesised in this Chapter.

6.3.3.1 Atomic spin densities of the 35-electron species [{Cp'(dppe)M}(C≡CC≡CC≡C){M(dppe)Cp'}]PF_6 (M = Fe, Ru; Cp' = Cp, Cp)*

As in Chapter 4 (Section 4.3.4), atomic spin densities of the four symmetric and asymmetric 35-e species [**30**]PF_6, [**31**]PF_6, [**34**]PF_6 and [**35**]PF_6 were calculated in order to study the effect of the metals (iron or ruthenium) and the ligands (Cp or Cp*). The values and representations of the atomic spin densities are shown in Figure 6.9 while the overall values are summarised in Table 6.3. In the symmetrical diiron complex [**30**]PF_6, the atomic spin density is mainly localised on the iron atoms with a value of 0.354 for each metal, whereas the atomic spin densities on the carbon chain (0.054, 0.069 and 0.056) are low. This indicates that the unpaired electron in [**30**]PF_6 is mainly localised on the iron atoms. In contrast, in the symmetrical diruthenium complex [**31**]PF_6 there are much smaller atomic spin densities on the metal centres (0.167 for both ruthenium atoms) and much larger on the carbon chain which suggests that the unpaired electron density is delocalised on the carbon chain between both ruthenium atoms. The spin density on C_1 is very large with a value of 0.124, while the spin densities on C_2 and C_3 (0.078 and 0.091 respectively) are slightly lower. On the other hand, the unsymmetrical complexes [**34**]PF_6 and [**35**]PF_6, which have very different kinetic stabilities, have similar atomic spin density distributions, being between the spin densities found for the symmetrical complexes [**30**]PF_6 and [**31**]PF_6. Indeed, large spin densities are found on the metallic atoms, values being higher for the iron (0.362 and 0.390) than for the ruthenium (0.168 and 0.147) in [**34**]PF_6 and [**35**]PF_6, respectively. In both cases, C_6, which is bonded to the ruthenium, has a large spin density being over 0.1 (0.103 and 0.117 for [**34**]PF_6 and [**35**]PF_6, respectively). Atomic spin densities on the rest of the carbon chains alternate from 0.049 to 0.095, being stronger on the even-numbered and weaker on the odd-numbered carbons. The carbon chain spin densities are slightly more equally distributed in

[**34**]PF_6 than in [**35**]PF_6, where the spin densities on the C_2 and C_4 (0.095 and 0.092, respectively) are quite large. The nature of the metal atoms has a significant effect on the carbon chain atomic spin densities: carbon atoms nearer to Fe usually have weak spin densities whereas carbons on the Ru side have large spin densities: cf. C_6 in [**34**]PF_6 and [**35**]PF_6 and C_1 in [**31**]PF_6. This is due to the ruthenium orbitals being more diffuse than the iron ones, decreasing the localisation of the unpaired electron on the metallic sites. Exchange of Cp* for Cp does not seem to have a strong effect on the distribution of the atomic spin densities, the value on the ruthenium atom being slightly larger in [**34**]PF_6 (0.168) than that in [**35**]PF_6 (0.147), whereas for the C_6, the opposite trend is found (0.103 and 0.117 for [**34**]PF_6 and [**35**]PF_6, respectively).

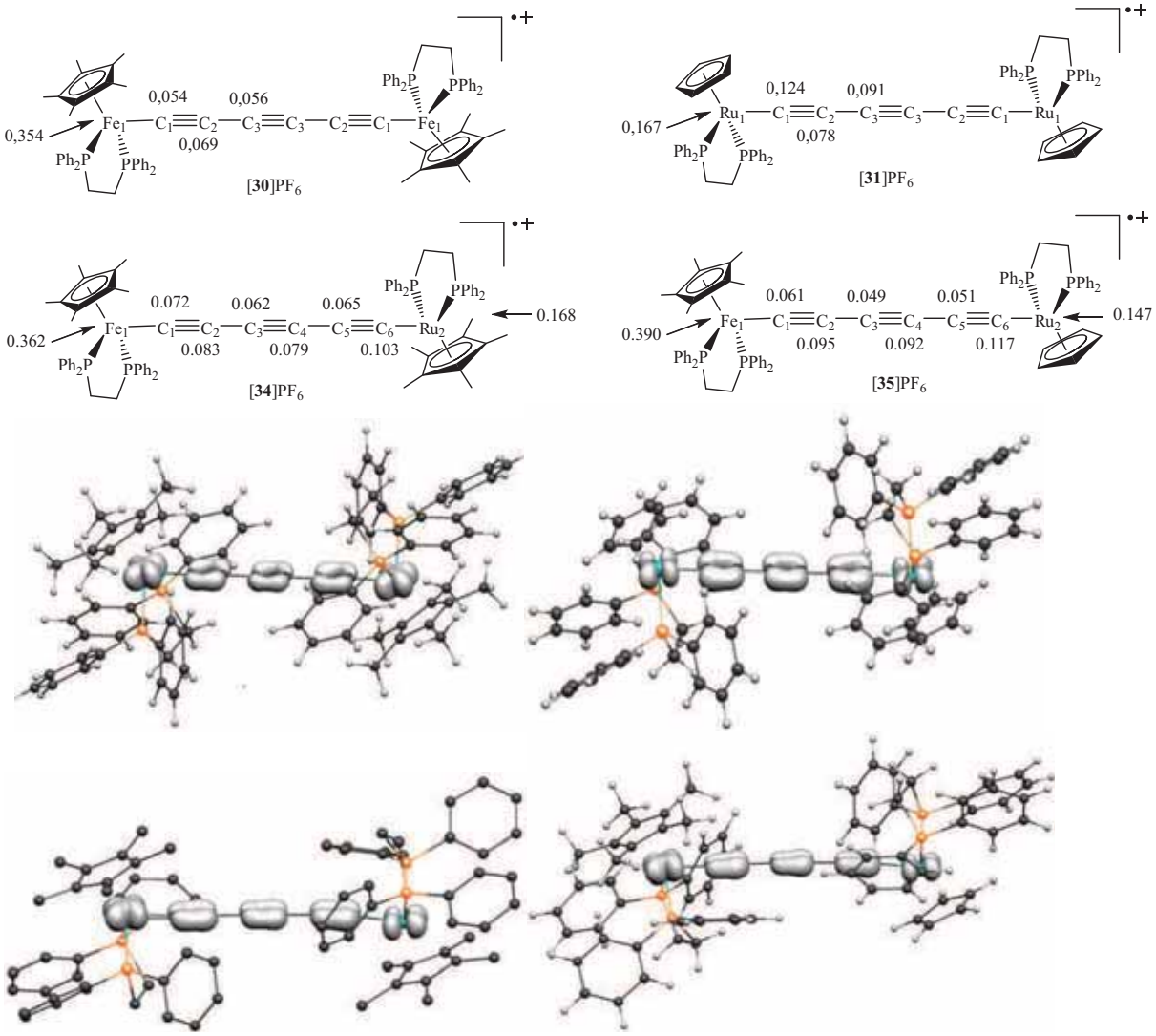

Figure 6.9. *Calculated (top) and representation (bottom) of the atomic spin densities in [**30**]PF_6, [**31**]PF_6, [**34**]PF_6 and [**35**]PF_6.*

Table 6.3. Atomic spin densities of the [{Cp'(dppe)M}(C≡CC≡CC≡C){M(dppe)Cp'}]PF_6 (M = Fe, Ru; Cp' = Cp, Cp*).

Compound	M_1	C_1	C_2	C_3	C_4	C_5	C_6	M_2
[**30**]PF_6	0.354	0.054	0.069	0.056				
[**31**]PF_6	0.167	0.124	0.078	0.091				
[**34**]PF_6	0.362	0.072	0.083	0.062	0.079	0.065	0.103	0.168
[**35**]PF_6	0.390	0.061	0.095	0.049	0.092	0.051	0.117	0.147

6.3.3.2 Proposed mechanisms for the formation of the dimers [43][PF_6]$_2$ and [44][PF_6]$_2$

Guided by the atomic spin density calculations, mechanisms based on radical coupling, as for the dimerisation of [Fe(C≡CC≡CPh)(dppe)Cp*]$^{\bullet+}$ (**2a**$^{\bullet+}$) in Chapter 4, can be proposed for the dimerisation of 35-e species **31**$^{\bullet+}$ and **35**$^{\bullet+}$. The proposed mechanism for the formation of the tetraruthenium dimer [**43**][PF_6]$_2$ is represented in Scheme 6.6. According to the atomic spin densities, the most favourable radical coupling would be between the C_1 atoms of two molecules of **31**$^{\bullet+}$, where the largest atomic spin density (0.124) of the carbon chain is located. However, evident steric hindrance between C_1 and the Cp and dppe ligands precludes this C_1-C_1 coupling. The C_3-C_3 radical coupling which would lead to the targeted symmetrical dimer (Scheme 6.4) does unfortunately not occur. This cannot be for steric hindrance reasons: the central C_3≡C_3 triple bond is sterically the most accessible. However, the lack of C_3-C_3 coupling may be due to the relatively small atomic spin density on C_3 (0.091). It has been proposed that for the radical to be reactive and to couple to form carbon-carbon bonds, the atomic spin density on the carbon atom has to be greater than 0.1.[14] The second most favourable radical coupling is thus between C_1 and C_3, which bears the second largest atomic spin density (0.091) in the carbon chain, and leads to the dimer [**43**][PF_6]$_2$. The C_3'-C_2 coupling which could also form the dimer [**43**][PF_6]$_2$ is unlikely, according to the atomic spin densities.

The intermediate resulting from the C_1-C_3 bond formation, which contains both the highly reactive butatrienylidene and hexapentaenylidene units, rapidly reacts

further to complete intramolecular cyclisation and afford the stable, fully delocalised dimer [**43**][PF_6]$_2$. The driving force of this reaction might be due to the formation of the much more stable cyclic product [**43**][PF_6]$_2$.

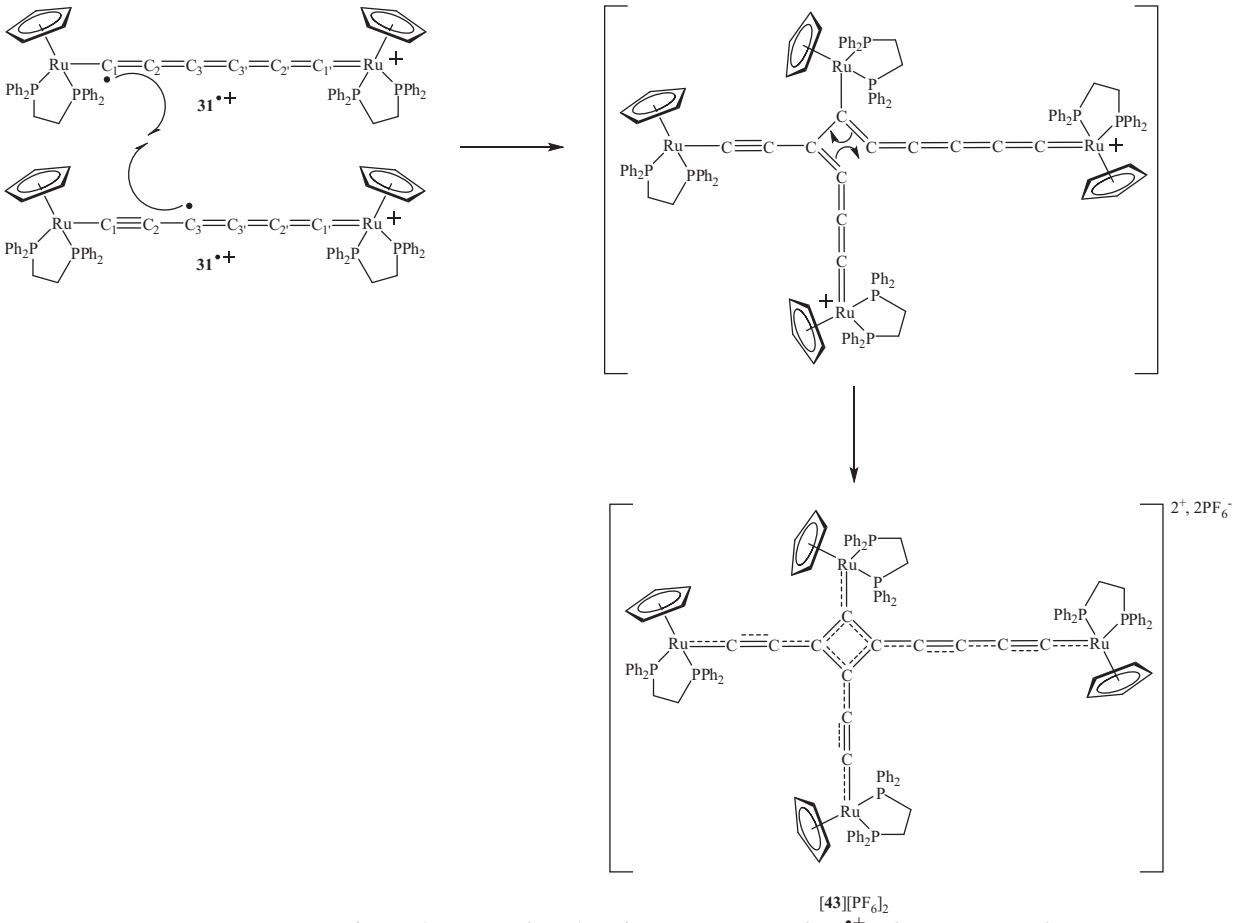

Scheme 6.6. *Proposed mechanism for the dimerisation of* ***31***$^{\bullet+}$*: formation of [**43**][PF_6]$_2$.*

The mechanism of the dimerisation of **35**$^{\bullet+}$ to give [**44**][PF_6]$_2$ in which the two Fe(dppe)Cp* and Ru(dppe)Cp fragments are diagonally opposed, can be only partially explained by considering the atomic spin densities of the carbon atoms of the bridging ligand. Indeed, according to the calculated atomic spin densities, several different couplings could occur to give different dimers. As in **31**$^{\bullet+}$, the carbon atom attached to the Ru(dppe)Cp fragment in **35**$^{\bullet+}$, C_6, has the largest atomic spin density of the carbon chain (0.117) suggesting that C_6 should be the reactive site. Two carbons of the chain with similar strong spin density could couple with C_6: C_2 (0.095) and C_4 (0.092). The C_6-C_2 coupling would afford a hypothetical dimer containing one Ru(dppe)Cp and one Fe(dppe)Cp* fragment

directly attached to the central C_4 square; this is unfavoured for steric hindrance reasons as observed for the dimerisation of $[Fe(C{\equiv}CC{\equiv}CPh)(dppe)Cp^*]^{\bullet+}$ (**2a**$^{\bullet+}$) (Chapter 4). However, no steric hindrance prevents the C_6-C_4 coupling (Scheme 6.7, Path B); then, as above, the highly unstable intermediate would immediately react further by intramolecular cyclisation to give the hypothetical dimer [**45**][PF_6]$_2$ containing two mutually *cis* Ru(dppe)Cp and two Fe(dppe)Cp* moieties. Surprisingly, we obtained the fully delocalised dimer [**44**][PF_6]$_2$, which originates from the radical coupling C_6-C_3 (Scheme 6.7, Path A), the atomic spin density on C_3 (0.049) being the lowest of the chain in **35**$^{\bullet+}$. This result might be explained by the fact that the C_6 is definitely the reactive site which can couple randomly (or not) with any sterically free carbon of the chain, the atomic spin densities on these carbon atoms being of secondary importance. Therefore, the dimers [**44**][PF_6]$_2$ and [**45**][PF_6]$_2$ might both be formed during the oxidative coupling of **35**, dimer [**44**][PF_6]$_2$ being the easiest to crystallise. The formation of dimer [**44**][PF_6]$_2$ could also be explained by a more favourable spatial approach of both **35**$^{\bullet+}$ molecules due to charge repulsive interactions. Indeed, in **35**$^{\bullet+}$ the charge is more localised on the iron than on the ruthenium atom and an approach of the two molecules with the iron centres on the same side could be less favoured that an approach of an iron and a ruthenium centre on the same side (Scheme 6.7).

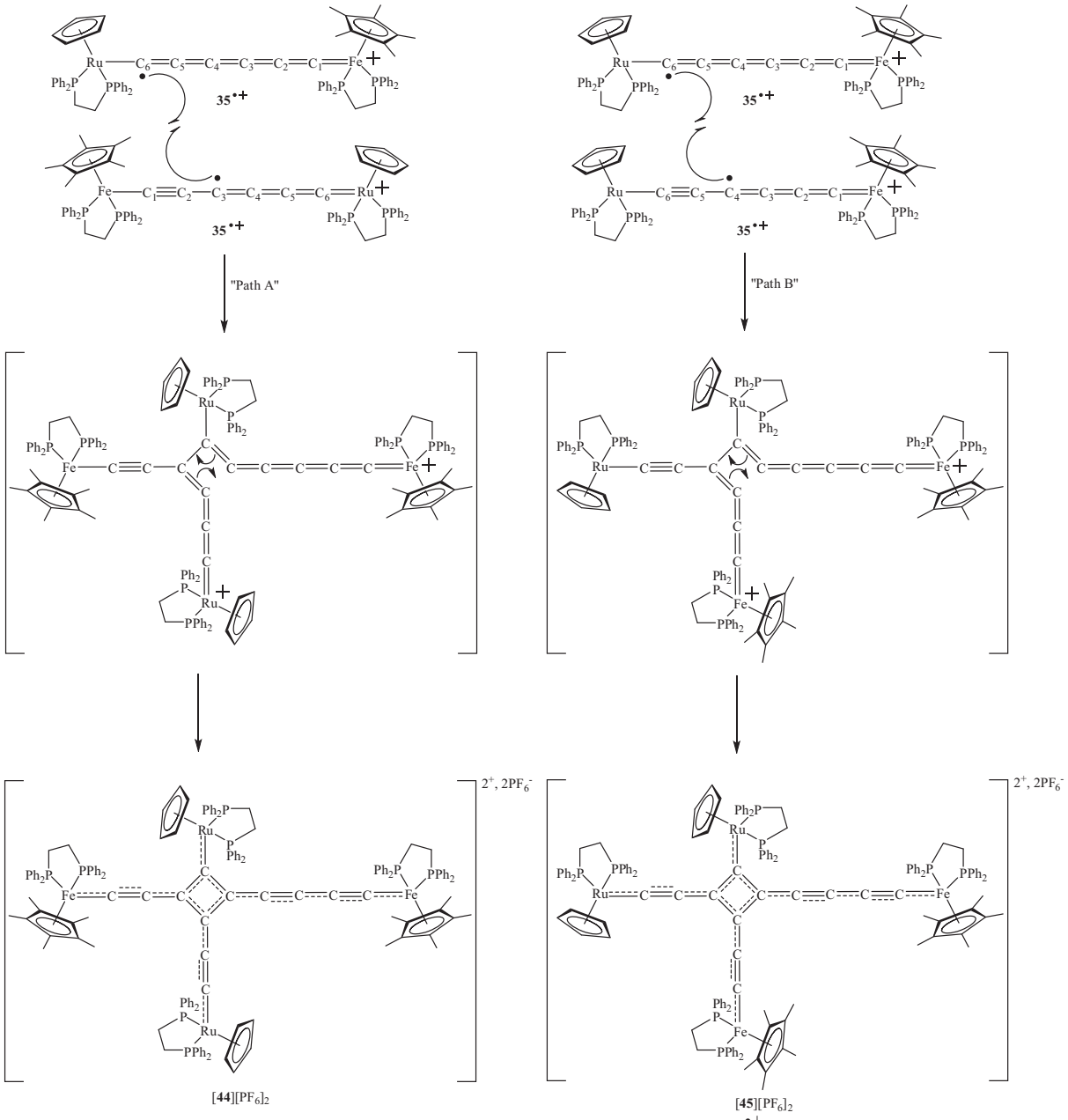

Scheme 6.7. *Proposed mechanism for the dimerisation of* ***35***$^{\bullet+}$*: formation of* ***[44]*** *[PF_6]$_2$ and hypothetical dimer* ***[45]*** *[PF_6]$_2$.*

Combining theoretical and experimental data obtained for the kinetically stable mixed-valence complexes [{Cp'(dppe)M}(C≡CC≡CC≡C){M(dppe)Cp'}]PF_6 (M = Fe, Ru; Cp' = Cp, Cp*) [**30**]PF_6, [**34**]PF_6 (see Chapter 5), and [**31**]PF_6, [**35**]PF_6 (this Chapter), which are subject to selective dimerisation, some pertinent conclusions can be drawn. It is clear that oxidative dimerisation occurs only with complexes containing the Ru(dppe)Cp fragment. Indeed, the combined presence of a ruthenium atom and the Cp ligand in this motif is important for dimerisation to occur. The ruthenium atom interacts with the first connected carbon (C_1 in [**31**]PF_6

and C_6 in [**34**]PF_6 and [**35**]PF_6), so that their atomic spin densities are the largest of the carbon chain and over 0.1, which makes these carbon atoms reactive. This is probably because the ruthenium atom orbitals are more diffuse than the iron ones; indeed, the carbons attached to the Fe(dppe)Cp* fragments (C_1 in [**30**]PF_6, [**34**]PF_6 and [**35**]PF_6) have lower atomic spin densities than carbons connected to the Ru(dppe)Cp fragments (Table 6.3). However, no experiments were carried out using Fe(dppe)Cp fragments even though the atomic spin densities of the C_1 would not be significantly different in comparison with the C_1 attached to the Fe(dppe)Cp* motif. The Cp ligand does not sterically hinder the radical coupling reaction; indeed, when Cp in [**35**]PF_6 is replaced by the bulkier Cp* ligand in [**34**]PF_6, dimerisation does not occur even if the atomic spin density of the carbon connected to the Ru(dppe)Cp* fragment is large enough (0.103) for the coupling to be expected. This indicates that the Cp* ligand sterically prevents radical coupling of the carbon directly attached to the ruthenium atom.

6.3.3.3 Atomic percentage in the molecular orbitals of [43][PF$_6$]$_2$

DFT calculations were also carried out on the tetraruthenium complex [**43**][PF_6]$_2$ in order to understand its electronic structure. The molecular orbital diagram and selected frontier orbital representations are shown in Figure 6.10 while atomic percentages of the different fragments of [**43**][PF_6]$_2$ in the frontier MOs are collected in Table 6.4. As expected, HOMOs 364a and 365a have strong metallic character with percentage contributions from the Ru(dppe)Cp fragments being 37 and 42%, respectively. However, the organic character of the HOMOs is also significant, especially originating from the carbons of the both C_2 and the C_4 chains with combined percentage values being of 38 and 29% in 364a and 365a, respectively. This is a characteristic feature for this type of ruthenium alkynyl complex: the ligands (bridges) have non-innocent behaviour[15] and largely contribute to the electrochemical processes, in contrast to their iron analogues. The LUMOs 366a and 367a have a very strong organic character with spin distribution percentages on the C_{12} ligand being of 77 and 70%, respectively. In comparison, the percentage contribution of the Ru(dppe)Cp fragments in the LUMOs is very small (14% in 366a and 22% in 367a). As with the iron dimer [**27a**][PF_6]$_2$ (see

Chapter 4), atomic percentages in the LUMOs of the C_4 centre are large with values of 36 and 50% in 366a and 367a, respectively.

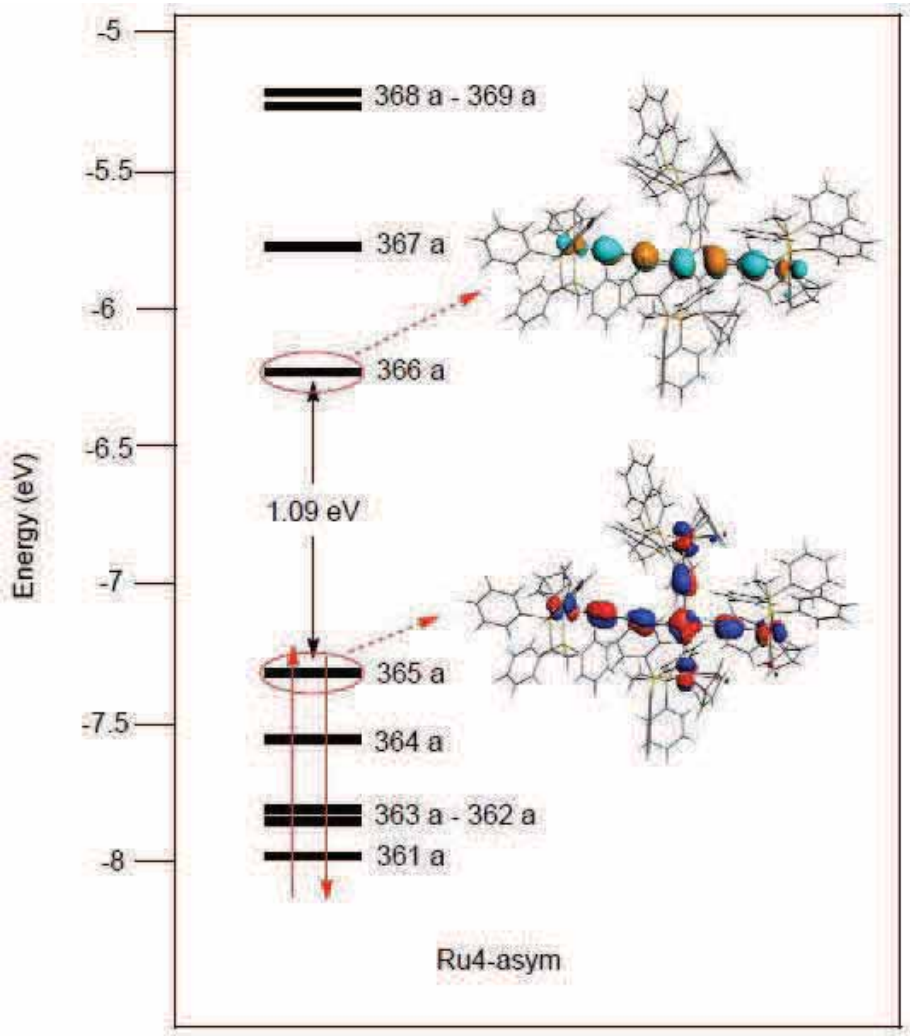

Figure 6.10. *Molecular orbital diagram and selected frontier orbital representations of dimer [**43**][PF_6]$_2$.*

Table 6.4. Atomic percentage (%) in molecular orbitals (MOs) of [**43**][PF_6]$_2$.

MOs	% [Ru(dppe)Cp]	% C≡C	% C_4 centre
371a	87	0	0
370a	78	0	0
367a	22	20	50
366a	14	41	36
365a	42	29	2
364a	37	38	2
361a	48	20	2
358a	56	3	1

Therefore, it is expected that the oxidation processes take place not only on the metal centres but on the overall metal centres and the carbon chains bearing by the C_4 ring. In contrast, the reduction processes are expected to be mainly centred on the C_4 ring with only a small contribution from the metal-alkynyl groups.

6.3.4 Electrochemistry of [43][PF$_6$]$_2$

The electrochemical behaviour of the tetraruthenium complex [**43**][PF_6]$_2$ was studied to determine its redox potentials and hence, the chemical accessibility of its different redox states. The cyclic voltammogram of [**43**][PF_6]$_2$, which has been recorded under the same conditions as in Chapter 2, is presented in Figure 6.11. The voltammogram displayed four very clear and well-separated 1-e processes: two reduction waves at E^0_2 = -0.65 and E^0_1 = -1.42 V; the first one is fully reversible whereas for the second one, close to the solvent front, the reversibility degree is difficult to determine. Two other oxidation waves are at E^0_3 = +0.68 and E^0_4 = + 0.89 V and are fully reversible.

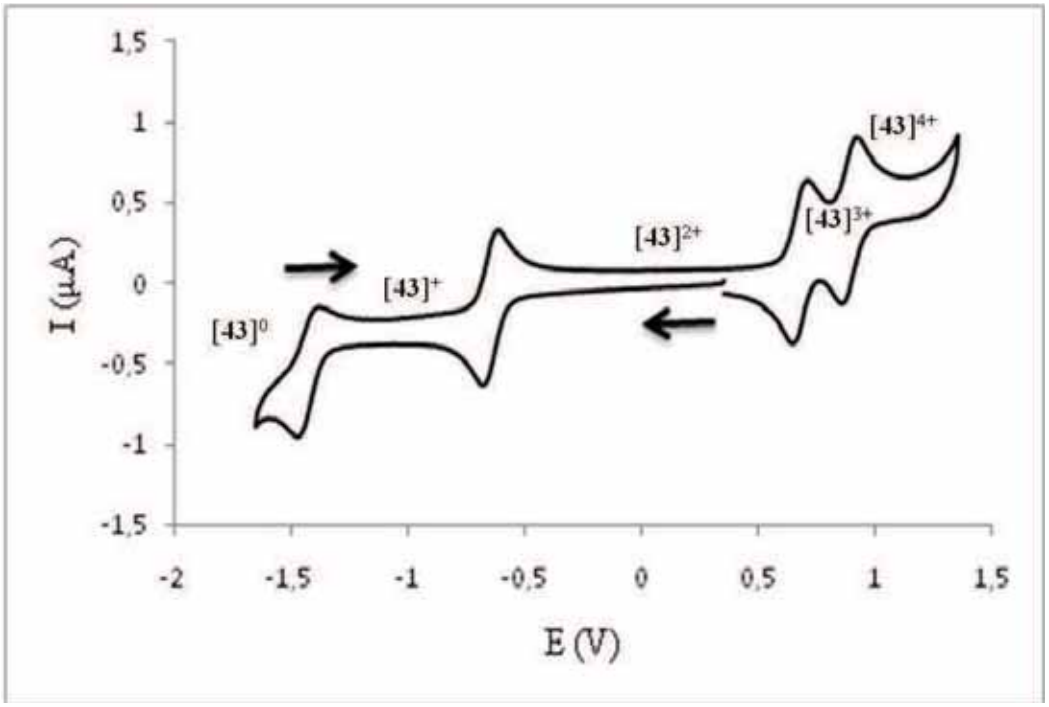

Figure 6.11. *Cyclic voltammogram of [43][PF$_6$]$_2$.*

From the DFT calculations, both metal- and organic carbon chain make important contributions to the two oxidation processes. The two reduction processes are mostly centred on the C_{12} ligand and more especially on the C_4 centre. Additionally, the four redox processes observed in the studied electrochemical region represent the four couples $[\mathbf{43}]^0/[\mathbf{43}]^+$, $[\mathbf{43}]^+/[\mathbf{43}]^{2+}$, $[\mathbf{43}]^{2+}/[\mathbf{43}]^{3+}$ and $[\mathbf{43}]^{3+}/[\mathbf{43}]^{4+}$. The potential differences between the redox waves are ΔE (E^0_2-E^0_1) = 0.77, ΔE (E^0_3-E^0_2) = 1.33 and ΔE (E^0_4-E^0_3) = 0.21 V, from which the following comproportionation equilibria can be generated:

$$[\mathbf{43}]^0 + [\mathbf{43}]^{2+} \rightleftharpoons 2([\mathbf{43}]^+) \qquad K_c = 1.1 \times 10^{13}$$

$$[\mathbf{43}]^+ + [\mathbf{43}]^{3+} \rightleftharpoons 2([\mathbf{43}]^{2+}) \qquad K_c = 3.5 \times 10^{22}$$

$$[\mathbf{43}]^{2+} + [\mathbf{43}]^{4+} \rightleftharpoons 2([\mathbf{43}]^{3+}) \qquad K_c = 3.6 \times 10^{3}$$

The redox state $[\mathbf{43}]^{2+}$ which is the starting point for these measurements, is thermodynamically extremely stable as indicated by its huge K_c value. The other states $[\mathbf{43}]^+$ and $[\mathbf{43}]^{3+}$ which each contains an unpaired electron are also thermodynamically stable, especially $[\mathbf{43}]^+$ which has a very large K_c value. From these electrochemical observations where the four redox processes are fully reversible (or almost for E^0_1) at the electrode, it appears likely that all four states $[\mathbf{43}]^0$, $[\mathbf{43}]^+$, $[\mathbf{43}]^{3+}$ and $[\mathbf{43}]^{4+}$ could be generated and isolated.

6.3.5 Spectroelectrochemistry of [43][PF$_6$]$_2$

Guided by the electrochemical observations on $[\mathbf{43}][PF_6]_2$, attempts to access the $[\mathbf{43}]^+$,$[\mathbf{43}]^{3+}$ and $[\mathbf{43}]^{4+}$ species from $[\mathbf{43}]^{2+}$, by chemical means, using $CoCp_2$ and $AgPF_6$ as the reducing and oxidising agents[16], respectively, were carried out. Unfortunately, these attempts had no success: immediate decomposition of the products was observed. Therefore, the five different states were generated and studied "in situ" by IR, UV-Vis and Near-IR spectroscopy. These experiments were achieved by Dr Schauer from the Low group in Durham. Conditions of the spectroelectrochemical measurements are given in the Experimental section.

6.3.5.1 IR spectroelectrochemistry

The four states $[\mathbf{43}]^{0}$, $[\mathbf{43}]^{+}$, $[\mathbf{43}]^{3+}$ and $[\mathbf{43}]^{4+}$ were generated in the spectroelectrochemical cell from a pure sample of $[\mathbf{43}]^{2+}$ in CH_2Cl_2. The IR ν(CC) bands, in the 1700-2200 cm^{-1} region, of the different redox states are summarised in Table 6.5 and compared with the original spectrum of $[\mathbf{43}]^{2+}$ in CH_2Cl_2 (Figure 6.9).

Table 6.5. IR ν(CC) bands for the $[\mathbf{43}]^{n+}$ (n = 0,1,2,3,4).

Oxidation: ν(CC) bands (cm^{-1})					
n	**Band 1**	**Band 2**	**Band 3**	**Band 4**	**Band 5**
2	2072	1984(sh)	1960	1929	---
3	2064	---	---	1920	1890(sh)
4	---	1977	---	---	---
Reduction: ν(CC) bands (cm^{-1})					
n	**Band 1**	**Band 2**	**Band 3**	**Band 4**	**Band 5**
2	2071	1982(sh)	1961	1929	---
1	---	1985	---	---	---
0	*no relevant absorptions*				

The supposedly independent IR spectra of $[\mathbf{43}]^{2+}$, $[\mathbf{43}]^{3+}$ and $[\mathbf{43}]^{4+}$ states recorded during the spectroelectrochemical experiment are shown in Figure 6.12. The redox cycle $[\mathbf{43}]^{2+} \rightarrow [\mathbf{43}]^{3+} \rightarrow [\mathbf{43}]^{4+} \rightarrow [\mathbf{43}]^{3+} \rightarrow [\mathbf{43}]^{2+}$ did not seem to be fully reversible, which was indicated by only partial recovery of the initial spectrum, suggesting a little decomposition of the sample had occurred during the redox cycle. This might appear to contrast with the electrochemical observations presented above where the four redox processes are fully reversible (except for the second reduction processes); however, the generation time of the different redox species is dramatically longer in the spectroelectrochemistry than in the cyclic voltammetry experiment allowing subsequent chemical reaction to occur. Upon oxidation of $[\mathbf{43}]^{2+}$, the intensity of the ν(CC) bands largely decreases and slightly shifts (ca -10 cm^{-1}), as the bands found at 2064 and 1920 cm^{-1} (the last one having

a shoulder at 1890 cm^{-1}) in $[\mathbf{43}]^{3+}$ confirm. However, when further oxidised, supposedly to $[\mathbf{43}]^{4+}$, the IR spectrum is almost silent in this region, only one weak band remaining at 1977 cm^{-1}. The almost total disappearance of the ν(CC) bands in $[\mathbf{43}]^{4+}$ is unexpected and might indicate that this species is not stable and decomposes when generated.

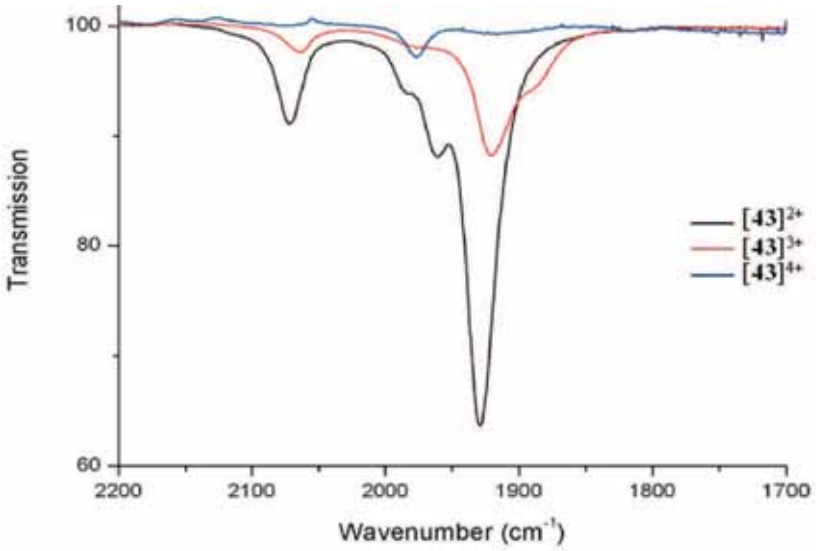

Figure 6.12. *Independent IR spectra of $[43]^{2+}$, $[43]^{3+}$ and $[43]^{4+}$ during the oxidation cycle.*

The reduction cycle $[\mathbf{43}]^{2+} \rightarrow [\mathbf{43}]^{+} \rightarrow [\mathbf{43}]^{0} \rightarrow [\mathbf{43}]^{+} \rightarrow [\mathbf{43}]^{2+}$ seemed to be very much less reversible than the oxidation cycle. The reduction was thus carried out rapidly and the two independent spectra (with the IR spectrum of $[\mathbf{43}]^{2+}$) displayed in Figure 6.13 are believed to correspond to the $[\mathbf{43}]^{+}$ and $[\mathbf{43}]^{0}$ redox states. As with oxidation, the intensity of the ν(CC) bands largely decreases upon reduction to become null when further reduced. Therefore, in the IR spectrum of supposed $[\mathbf{43}]^{+}$, only one weak ν(CC) band at 1985 cm^{-1} remains, whereas no ν(CC) bands were observed in the spectrum of $[\mathbf{43}]^{0}$. Observation of more than one ν(CC) band would be expected in this region for $[\mathbf{43}]^{+}$ and $[\mathbf{43}]^{0}$. This might also indicate that fast decomposition occurs upon reduction of $[\mathbf{43}]^{2+}$.

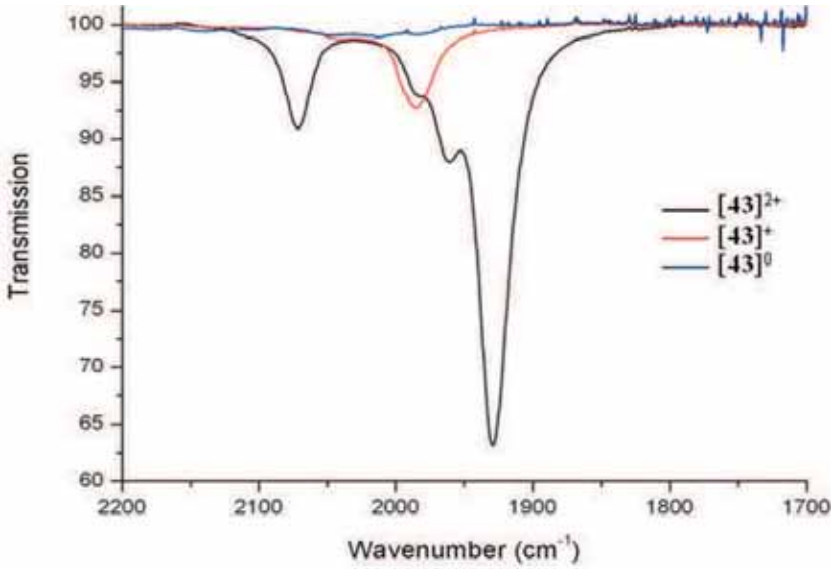

Figure 6.13. *Independent IR spectra of [43]$^{2+}$, [43]$^{+}$ and [43]^{0} during the reduction cycle.*

During the oxidation and reduction cycles, the intensity of the IR ν(CC) bands significantly decrease whereas no significant shifts were observed, then when further oxidised or reduced, the IR spectra became almost silent in the ν(CC) region. This suggests that the generated redox states [**43**]^{0}, [**43**]$^{+}$ and [**43**]$^{4+}$ are unstable and decompose quickly, [**43**]$^{3+}$ probably being slightly more stable than the other states.

6.3.5.2 UV-Vis and Near-IR spectroelectrochemistry

The redox cycles observed by IR spectroscopy were also studied in the UV-Vis and Near-IR range. The UV-Vis spectrum of [**43**]$^{2+}$ recorded during the partially reversible oxidation cycle, with the supposed independent spectra of [**43**]$^{3+}$ and [**43**]$^{4+}$, is shown in Figure 6.14. The spectrum of [**43**]$^{2+}$ is dominated by two intense bands at 12060 (ε 20200 $dm^3.mol^{-1}.cm^{-1}$) and 16640 cm^{-1} (ε 17600 $dm^3.mol^{-1}.cm^{-1}$), and a weaker feature at 21460 cm^{-1} (ε 5460 $dm^3.mol^{-1}.cm^{-1}$). Upon oxidation, in the supposed UV-Vis spectrum of [**43**]$^{3+}$, a small red shift of these bands is observed together with a splitting of the band near 16000 cm^{-1}. The supposed spectrum of [**43**]$^{4+}$ cannot be regarded as the pure signature of the [**43**]$^{4+}$ species.

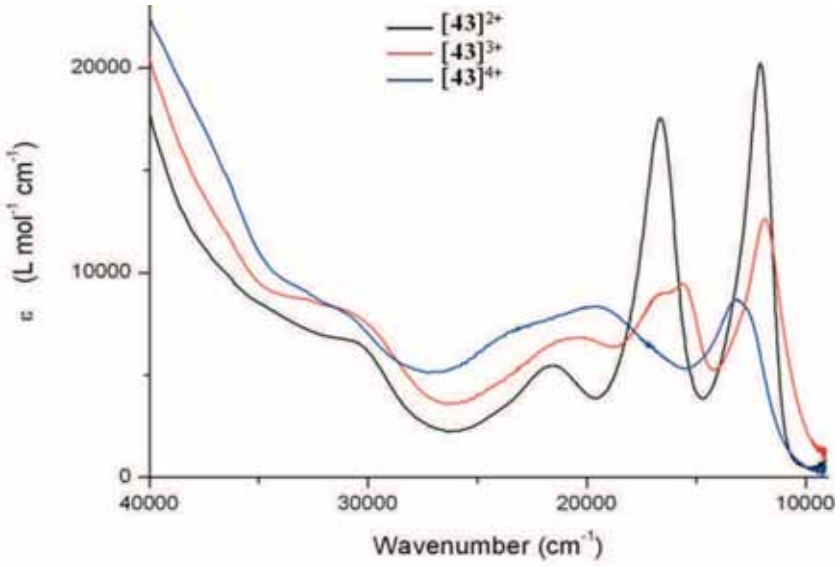

Figure 6.14. *Independent UV-Vis spectra of [43]$^{2+}$, [43]$^{3+}$ and [43]$^{4+}$ during the oxidation cycle.*

The reduction cycle was also studied in this range and the UV-Vis spectra, which are believed to be those of the reduced species [**43**]$^{+}$ and [**43**]^{0}, are presented in Figure 6.15. When reoxidised, the initial spectrum was recovered with very much less intensity, indicating a loss of the starting material. As above, no clear interpretation can be drawn out from these spectra, IR spectroscopy suggesting decomposition.

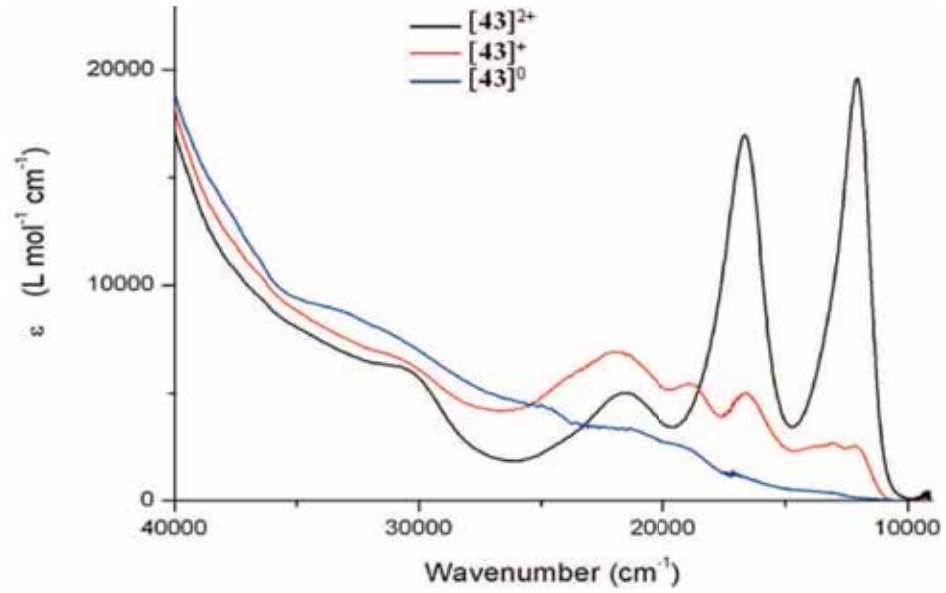

Figure 6.15. *Independent UV-Vis spectra of [43]$^{2+}$, [43]$^{+}$ and [43]^{0} during the reduction cycle.*

None of the electro-generated species were active in the Near-IR range. For [**43**][PF_6]$_2$ which is believed to be the most stable state, the lack of Near-IR transitions strongly suggests that [**43**]$^{3+}$ is not a mixed-valence species.

Spectroelectrochemical investigations achieved on the tetraruthenium dimer [**43**][PF_6]$_2$ were complex and proved to be very difficult to interpret. Even if the redox processes were fully reversible under electrochemical conditions (Section 6.3.4), the different spectra obtained for the states [**43**]^{0}, [**43**]$^{+}$,[**43**]$^{3+}$ and [**43**]$^{4+}$ seemed to be more characteristic of decomposition (intensity loss and no significant shift or appearance of different bands) than to be the signature of pure products, [**43**]$^{3+}$ being probably the most stable state.

6.4 Conclusion

Two new tetranuclear complexes containing a C_{12} ligand with a square four-carbon centre have been synthesised by radical coupling of two mixed-valence molecules. Surprisingly, these two dimers, which have been characterised by X-ray analyses, have been found to be unsymmetrical with a C_{12} ligand consisting of one C_4 square bearing two C_2 chains and one C_4 chain. The dimer [**43**][PF_6]$_2$, obtained from coupling of the symmetrical complex [**31**]PF_6, contains four Ru(dppe)Cp

fragments, whereas the dimer [**44**][PF_6]$_2$ obtained from the coupling of the unsymmetrical mixed-valence complex [**35**]PF_6, contains two Ru(dppe)Cp and Fe(dppe)Cp* fragments, identical motifs being diagonally opposed.

The expected symmetrical dimers (Scheme 6.1) were not formed during the oxidative coupling. In order to explain why this C_3-C_3 coupling does not occur, a hypothesis, supported by the DFT calculations, has been proposed: the atomic spin densities of the central C≡C triple bonds are not large enough (< 0.1), therefore, these carbons are not reactive enough to couple with each other to form the symmetrical dimer. Only the mixed-valence complex containing the Ru(dppe)Cp fragment dimerised; the carbons attached to this moiety, having the strongest atomic spin densities of the carbon chain (> 0.1), coupled (probably randomly or by the more favourable approach) with one carbon of the central C≡C triple bond which is not sterically hindered. If the coupling occurs randomly, not only is dimer [**44**][PF_6]$_2$ formed during the oxidative coupling of **35**, but a hypothetical dimer [**45**][PF_6]$_2$, having identical fragments on each side, should also be formed. In contrast, when the Cp is replaced by a Cp* ligand in [**34**]PF_6, the Cp* sterically protects the carbon connected to the Ru(dppe)Cp fragment and prevents the radical coupling occurring.

Finally, the properties of the tetraruthenium complex [**43**][PF_6]$_2$ were investigated and surprisingly, it has been found that the positive charge is fully delocalised over the whole molecule. This is interesting, because even if unsymmetrical, [**43**][PF_6]$_2$ might be a potential molecular QCA model. Indeed, on a surface and applying external factors (for example an applied electric field or localisation of a biasing charge next to the molecule), the charge in [**43**][PF_6]$_2$ could be localised (or delocalised) on only (or between) two Ru(dppe)Cp fragments (probably being on the same diagonal); and then by switching the external factors, the charge could be localised (or delocalised) on (or between) the other two Ru(dppe)Cp fragments (probably along the opposed diagonal).

Electrochemical studies indicate that four reversible redox processes (at the electrode) generate the four states [**43**]^{0}, [**43**]$^{1+}$, [**43**]$^{3+}$ and [**43**]$^{4+}$, which might be generated as stable and isolable species. However, spectroelectrochemical

measurements suggest that these four states are actually very unstable and that they decompose quickly, the recorded spectra, believed to be the ones of the redox species [**43**]^{0}, [**43**]$^{1+}$, [**43**]$^{3+}$ and [**43**]$^{4+}$, probably being more characteristic of decomposition than of pure products. Similarly, attempts to isolate the different redox species by chemical oxidation or reduction were unsuccessful.

Further characterisation of the dimers [**44**][PF_6]$_2$ and [**45**][PF_6]$_2$ are in progress, as the presence of the Fe(dppe)Cp* fragments might change the properties in comparison with [**43**][PF_6]$_2$. Additionally, the redox species might be more stable as a result of the presence of the Fe(dppe)Cp* fragments which facilitate the localisation of the unpaired electron(s).

Experimental

General experimental conditions are detailed in Chapter 2, Experimental section.

Spectro-electrochemistry: Spectroelectrochemical measurements were made in an OTTLE cell of Hartl design[17] from CH_2Cl_2 solutions containing 0.1 M NBu_4PF_6 electrolyte. The cell was filled in an inert atmosphere dry box (Innovative Technology) before being fitted into the sample compartment of a Thermo Scientific 6700 FT-IR/NIR or Thermo Scientific Evolution Array UV-vis spectrometer. Bulk electrolysis was performed with a home-built potentiostat.
Reagent: $[FeCp_2]PF_6$[16] was prepared using the cited method.

Synthesis of [{Ru(dppe)Cp}$_4${μ-C_{12}}][PF_6]$_2$ ([43][PF_6]$_2$)

{Ru(dppe)Cp}$_2$(μ-C≡CC≡CC≡C) (**31**) (60 mg, 0.05 mmol) and $[FeCp_2]PF_6$ (16 mg, 0.05 mmol) were dissolved in 6 ml of THF at -78°C when the colour changed immediately from yellow to deep red. After stirring 1 h at -78°C, the solution was slowly allowed to warm up to room temperature over a period of 5 h. When the temperature reached -10°C, the colour of the solution changed from deep red to deep blue. After stirring 1 h at room temperature, hexane (50 ml) was added to the mixture and the resulting precipitate was filtered off and washed with hexane (2 × 15 ml) to give [{Ru(dppe)Cp}$_4${μ-C_{12}}][PF_6]$_2$ [**43**][PF_6]$_2$ (62 mg, 92%) as a deep blue powder. Anal. Calcd for $C_{136}H_{116}F_{12}P_{10}Ru_4$: C, 60.67; H, 4.34. Found: C, 60.83; H, 4.44. IR (nujol): ν(C≡C) 2069, ν(C=C=C) 1941, ν(C=C) 1505, ν(P-F) 836 cm^{-1}. ^{1}H NMR (d_6-acetone, 300 MHz): δ 2.62, 3.08 (2 × m, 2 × 8H, 2 × CH_2), 4.86 (s, 5H, Cp), 5.15 (s, 5H, Cp), 5.20 (s, 5H, Cp), 5.64 (s, 5H, Cp), 7.01-8.01 (m, 80H, Ph). ^{13}C NMR (d_6-acetone, 150 MHz, ppm): δ 29.11-30.00 (m, dppe), 86.62 (s, C_5H_5), 87.04 (s, C_5H_5), 88.26 (s, C_5H_5), 89.49 (s, C_5H_5), 125.59-143.39 (m, Ph and C_{chain}), 159.69, 187.15, 226.10, 258.64, 227.81 [5 × s(br), $C_α$ and C_{chain}). ^{31}P NMR (d_6-acetone, 121 MHz): δ 80.7 (broad, 2P), 85.3 (broad, 4P), 94.8 (broad, 2P), -143.2 (septet, J_{PF} = 710 Hz, PF_6). ES-MS (*m/z*): calcd for $C_{136}H_{116}P_8Ru_4$ 1201.661, found 1201.740 $[M]^{2+}$.

Synthesis of [{Fe(dppe)Cp*}$_2${Ru(dppe)Cp}$_2${μ-C_{12}}][PF_6]$_2$ ([44][PF_6]$_2$)

Similarly, from {Cp*(dppe)Fe}(C≡CC≡CC≡C){Ru(dppe)Cp} (**35**) (11 mg, 0.009 mmol) and [$FeCp_2$]PF_6 (3 mg, 0.009 mmol) was obtained [{Fe(dppe)Cp*}$_2${Ru(dppe)Cp}$_2${μ-C_{12}}][PF_6]$_2$ [**44**][PF_6]$_2$ (8 mg, 65%) as a deep purple powder. ES-MS (*m/z*): calcd for $C_{146}H_{136}P_8Fe_2Ru_2$ 1226.2664, found 1226.2818 $[M]^{2+}$.

References

1. Tanaka, Y.; Ozawa, T.; Inagaki, A.; Akita, M., *Dalton Trans.* **2007**, 928–933.
2. (a) Lent, C. S., *Science* **2000,** *288*, 1597-1599; (b) Braun-Sand, S. B.; Wiest, O., *J. Phys. Chem. C* **2003,** *107*, 9624-9628; (c) Low, P. J., *Dalton Trans.* **2005**, 2821-2824.
3. (a) Cotton, F. A.; Daniels, L. M.; Lin, C.; Murillo, C. A., *J. Am. Chem. Soc.* **1999,** *121*, 4538-4539; (b) Cotton, F. A.; Lin, C.; Murillo, C. A., *Inorg. Chem.* **2001,** *40*, 478-484.
4. Lau, V. C.; Berben, L. A.; Long, J. R., *J . Am. Chem. Soc.* **2002,** *124*, 9042-9043.
5. Creutz, C.; Taube, H., *J. Am. Chem. Soc.* **1973,** *95*, 1086-1094.
6. Oshio, H.; Onodera, H.; Tamada, O.; Mizutani, H.; Hikichi, T.; Ito, T., *Chem.–Eur. J.* **2000,** *6*, 2523-2530.
7. Oshio, H.; Onodera, H.; Ito, T., *Chem.–Eur. J.* **2003,** *9*, 3946-3950.
8. (a) Hush, N. S., *Prog. Inorg. Chem.* **1967,** *8*, 391; (b) Creutz, C., *Prog. Inorg. Chem.* **1983,** *30*, 1.
9. Hush, N. S., *Coord. Chem. Rev.* **1985,** *64*, 135-157.
10. (a) Jiao, J.; Long, G. J.; Grandjean, F.; Beatty, A. M.; Fehlner, T. P., *J. Am. Chem. Soc.* **2003,** *125*, 7522-7523; (b) Jiao, J.; Long, G. J.; Rebbouh, L.; Grandjean, F.; Beatty, A. M.; Fehlner, T. P., *J. Am. Chem. Soc.* **2005,** *127*, 17819-17831.
11. Nemykin, V. N.; Rohde, G. T.; Barrett, C. D.; Hadt, R. G.; Bizzarri, C.; Galloni, P.; Floris, B.; Nowik, I.; Herber, R. H.; Marrani, A. G.; Zanoni, R.; Loim, N. M., *J. Am. Chem. Soc.* **2009,** *131*, 14969–14978.
12. Bruce, M. I.; Dean, C.; Duffy, D. N.; Humphrey, M. G.; Koutsantonis, G. A., *J. Organomet. Chem.* **1985,** *295*, c40-c44.
13. Bruce, M. I.; Morris, J. C.; Parker, C. R.; Skelton, B. W., *J. Organomet. Chem.* **2011,** *696*, 3292-3295.
14. Costuas, K., *personal communication*.
15. (a) Fox, M. A.; Farmer, J. D.; Roberts, R. L.; Humphrey, M. G.; Low, P. J., *Organometallics* **2009,** *28*, 5266-5269; (b) Costuas, K.; Rigaut, S., *Dalton Trans.* **2011,** *40*, 5643-5658.
16. Connelly, N. G.; Geiger, W. E., *Chem. Rev.* **1996,** *96*, 877-910.
17. Krejčik, M.; Daněk, M.; Hartl, F., *J. Electroanal. Chem.* **1991,** *317*, 179-187.

Chapter Seven

Reactions of 7,7,8,8-Tetracyanoquinodimethane (TCNQ) with Alkynyl-Ruthenium and -Iron Complexes: Electronic Coupling Between Inorganic and Organic Electrophores

7.1 Introduction

Organometallics comprising two redox-active centres connected by a carbon bridge provide an ideal template from which intricate mechanistic details of the factors controlling electron transfer and electron delocalisation can be extracted.[1] Consequently, over the last years, one thrust has involved extremes in oxidation states of this type of compound with different metal end-groups and the consequences for electronic, magnetic and geometric structure as well as electron transfer have been extensively studied[2]. Many organometallics with various donor-bridge-acceptor arrangements have been designed and synthesised. Their electronic, magnetic and optical properties have been investigated in order to understand the key factors affecting the properties of these multifunctional molecular systems. More recently, hybrid systems involving organic and inorganic electron-donating electrophores connected by alkyndiyl bridges have been found to show promising properties suitable for the realisation of nanoscale devices, including components for molecular electronics and NLO-active assemblies.

On the basis of this approach, we report in this Chapter the synthesis and the characterisation of new hybrid complexes. In these compounds, two electro-active units, namely the organometallic electron-donor centre $M(PP)_2Cp'$ [M = Fe, Ru; PP = $(PPh_3)_2$, dppe; Cp' = Cp, Cp*] and the organic acceptor 7,7,8,8-tetracyanoquinodimethane (TCNQ) are σ-linked to an alkyndiyl bridge to favour π-d interaction between them. The intramolecular charge transfer which can take place in such compounds is the subject of X-ray, electrochemical and spectroscopic analyses.

Synthetic access to these compounds is interesting chemistry in itself. Indeed, the chemistry of tetracyanoethene, $C_2(CN)_4$ (TCNE) (Chart 7.1), with organo-transition metal substrates is well developed, including, in particular, [2 + 2]-cycloaddition to a variety of alkynyl- and poly-ynyl-metal complexes (Scheme 7.1)[3]. These reactions proceed via deep coloured paramagnetic intermediates **A** which rapidly evolve via zwitter-ion **B** to tetracyanocyclobutenyl complexes **C**. Ring-opening (retro-electrocyclic) reactions of **C** then afford tetracyanobutadienyls **D**. In many cases, species **A**, **B** and **C** are not observed and, indeed, the structure of **A** has only been resolved by X-ray determination once for the organoiron complex $[Fe\{C{\equiv}C(Ant\text{-}CN)\}(dppe)Cp^*]^{\bullet+}[TCNE]^{\bullet-}$ [4], while the structure of **B** remains unknown. A further reaction may result by chelation of the dienyl ligand in **D** to the metal centre, with concomitant loss of a 2-e donor ligand, to give the η^3-tetracyanobutadienyl complex **E**.

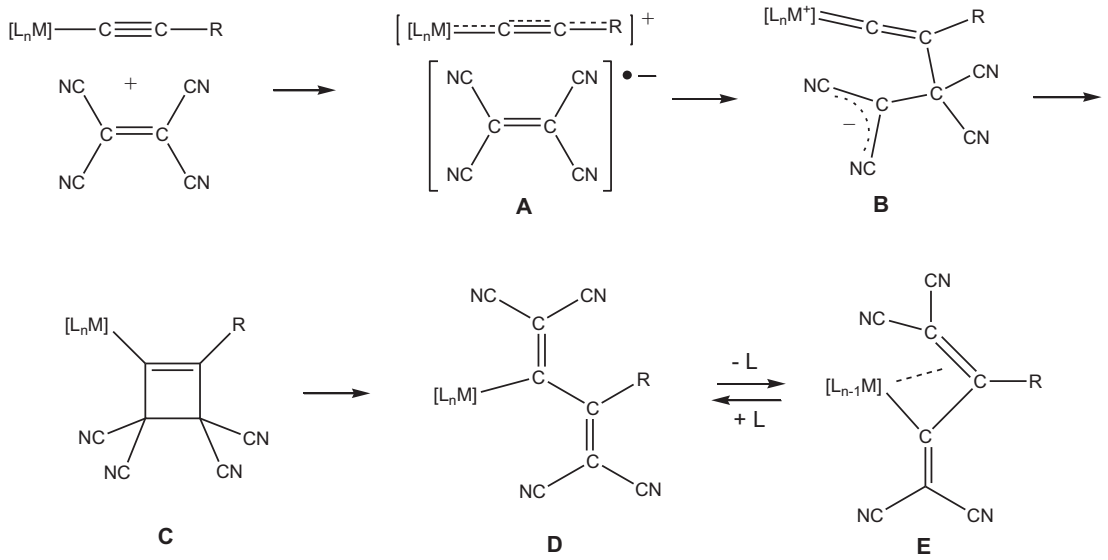

Scheme 7.1. *Reactions of TCNE with alkynyl-transition metal complexes.*

Analogous reactions of 7,7,8,8-tetracyanoquinodimethane, $(NC)_2C=C_6H_4=C(CN)_2$ (TCNQ) and its 2,3,5,6-tetrafluoro- analogue, $(NC)_2C=C_6F_4=C(CN)_2$ (F_4-TCNQ), are few and far between. Indeed, as Kato and Diederich have commented, "… in sharp contrast to TCNE, the reactivity of TCNQ toward donor-substituted alkynes remain(s) unexplored in both organometallic and organic chemistry …"[5].

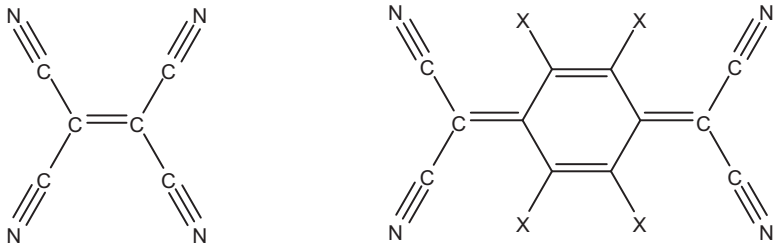

Chart 7.1

An early report described compounds formed in reactions of TCNQ with *trans*-$Pt(C\equiv CR)_2(PR'_3)_2$ (R = H, Me; R' = Me, Et) which were thought to be charge-transfer complexes on account of their deep red-purple colours[6]. A later X-ray diffraction study[7] showed that these compounds were the butadienyl-platinum(II) derivatives, *trans*-$Pt(C\equiv CR)\{C[=C_6H_4=C(CN)_2]CR=C(CN)_2\}(PR'_3)_2$, formed by [2 + 2]-cycloaddition of TCNQ to one C≡C triple bond, followed by ring-opening of the resulting cyclobutenyls, reactions entirely analogous to those found for TCNE. However, subsequent accounts of related chemistry of TCNQ appear to be limited to the reactions of several arylalkynyl-nickel complexes, $Ni(C\equiv CAr)(PPh_3)Cp$[8], and [2 + 2]-cycloaddition to the C_7 complex $\{Cp^*(dppe)Ru\}C\equiv CC\equiv CC\equiv CC\equiv\{Co_3(\mu\text{-}dppm)(CO)_7\}$[9]. In both cases the reactions gave butadienyls resulting from ring-opening of the presumed first-formed but undetected cyclobutenyls. Alternatively, TCNQ has acted as an oxidant in reactions with the electron-rich binuclear $\{Cp^*(dppe)Fe\}_2(\mu\text{-}C\equiv C\text{-}X\text{-}C\equiv C)$ (X = 1,8-$C_{10}H_6$, 9,10-$C_{14}H_8$) to give the $[TCNQ]^{\bullet-}$ radical anion salts of the corresponding metal cations, $[\{Cp(dppe)Fe\}_2(\mu\text{-}CC\text{-}X\text{-}CC)]^{n+}(TCNQ^{\bullet-})_n$ (n = 1,2)[10]. Oxidation of biferrocene-1',1'''-$\{C\equiv C[Fe(dppe)Cp^*]\}_2$ with one or two equivalent of TCNQ afforded [biferrocene-1',1'''-$\{CC[Fe(dppe)Cp^*]\}_2]^{n+}(TCNQ^{\bullet-})_n$ (n = 1 and 2, respectively)[11]. The course of the latter reactions is consistent with most of the electron density of the HOMOs residing on the metal centre.

This chemistry also illustrates the strong electron accepting nature of TCNE and TCNQ, the electron affinities of which have been measured at 3.17 ± 0.2[12] and 2.8 ± 0.1 eV[13], respectively.

7.2 Aims

Following extensive studies of the reactions of alkynyl- and poly-ynyl-metal complexes with TCNE[3b-e], we were interested to learn whether addition of TCNQ to mononuclear Group 8 alkynyl or poly-ynyl complexes would lead to the familiar [2 + 2]-cycloadducts and/or their retrocyclisation products, or would afford the $[TCNQ]^{\bullet-}$ salts of the 17-e alkynyl- or poly-ynyl-metal cations which could dimerise in some cases to give dimers similar as the ones characterised in Chapter 3 and 4. This work describes the rich chemistry found in reactions of Ru{$(C\equiv C)_nR$)(PP)Cp' [n = 1-3, R = H, Ph, (PP)Cp' = $(PPh_3)_2Cp$, (dppe)Cp* (not all combinations)] with this cyanocarbon, from which we have observed (a) complexes formed by [2 + 2]-cycloaddition and subsequent ring-opening reactions, (b) zwitter-ionic complexes, (c) elimination of HCN from a product (b), and (d) coupling of two molecules of a diynyl to a single TCNQ moiety. A comparison is made with similar reactions of iron analogues, Fe(C≡CR)(dppe)Cp* (R = C_6H_4-C_6H_5[10a], Ant-CN[4]), for which only oxidation to the mono-cation is found (Scheme 7.2), whereas with Fe(C≡CC≡CPh)(dppe)Cp*, a reaction similar to that of the Ru analogue is found. Guillaume Grelaud from Rennes contributed to some parts of this work during his Master 1 internship in the Chemistry department of the University of Adelaide.

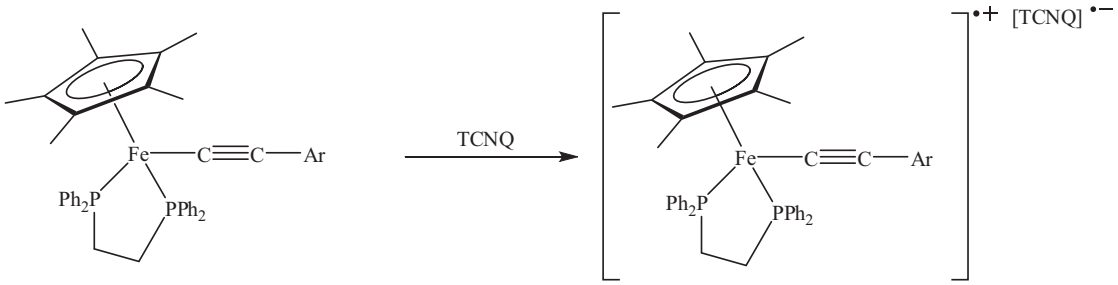

Ar = C_6H_4-C_6H_5, Ant-CN

Scheme 7.2

7.3 Results and discussion

7.3.1 Reactions of TCNQ with M(C≡CR)(PPh$_3$)$_2$Cp (M = Ru, R = H, Ph)

Reaction of TCNQ with Ru(C≡CH)(PPh$_3$)$_2$Cp

During the reaction between TCNQ and Ru(C≡CH)(PPh$_3$)$_2$Cp, carried out in THF at room temperature, the solution changes from yellow to green and affords Ru{=C=CHC(CN)$_2$C$_6$H$_4$C(CN)$_2$}(PPh$_3$)$_2$Cp **46** as a somewhat unstable green solid (Scheme 7.3). This is a 1/1 adduct formed by attack of C$_\beta$ of the ethynyl on one of the C(CN)$_2$ groups of TCNQ, and thus differs from the anticipated [2 + 2]-cycloadduct. In the IR spectrum, there are two ν(CN) bands at 2180, 2070 cm^{-1} and two ν(C=C) bands at 1597, 1587 cm^{-1}, but no ν(C≡C) absorption. The ^{1}H and ^{31}P NMR spectra contained resonances arising from the Ru(PPh$_3$)$_2$Cp group at δ$_H$ 4.24 (Cp), 7.01-7.57 (Ph + C$_6$H$_4$), δ$_P$ 49.4, the =CH proton giving a singlet resonance at δ$_H$ 5.05. No ^{13}C NMR spectrum could be obtained because of rapid decomposition. The ES-MS contains [M]$^+$ at *m/z* 920. No crystals suitable for an X-ray study were obtained, but the molecular structure shown is assigned by comparison with that of the product **48** obtained from the reaction of Ru(C≡CPh)(PPh$_3$)$_2$Cp with TCNQ (see below).

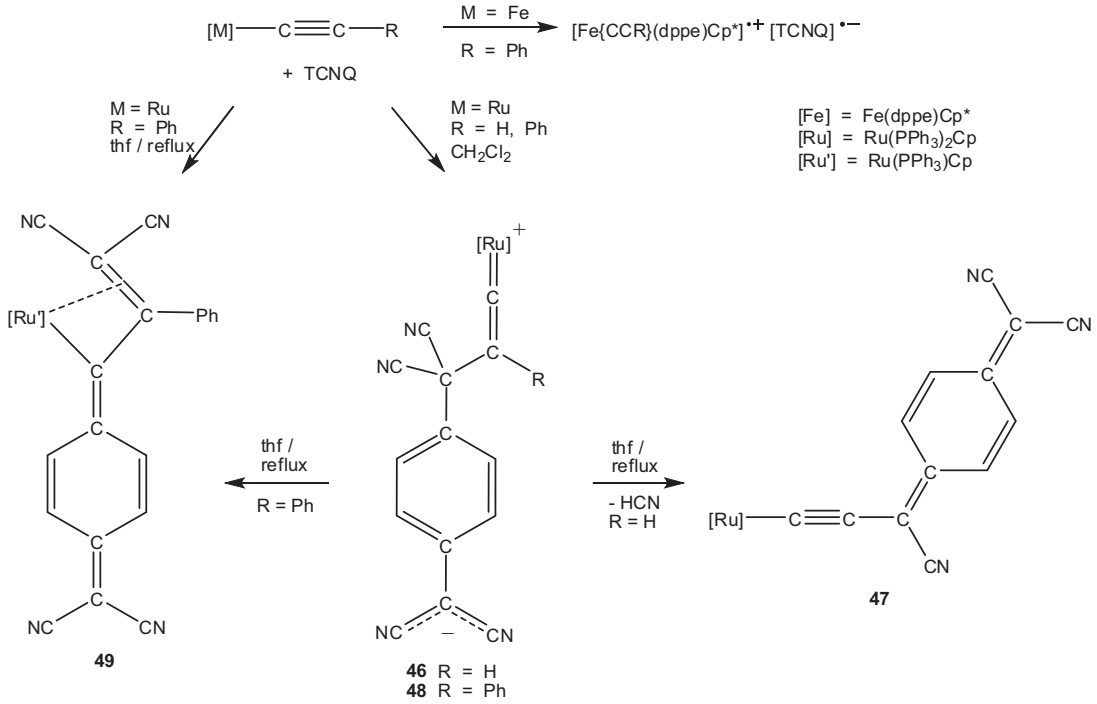

Scheme 7.3. *Reactions of Ru(C≡CR)(PPh$_3$)$_2$Cp (R = H, Ph) with TCNQ.*

If **46** is heated in refluxing THF, or if the initial reaction is carried out under these conditions, purification of the product by preparative t.l.c. (acetone / hexane, 3:7) afforded dark turquoise Ru{C≡CC(CN)=C_6H_4=C(CN)$_2$}(PPh_3)$_2$Cp **47** by elimination of HCN. The composition of **47** was confirmed by a high resolution ES-MS determination where $[M + H]^+$ was found at *m/z* 894.1738 (calculated: 894.1741) and the IR spectrum contains ν(CN) and ν(C=C) bands at 2201 and 1590 cm^{-1}, respectively, together with a strong ν(C≡C) absorption at 1974 cm^{-1}. The increased intensity of the latter band results from polarisation of the C≡C triple bond by the donor-acceptor (D→A) interaction of the electron-rich Ru(PPh_3)$_2$Cp moiety (D) with the strongly electron-withdrawing cyanocarbon group (A). In the ^{1}H and ^{31}P NMR spectra, there are resonances at δ_H 4.62 (Cp), 7.05-7.60 (Ph + C_6H_4) and at δ_P 48.0. The ^{13}C NMR spectrum contains resonances at δ_C 88.83 (Cp), 209.94 (Ru-C) and three CN signals at δ_C 116.23, 116.98 and 117.29, together with aromatic carbons between δ_C 122.40 and 139.75. Four other ^{13}C resonances between δ_C 107.56 and 153.45 can be assigned to carbons of the organic ligand.

A plot of a molecule of **47** is shown in Figure 7.1 while selected bond parameters are given in Table 7.1. From the X-ray structure, it can be seen that the organic ligand is closely related to that in tricyanovinylethynyl complexes obtained recently from TCNE and Ru(C≡CH)(dppe)Cp*[14]. It is attached to the usual pseudo-octahedral Ru(PPh_3)$_2$Cp group via C(1) [Ru-C(1) 1.933(2) Å], with C(1)-C(2) [1.239(3) Å] being a somewhat long C≡C triple bond. Similarly, C(3)-C(31) [1.452(4) Å] is longer than C(5)-C(51,52) [1.383(13), 1.411(14) Å], a result also emphasising the similarity to the tricyanovinylethynyl structures. We defer further consideration of the geometries of the =C_6H_4=C(CN)$_2$ groups until later, although here we note that the quinoid formulation is found here.

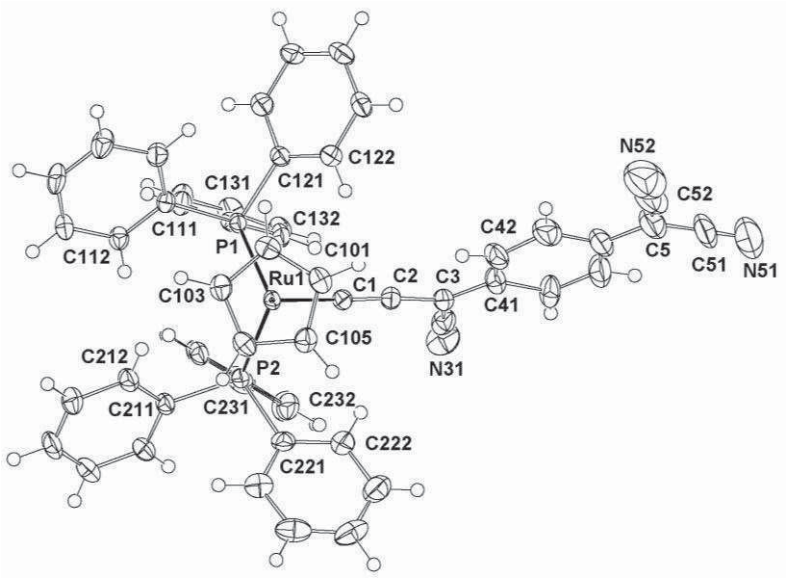

Figure 7.1. *Plot of a molecule of Ru{C≡CC(CN)=C$_6$H$_4$=C(CN)$_2$}(PPh$_3$)$_2$Cp **47**.*

Table 7.1. Selected bond parameters for TCNQ complexes **47** and **48**.

Compound	**47**	**48**
	Bond distances (Å)	
Ru-P(1)	2.3032(7)	2.369(2)
Ru-P(2)	2.3037(2)	2.349(2)
Ru-C(cp)	2.234-2.267(2)	2.241-2.262(6)
(av.)	2.250	2.252
Ru-C(1)	1.933(2)	1.855(6)
C(1)-C(2)	1.239(3)	1.316(7)
C(2)-C(3)	1.370(3)	1.559(8)
C(2)-C(21)		1.503(8)
C(3)-C(31, 32)	1.452(4)	1.491, 1.504(8)
C(3)-C(41)	1.409(10)	1.539(7)
C(5)-C(44)	1.454(15)	1.449(8)
C(5)-C(51, 52)	1.383(13), 1.411(14)	1.384, 1.422(8)
	Bond angles (º)	
P(1)-Ru-P(2)	102.14(2)	101.81(6)
P(1)-Ru-C(1)	89.79(7)	98.0(2)
P(2)-Ru-C(1)	88.79(7)	91.9(2)
Ru-C(1)-C(2)	172.9(2)	172.3(5)
C(1)-C(2)-C(3)	176.5(3)	120.6(5)
C(1)-C(2)-C(21)		119.7(5)
C(2)-C(3)-C(31, 32)	116.0(3)	110.2, 108.3(5)
C(2)-C(3)-C(41)	123.6(4)	113.1(4)
C(44)-C(5)-C(51, 52)	117.0(9), 123.1(9)	123.2, 120.9(6)
C(51)-C(5)-C(52)	119.9(10)	115.8(5)

Reaction of TCNQ with $Ru(C{\equiv}CPh)(PPh_3)_2Cp$

The reaction of TCNQ with $Ru(C{\equiv}CPh)(PPh_3)_2Cp$ resulted in a rapid change from yellow to dark purple within one minute of addition, with the reaction being complete after five minutes. Conventional work-up afforded a dark purple solid characterised as the 1/1 adduct $Ru\{=C=CPhC(CN)_2C_6H_4C(CN)_2\}(PPh_3)_2Cp$ **48** (41%) by ES-MS with $[M]^+$ at *m/z* 996. Fragment ions include $[Ru(PPh_3)_nCp]^+$ (n = 1, 2). In the IR spectrum, two ν(CN) bands at 2169, 2126 cm^{-1} are accompanied by two ν(C=C) bands at 1619, 1595 cm^{-1}. The ^1H and ^{31}P NMR spectra contain signals at δ_H 5.19 (Cp), 6.60-7.49 (Ph + C_6H_4) and δ_P 39.0. In addition, resonances at δ_C 95.59 (Cp), 115.66, 119.75 (2 x CN) and 342.13 (Ru=C) were found in the ^{13}C NMR spectrum.

The molecular structure of **48** was determined from a single crystal X-ray diffraction study and is shown in Figure 7.2 (key parameters are given in Table 7.1). The geometry of the Ru=C(1)=C(2)PhC(3) fragment is consistent with its formulation as a vinylidene, with a short Ru-C(1) bond [1.855(6) Å] and long C(1)-C(2) separation [1.316(7) Å], together with angle C(3)-C(2)-C(21) [119.7(4)°] [cf. Ru=C(1) 1.85(1), C(1)-C(2) 1.31(2) Å in $[Ru(=C=CH_2)(dppe)Cp^*]^+$ [15]]. The implied positive charge on the Ru centre results in Ru-P(1,2) distances [2.369, 2.349(2) Å] which are considerably longer than those found in **47** [2.3032, 2.3037(7) Å], as a result of reduced back-bonding into the P ligand. Within the C_6 ring, C-C bonds range between 1.380(7) and 1.420(7) Å (av. 1.390 Å), consistent with its being a substituted benzene rather than having the quinoid formulation. Neutrality is achieved by localisation of negative charge on the $C(5)(CN)_2$ group, with C(5)-C(51,52) [1.384, 1.422(8) Å] both shorter than C(3)-C(31,32) [1.491, 1.504(8) Å], i.e., the molecule is a zwitter-ion with well-separated charges.

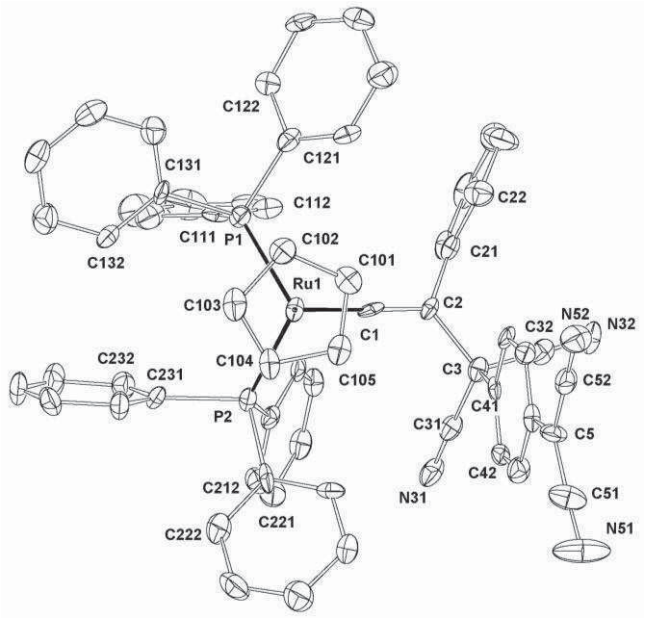

Figure 7.2. *Plot of a molecule of Ru{=C=CPhC(CN)$_2$C$_6$H$_4$C(CN)$_2$}(PPh$_3$)$_2$Cp* ***48****.*

When heating the reaction between TCNQ and Ru(C≡CPh)(PPh$_3$)$_2$Cp or **48** directly in refluxing THF, the η^3-butadienyl complex Ru{η^3-C(CN)$_2$CPhC=C$_6$H$_4$=C(CN)$_2$}(PPh$_3$)Cp **49** is formed[16] (Scheme 7.3) by loss of PPh$_3$ and chelation of the cyanoalkene ligand in a presumed but unobserved intermediate Ru{C[=C$_6$H$_4$=C(CN)$_2$]CPh=C(CN)$_2$}(PPh$_3$)$_2$Cp, by comparison with the TCNE chemistry[17].

7.3.2 Electrochemical and UV-Vis studies of 47

In order to investigate the effect of the electron withdrawing tricyanovinyl group on the redox potential of the ruthenium centre in **47**, electrochemical and UV-Vis studies were carried out. The cyclic voltammogram of **47** was recorded under conditions similar to those described earlier in Chapter 2 (Section 2.3.4) and is shown in Figure 7.3. Three redox processes are observed: one irreversible oxidation at E^0_4 = +0.76 V, and two reductions at E^0_2 = -0.51 and E^0_1 = -1.40 V, the first being fully reversible (i_a/i_c = 1) whereas for the second one, close to the solvent front, the degree of reversibility is difficult to determine. Additionally, one small redox process is observed at E^0_3 = +0.22 V as can be seen in Figure 7.3.

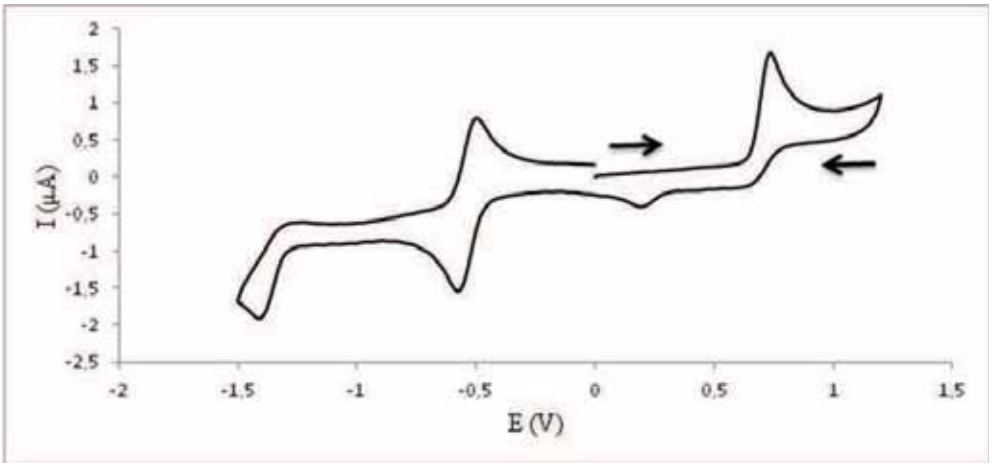

Figure 7.3. *Cyclic voltammogram of **47** (V vs SCE).*

The oxidation wave is assigned to the 1-e oxidation of the metal centre while both reduction waves are assigned to the successive 1-e reduction of the "substituted TCNQ". Complex **47** is more difficult to oxidise than typical $Ru(II)(PPh_3)_2Cp$ complexes such as $Ru(C{\equiv}CPh)(PPh_3)_2Cp$ (E^0 = +0.55 V)[18] by ca 0.20 V, which is due to the strong electron-withdrawing cyanocarbon group capturing some electron density from the electron-rich metal centre. Similarly, redox properties of the "substituted TCNQ" are significantly different than TCNQ itself which exhibits two reduction waves at +0.21 and -0.33 V (*vs* SCE)[8]. Molecule **47** is more difficult to reduce than TCNQ, which is due to the electron-rich ruthenium centre releasing electron density to the cyanocarbon ligand. These observations suggest a strong contribution from the mesomeric form **47B** (Scheme 7.4).

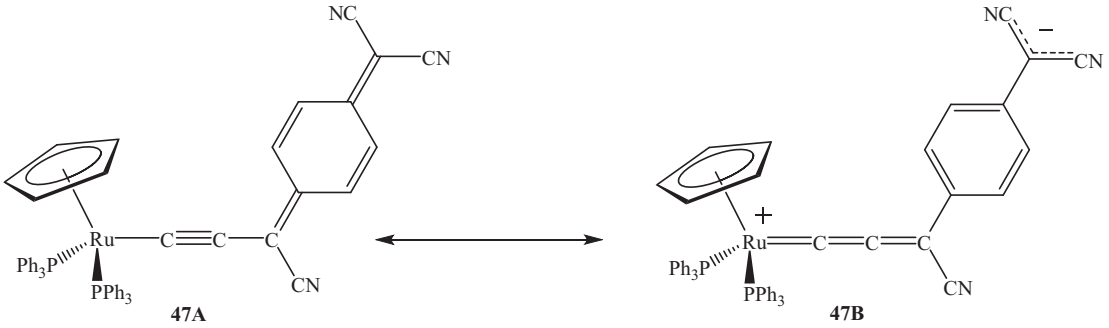

Scheme 7.4

UV-Vis studies were also carried out in two different solvent mixtures, pure CH_2Cl_2 and a more polar mixture CH_2Cl_2 / MeOH (1:9) in order to study solvatochromism. The UV-Vis spectra of **47** are presented in Figure 7.4 while spectral data are collected in Table 7.2. In pure CH_2Cl_2, the spectrum is dominated by two very intense bands at 748 and 814 nm

which give **47** its dark turquoise colour, and a less intense band at 488 nm. In the more polar mixture CH_2Cl_2 / MeOH (1:9), both bands at 748 and 814 nm significantly decrease in intensity and an intense band centred at 604 nm is observed. Additionally, in both spectra, $\pi \rightarrow \pi^*$ ligand-centred transitions are also observed at ca 260 nm. The intense band at 604 nm in CH_2Cl_2 / MeOH (1:9) might arise from a red shift of the small band centred at 488 nm in pure CH_2Cl_2, which significantly increases in intensity in the more polar solvent and could be assigned to a charge transfer band. This band might be almost forbidden in pure CH_2Cl_2, whereas in the more polar CH_2Cl_2 / MeOH (1:9) mixture, it might become permitted. Another small band is observed at 398 nm in CH_2Cl_2 / MeOH (1:9) and could also come from a red shift of one band being in the $\pi \rightarrow \pi^*$ transition shoulder at ca 350 nm in CH_2Cl_2. The two bands at 748 and 814 nm are present in both spectra with identical frequencies and thus are not due to charge transfer transitions.

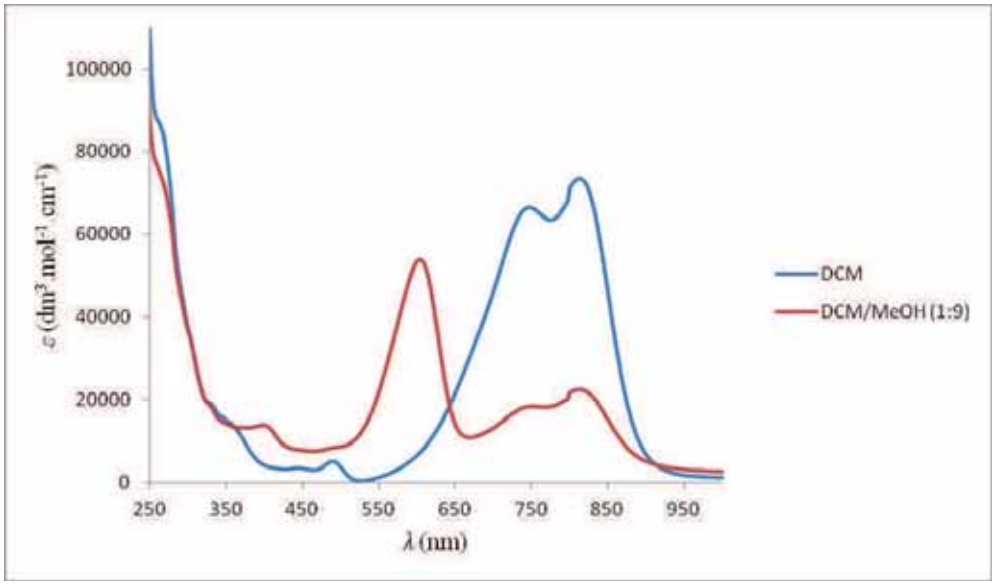

Figure 7.4. *UV-Vis spectra of 47 in CH_2Cl_2 and CH_2Cl_2 /MeOH, 1:9.*

Table 7.2. UV-Vis spectral data for **47**.

Solvent	λ/nm (ε × 10^{-3}/dm^3.mol^{-1}.cm^{-1})			
CH_2Cl_2		488 (5.1)	748 (66.7)	814 (73.6)
CH_2Cl_2 / MeOH (1:9)	398 (14.0)	604 (54.0)	748 (18.4)	814 (22.5)

Solvatochromism is observed in the UV-Vis spectra confirming charge transfer in **47** between the electron-rich ruthenium centre and the strongly electron-withdrawing cyanocarbon ligand. However, further UV-Vis measurements and theoretical calculations are necessary for a better interpretation of these observations. Finally, it is clear that the

mesomeric form **47B** is dominant in the more polar solvent CH_2Cl_2 / MeOH (1:9) and makes a strong contribution to the formulation of **47**, which is confirmed by the electrochemical data.

7.3.3 Reactions of TCNQ with metal-poly-alkynyl complexes containing C_4 and C_6 carbon chains

Reaction of TCNQ with Ru(C≡CC≡CH)(dppe)Cp*

Two complexes have been obtained from reactions between TCNQ and the diynyl-ruthenium complex Ru(C≡CC≡CH)(dppe)Cp* (Scheme 7.5). If the reaction is carried out in THF with an excess of TCNQ, an instantaneous colour change from yellow to dark green results and purification by preparative t.l.c. affords a low yield of Ru{C≡CC[=C_6H_4=$C(CN)_2$]CH=$C(CN)_2$}(dppe)Cp* **50** which is obtained as a dark green solid. The composition was confirmed by a high resolution ES-MS spectrum where $[M]^+$ was found at *m/z* 888.2128 (calculated: 888.2085). The IR spectrum contains ν(CN) (2193), ν(C≡C) (1940) and ν(C=C) bands (1586 cm^{-1}). In the ^1H NMR spectrum, Cp* (δ_H 1.38), CH_2 (1.94, 2.57) and aromatic (7.01-7.42) resonances are accompanied by a singlet at δ_H 6.72 assigned to the CH=$C(CN)_2$ proton. In the ^{13}C NMR spectrum, resonances occur at δ_C 9.79, 96.61 (Cp*), 29.42-30.30 (CH_2), 124.75-138.22 (Ph + C_6H_4) and 218.70 (Ru-C, t), together with four CN signals between δ_C 111.73 and 120.89. In addition, resonances at δ_C 86.13, 145.01, 152.70, 155.26 arise from the cyanocarbon ligand.

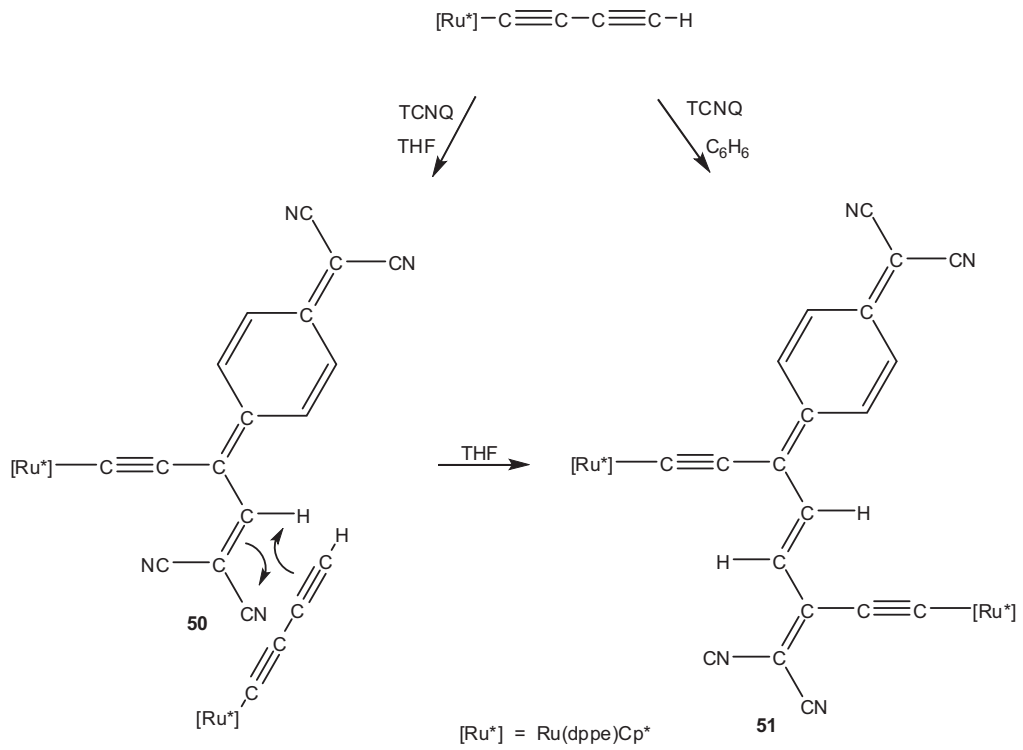

Scheme 7.5. *Reactions of Ru(C≡CC≡CH)(dppe)Cp* with TCNQ.*

The molecular structure of **50** was determined from a single-crystal X-ray diffraction study and a plot of the molecule is given in Figure 7.5 while selected structural parameters are displayed in Table 7.3. The structure is that expected from ring-opening of the [2 + 2]-cycloadduct of one of the $=C(CN)_2$ double bonds with the outer C≡C triple bond of the precursor diynyl complex. Thus, the ruthenium centre is attached to the remaining C≡C triple bond [Ru-C(1) 1.939(12), C(1)-C(2) 1.21(2) Å] which in turn is a substituent on the dienyl system C(31)=C(3)-C(4)=C(41). The structure determination reveals that the C_6 quinoid group is attached to C(3), i.e., nearer to the electron-rich metal centre, with the $=C(CN)_2$ group being attached to C(4). This mode of addition was previously found in reactions of TCNQ with $Ni(C{\equiv}CR)(PPh_3)Cp$[8] and $Ru\{C{\equiv}CC{\equiv}CC{\equiv}C[CCo_3(\mu\text{-}dppm)(CO)_7]\}(dppe)Cp^*$.[9] No evidence was found for the formation of any isomeric product resulting from the alternative mode of addition.

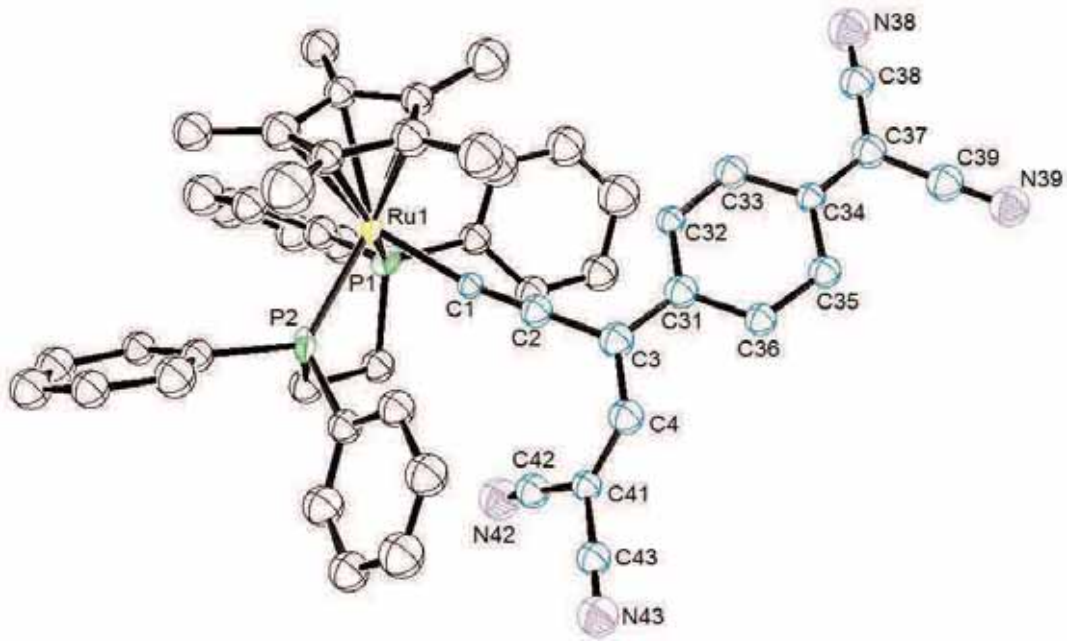

Figure 7.5. *Plot of a molecule of Ru{C≡CC[=C$_6$H$_4$=C(CN)$_2$]CH=C(CN)$_2$}(dppe)Cp** ***50***.

Table 7.3. Selected bond parameters for TCNQ complexes **50** and **51**.

Compound	**50**	**51**
	Bond distances (Å)	
Ru(1,2)-P(1,3)	2.294(4)	2.290(1), 2.274(1)
Ru(1,2)-P(2,4)	2.287(4)	2.298(1), 2.277(1)
Ru(1,2)-C(Cp)	2.229-2.301(15)	2.232-2.285(4), 2.235-2.286(4)
(av.)	2.260	2.249, 2.261
Ru(1,2)-C(1,8)	1.939(12)	1.952(4), 1.943(4)
C(1,8)-C(2,7)	1.21(2)	1.233(5), 1.228(5)
C(2,7)-C(3,6)	1.45(2)	1.388(5), 1.395(5)
C(3)-C(31)	1.42(2)	1.425(5)
C(34)-C(37)	1.39(2)	1.409(5)
C(37)-C(38,39)	1.39(2), 1.42(2)	1.418(6), 1.429(6)
C(3,6)-C(4,5)	1.45(2)	1.457(5), 1.464(5)
C(4,6)-C(41,61)	1.35(2)	1.398(5)
C(41,61)-C(42,43;62,63)	1.47(2), 1.43(2)	1.434(6), 1.425(6)
C(4)-C(5)		1.339(5)

Bond angles (°)		
P(1,3)-Ru(1,2)-P(2,4)	83.5(1)	85.10(4), 83.63(4)
P(1,3)-Ru(1,2)-C(1,8)	79.2(4)	85.7(1), 82.2(1)
P(2,4)-Ru(1,2)-C(1,8)	88.6(4)	82.6(1), 85.6(1)
Ru(1,2)-C(1,8)-C(2,7)	166.9(1)	176.0(4), 178.8(3)
C(1,8)-C(2,7)-C(3,6)	178.8(2)	173.1(4), 177.1(4)
C(2,7)-C(3,6)-C(4,5)	116.8(1)	119.7(4), 119.5(4)
C(2,7)-C(3,6)-C(31,61)	120.2(1)	119.6(4), 120.6(4)
C(34)-C(37)-C(38,39)	124.6(1), 115.7(1)	122.9(4), 118.7(4)
C(3)-C(4)-C(41)	126.8(1)	
C(4;6)-C(41;61)-C(42,43;62,63)	123.4(1), 120.9(1)	121.0(4), 122.0(4)
C(3)-C(4)-C(5)		125.1(4)
C(4)-C(5)-C(6)		121.6(4)
C(4)-C(3)-C(31)		120.7(3)
C(5)-C(6)-C(61)		119.9(4)

A different product was formed when the reaction between TCNQ and Ru(C≡CC≡CH)(dppe)Cp* was carried out in benzene, namely dark brown Cp*(dppe)Ru{C≡CC[=C_6H_4=C(CN)$_2$]CH=CHC[=C(CN)$_2$]C≡C}Ru(dppe)Cp* **51**, also obtained in low yield. The dimeric formulation was confirmed by high resolution ES-MS where $[M + H]^+$ was found at *m/z* 1573.3752 (calculated: 1573.3812), and the two Ru(dppe)Cp* groups could be distinguished in the NMR spectra. Thus, in the ^{1}H NMR spectrum, two Cp* resonances are at δ_H 1.51, 1.53 and two dppe CH_2 signals are at δ_H 1.99-2.12 (4H) and 2.68, 2.82 (2 x 2H). In the ^{13}C NMR spectrum, the two Cp* groups give Me resonances at δ_C 10.28, 10.41 and ring C signals at δ_C 95.56 and 96.62. There are also two broad Ru-C triplet resonances at δ_C 191.89 and 210.57. The four CN signals were displayed between δ_C 114.43 and 118.95. Two ^{31}P signals at δ_P 80.7, 81.8 arise from the two dppe ligands. The IR spectrum was similar to that of **50**, with ν(CN) (2186), two ν(C≡C) (1983, 1947) and ν(C=C) (1579 cm^{-1}) bands.

Figure 7.6 is a plot of a molecule of **51** showing two Ru(dppe)Cp* groups at each end of a C_8 chain which bears the =C(CN)$_2$ and =C_6H_4=C(CN)$_2$ components of TCNQ attached to C(6) and C(3), respectively [C(6)-C(61) 1.398(5), C(3)-C(31) 1.425(5) Å]. The C(4)=C(5) fragment [1.339(5) Å] carries one H atom on each carbon, with angles C(3)-C(4)-C(5), C(4)-C(5)-C(6) 125.1(4), 121.6(4)°, respectively. The ruthenium atoms are attached to C(1) and C(8) of the two end C≡C triple bonds [Ru(1)-C(1) 1.952(4), Ru(2)-C(8) 1.943(4), C(1)-C(2) 1.233(5), C(7)-C(8) 1.228(5) Å].

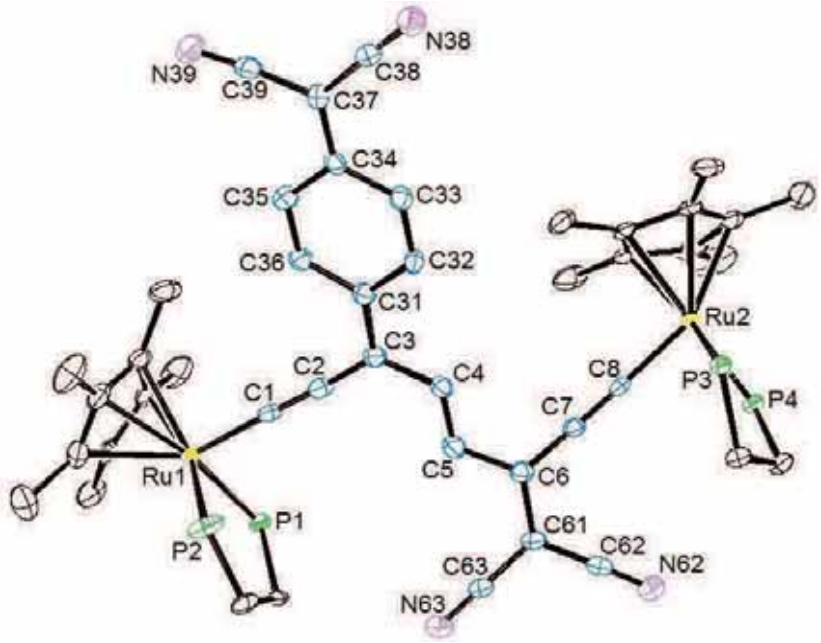

Figure 7.6. *Plot of a molecule of Cp*(dppe)Ru{C≡CC[=C$_6$H$_4$=C(CN)$_2$]CH=CHC[=C(CN)$_2$]C≡C}Ru(dppe)Cp* **51** (the phenyl rings of the dppe ligands have been omitted for clarity).*

In considering a possible mechanism of formation of **51**, which is interesting in that addition occurs to the butadienyl C=C double bond rather than to the other C$_6$=C(CN)$_2$ moiety of the TCNQ, we note that the two components of the original TCNQ reactant are now separated by the -CH=CH- fragment, so that it is unlikely that **51** was formed by addition of TCNQ to an Ru-(C≡C)$_4$-Ru precursor, perhaps formed by oxidative coupling of the diynyl complex. Instead we favour a reaction in which a molecule of **50** reacts with a second molecule of the diynyl-ruthenium complex, with a [2 + 2]-cycloaddition to the =C(CN)$_2$ fragment, followed by the usual ring-opening step (Scheme 7.5). This mechanism has been confirmed by reacting one equivalent of the mononuclear complex **50** with one equivalent of TCNQ in THF. After purification and comparison with a pure sample, the di-ruthenium complex **51** was obtained in 56% yield.

Reaction of TCNQ with M(C≡CC≡CPh)(dppe)Cp*

A rapid colour change from orange / yellow to dark purple / blue (respectively) followed the addition of TCNQ to solutions of M(C≡CC≡CPh)(dppe)Cp* (**2a**, M = Fe; **4** M = Ru) in THF at room temperature. Purification by precipitating the product by addition of hexane to the reaction mixture (M = Fe) or by preparative t.l.c. (M = Ru), afforded dark

purple (M = Fe) and dark blue (M = Ru) M{C≡CC[=C_6H_4=C(CN)$_2$]CPh=C(CN)$_2$}(dppe)Cp* (**52a**: M = Fe, **52b**: M = Ru) in moderate yields (Scheme 7.6). In the IR spectrum, ν(CN), ν(C≡C) and ν(C=C) bands are found at 2223 and 2183, 1914, 1579 and 2194, 1946, 1585 cm^{-1}, respectively, for **52a** and **52b**, respectively.

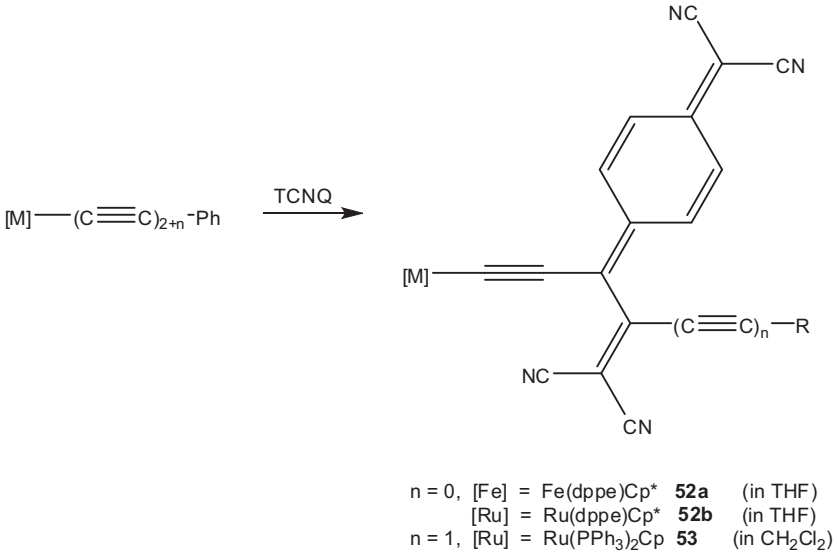

Scheme 7.6. *Reactions of M{(C≡C)$_{2+n}$Ph}(PP)Cp′ [n = 0, M = Fe, Ru, (PP)Cp′ = (dppe)Cp*; n = 1, M(PP)Cp′ = Ru(PPh$_3$)$_2$Cp] with TCNQ.*

In the NMR spectra of **52a**, resonances for the Cp* ligand were found at δ_H 1.21 and δ_C 9.52, 96.54, while for the CH_2 of the dppe, a well-resolved triplet was displayed at δ 30.87 ($^1J_{PC}$ = 22 Hz) in the ^{13}C NMR spectrum. In the ^{31}P NMR spectrum, singlet corresponding to the two equivalent phosphorus atoms of the dppe was found at δ 94.3. In the ^{13}C NMR spectrum, the C_α was displayed at δ 244.90 as a triplet ($^2J_{PC}$ = 35 Hz) and the signals corresponding to the four CN groups were observed at δ 112.85, 113.01, 120.30 and 121.14 (4 x s). Similar features were found in the ^{1}H, ^{13}C and ^{31}P NMR spectra of **52b**, containing the expected resonances for the Cp* (δ_H 1.53, δ_C 10.24, 98.17), dppe [δ_H 2.22, δ_C 30.01-30.62, δ_P 80.5 (br)] and Ph (δ_H 6.96-7.50, δ_C 128.38-137.47) groups. In addition, the ^{13}C NMR spectrum contains resonances at δ_C 58.28, 83.18, 150.24, 153.81, 171.56 assigned to carbons in the butadienyl skeleton, four resonances between 113.03 and 123.20, assigned to CN groups, and a broad down-field signal at δ 217.10, arising from the Ru-bonded carbon.

The single-crystal X-ray diffraction molecular structure determinations of **52a** and **52b** are presented in Figure 7.7 while key parameters are collected in Table 7.4. The X-ray structures showed that the product is a butadienyl formed from the undetected [2 + 2]-cycloadduct with the outer C≡C triple bond, very similar to **50**. The $=C_6H_4=C(CN)_2$ and $=C(CN)_2$ fragments from the TCNQ are bonded to C(3) [C(3)-C(31) 1.423(4) for **52a** and 1.430(9) Å for **52b**] and C(4) [C(4)-C(41) 1.359(4) for **52a** and 1.341(9) Å for **52b**], the diene again being non-planar.

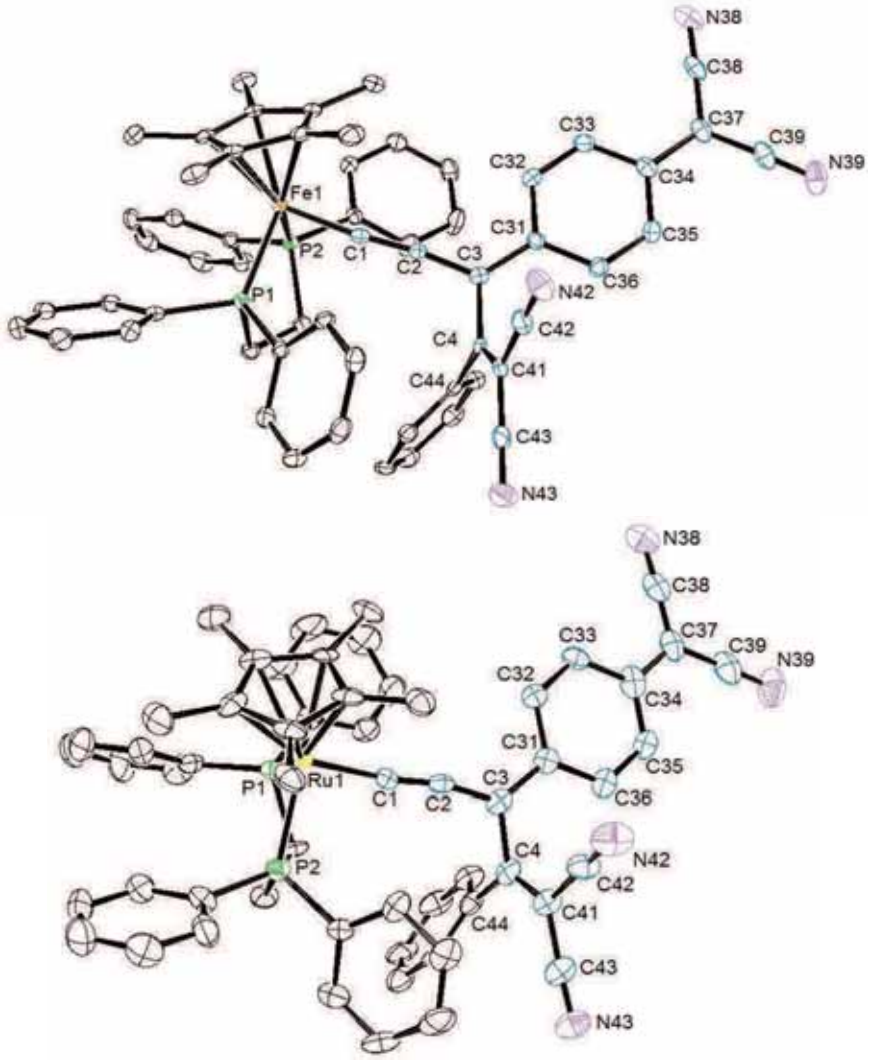

Figure 7.7. *Plots of a molecule of Fe{C≡CC[=C_6H_4=C(CN)$_2$]CPh=C(CN)$_2$}(dppe)Cp* **52a** (top) and a molecule of Ru{C≡CC[=C_6H_4=C(CN)$_2$]CPh=C(CN)$_2$}(dppe)Cp* **52b** (bottom).*

Table 7.4. Selected bond parameters for the TCNQ complexes **52a** and **52b**.

Compound	**52a**	**52b**
	Bond distances (Å)	
M-P(1)	2.2186(8)	2.287(2)
M-P(2)	2.2160(8)	2.292(2)
M-C(Cp*)	2.122-2.156(2)	2.230-2.281(6)
(av.)	2.141	2.259
M-C(1)	1.811(3)	1.943(6)
C(1)-C(2)	1.251(4)	1.223(9)
C(2)-C(3)	1.383(4)	1.370(9)
C(3)-C(4)	1.494(4)	1.497(9)
C(4)-C(44)	1.480(4)	1.480(10)
C(3)-C(31)	1.423(4)	1.430(9)
C(4)-C(41)	1.359(4)	1.341(9)
C(41)-C(42,43)	1.439(4), 1.433(4)	1.452(10), 1.450(10)
C(34)-C(37)	1.418(4)	1.410(10)
C(37)-C(38,39)	1.416(4), 1.426(4)	1.400(11), 1.419(11)
	Bond angles (°)	
P(1)-M-P(2)	85.97(3)	82.69(6)
P(1)-M-C(1)	89.59(9)	84.5(2)
P(2)-M-C(1)	82.96(8)	89.8(2)
M-C(1)-C(2)	174.3(2)	172.3(5)
C(1)-C(2)-C(3)	172.6(3)	169.0(6)
C(2)-C(3)-C(4)	112.7(2)	113.2(6)
C(2)-C(3)-C(31)	125.3(3)	127.0(6)
C(3)-C(4)-C(41)	120.4(2)	120.3(6)
C(3)-C(4)-C(44)	116.4(2)	115.1(6)
C(34)-C(37)-C(38,39)	121.3(3), 120.3(3)	121.2(7), 121.3(7)
C(4)-C(41)-C(42,43)	121.8(3), 122.7(3)	120.5(6), 124.2(7)

The usual M(dppe)Cp* moiety is attached to C(1) of the alkynyl-butadiene group [Fe-C(1) 1.811(3), C(1)-C(2) 1.251(4) and Ru-C(1) 1.943(6), C(1)-C(2) 1.223(9) Å for **52a** and **52b**, respectively]. Of interest is the contraction of the M-C bond from the ca 1.88 (M = Fe) and 2.00 Å (M = Ru) expected for an M-C(sp) bond [cf. 1.894(3) and 2.011(4) Å in M(C≡CPh)(dppe)Cp* for M = Fe[19] and M = Ru[20], respectively], supporting a contribution to the structure from the zwitterionic formulation, with positive charge centred on the metal centre, resulting in some multiple bond character for the M-C(1) link. The localisation of negative charge on the furthest $=C(CN)_2$ group is also indicated by the shortening of C-C bonds [C(37)-C(38,39) 1.416(4), 1.426(4) and 1.400(11), 1.419(11) for **52a** and **52b**, respectively], compared with the values found for C-C bonds in the closest $=C(CN)_2$ group [C(41)-C(42,43) 1.439(4), 1.433(4) and 1.452(10), 1.450(10) for **52a** and **52b**, respectively].

The cyclic voltammogram of **52b** has been recorded for comparison with the CV of the starting material Ru(C≡CC≡CPh)(dppe)Cp* (**4**) (Chapter 2) and is presented in Figure 7.8. Four redox processes are observed: two fully reversible in reduction at E^0_2 = -0.41 and E^0_1 = -0.62 V, one in oxidation being irreversible at E^0_4 = +0.67 V and as found in **47**, an additional small redox processes at E^0_3 = +0.18 V. The irreversible oxidation wave is assigned to the 1-e oxidation of the electron-rich metal centre. This oxidation process is shifted toward higher potentials in comparison with the CV of **4** where an irreversible wave is observed at E^0 = +0.44 V, indicating that **52b** is more difficult to oxidise than **4** by ca 0.2 V. As for **47**, this is due to the strongly electron-withdrawing cyanocarbon ligand capturing electron density from the electron-rich metal centre. The reduction waves are assigned to the two successive reversible 1-e reductions of the cyanocarbon ligand. These observations also suggest a strong contribution from a mesomeric form with positive charge centred on the metal moiety and negative charge mainly localised on the C_6H_4=C(CN)$_2$ group (rather than on the =C(CN)$_2$ group as shown by the X-ray data).

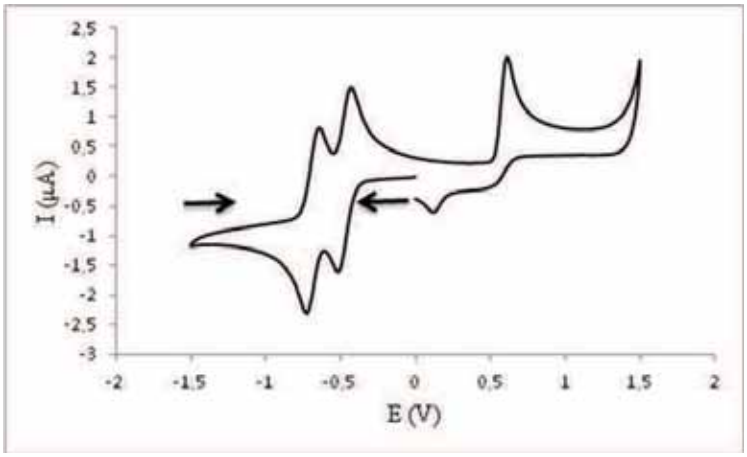

Figure 7.8. *Cyclic voltammogram of **52b** (V vs SCE).*

Reaction of TCNQ with Ru(C≡CC≡CC≡CPh)(PPh$_3$)$_2$Cp

Addition of TCNQ to a solution of Ru(C≡CC≡CC≡CPh)(PPh$_3$)$_2$Cp in dichloromethane resulted in immediate change of colour to dark blue, the complex Ru{C≡CC[=C_6H_4=C(CN)$_2$]C[=C(CN)$_2$]C≡CPh}(PPh$_3$)$_2$Cp **53** being precipitated by addition of hexane to the concentrated reaction mixture (Scheme 7.6). The composition was confirmed by a high resolution ES-MS where $[M + H]^+$ was found at *m/z* 1045.2221 (calculated: 1045.2163). In the IR spectrum, ν(CN), ν(C≡C) and ν(C=C) bands are found at

2198, 1956 and 1590 cm^{-1}, respectively. The usual signals are present in the ^{1}H and ^{31}P NMR spectra [at δ_H 4.64 (Cp), 7.01-7.52 (Ph + C_6H_4), δ_P 48.0], while the ^{13}C NMR spectrum has resonances at δ_C 88.86 (Cp), 127.98-136.80 (Ph + C_6H_4) and 217.99 (Ru-C, t), together with several other cyanocarbon ligand signals (skeleton + 4 x CN) between δ_C 61.77 and 154.05.

Figure 7.9 is a plot of a molecule of **53** while selected structural parameters are collected in Table 7.5. It can be seen that the $=C_6H_4=C(CN)_2$ fragment is attached to C(3) [C(3)-C(31) 1.412(2) Å] and the $=C(CN)_2$ group to C(4) [C(4)-C(40) 1.361(2) Å], i.e., the central two carbons of the C_6 chain in the triynyl precursor. Consequently, the $Ru(PPh_3)_2Cp$ and Ph groups are attached to the C≡C groups at the ends of the chain [Ru-C(1) 1.931(1), C(1)-C(2) 1.248(2), C(5)-C(6) 1.208(2), C(6)-C(61) 1.429(2) Å]. In general, this structure has features similar to the others already discussed. Notable here, however, is the bending of the C_6 chain. Angles at individual C(sp) [C(1,2,5,6)] and at C(sp^2) atoms [C(3,4)] sum to 151.2° from linear in a cumulative sense.

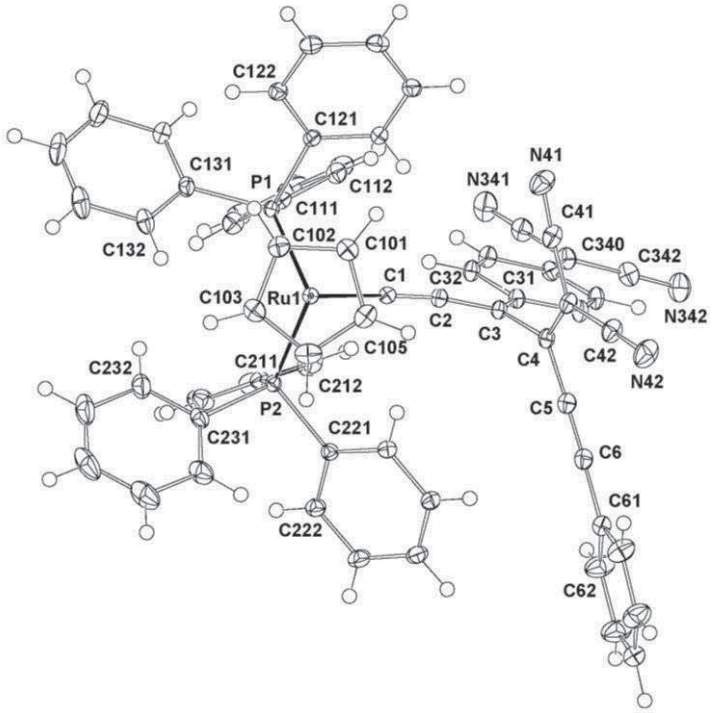

Figure 7.9. *Plot of a molecule of* *$Ru\{C{\equiv}CC[{=}C_6H_4{=}C(CN)_2]C[{=}C(CN)_2]C{\equiv}CPh\}(PPh_3)_2Cp$* ***53***.

Table 7.5. Selected bond parameters for TCNQ complex **53**.

Bond distances (Å)		Bond angles (°)	
Ru-P(1)	2.3059(3)	P(1)-Ru-P(2)	102.91(1)
Ru-P(2)	2.3100(3)	P(1)-Ru-C(1)	89.68(4)
Ru-C(cp)	2.235-2.266(1)	P(2)-Ru-C(1)	89.21(4)
(av.)	2.249	Ru-C(1)-C(2)	174.7(1)
Ru-C(1)	1.931(1)	C(1)-C(2)-C(3)	169.9(1)
C(1)-C(2)	1.248(2)	C(2)-C(3)-C(4)	114.1(1)
C(2)-C(3)	1.379(2)	C(2)-C(3)-C(31)	125.7(1)
C(3)-C(4)	1.497(2)	C(3)-C(4)-C(5)	120.0(1)
C(3)-C(31)	1.412(2)	C(3)-C(4)-C(40)	120.4(1)
C(4)-C(40)	1.361(2)	C(4)-C(5)-C(6)	174.8(1)
C(4)-C(5)	1.416(2)	C(5)-C(6)-C(61)	175.3(2)
C(5)-C(6)	1.208(2)	C(34)-C(340)-C(341,342)	121.8(1), 120.7(1)
C(6)-C(61)	1.429(2)	C(340)-C(341)-C(342)	117.5(1)
C(340)-C(341, 342)	1.420(2), 1.422(2)	C(4)-C(40)-C(41,42)	122.9(1), 120.8(1)
C(40)-C(41,42)	1.430(2), 1.431(2)		

7.3.4 Discussion

The chemistry described above and summarised in Schemes 7.2-6 allows a comparison between the well-established reactions of TCNE with alkynyl-ruthenium complexes Ru(C≡CR)(PP)Cp' [3b-e] and those of the more potent oxidising agent TCNQ, for which until now, there has been only a cursory examination of related chemistry. Based upon experience with TCNE (summarised in Scheme 7.1), one might expect reactions of TCNQ with alkynyl-metal complexes (Scheme 7.7) to produce initial adducts such as **F** and **G** which evolve to complexes formed by (i) [2 + 2]-cycloaddition of the electron-deficient C=C double bonds with the C≡C triple bond in the complexes to give the cyclobutenyls **H**, which might be followed by (ii) a ring-opening (retro-electrocyclic) reaction to afford the corresponding butadienyls **I**; (iii) subsequent chelation of the diene to the metal centre to give **J** may occur if a ligand can be displaced easily. We note that with TCNE, the reaction may be preceded by formation of a short-lived deeply-coloured intermediate, which in a few cases, has been shown to be EPR-active, and thus formulated as a radical species[3c]. Alternatively, following the recently described precedent, (iv) displacement of a CN group (lost as HCN) from one of the cyano-alkene fragments may occur to afford **K**[14].

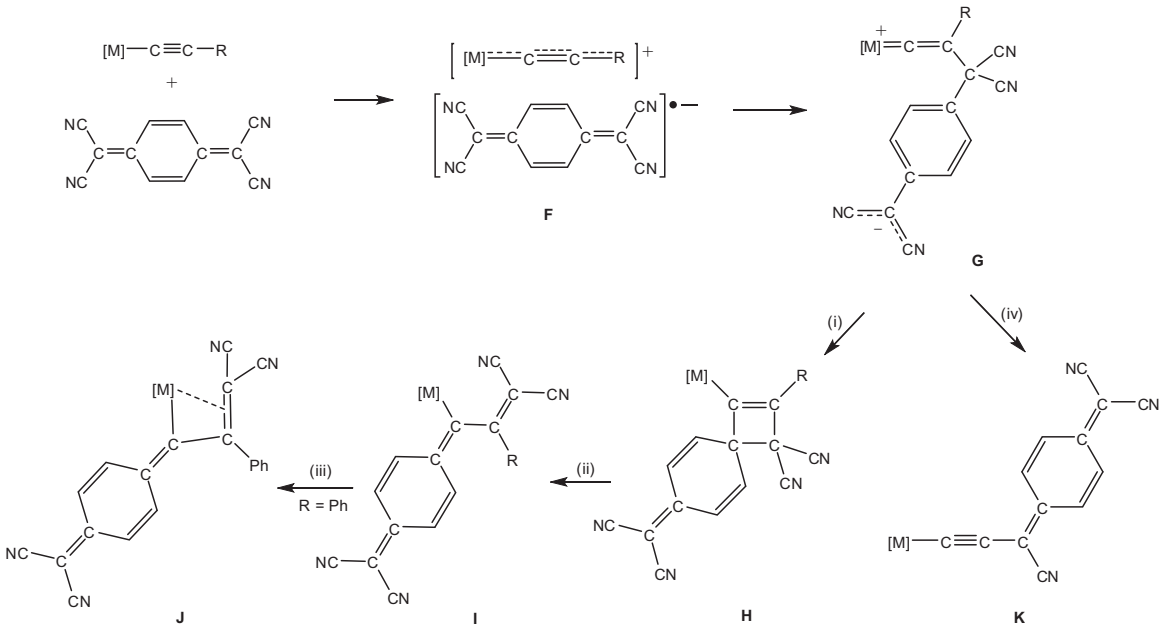

Scheme 7.7. *Possible courses of reactions of TCNQ with alkynyl-metal complexes. (i) [2 + 2]-cycloaddition; (ii) ring-opening; (iii) displacement of a ligand from metal centre; (iv) loss of HCN.*

Reactions between the oxidising agent TCNQ and metal-alkynyl complexes afford initially the 17-e intermediate **F**, which have been characterised in some iron examples[4, 10a] (Scheme 7.2). However, both 17-e species $[Ru(C{\equiv}CPh)(PPh_3)_2Cp]^{\bullet+}$ (**16**$^{\bullet+}$) and $[Fe(C{\equiv}CC{\equiv}CPh)(dppe)Cp^*]^{\bullet+}$ (**2a**$^{\bullet+}$), which were studied in Chapters 3 and 4 with a PF_6^- anion instead of a $[TCNQ]^{\bullet-}$ radical anion found in this work, dimerised by intermolecular radical coupling to afford dimers **17** and **27a**, respectively. When TCNQ is used as the oxidising agent, dimerisation does not occur; dimers **17** and **27a** were undetected in the reaction mixtures. Instead, radical coupling between the 17-e species (**16**$^{\bullet+}$ and **2a**$^{\bullet+}$) and the $[TCNQ]^{\bullet-}$ radical anion occurs to give the intermediate **G** which has been isolated as **48** in the ruthenium case, and which further reacted in the iron case to give adduct **I**, isolated as **52a**.

In refluxing THF, the reaction between TCNQ and $Ru(C{\equiv}CPh)(PPh_3)_2Cp$ afforded the η^3-butadienyl complex **49** (represented as **J** in Scheme 7.5)[16]. Tracing the reaction back to the likely cyclobutenyl intermediate **H**, it can be seen that addition has occurred between C_β of the phenylethynyl complex and one methylene carbon of TCNQ, perhaps via an intermediate such as **G**. Cleavage of the C=C double bond then leaves the $C(CN)_2$ group on C_β while the $C_6H_4{=}C(CN)_2$ fragment is attached to C_α. Subsequent cyclisation with

concomitant loss of a PPh_3 ligand affords the product. The reactions and transformations shown in Scheme 7.7 are thus similar to the analogous reactions of TCNE.

Some reactions of TCNE with alkynyl-ruthenium complexes have been noted to proceed with initial development of a deep green colouration, which fades within minutes with formation of the η^1- or η^3-tetracyanobutadienyl complexes. Although the intermediate has not been conclusively identified, EPR studies showed that it is paramagnetic, and it has been assumed that it is a radical species[3c]. The related chemistry of TCNQ does not give any deep coloured intermediates (although several products are notable for their deep purple or green colours), but reaction at room temperature in CH_2Cl_2 gives **G** in which is formed by attack of TCNQ at C_β, but not followed by cycloaddition. The first-formed complex **G** is a zwitter-ion, a vinylidene formed by conventional addition of an electrophile (TCNQ) to C_β of the alkynyl complex. Charge separation is encouraged by localisation of charge on the distant $-C(CN)_2$ group and stabilisation of positive charge on the electron-rich metal centre. The structure of this complex may be related to that of the radical species obtained with TCNE.

For the parent diynyl, heating **G** in refluxing THF results in elimination of HCN to give **K** in which the $-C\equiv C-Ru(PPh_3)_2Cp$ fragment has replaced one CN group. Loss of HCN on heating **46** in refluxing THF to give **K** is similar to the reaction we have described between TCNE and Ru(C≡CH)(dppe)Cp*, which affords only $Ru\{C\equiv CC(CN)=C(CN)_2\}$(dppe)Cp* at room temperature[14]. With less electron-rich metal centres, either mixtures with, or only, the usual [2 + 2]-cycloadduct and ring-opened products are obtained. In the present work, this product with the $Ru(PPh_3)_2Cp$ centre is only obtained after heating and suggests that TCNQ is more prone to nucleophilic substitution of CN than is TCNE.

Reactions of Ph-diynyl- or Ph-triynyl-iron and -ruthenium complexes with TCNQ afford products **52a**, **52b** and **53** in which the cyanocarbon has added to the C≡C triple bond one removed from the metal centre. This may be the result of steric protection of the inner C≡C triple bond, as has been found for similar reactions of TCNE with diynyl- and triynyl-ruthenium derivatives. Only in one case, Ru(C≡CC≡CFc)(dppe)Cp, are two products formed by addition to either C≡C triple bond formed, perhaps either as a result of the smaller size of Cp vs Cp*, or possibly the redox properties of the ferrocenyl group[21].

A similar adduct **50** has been identified as the initial product from the reaction between TCNQ and Ru(C≡CC≡CH)(dppe)Cp*, but this is accompanied by a binuclear adduct **51**. This complex is an adduct of two ruthenium centres to one TCNQ molecule, and we suggest that it is formed by further cycloaddition of a second molecule of Ru(C≡CC≡CH)(dppe)Cp* to **50** and subsequent ring-opening. Indeed, reaction of pure **50** with Ru(C≡CC≡CH)(dppe)Cp* gives **51** in high yield. Formally, this reaction corresponds to insertion of a C≡C triple bond into the =C-H bond present in **50**.

Of interest is the double addition of the alkynyl-ruthenium complex to TCNQ which affords **51**. Double addition of TCNE has been observed previously for $\{Ru(PPh_3)_2Cp\}_2(\mu\text{-}C_8)$ to give $\{Cp(Ph_3P)_2Ru\}C{\equiv}C\{C[=C(CN)_2]\}_4C{\equiv}C\{Ru(PPh_3)_2Cp\}$[22], but this is the first occasion in which double addition of the metal fragment to a single cyanocarbon molecule has been demonstrated. In principle, this mode of action should be available to other tetracyanobutadiene complexes and we note that Diederich and coworkers have described the preparation of oligomeric products formed by double or triple addition of TCNQ[23], and sequential additions of the donor $HC{\equiv}CC_6H_4NMe_2$-4 to the pentacyanobuta-1,3-diene $(NC)_2C{=}C(C_6H_4NMe_2\text{-}4)C(CN){=}C(CN)_2$[24].

The molecular structures of most complexes described above have been confirmed by single-crystal X-ray diffraction studies. General features on the structural parameters of organometallic TCNQ adducts can be drawn. Characteristic values for M-C bonds to C(sp) atoms in alkynyl complexes are ca 1.88 (M = Fe) and 2.00 Å (M = Ru) [cf. 1.894(3) and 2.011(4) Å in M(C≡CPh)(dppe)Cp* for M = Fe[19] and M = Ru[20], respectively] and for M=C(sp) bonds in vinylidenes are ca 1.76 (M = Fe) and 1.85 Å (M = Ru) [cf. 1.763(7) and 1.85(1) Å in $[M(=C{=}CH_2)(dppe)Cp^*]^+$ for M = Fe[25] and M = Ru[15], respectively]. In the seven molecules whose structures are reported, the Ru-C distances range between 1.855(6) Å in **48** and 1.952(4) Å in **51**, and the Fe-C bond length in **52a** is 1.811(3) Å. All are considerably shorter than the M-C(sp) single bond, but approach the value expected for an M=C(sp) double bond in vinylidenes. Consequently, we consider that there is a considerable contribution from the mesomeric zwitter-ionic structure, with charge separation between positively-charged metal centre and the anion stabilised by the distant cyanocarbon group (Scheme 7.8). This will have a further effect upon the geometry of the $=C_6H_4{=}C(CN)_2$ group, which will tend towards the fully aromatic structure.

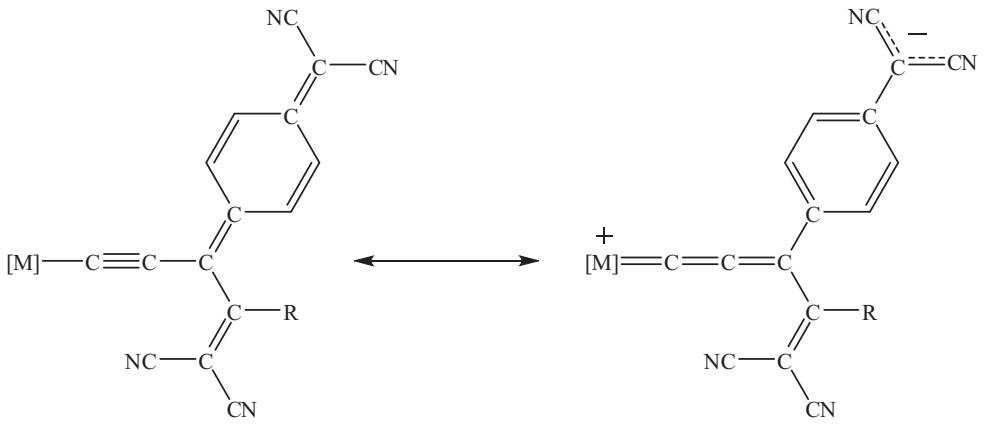

Scheme 7.8. *General mesomeric formulations of TCNQ adducts.*

7.4 Conclusion

Reactions between the electron-poor compound TCNQ and electron-rich metal-alkynyl complexes have been described out in this Chapter. The syntheses, characterisations and X-ray structure determinations of new organometallic complexes containing two electro-active units: one electron donor metal centre and one organic acceptor have been described. The intramolecular charge transfer which takes place in these compounds was probed by X-ray studies, where the M-C and $C(CN)_2$ bonds are shortened, indicating localisation of the positive and negative charge, respectively. For some compounds, this feature has been supported by electrochemistry where the TCNQ adducts were more difficult to oxidise than their parent complexes by ca 0.20 V. For **47**, charge transfer was also confirmed by UV-Vis investigations where remarkable solvatochromism was observed. More UV-Vis and electrochemical studies of all the new complexes synthesised in this Chapter will be the subject of future work in order to investigate the charge transfer transitions and the contribution of mesomeric forms (Scheme 7.8) in them.

There is an interesting contrast between the rich chemistry afforded by the ruthenium systems and the results of reactions of TCNQ with similar iron complexes, which further highlight differences in electronic structures of the two series of complexes. DFT calculations have shown the high tendency for electron density to be centred on the iron atom in these complexes, compared to higher coefficients found on carbon atoms of the chain for ruthenium analogues. Evidently, for the arylethynyl complex, loss of an electron from the iron centre to generate the related cation is preferred over extended conjugation with the unsaturated chain which leads to formation of more electron-rich centres which

can attack the cyanocarbon at the $C(CN)_2$ groups. On the other hand, lengthening of the C(sp) chain allows the iron and ruthenium systems to display similar chemistry, as found here for M(C≡CC≡CPh)(dppe)Cp* (M = Fe, Ru).

Experimental

General experimental conditions are detailed in Chapter 2, Experimental section.

Reagents. $Ru(C{\equiv}CH)(PPh_3)_2Cp$[26], $Ru(C{\equiv}CPh)(PPh_3)_2Cp$[27], $Ru(C{\equiv}CPh)(dppe)Cp^*$[28], $Ru(C{\equiv}CC{\equiv}CH)(dppe)Cp^*$[29], $Ru(C{\equiv}CC{\equiv}CC{\equiv}CPh)(PPh_3)_2Cp$[30], were made by the literature methods. TCNQ was a commercial sample (Aldrich).

Reactions of TCNQ

(i) $Ru(C{\equiv}CH)(PPh_3)_2Cp$.

(a) To a solution of $Ru(C{\equiv}CH)(PPh_3)_2Cp$ (50 mg, 0.07 mmol) in THF (5 ml), TCNQ (14 mg, 0.07mmol) was added, resulting an instantaneous darkening of the solution. After 1 h at room temperature the solvent was removed under reduced pressure to afford $Ru\{=C=CHC(CN)_2C_6H_4C(CN)_2\}(PPh_3)_2Cp$ **46** (74 mg, 95%) as a green powder which decomposed in time. IR (CH_2Cl_2): ν(C≡N) 2180w, 2070m, ν(C=C) 1597m, 1587m cm^{-1}. ^1H NMR ($CDCl_3$): δ 4.24 (s, 5H, Cp), 5.05 (s, 1H,C=C*H*), 7.01-7.57 (m, 34H, Ph). ^{31}P NMR ($CDCl_3$): δ 49.4. ES-MS (*m/z*): 920 $[M]^+$.

(b) Thermolysis of $Ru\{=C=CHC(CN)_2C_6H_4C(CN)_2\}(PPh_3)_2Cp$ (46).

A solution of $Ru\{=C=CHC(CN)_2C_6H_4C(CN)_2\}(PPh_3)_2Cp$ **46** (50 mg, 0.054 mmol) in THF (5 ml) was heated at reflux point for 4 h, after which solvent was removed under reduced pressure. The residue was purified by preparative TLC (acetone/hexane, 3:7) and the turquoise band (R_f = 0.54) was collected to afford $Ru\{C{\equiv}CC(CN){=}C_6H_4{=}C(CN)_2\}(PPh_3)_2Cp$ **47** (4 mg, 8%) as a dark turquoise solid. X-ray quality crystals were obtained from dichloromethane / hexane. Anal. Calcd for $C_{54}H_{39}N_3P_2Ru$: C, 72.64; H, 4.40; N, 4.71. Found: C, 72.66; H, 5.15; N, 4.70. IR (CH_2Cl_2): ν(C≡N) 2201w, ν(C≡C) 1974s, ν(C=C) 1590m cm^{-1}. ^1H NMR ($CDCl_3$): δ 4.62 (s, 5H, Cp), 7.05-7.60 (m, 34H, Ph). ^{13}C NMR ($CDCl_3$): δ 88.83 (s, Cp), 107.56 (s), 114.01 (s), 116.23, 116.98, 117.29 (3 x s, CN), 122.40-139.75 (m, Ph), 148.64 (s), 153.45 (s), 209.94 [t, ^2J(CP) = 22 Hz, Ru-*C*≡). ^{31}P NMR ($CDCl_3$): δ 48.0 (s). ES-MS (*m/z*): calcd for $C_{54}H_{40}N_3P_2Ru$ 894.1741, found 894.1738 $[M + H]^+$.

(ii) Ru(C≡CPh)(PPh$_3$)$_2$Cp.

(a) Addition of TCNQ (20 mg, 0.1 mmol) to a solution of Ru(C≡CPh)(PPh$_3$)$_2$Cp (77 mg, 0.1 mmol) in CH_2Cl_2 (15 ml) resulted an instantaneous darkening of the solution. After 1 h solvent was reduced to approximately 1 ml and hexane (50 ml) was added to give a dark purple precipitate. Purification by preparative t.l.c, (acetone-petroleum spirit-ethyl acetate, 2/2/1) and extraction with acetone of the dark purple band (R_f = 0.24) afforded Ru{=C=CPhC(CN)$_2$C$_6$H$_4$C(CN)$_2$}(PPh$_3$)$_2$Cp **48** as a dark purple powder (21 mg, 41%). Crystals suitable for X-ray study were obtained from C_6H_6 / MeCN. Anal. Calcd for $C_{62}H_{49}N_4P_2Ru.2H_2O$: C, 70.99; H, 4.69; N, 5.43. Found: C, 71.45; H, 4.45; N, 5.45%. IR (nujol): ν(C≡N) 2169s, 2126s; ν(C=C) 1619m, 1595s cm^{-1}. ^{1}H NMR ($CDCl_3$): δ 5.19 (5H, Cp), 6.60-7.49 (39H, Ph). ^{13}C NMR ($CDCl_3$) δ 39.79 [s, *C*(CN)$_2$=C$_6$H$_4$], 95.59 (s, Cp), 96.76, 122.36 [2 x s, =*C*PhC(CN)$_2$ and *C*-], 115.66, 119.75 (2 x s, CN),122.65-131.66 (m, Ph), 342.13 [s (br), Ru=*C*]. ^{31}P NMR ($CDCl_3$): δ 39.0. ES-MS (*m/z*): 996 [M]$^+$, 792 [M - TCNQ]$^+$, 691 [Ru(PPh$_3$)$_2$Cp]$^+$, 429 [Ru(PPh$_3$)Cp]$^+$.

(iii) Ru(C≡CC≡CH)(dppe)Cp*.

(a) In THF. THF (8 ml) was added to a Schlenk flask containing Ru(C≡CC≡CH)(dppe)Cp* (50 mg, 0.073 mmol) and TCNQ (18 mg, 0.088 mmol) to give a dark green solution. After 2 h at room temperature, solvent was removed and the residue was purified by preparative t.l.c (acetone/hexane, 3:7). The green band (R_f = 0.41) was collected to afford Ru{C≡CC[=C$_6$H$_4$=C(CN)$_2$]CH=C(CN)$_2$]}(dppe)Cp***** **50** (6 mg, 9%) as a dark green solid. X ray quality crystals were obtained from benzene/hexane. Anal. Calcd for $C_{52}H_{44}N_4P_2Ru$: C, 70.34; H, 4.99; N, 6.31. Found: C, 70.74; H, 5.16; N, 6.50. IR (CH_2Cl_2): ν(C≡N) 2193w, ν(C≡C) 1940s, ν(C=C) 1586m cm^{-1}. ^{1}H NMR (C_6D_6): δ 1.38 (s, 15H, Cp*), 1.94, 2.57 (2 x m, 4H, CH_2), 6.72 [s, 1H, C*H*=C(CN)$_2$], 7.01-7.42 (m, 24H, Ph). ^{13}C NMR (C_6D_6): δ 9.79 (s, C$_5$*Me$_5$*), 29.42-30.30 (m, dppe), 86.13 (s), 96.61 (s, *C*$_5$Me$_5$), 111.73, 113.89, 117.53, 120.89 (4 x s, CN), 124.75-138.22 (m, Ph), 145.01 (s), 152.70 (s), 155.26 (s), 218.70 [t, ^{2}*J*(CP) = 23 Hz, Ru-*C*≡]. ^{31}P NMR (C_6D_6): δ 80.4 (s). ES-MS (*m/z*): calcd for $C_{52}H_{44}N_4P_2Ru$ 888.2085, found 888.2128 [M]$^+$.

(b) In C$_6$H$_6$. To a solution of Ru(C≡CC≡CH)(dppe)Cp* (50 mg, 0.073 mmol) in benzene was added TCNQ (15 mg, 0.073 mmol); the solution turns slowly from yellow to dark green. After 2 h at room temperature, solvent was removed and the residue was

purified by preparative t.l.c (acetone/hexane, 3:7). The brown band (R_f = 0.38) was collected to afford {Ru(dppe)Cp*}{C≡CC[=C_6H_4=C(CN)$_2$]CH=CHC[=C(CN)$_2$]C≡C}{Ru(dppe)Cp*} **51** (6 mg, 10%) as a dark brown solid. X-ray quality crystals were obtained from benzene/diethyl ether. Anal. Calcd for $C_{92}H_{84}N_4P_4Ru_2$: C, 70.30; H, 5.39; N, 3.56. Found: C, 70.01; H, 5.59; N, 3.52. IR (CH_2Cl_2): ν(C≡N) 2186w, ν(C≡C) 1983s, 1947s, ν(C=C) 1579m cm^{-1}. ^{1}H NMR (C_6D_6): δ 1.51 (s, 15H, Cp*), 1.53 (s, 15H, Cp*), 1.99-2.12 (m, 4H, 2 × CH_2), 2.68, 2.82 (2m, 4H, 2 × CH_2), 6.88-7.63 (m, 46H, Ph and *H*C=C*H*). ^{13}C NMR (C_6D_6): δ 10.28 (s, C_5*Me*$_5$), 10.41 (s, C_5*Me*$_5$), 29.31-30.91 (m, dppe), 77.10 (s), 95.56 (s, *C*$_5$Me$_5$), 96.62 (s, *C*$_5$Me$_5$), 114.43, 117.49, 118.05, 118.95 (4 x s, CN), 121.17 (s), 127.52-153.58 (m, Ph), 191.89, 210.57 [2 × t(br), Ru-*C*≡]. ^{31}P NMR (C_6D_6): δ 80.7 (s), 81.8 (s). ES-MS (*m/z*): calcd for $C_{92}H_{85}N_4P_4Ru_2$ 1573.3812, found 1573.3752 [M + H]$^+$.

Synthesis of 51 from 50.

When THF was added to a Schlenk flask containing Ru{C≡C-C≡C-H}(dppe)Cp* (5 mg, 0.007 mmol) and Ru{C≡C-C[=C_6H_4=C(CN)$_2$]-C[=C(CN)$_2$]-H}(dppe)Cp* **50** (6 mg, 0.007 mmol), the solution became dark brown instantaneously. After 1 h at room temperature, the solvent was removed and the residue was purified by preparative t.l.c (acetone/hexane, 3:7). The brown band (Rf = 0.38) was collected to afford {Ru(dppe)Cp*}$_2$(C≡C-C[=C_6H_4=C(CN)$_2$]-CH=CH-C[=C(CN)$_2$]-C≡C) (6 mg, 56%) as a dark brown solid.

(iv) Fe(C≡CC≡CPh)(dppe)Cp*.

THF (15 ml) was added to a Schlenk flask containing Fe(C≡CC≡CPh)(dppe)Cp* **2a** (200 mg, 0.280 mmol) and TCNQ (57 mg, 0.280 mmol) at -78°C to give a dark purple solution. After 1 h at -78°C, the solution was allowed to warm to room temperature over 4 h. Pentane (50 ml) was then added to the solution and the purple precipitate was filtered off and washed with pentane (3 × 10 ml) to afford Fe{C≡CC[=C_6H_4=C(CN)$_2$]CPh=C(CN)$_2$}(dppe)Cp* **52a** (184 mg, 71%) as a dark purple solid. X-ray quality crystals were obtained from dichloromethane/pentane. Anal. Calcd for $C_{58}H_{48}N_4P_2Fe$, 0.33CH_2Cl_2: C, 73.97; H, 5.18; N, 5.92. Found: C, 74.28; H, 5.18; N, 5.83. IR (KBr): ν(C≡N) 2223w, 2183w, ν(C≡C) 1914s, ν(C=C) 1579m cm^{-1}. ^{1}H NMR ($CDCl_3$): δ 1.21 (s, 15H, Cp*), 1.76-2.42 (m, 4H, PCH_2), 6.85-7.60 (m, 29H, Ph). ^{13}C NMR

($CDCl_3$): δ 9.52 (s, C_5Me_5), 30.87 [t, $^1J_{PC}$ = 22 Hz, dppe], 82.39 (s), 96.54 (s, C_5Me_5), 112.85, 113.01, 120.30, 121.14 (4 x s, CN), 127.86-136.97 (m, Ph), 150.95 (s), 170.97 (s), 178.01 (s), 244.90 [t, $^2J_{PC}$ = 35 Hz, Ru-*C*≡]. ^{31}P NMR ($CDCl_3$): δ 94.3 (s). ES-MS (*m/z*): calcd for $C_{58}H_{49}N_4P_2Fe$ 919.2782, found 919.2786 $[M + H]^+$.

(v) Ru(C≡CC≡CPh)(dppe)Cp*.

When THF (8 ml) was added to a Schlenk flask containing Ru(C≡CC≡CPh)(dppe)Cp* **4** (53 mg, 0.070 mmol) and TCNQ (16 mg, 0.077 mmol), the solution became dark blue instantaneously. After 1 h at room temperature, solvent was removed and the residue was taken up in a small amount of CH_2Cl_2 and purified by chromatography (acetone-hexane, 3/7, silica gel) to afford Ru{C≡CC[=C_6H_4=$C(CN)_2$]CPh=$C(CN)_2$}(dppe)Cp* **52b** (49 mg, 73%) as a dark blue solid (R_f = 0.11). X ray quality crystals were obtained from CH_2Cl_2 / C_6H_6. Anal. Calcd for $C_{58}H_{48}N_4P_2Ru$: C, 72.26; H, 5.02; N, 5.81. Found: C, 71.74; H, 5.11; N, 5.63. IR (CH_2Cl_2): ν(C≡N) 2194w, ν(C≡C) 1946s, ν(C=C) 1585m cm^{-1}. ^{1}H NMR ($CDCl_3$): δ 1.53 (s, 15H, Cp*); 2.22 (m, 4H, CH_2); 6.96-7.50 (m, 29H, Ph). ^{13}C NMR ($CDCl_3$): δ 10.24 (s, C_5Me_5), 30.01-30.62 (m, dppe), 58.28 (s), 83.18 (s), 98.17 (s, C_5Me_5), 113.03, 113.50, 121.33, 123.20 (4 x s, CN), 128.38-137.47 (m, Ph), 150.24 (s), 153.81 (s), 171.56 (s), 217.10 (br, Ru-*C*≡). ^{31}P NMR ($CDCl_3$): δ 80.5 [s(br)]. ES-MS (*m/z*): 965 $[M + H]^+$, 987 $[M + Na]^+$.

(vi) Ru(C≡CC≡CC≡CPh)(PPh_3)$_2$Cp.

TCNQ (41 mg, 0.2 mmol) was added to a solution of Ru(C≡CC≡CC≡CPh)(PPh_3)$_2$Cp (168 mg, 0.2 mmol) in CH_2Cl_2 (20 ml), resulting an instantaneous darkening of the solution. After 1h the volume was reduced to approximately 1 ml and hexane (50 ml) was added to give a dark blue precipitate. The precipitate was collected and then washed with diethyl ether (10 ml) to afford Ru{C≡CC[=C_6H_4=$C(CN)_2$]C(C≡CPh)=$C(CN)_2$}(PPh_3)$_2$Cp **53** (183 mg, 88%) as a dark blue solid. X-ray quality crystals were grown from dichloromethane / MeCN. Anal. Calcd for $C_{65}H_{44}N_4P_2Ru$: C, 74.77; H, 4.25; N, 5.37. Found: C, 74.18; H, 4.86; N, 5.19. IR (CH_2Cl_2): ν(C≡N) 2198w, ν(C≡C) 1956s, ν(C=C) 1590m cm^{-1}. ^{1}H NMR ($CDCl_3$): δ 4.64 (s, 5H, Cp); 7.01-7.52 (m, 39H, Ph). ^{13}C NMR ($CDCl_3$): δ 61.77 (s), 86.75 (s), 88.86 (s, Cp), 90.32 (s), 111.86 (s), 112.90, 113.46 (2 x s, CN), 117.69 (s), 119.91 (s), 121.49, 123.55 (2 x s, CN), 127.98-136.80 (m, Ph), 146.99 (s), 153.86 (s), 154.05 (s), 217.99 [t, ^2J(CP) = 23 Hz, Ru-*C*≡]. ^{31}P NMR ($CDCl_3$): δ 48.0 (s). ES-MS (*m/z*): calcd for $C_{65}H_{45}N_4P_2Ru$ 1045.2163, found 1045.2221 $[M + H]^+$.

References

1. (a) Ward, M. D., *Chem. Soc. Rev.* **1995,** *24*, 121-134; (b) Ward, M. D., *Chem. Ind.* **1996**, p568(6); (c) Paul, F.; Lapinte, C., Unusual Structures and Physical Properties in Organometallic Chemistry. Gielen, M.; Willem, R.; Wrackmeyer, B., Eds. Wiley: New York, 2002; pp 220-279; (d) Demadis, K. D.; Hartshorn, C. M.; Meyer, T. J., *Chem. Rev.* **2001,** *101*, 2655-2686; (e) Brunschwig, B. S.; Creutz, C.; Sutin, N., *Chem. Soc. Rev.* **2002,** *31*, 168-184; (f) Paul, F.; Lapinte, C., *Coord. Chem. Rev.* **1998,** *178-180*, 431-509.
2. (a) Ren, T., *Chem. Rev.* **2008,** *108*, 4185-4207; (b) Schwab, P. F. H.; Smith, J. R.; Michl, J., *Chem. Rev.* **2005,** *105*, 1197-1280; (c) Blum, A. S.; Ren, T.; Parish, D. A.; Trammell, S. A.; Moore, M. H.; Kushmerick, J. G.; Xu, G.-L.; Deschamps, J. R.; Pollack, S. K.; Shashidhar, R., *J. Am. Chem. Soc.* **2005,** *127*, 10010-10011; (d) Ren, T., *Organometallics* **2005,** *24*, 4854-4870; (e) Akita, M.; Koike, T., *Dalton Trans.* **2008**, 3523-3530.
3. (a) Davison, A.; Solar, J. P., *J. Organomet. Chem.* **1978,** *155*, C8-C12; (b) Bruce, M. I., *Aust. J. Chem.* **2011,** *64*, 77–103; (c) Bruce, M. I.; Hambley, T. W.; Snow, M. R.; Swincer, A. G., *Organometallics* **1985,** *4*, 494-500; (d) Bruce, M. I.; Hambley, T. W.; Snow, M. R.; Swincer, A. G., *Organometallics* **1985,** *4*, 501-508; (e) Bruce, M. I.; Humphrey, P. A.; Snow, M. R.; Tiekink, E. R. T., *J. Organomet. Chem.* **1986,** *303*, 417-427.
4. de Montigny, F.; Argouarch, G.; Roisnel, T.; Toupet, L.; Lapinte, C.; Lam, S. C.-F.; Tao, C.-H.; Yam, V. W.-W., *Organometallics* **2008,** *27*, 1912–1923.
5. Kato, S.-i.; Diederich, F., *Chem. Commun.* **2010,** *46*, 1994-2006.
6. Masai, H.; Sonogashira, K.; Hagihara, N., *J. Organomet. Chem.* **1972,** *34*, 397-404.
7. Onuma, K.; Kai, Y.; Yasuoka, N.; Kasai, N., *Bull. Chem. Soc. Jpn* **1975,** *48*, 1696-1700.
8. Butler, P.; Manning, A. R.; McAdam, C. J.; Simpson, J., *J. Organomet. Chem.* **2008,** *693*, 381-392.
9. Bruce, M. I.; Cole, M. L.; Parker, C. R.; Skelton, B. W.; White, A. H., *Organometallics* **2008,** *27*, 3352–3367.
10. (a) Ghazala, S. I.; Paul, F.; Toupet, L.; Roisnel, T.; Hapiot, P.; Lapinte, C., *J. Am. Chem. Soc.* **2006,** *128*, 2463-2476; (b) de Montigny, F.; Argouarch, G.; Costuas, K.; Halet, J.-F.; Roisnel, T.; Toupet, L.; Lapinte, C., *Organometallics* **2005,** *24*, 4558-4572.
11. Lohan, M.; Justaud, F.; Roisnel, T.; Ecorchard, P.; Lang, H.; Lapinte, C., *Organometallics* **2010,** *29*, 4804-4817.
12. Chowdhury, S.; Kebarle, P., *J. Am. Chem. Soc.* **1986,** *108*, 5453-5459.
13. (a) Klots, C. E.; Compton, R. N.; Raaen, V. F., *J. Chem. Phys.* **1974,** *60*, 1177; (b) Compton, R.; Cooper, C. D., *J. Chem. Phys.* **1977,** *66*, 4325.

14. Bruce, M. I.; Burgun, A.; Kramarczuk, K. A.; Nicholson, B. K.; Parker, C. R.; Skelton, B. W.; White, A. H.; Zaitseva, N. N., *Dalton Trans.* **2009**, 33-36.
15. Bruce, M. I.; Ellis, B. G.; Low, P. J.; Skelton, B. W.; White, A. H., *Organometallics* **2003,** *22*, 3184-3198.
16. Bruce, M. I.; Zaitseva, N. N., *unpublished results*.
17. Bruce, M. I.; Fox, M. A.; Low, P. J.; Skelton, B. W.; Zaitseva, N. N., *Dalton Trans.* **2010,** *39*, 3759-3770.
18. Whittall, I. R.; Humphrey, M. G.; Hockless, D. C. R.; Skelton, B. W.; White, A. H., *Organometallics* **1995,** *14*, 3970-3979.
19. Denis, R.; Toupet, L.; Paul, F.; Lapinte, C., *Organometallics* **2000,** *19*, 4240-4251.
20. Paul, F.; Ellis, B. G.; Bruce, M. I.; Toupet, L.; Roisnel, T.; Costuas, K.; Halet, J.-F.; Lapinte, C., *Organometallics* **2005,** *25*, 649-665.
21. Bruce, M. I.; de Montigny, F.; Jevric, M.; Lapinte, C.; Skelton, B. W.; Smith, M. E.; White, A. H., *J. Organomet. Chem.* **2004,** *689*, 2860-2871.
22. Bruce, M. I.; Kelly, B. D.; Skelton, B. W.; White, A. H., *J. Organomet. Chem.* **2000,** *604*, 150-156.
23. Kivala, M.; Boudon, C.; Gisselbrecht, J.-P.; Seiler, P.; Gross, M.; Diederich, F., *Chem. Commun.* **2007**, 4731-4733.
24. Jayamurugan, G.; Gisselbrecht, J.-P.; Boudon, C.; Schoenebeck, F.; Schweizer, W. B.; Bernet, B.; Diederich, F., *Chem. Commun.* **2011,** *47*, 4520-4522.
25. Argouarch, G.; Thominot, P.; Paul, F.; Toupet, L.; Lapinte, C., *C. R. Chimie* **2003,** *6*, 209-222.
26. Bruce, M. I.; Hameister, C.; Swincer, A. G.; Wallis, R. C., *Inorg. Synth.* **1990,** *28*, 270.
27. Bruce, M. I.; Hameister, C.; Swincer, A. G.; Wallis, R. C., *Inorg. Synth.* **1982,** *21*, 82.
28. Bruce, M. I.; Skelton, B. W.; White, A. H.; Zaitseva, N. N., *J. Organomet. Chem.* **2002,** *650*, 141-150.
29. Bruce, M. I.; Ellis, B. G.; Gaudio, M.; Lapinte, C.; Melino, G.; Paul, F.; Skelton, B. W.; Smith, M. E.; Toupet, L.; White, A. H., *Dalton Trans.* **2004**, 1601-1609.
30. Bruce, M. I.; Grelaud, G., *unpublished results*.

General Conclusions and Future Work

The major aim of this thesis, which was to synthesise square molecules containing four redox-active metal centres and two positive charges, has been successfully achieved. To accomplish this goal, the syntheses and characterisation of new mono- and binuclear organo-iron and -ruthenium complexes containing long carbon chains (C_4 and C_6) were achieved. Their physico-chemical properties have been studied and guided by these data, chemical oxidations have been carried out. In some cases, depending on the nature of the metal fragments and the length of the carbon chain, dimerisation occurred to give new multi-nuclear complexes, some of them containing a planar square cyclobutene centre and four metal fragments. These are potential molecular QCA candidates.

For the 17-e species containing a C_2 chain of general formula $[M](C{\equiv}CAr)^{\bullet+}$ (M = Fe(dppe)Cp*, $Ru(PPh_3)_2Cp$), the iron complexes were stable and isolated[1], whereas the ruthenium analogues, which have a larger atomic spin density on the aryl-ethynyl ligand, dimerise. In the case where Ar = phenyl (**16**), dimerisation occurred between the C_β and the C_{para} of the phenyl group to afford the dicationic dimer **17**. When the *para* position is blocked by a methyl group in **19** (Ar = tolyl), dimerisation occurred between C_β and one of the C_{Cp} atoms of the cyclopentadienyl group, where average atomic spin densities were found, to afford the very sensitive dicationic dimer **20**, which decomposed quickly in the presence of air to give the carbonyl dimer **22**. Blocking the C_{para} position on the phenyl group and additionally the C_{Cp} positions (by replacing the Cp by a Cp* ligand) will constitute the next step of this work. By carrying out careful chemical oxidation (no traces of H_2O and O_2), the mononuclear Ru(III) acetylide (Scheme 8.1) might be isolated and characterised by an X-ray determination, which has never been achieved for this type of Ru(III) complex.

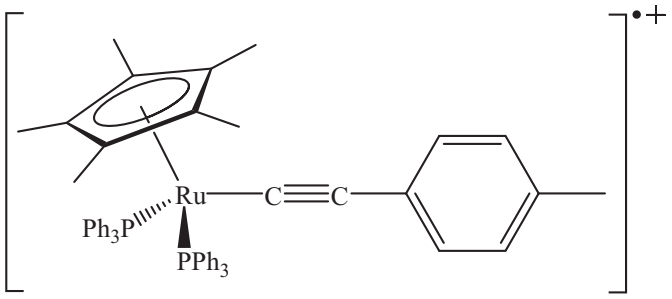

Scheme 8.1. *Hypothetical stable Ru(III) acetylide complex.*

Surprisingly, replacing Ru by Fe in the 17-e complexes containing a C_4 chain of general formula [{Cp'(dppe)M}(C≡CC≡CAr)]$^{\bullet+}$ (M = Fe, Ru; Cp' = Cp, Cp*) did not significantly change the atomic spin density of the butadiynyl ligand. However, replacing the Cp by a Cp* ligand changed the reactivity of the 17-e species (**2a**$^{\bullet+}$) by sterically protecting C_β from coupling. Thus, in contrast to the RuCp example (see Section 4.1.1), dimerisation of the FeCp* species **2a**$^{\bullet+}$ afforded only one symmetric binuclear product containing a planar cyclobutene centre ([**27a**][PF_6]$_2$), which has been characterised by the usual spectroscopic methods and an X-ray structure determination. The iron dimer [**27a**][PF_6]$_2$ showed interesting magnetic properties, unexpectedly being EPR-active, which indicates the existence of a singlet-triplet equilibrium. Further theoretical calculations are under way to rationalise these observations.

Mixed-valence complexes homo- and hetero-nuclear (Fe and Ru) containing a C_6 chain have been synthesised. The 35-e species [**30**]PF_6 and [**34**]PF_6 are stable and isolable, whereas complexes [**31**]PF_6 and [**35**]PF_6, both containing the Ru(dppe)Cp moiety, are kinetically unstable and were only characterised "in-situ" by EPR spectroscopy. For the first time, mixed-valence complexes containing a carbon chain longer than C_4 have been characterised by X-ray analyses (Figure 8.1). Electron transfer within the stable mixed-valence complexes [**30**]PF_6 and [**34**]PF_6 was probed using Near-IR spectroscopy. The diiron complex [**30**]PF_6 was classified as a class III mixed-valence system (strong electron delocalisation), its electronic coupling parameter (V_{ab} = 0.38 eV) correlating well with values found previously for related complexes containing C_4 (V_{ab} = 0.47 eV)[2] and C_8 chains (V_{ab} = 0.32 eV)[3]. However, a vibronic coupling between the intramolecular electron transfer and some of the molecular vibrational states was observed in [**30**]PF_6. Vibronic coupling was also observed in the hetero-nuclear mixed-valence complex [**34**]PF_6, in

which the electronic coupling was surprisingly strong for an unsymmetrical mixed-valence system. Spectroscopic data (IR, EPR and Near-IR) are all consistent with strong electron delocalisation existing in [**34**]PF_6, although it has been reported that electronic coupling in the C_4 analogue complex is weaker[4]. Further experiments investigating solvent effects on the IVCT band are under way.

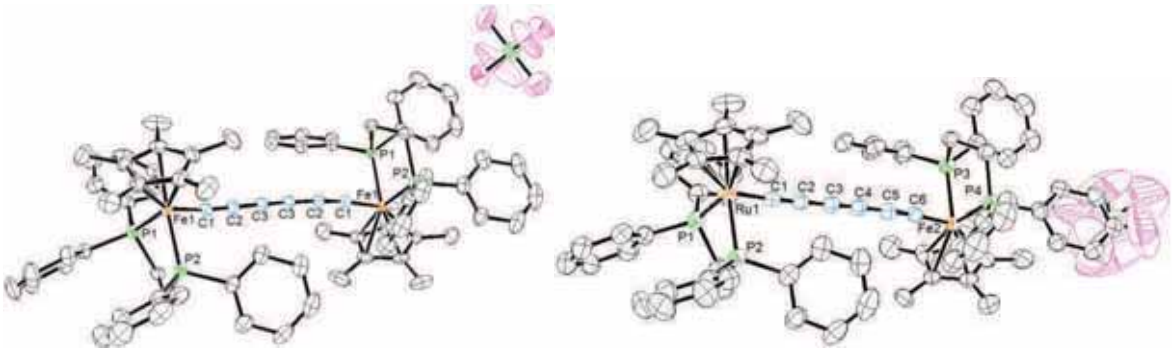

Figure 8.1. *X-ray structures of [{Cp*(dppe)Fe}$_2$(μ-C≡CC≡CC≡C)]PF_6 [**30**]PF_6 (left) and [{Cp*(dppe)Fe}(C≡CC≡CC≡C){Ru(dppe)Cp*}]PF_6 [**34**]PF_6 (right).*

The synthesis of square molecules with four metal centres by radical coupling and carbon-carbon bond formation from mixed-valence species was successfully achieved. Surprisingly, unsymmetrical dimers were formed and the positive charge was found to be fully delocalised over the whole molecule, even in dimer [**44**][PF_6]$_2$ which contains two Fe(dppe)Cp* and two Ru(dppe)Cp fragments (Figure 8.2). The tetraruthenium dimer ([**43**][PF_6]$_2$) could be a model for molecular QCA applications. Even if unsymmetrical, the two charges are fully delocalised, and adding a biasing charge or applying an electric field to the system could localise them on one or the other diagonal. Switching the state could be possible by changing external factors. The hetero-nuclear dimer [**44**][PF_6]$_2$, recently synthesised, was not fully characterised and another dimer [**45**][PF_6]$_2$ might also exist: further work is currently in progress.

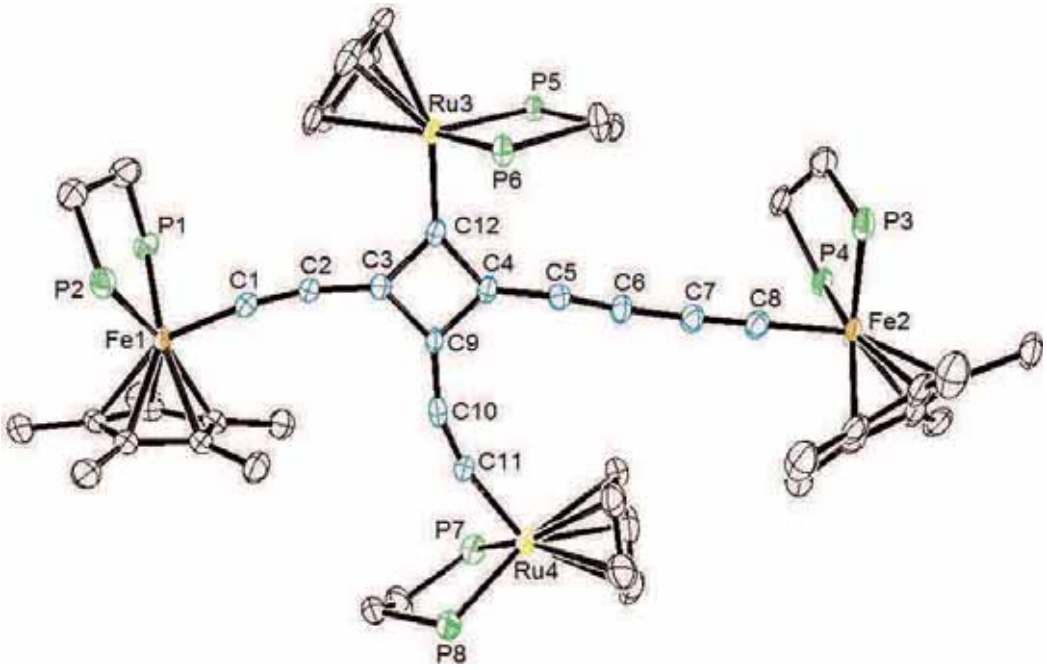

Figure 8.2. *X-ray structure of [{Fe(dppe)Cp*}$_2${Ru(dppe)Cp}$_2${μ-C_{12}}][PF_6]$_2$ [**44**][PF_6]$_2$.*

Finally, from these results and supported by DFT calculations, several conclusions have been drawn. Dimerisation of the mixed-valence complexes is due to the presence of the Ru(dppe)Cp fragment: the ruthenium atom permits the carbon chain to bear large atomic spin densities, especially on the carbon directly attached to the ruthenium; the Cp ligand does not sterically hinder coupling from occurring on the carbon directly attached to the ruthenium. In order to couple, the carbon atom should have an atomic spin density > 0.1.[5] From these conclusions, it might be possible to tune the properties of the mixed-valence complex by choosing appropriate metals and ligands. With the aim of obtaining a symmetrical tetranuclear dimer, we propose to synthesise a symmetrical mixed-valence complex (Scheme 8.2) containing a C_6 chain bridging ruthenium atoms (in order to have a large atomic spin density on the carbon chain), Cp* ligands to prevent the dimerisation occurring on the carbon directly attached to the ruthenium, and a more electron-rich ligand than dppe such as dippe [ethylenebis(diisopropylphosphine)][6], or an NHC, which would hopefully allow a slight increase in atomic spin density of the central carbons > 0.1. The carbons of the central C≡C bond would be reactive and intermolecular radical coupling between these carbons could occur to give a symmetric square dimer containing a central cyclic C_4 centre, four redox-active metal fragments and two positive charges.

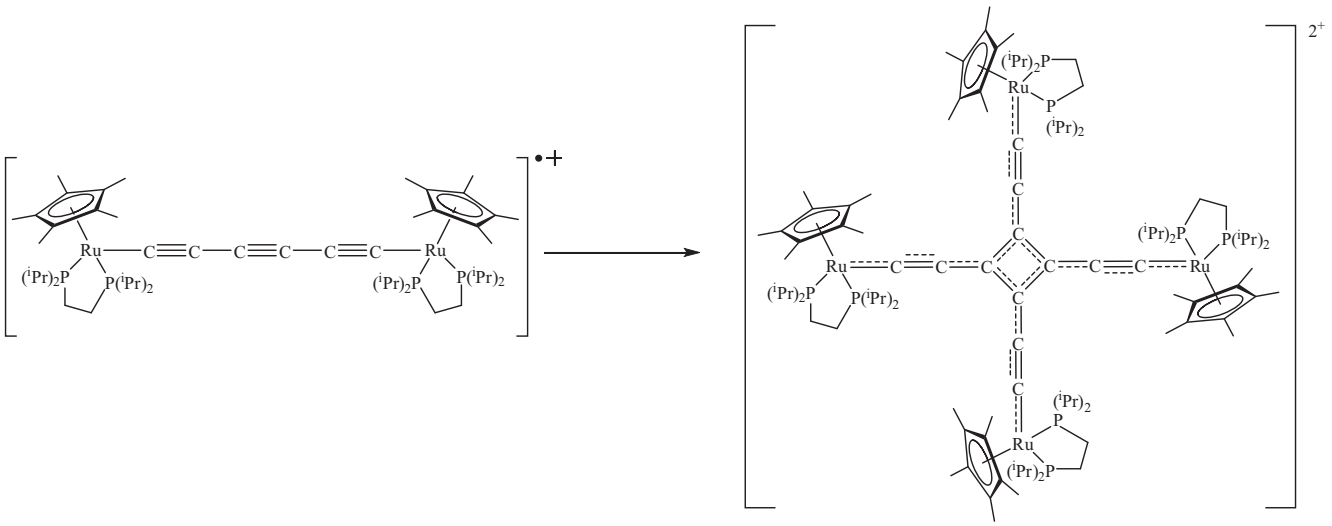

Scheme 8.2. *Proposed mixed-valence complex for the formation of a symmetric tetranuclear dimer.*

References

1. Denis, R.; Toupet, L.; Paul, F.; Lapinte, C., *Organometallics* **2000,** *19*, 4240-4251.
2. Le Narvor, N.; Toupet, L.; Lapinte, C., *J. Am. Chem. Soc.* **1995,** *117*, 7129-7138.
3. Coat, F.; Lapinte, C., *Organometallics* **1996,** *15*, 477-479.
4. Bruce, M. I.; Costuas, K.; Davin, T.; Ellis, B. G.; Halet, J.-F.; Lapinte, C.; Low, P. J.; Smith, M. E.; Skelton, B. W.; Toupet, L.; White, A. H., *Organometallics* **2005,** *24*, 3864-3881.
5. Costuas, K., *personal communication*.
6. Guillemot, M.; Toupet, L.; Lapinte, C., *Organometallics* **1998,** *17*, 1928-1930.